Dust in galaxies throughout cosmic time

Kate Rowlands

The University of Nottingham

Thesis submitted to the University of Nottingham
for the degree of Doctor of Philosophy, April 2013

“ Some part of our being knows this is where we came from. We long to return, and we can, because the cosmos is also within us. We’re made of star stuff. We are a way for the cosmos to know itself.”

– Carl Sagan

Supervisors:	Prof. Alfonso Aragón-Salamanca
	Dr. Loretta Dunne
	Dr. Simon Dye
	Dr. Steve Maddox
Examiners:	Dr. Frazer Pearce
	Dr. David Elbaz

Abstract

One of the most fundamental observational probes of galaxy evolution is determining the build-up of stellar mass. However, around half of all energy ever emitted from galaxies has been absorbed and reprocessed by dust, which is an end-product of stellar evolution. In order to obtain a more complete understanding of galaxy evolution, sensitive observations in the far-infrared and submillimetre are required where the dust emission peaks. Previous surveys have found galaxies were significantly dustier at earlier times, but the cause of this evolution, and the origin of the dust, are hotly debated topics in astrophysics. With the *Herschel Space Observatory*, a complete census of the dusty galaxy population has now recently been obtained. In this thesis I investigate the properties of the diverse dusty galaxy population via a panchromatic approach, utilising data from the UV to the submillimetre to study galaxy evolution.

Using the first unbiased survey of dust in the local Universe, I explore the properties of galaxies in the local Universe as a function of morphology and highlight particularly interesting populations which are traditionally thought to be passive. The star-formation histories, dust content and environments of dusty early-type galaxies and passive spirals are investigated. I show that dusty early-type galaxies comprise a small minority of the general early-type galaxy population (5.5%), and harbour on average 5.5×10^{7} $\mathrm{M}_{\odot}$ of dust, which is comparable to that of some spiral galaxies in our sample. I compare these dusty populations to control samples to investigate how these galaxies are different to the general galaxy population.

High redshift submillimetre galaxies are the most actively star-forming and dusty galaxies in the Universe. Constraining the properties of these galaxies is important for understanding the evolution of massive galaxies and galaxy evolution models in general. Using panchromatic data from the UV to the submillimetre, I explore the

physical properties of a sample of $\sim 250\mu$m rest-frame selected galaxies at high redshift, and compare them to dusty galaxies at low redshift selected in a similar way, to investigate the differences in the dusty galaxy populations over cosmic time. I find high redshift dusty galaxies have significantly higher star-formation rates and dust masses than $z < 0.5$ dusty galaxies selected to have a similar stellar mass. Galaxies which are as highly star forming and dusty as those at $z \sim 2$ are rare in the local Universe. My results support the idea that the most dusty galaxies at high redshift are a heterogeneous population, with around 60% of our sample consistent with secular evolution, and the other 40% of galaxies are starbursting, possibly merger-driven systems.

The origin of dust in galaxies at both low and high redshifts presents a challenge to current theories of galaxy evolution. Recent work has revealed a *'dust budget crisis'*, whereby the mass of dust observed in galaxies at low and high redshift cannot be accounted for by stellar mass loss from low–intermediate mass stars. I tackle this challenge using chemical evolution modelling of the high redshift submillimetre galaxies, with a detailed treatment of the star-formation histories and the dust sources and sinks in these galaxies. It is clear that a significant mass of dust must be from supernovae and/or grain growth; however, the origin of dust in high redshift dusty galaxies remains uncertain. I also consider the impact of inflows and outflows of gas, and the effect of changing the IMF on the physical properties of high redshift dusty galaxies.

Acknowledgements

I would like to thank everyone who has helped and supported me throughout my PhD. Firstly, I thank my supervisors, Loretta, Steve, Alfonso and Simon, for their guidance and support, and for teaching me so many things. I thank Loretta for her great ideas and sharing her passion for all things dusty, and Steve for being a statistical genius. I also thank them for their continued guidance from New Zealand. I am so grateful to Alfonso and Simon, who adopted me as their student part-way through my PhD and put so much effort into supervising a research project that they inherited. Your encouragement during the last few months of writing up helped keep me sane. I am very lucky to have been able to work with all of you. Although it has not been plain sailing all the time, I think this has made me a better scientist in the end. I also thank the astronomers at Cardiff University, especially Haley Gomez, whose inspiring undergraduate tutorials and lectures led me to pursue research of the dusty Universe. Without your encouragement I would not be where I am today.

There are so many people that have shared their knowledge and expertise with me throughout my PhD. I thank Elisabete da Cunha for sharing early versions of MAGPHYS with our *Herschel*-ATLAS research group at Nottingham, and for all her help including creating custom sets of priors for me. I thank Haley Gomez for providing her chemical evolution code, and for her advice on the modifications. Thank you to all of the wonderful people in the *Herschel*-ATLAS and GAMA collaborations who provided insightful comments on my papers, in particular Steve Eales, Simon Driver, Andrew Hopkins, Sugata Kaviraj, Sarah Brough, Anne Sansom, Steven Bamford, Carlos Hoyos and Luca Cortese, and too many more to mention here.

My thanks go to Cafe Alice and her customers for the 11am banter and getting me addicted to excellent coffee (I'm now ruined for life!). Nathan for all his help and

advice, for listening to my insane babbling during my PhD, and for being my dusty partner in crime. I thank Alice and Stuart for keeping me sane, particularly during writing this thesis. I thank Dan for his help with SED fitting and IDL wizardry; and Boris for making the office a fun place to work, for teaching me some new German swear words, and that “it’s not IDL being stupid, it’s you!”. Thank you to my friends Alice, Stuart, Nathan, Emma, Sophie, Lindsay, Sam, Fernando, Ruth, Markus, Ismael, Ana, Evelyn, Cat, Boris, Jamie, Bradley, Will, Ian, Bruno, Adam and the JA for being there to relieve the stress, and for making my time at Nottingham unforgettable. I thank everyone in the Centre for Astronomy and Particle Theory for making the department such a welcoming and enjoyable place to work. I am also grateful for the financial support from the department to go observing to UKIRT and IRAM, and to present my work and meet new people at many conferences. I also acknowledge financial support to attend conferences from the Royal Astronomical Society, the International Astronomical Union and the University of Nottingham Graduate School, and the STFC for financially supporting my PhD.

Thank you to my family and Kieren’s for their unending support in everything that I have done. Thank you to Mum and Dad for accompanying me when I was young to the local Callington astronomy group (whose members nurtured an early interest in astronomy), and for standing around in the freezing cold in the night waiting for the Cornish clouds to clear. Special thanks also goes to Mum, Dad and Kay, who undertook the proof reading of this thesis. My biggest thanks go to Kieren, for his love and support, and for believing in me. Thank you for your patience and understanding with the stressing out, crazy working hours, and jetting off to places without you.

This research has made use of NASA’s Astrophysics Data System, the NASA/IPAC Infrared Science Archive, arxiv.org, the TOPCAT software, the Starlink software packages, the NASA IDL library and David Fanning’s IDL Coyote library.

Publications

The results presented in Chapters 2, 4 and 5 are to be published in Rowlands *et al.* in prep.

The results presented in Chapter 3 have been published in Rowlands *et al.* 2012, MNRAS, 419, 2545.

Contents

List of Figures

List of Tables

Dust in galaxies throughout cosmic time

Chapter 1

Introduction

The current theory of galaxy formation suggests that the growth of structure in the Universe is a result of overdensities in the primordial density fluctuations observed in the cosmic microwave background (CMB). The overdensities were amplified by inflation and dark matter, followed by gas, collapsed under gravity into these regions to form stars and galaxies. One of the most hotly debated topics in astrophysics is the build-up of stellar mass. Galaxies are thought to grow hierarchically, with dark matter halos merging over time to form larger structures (White & Rees, 1978). Simulations have been very successful at reproducing the large-scale distribution of dark matter in the Universe (Springel *et al.*, 2005). However, the processes which govern the evolution of baryons (gas, stars and metals) are far less clear. For example, the stars in galaxies appear to have assembled anti-hierarchically, with the most massive galaxies having older stellar populations, which indicates more massive galaxies formed at earlier epochs (Heavens *et al.*, 2004; Panter *et al.*, 2007; Gallazzi *et al.*, 2008; Pérez-González *et al.*, 2008; Fontanot *et al.*, 2009). In order to understand galaxy evolution we must study the physical properties of galaxy populations over a wide range of cosmic time. This thesis constitutes such a study.

1.1 The diverse nature of galaxies

It has long been known that the galaxy population displays bimodality in many properties, such as colour and morphology. The diversity of galaxy morphologies was first

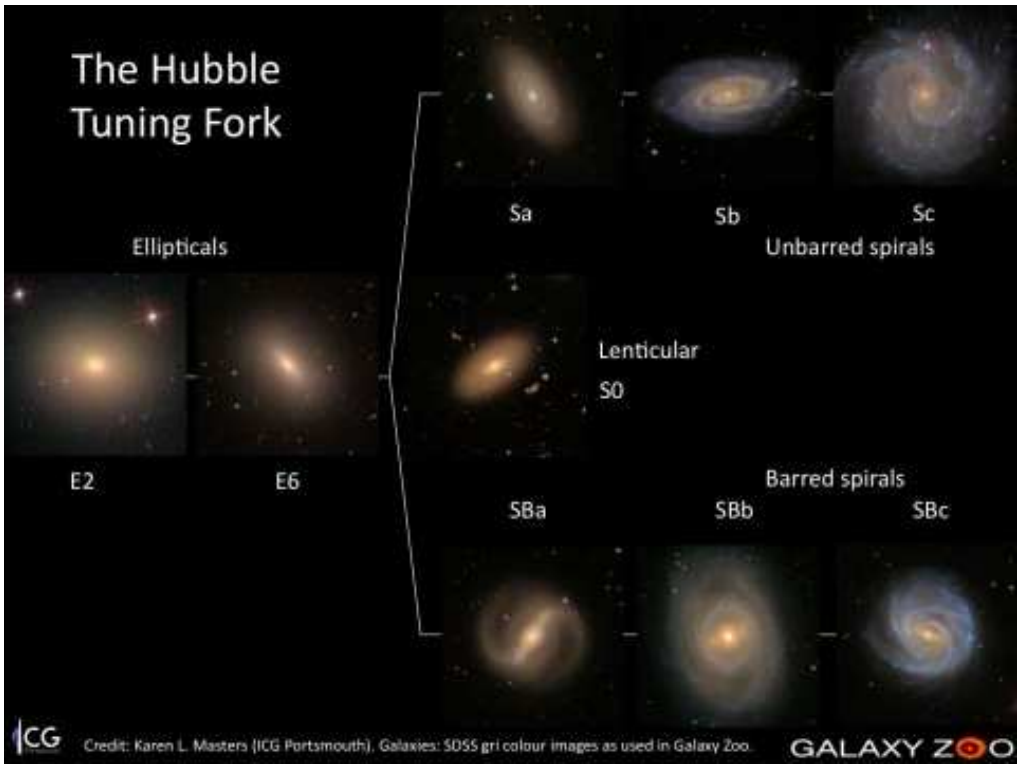

Figure 1.1: Classification of galaxy morphologies according to the Hubble tuning fork. Image credit: Karen Masters and the Galaxy Zoo team.

noted by Hubble (1926), who classified galaxies into early-types and late-types (see Fig. 1.1). Early-type galaxies (ETGs, those that have elliptical or S0 (lenticular) morphology) are smooth in appearance with no visible spiral arms. Late-type or spiral galaxies show clear spiral structure and dust features embedded in a disk. There are branches for spirals with and without bars, with the tightness and prominence of the spiral arms, and bulge size decreasing from Sa to Sc types. Irregular galaxies show no clear structure such as a disk or spheroid. The classifications represent the order of complexity in galaxy structure and do not represent an evolutionary sequence from early to late type.

Morphological evolution can occur through galaxy mergers and interactions, as spheroids can be formed by the merger of two disks (Barnes & Hernquist, 1992). Furthermore, galaxies can be transformed in dense environments, for example, by ram-pressure stripping (Gunn & Gott, 1972), harassment (Moore, Lake & Katz, 1998) and strangulation (Larson, Tinsley & Caldwell, 1980). Many revisions to Hubble's classification scheme have been proposed (e.g. de Vaucouleurs, 1959, 1974; Buta, 2011; Cappellari *et al.*, 2011; Kormendy & Bender, 2012), although the two main distinctions of early and late

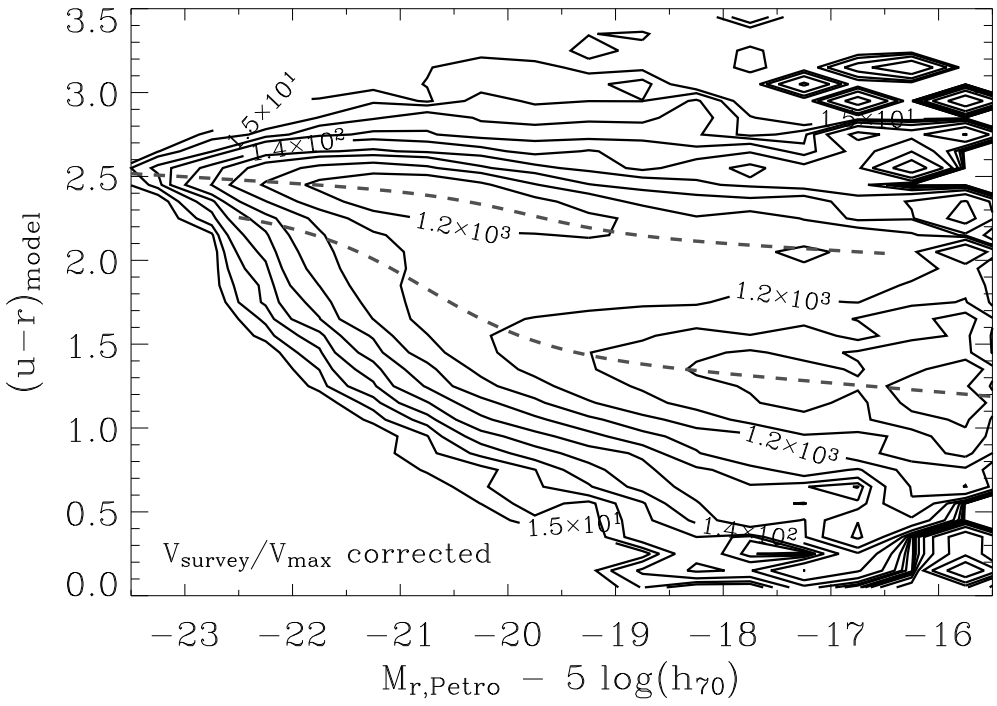

Figure 1.2: The colour bimodality of galaxies is shown in the colour-magnitude diagram. The overdensities in the galaxy distribution are the blue cloud and the red sequence, with a significant number of galaxies occupying an intermediate region known as the green valley. The galaxies in the colour-magnitude diagram have been weighted to account for Malmquist bias. This is where bright galaxies are dominant at greater distances in a flux limited sample (Malmquist, 1922). Figure credit: Baldry *et al.* (2004).

type galaxies defined by Hubble are still widely used. There are many galaxy properties, such as gas and dust content, and star-formation activity that are related to galaxy morphology (see the review in Roberts & Haynes 1994). Current theories of galaxy formation have yet to fully explain the wide range of observed galaxy morphologies. It is therefore important to study galaxy properties as a function of morphology, in order to gain insight into the evolutionary processes which shape galaxies.

In the local Universe, ETGs are generally passive, with negligible ongoing star formation, resulting in a lack of emission lines and red broad-band colours in the optical. Spiral and irregular galaxies typically have strong nebular emission lines and blue optical colours as a result of emission from HII regions and young stars. As with morphology, there is a clear bimodality in galaxy colour (Strateva *et al.*, 2001; Blanton *et al.*, 2003; Baldry *et al.*, 2004; Bell *et al.*, 2004b), with galaxies occupying a red sequence and a blue cloud as shown in Fig. 1.2. There are also galaxies which reside in an intermediate region ("the green valley"), which may have undergone recent quenching of star formation. Alternatively, some galaxies may have experienced rejuvenation of their in-

terstellar medium (ISM) via gas inflow from mergers or accretion (Cortese & Hughes, 2009; Kannappan, Guie & Baker, 2009; Wei *et al.*, 2010), which may drive galaxies from the red sequence towards the blue cloud. The star-formation history (SFH) of galaxies is therefore related to the availability of cold, molecular gas which is the fuel for star formation. ETGs have exhausted or expelled their cold ISM, whereas spirals have retained their gas.

Whilst galaxy colour is broadly linked with morphology, large multiwavelength surveys such as the Sloan Digital Sky Survey (SDSS; York *et al.* 2000) have shown that galaxy mass, along with environment, may be the dominant processes governing galaxy star-formation histories. Massive galaxies are almost always red (Kauffmann *et al.*, 2003a; Bamford *et al.*, 2009; Peng *et al.*, 2010), with a transition mass occurring at $3 \times 10^{10}\mathrm{M}_{\odot}$ (Kauffmann *et al.*, 2003a), below which the majority of the galaxy population have blue optical colours. It is therefore important to study the physical properties of galaxies in order to understand the processes driving star formation and stellar mass growth.

1.2 Star formation in galaxies

The stellar component of galaxies is probed via ultra-violet (UV) to near-infrared (NIR) emission. The bulk of the stellar mass in galaxies is comprised of relatively cool, low-mass stars which are detected in the NIR. In star-forming galaxies, the UV luminosity ($< 0.3\mu$m) is typically dominated by young, hot O and B stars, with a colour temperature of ~ 10000K and lifetimes of $< 10^8$ years. These young stars can be used to probe the star-formation rate (SFR), and therefore the recent mass growth, in galaxies. The UV is the most commonly used tracer of star formation, although nebular emission lines, dust emission in the mid-infrared (MIR) and far-infrared (FIR), X-ray and radio emission can be used (see recent reviews in Kennicutt (1998a), Kennicutt & Evans (2012), and Calzetti 2012). Rest-frame UV emission has been used successfully to trace the SFR of galaxies locally (e.g. Donas & Deharveng, 1984; Kong *et al.*, 2004; Salim *et al.*, 2007), and out to $z \sim 7$, using UV emission redshifted into the optical-NIR (e.g. Giavalisco *et al.*, 2004; Bouwens *et al.*, 2007, 2009, 2011).

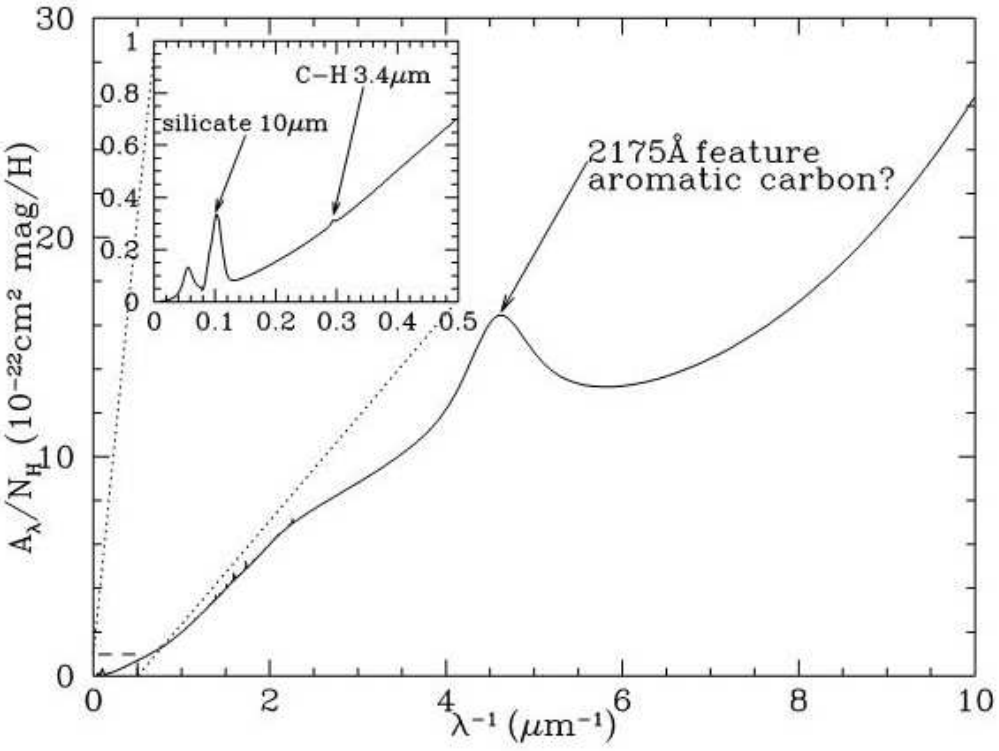

Figure 1.3: The galactic extinction per hydrogen column density (A_λ/N_H) as a function of wavelength for sightline in our Galaxy. The dust species responsible for the feature at 2175Å is not known, but could be due to small graphite grains (Stecher & Donn 1965; Draine & Malhotra 1993). The inset shows the mid-infrared extinction curve. Figure credit: Draine (2011).

One of the main difficulties with observing UV light is that it is absorbed and scattered by dust. The extinction curve describes the absorption and scattering of stellar light due to dust as a function of wavelength (e.g. Cardelli, Clayton & Mathis, 1989; Gordon *et al.*, 2003), as shown in Fig. 1.3. The extinction curve can vary within our galaxy and has a different form in other galaxies such as the Small Magellanic Cloud (Pei, 1992; Gordon *et al.*, 2003), which lacks the 2175Å feature present in the Milky Way extinction curve. The extinction curve shows that UV light is preferentially absorbed and scattered by dust compared to radiation at longer wavelengths, which means that the dust grain size is similar to that of UV radiation.

The effect of dust has a significant effect on the observed spectral energy distribution (SED) of a galaxy. This affects our ability to derive a reliable measurement of the SFR, as a young, dust reddened stellar population can easily be mistaken for an older, dust-free, stellar population. This is known as the age/dust degeneracy. A correction to the observed flux must therefore be made for the amount of dust attenuation. This can be accomplished by estimating the degree of reddening using the UV slope, as this

is correlated with the colour excess[1] Alternatively, emission line ratios such as Hα/Hβ (the Balmer decrement) can be used (e.g. Calzetti, Kinney & Storchi-Bergmann, 1994; Kauffmann *et al.*, 2003a). The best solution is to use a correction derived from a direct measurement of FIR emission from reprocessed starlight (Meurer, Heckman & Calzetti, 1999; Kennicutt, 1998b); using the full SED can therefore give us better constraints on galaxy physical properties. A correction for dust is very important in galaxies which are star forming, as these galaxies tend to require larger extinction corrections (e.g. Meurer, Heckman & Calzetti, 1999; Buat, 2002; Buat *et al.*, 2005; Kong *et al.*, 2004; Cortese *et al.*, 2006, 2008; Johnson *et al.*, 2007). Furthermore, galaxies at higher redshifts have higher levels of star formation (Madau *et al.*, 1996; Lilly *et al.*, 1996; Noeske *et al.*, 2007), and therefore higher infrared luminosities and extinction corrections (Le Floc'h *et al.*, 2005; Bouwens *et al.*, 2009; Magnelli *et al.*, 2009; Murphy *et al.*, 2011; Cucciati *et al.*, 2012).

1.3 The hidden side of galaxy evolution

It has long been known that dust is responsible for the obscuration of starlight in our galaxy (Trumpler, 1930; Oort & van de Hulst, 1946; van de Hulst, 1946). Around half of all energy ever emitted from galaxies has been absorbed and reprocessed by dust (Puget *et al.*, 1996; Dwek *et al.*, 1998; Fixsen *et al.*, 1998), which is an end-product of stellar evolution. Observations in the far-infrared (FIR) and submillimetre, where the dust emission peaks, are needed in order to recover the starlight which is hidden by dust. This is illustrated in Fig 1.4, where the dust in the disk of the galaxy obscures the light from stars but in the infrared the dust re-emits the absorbed starlight. Dust therefore significantly alters the SED of galaxies, a theme which is explored throughout this thesis.

[1]The colour excess is defined as $E(B-V)$; the difference in attenuation in the B band relative to the V band: $E(B-V) \equiv A_B - A_V$.

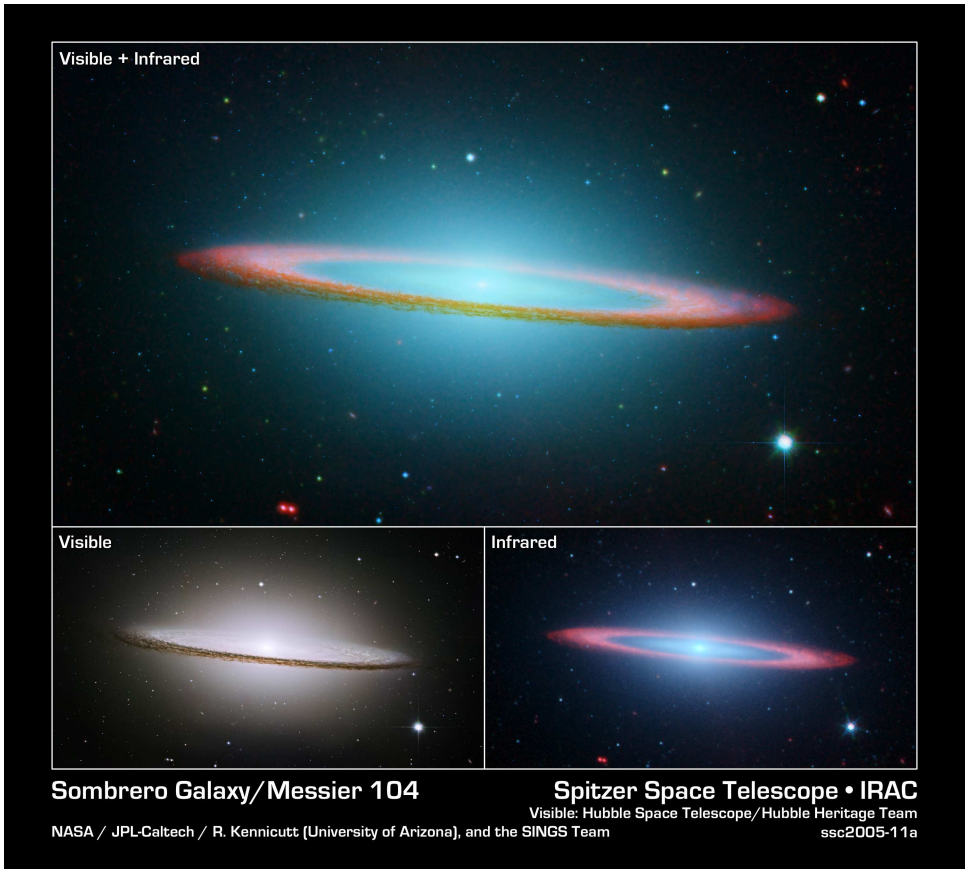

Figure 1.4: Optical and mid-infrared images of M104, a lenticular galaxy. This shows the dust in the disk absorbs and obscures starlight in the optical, but re-emits the light at longer wavelengths. Image credit: HST, Hubble Heritage Team, NASA, JPL-Caltech, R. Kennitcutt and the SINGS team.

1.3.1 What is dust?

Interstellar dust grains are solid particles $0.01 - 1\mu$m in size and are mostly comprised of carbon and silicates (Mathis, Rumpl & Nordsieck, 1977). The smallest dust grains are large molecules known as polycyclic aromatic hydrocarbons (PAHs), comprised of rings of hydrogen and carbon atoms. PAHs and other small grains emit at $3 - 100\mu$m and are thought to be stochastically heated by photons. Larger dust grains are in thermal equilibrium with the interstellar radiation field and emit at $> 100\mu$m, with the peak of the dust emission at $\sim 150\mu$m, depending on the dust heating mechanism. Young, UV-luminous stars heat dust to higher temperatures than older, UV-faint stars. The thermal emission spectrum (S_ν) from a perfect emitter (blackbody) at a temperature T can be described by the Planck function

$$B_\nu(T) = \frac{2h\nu^3}{c}\frac{1}{\exp(h\upsilon/k_BT) - 1}, \tag{1.1}$$

where h is the Planck constant, ν is the frequency of emission, c is the speed of light and k_B is the Boltzmann constant. The emission spectrum of a real emitter (e.g. dust grains) is modified from a blackbody by an emissivity term (e.g. Whittet, 2003), such that

$$S_\nu = Q_{em} B_\nu(T), \tag{1.2}$$

where the emissivity Q_{em} is dependent on frequency ν:

$$Q_{em} \propto \lambda^{-\beta} \propto \nu^{\beta}. \tag{1.3}$$

The value of the emissivity index (β) is thought be related to the composition, size and temperature of the dust grains and is usually in the range 1–2 . A value of $\beta = 2$ is adopted for crystalline materials, with lower values of β expected for more amorphous substances (Tielens & Allamandola, 1987; Whittet, 2003). A value of $\beta \sim 2$ is found for dust grains in our Galaxy (Reach *et al.*, 1995; Paradis *et al.*, 2010; Planck Collaboration *et al.*, 2011), and in other galaxies (Alton *et al.*, 1998; Bianchi *et al.*, 1998; Dunne & Eales, 2001).

The composition and size of the dust grains depends on the properties of the interstellar medium. Dust can form in a chemically-enriched medium when the temperature is relatively cool ($< 2000\,\mathrm{K}$) and dense. The dominant origin of dust in the local Universe is thought to be the relatively cool outer envelopes of low–intermediate mass stars (LIMS, $1 < M < 8\,\mathrm{M}_\odot$) in the asymptotic giant branch (AGB) phase of evolution (Ferrarotti & Gail, 2006). At high redshifts ($z > 5$) there is speculation about the source of dust as there is not enough time for LIMS to evolve to their dust producing phase ($\sim 0.5-1$ Gyr). It has been proposed that supernovae are prolific dust producers at early times (Morgan & Edmunds, 2003; Nozawa *et al.*, 2003; Dunne *et al.*, 2003a, 2009; Gall, Hjorth & Andersen, 2011), as supernovae can produce dust on timescales much shorter than that taken for LIMS to reach the AGB phase. Dust has been detected in Type II supernova remnants (Dunne *et al.*, 2003a; Krause *et al.*, 2004; Sugerman *et al.*, 2006; Gomez *et al.*, 2009; Rho *et al.*, 2008; Barlow *et al.*, 2010; Matsuura *et al.*, 2011; Temim *et al.*, 2012; Gomez *et al.*, 2012b), although evidence for large quanti-

ties of dust in supernova remnants remains controversial. Type Ia supernovae are not thought to contribute significantly to the dust budget (Gomez *et al.*, 2012a).

Dust grains can grow in interstellar clouds by accreting ice mantles which allow metals to stick to the dust grain surface (Tielens & Whittet, 1997). Dust grains are thought to grow in cold and dense ($\sim 10^3$ hydrogen molecules cm^{-3}) molecular clouds (Dwek & Scalo, 1980a), as metals are more depleted in cold clouds than in the warm intercloud medium (Savage & Sembach, 1996). Dust grain growth is thought to occur at both high redshift (Michałowski, Watson & Hjorth, 2010; Hirashita & Kuo, 2011) and at low redshift (Dwek, Galliano & Jones, 2007; Dunne *et al.*, 2011; Inoue, 2012; Kuo & Hirashita, 2012; Mattsson, Andersen & Munkhammar, 2012), leading to a rapid build-up of dust in galaxies. It has also been proposed that dust can form around supermassive black holes (SMBHs) if the surrounding gas clouds are in an outflowing wind. These regions are thought to have conditions similar to those found in the envelopes of AGB stars (Elvis, Marengo & Karovska, 2002). However, it is unclear whether dust produced around SMBHs is a dominant form of dust production at high redshift (Maiolino *et al.*, 2006; Pipino *et al.*, 2011).

Dust grains are removed from the ISM when they are Incorporated into new stars (astration), by sputtering and shattering by supernova shockwaves (e.g. McKee, 1989; Dwek, Galliano & Jones, 2007), and in SMBHs (Gall, Andersen & Hjorth, 2011). The amount and characteristics of the dust which survives supernova shocks is highly uncertain (Kozasa *et al.*, 2009; Jones & Nuth, 2011). Outflows of enriched ISM can remove dust along with gas from galaxies by supernovae or AGN driven winds. Significant outflows of enriched material are suggested by Ménard *et al.* (2010), who found evidence for dust in galaxy halos with a mass comparable to that of dust in the disk. The life cycle of dust in a galaxy is illustrated in Fig. 1.5.

1.3.2 Detecting dusty galaxy populations

One distinction between spirals and ETGs is their dust content, as spirals are typically dust–rich and ETGs are dust poor. However, many studies have found evidence that some ETGs harbour significant quantities of gas (e.g. Combes, Young & Bureau, 2007; Young *et al.*, 2011), and dust (e.g. van Dokkum & Franx, 1995; Bregman *et al.*, 1998;

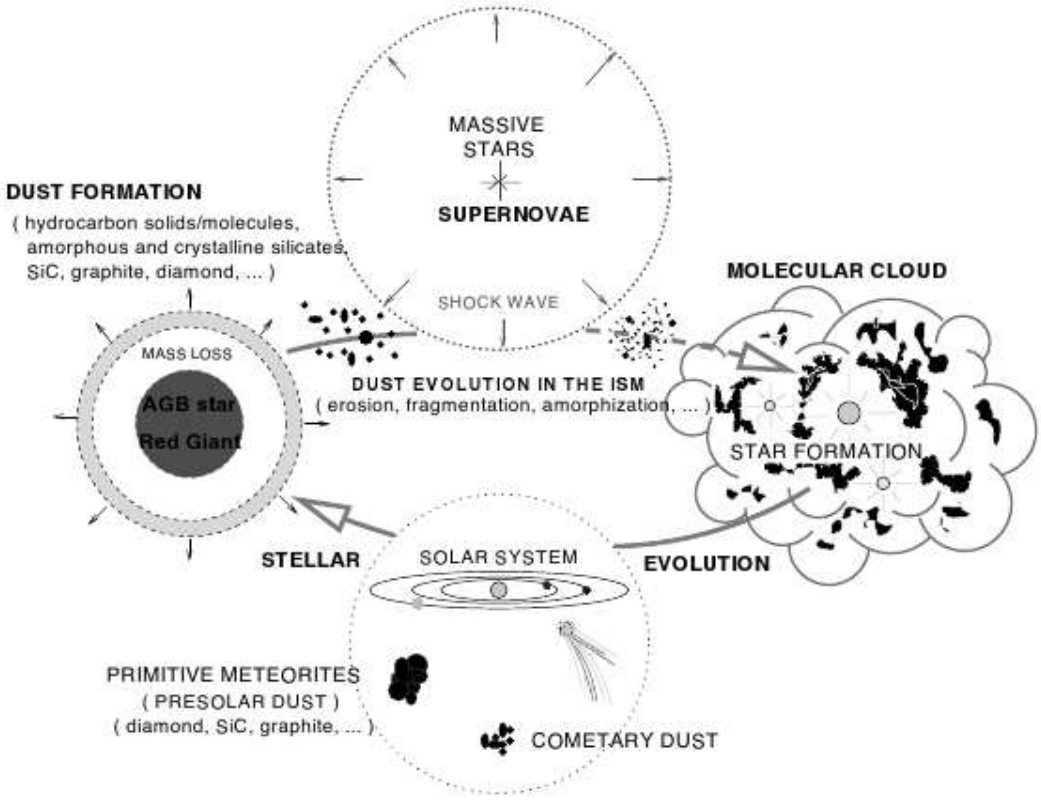

Figure 1.5: Graphical representation of the dust cycle in galaxies. Dust is produced by evolved stars (red giants, asymptotic giant branch phase stars, and supernovae). This dust is then processed by supernova shocks, and the dust which survives is incorporated into molecular clouds. Dust grains can then be locked up in asteroids and comets, and are the building blocks planets. Image credit: Jones (2004).

Rowlands *et al.*, 2012; Smith *et al.*, 2012c; di Serego Alighieri *et al.*, 2013; Agius *et al.*, 2013). This is the topic of Chapter 3. Normal spiral galaxies emit $30-50\%$ of their luminosity in the FIR (Calzetti *et al.*, 2000; Popescu & Tuffs, 2002). There are, however, galaxies which emit the majority of their bolometric luminosity in the FIR. These are termed luminous infrared galaxies (LIRGs; Soifer *et al.*, 1984) and have $\mathrm{L}_{8-1000\mu\mathrm{m}} > 10^{11}\mathrm{L}_{\odot}$, and ultra-luminous infrared galaxies (ULIRGs; Armus, Heckman & Miley, 1987; Soifer, Neugebauer & Houck, 1987; Sanders *et al.*, 1988) with $\mathrm{L}_{8-1000\mu\mathrm{m}} > 10^{12}\,\mathrm{L}_{\odot}$. (U)LIRGs in the local Universe were discovered in the 1980's by the *IRAS* satellite (Neugebauer *et al.*, 1984), which observed the whole sky in four bands from $12-100\mu$m. Follow-up observations revealed that many ULIRGs appeared morphologically disturbed or had close companions (Sanders & Mirabel, 1996, and references within). As the luminosity and space-density of ULIRGs were found to be similar to QSOs, it was proposed that ULIRGs were powered by dust-obscured QSOs, and would later evolve into optically bright quasars. Later follow-up

observations, including MIR spectroscopy with *ISO* (Kessler *et al.*, 1996), revealed that whilst the majority of ULIRGs host an AGN, the extreme infrared luminosity of ULIRGs is predominately driven by a compact, dust-obscured starburst as a result of a recent gas-rich major-merger (Moorwood, 1996; Murphy *et al.*, 1996; Sanders & Mirabel, 1996; Genzel *et al.*, 1998; Lutz *et al.*, 1998).

Great progress was made in the study of dust by *IRAS* and later *ISO*. However, these telescopes did not probe the cold dust emission ($\mathrm{T} > 30\mathrm{K}$). The Sub-millimetre Common-User Bolometer Array (SCUBA) camera on the JCMT (Holland *et al.*, 1999), and the Max Planck Millimeter Bolometer Array (MAMBO) instrument on the IRAM 30 metre telescope (Kreysa *et al.*, 1998) performed the first blind submillimetre surveys. These surveys discovered a population of FIR luminous ($\mathrm{L_{IR}} \sim 10^{12}\,\mathrm{L_{\odot}}$), highly star-forming ($100 - 1000\,\mathrm{M_{\odot}yr^{-1}}$), dusty submillimetre galaxies (SMGs) at high redshift (Smail, Ivison & Blain, 1997; Hughes *et al.*, 1998; Barger *et al.*, 1998; Eales *et al.*, 1999; Greve *et al.*, 2004).

SMGs have traditionally been found to reside at $z \sim 2 - 2.5$ (Chapman *et al.*, 2005; Wardlow *et al.*, 2011; Lapi *et al.*, 2011) due to a combination of survey sensitivity, the steep number counts of submillimetre sources and the negative k-correction. The latter effect allows galaxies which are bright at 850μm to be detected across a large range in redshift, as shown in Fig. 1.6 (Blain *et al.*, 2002). The Rayleigh-Jeans slope of the thermal dust emission is very steep. An increasingly luminous part of the dust SED is redshifted into the 850μm band at progressively higher redshifts. This counterbalances the decrease in brightness due to a galaxy being further away.

Locally, ULIRGs are relatively rare but are more common at high redshift. Since high redshift ULIRGs have such high SFRs, this galaxy population may represent an important phase in the evolution of massive galaxies. Most SMGs host an AGN, and since the bulge and SMBH mass are related (Magorrian *et al.*, 1998; Häring & Rix, 2004), SMGs may also be an important phase for SMBH growth in massive galaxies. Measurements of the stellar masses, star-formation histories, co-moving number densities and clustering properties of SMGs indicate that SMGs may be the progenitors of massive elliptical galaxies observed in the local Universe (Eales *et al.*, 1999; Dunlop, 2001; Scott *et al.*, 2002; Blain *et al.*, 2002; Chapman *et al.*, 2005; Swinbank *et al.*,

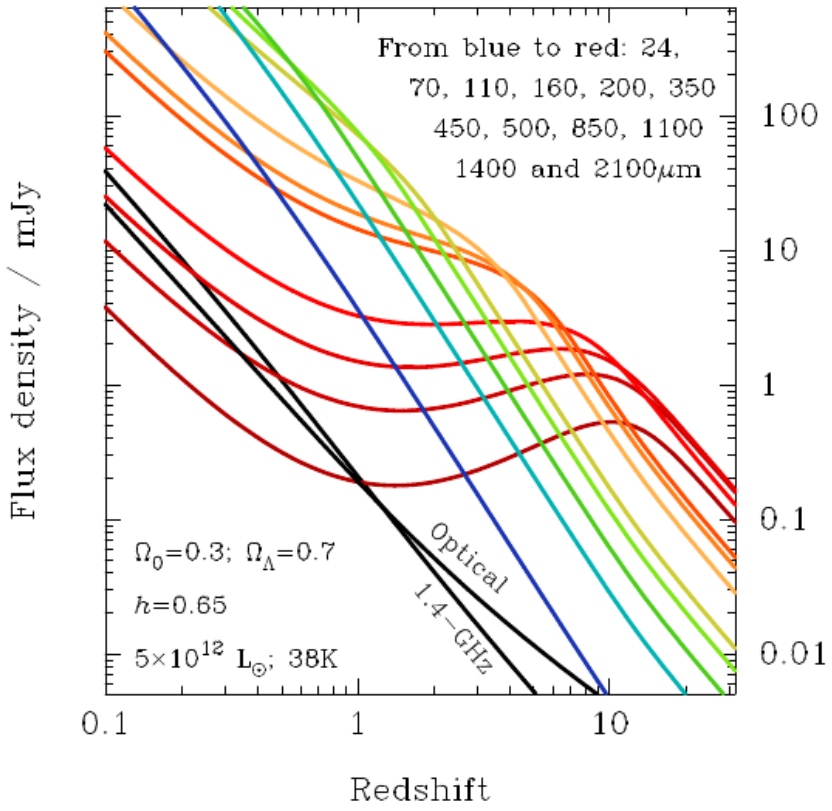

Figure 1.6: The predicted flux density of a representative submillimetre galaxy spectral energy distribution as a function of redshift in different observed wavebands. At relatively short wavelengths (e.g. optical and 24μm), the flux density decreases with redshift. In the submillimetre ($> 500\mu$m), the negative K-correction results in a flux density approximately constant (or even rising for $> 1100\mu$m) with redshift. Image credit: Blain *et al.* (2002).

2006; Hainline *et al.*, 2011; Hickox *et al.*, 2012). Evidence is now emerging that the SMG population is a mix of mergers and massive star-forming galaxies (Davé *et al.*, 2010; Hayward *et al.*, 2011; Targett *et al.*, 2012; Magnelli *et al.*, 2012), yet, there are still considerable uncertainties in the physical properties of SMGs (e.g. Michałowski, Hjorth & Watson, 2010; Michałowski *et al.*, 2012; Hainline *et al.*, 2011). How SMGs fit into the general picture of galaxy evolution is not yet clear. The physical properties of dusty galaxies at high redshift will be explored further in Chapters 4 and 5.

Observing in the FIR and submillimetre presents several technical challenges. Early surveys conducted in the submillimetre were limited in areal coverage ($< 1\mathrm{deg}^2$, Mortier *et al.* 2005; Coppin *et al.* 2006; Weiß *et al.* 2009) due to the relatively low sensitivity of bolometric detectors and small array sizes. This meant that small co-moving volumes were studied at low redshift, making blind, wide-field submillimetre surveys of the local Universe impractical. Instead, targeted studies of representative samples of local galaxies were conducted, for example the SCUBA Local Universe

Galaxy Survey (SLUGS; Dunne *et al.* 2000; Vlahakis, Dunne & Eales 2005) observed 184 *IRAS* and optically selected galaxies. However, targeted surveys can be biased towards particular populations of galaxies; an unbiased view of the dusty galaxy population was therefore needed.

Absorption of FIR-submillimetre radiation by water vapour in the atmosphere has limited observing to atmospheric windows (e.g. 450, 850 and 1100μm) from high-altitude sites and airborne experiments. Furthermore, as the diffraction-limited resolution of a telescope is inversely proportional to wavelength, angular resolution in the submillimetre has been limited to 10–15″for single dish 10–30m telescopes. Sub-arcsecond resolution can be achieved using submillimetre interferometers such as the Sub-Millimetre Array (SMA; Ho, Moran & Lo 2004), the Plateu de Bure Interferometer (PdBI; Guilloteau *et al.* 1992), and the Atacama Large Millimeter/submillimeter Array (ALMA; Nyman *et al.* 2010), although these telescopes are limited to a small field-of-view.

Many of the problems relating to sensitivity and atmospheric transmission have now been overcome by the *Herschel Space Observatory* (Pilbratt *et al.*, 2010). Using the Photodetector Array Camera and Spectrometer (PACS; Poglitsch *et al.* 2010), Spectral and Photometric Imaging Receiver (SPIRE; Griffin *et al.* 2010) and Heterodyne Instrument for the Far Infrared (HIFI; de Graauw *et al.* 2010) instruments, the telescope observes at wavelengths from $70 - 600\mu$m across the peak of the dust emission at $1 < z < 4$. *Herschel* probes the Rayleigh-Jeans slope at $z < 1$, making it an unbiased tracer of the dust mass in the local Universe. Its unprecedented sensitivity allows us to map large areas of sky in a relatively short amount of time. The largest extragalactic surveys are the *Herschel* Multi-tiered Extragalactic Survey (HerMES; Oliver *et al.* 2012), and The *Herschel* Astrophysical TeraHertz Large Area Survey (H-ATLAS; Eales *et al.* 2010a). These surveys have opened up a relatively unexplored wavelength range which allows us to probe the properties of large statistical samples of dusty galaxies over the last 12 billion years of cosmic time. The work presented in this thesis uses data from SCUBA and the *Herschel* surveys.

1.4 Structure of the thesis

It is clear that in order to get the full picture of galaxy evolution it is important to study the panchromatic SED of galaxies. *Herschel* provides a sensitive probe of the dust content of different galaxy populations over a wide range of redshifts. In this thesis FIR-submillimetre data from SCUBA and *Herschel* is combined with multi-wavelength data from large area surveys to probe the full galaxy SED. In this thesis I use information from all wavelengths to investigate the physical properties of dusty galaxy populations over cosmic time.

The physical properties of galaxies are derived using the MAGPHYS SED fitting code (da Cunha, Charlot & Elbaz, 2008), which is described in Chapter 2. I also present tests using different prior probability distributions, which are used to describe different populations of galaxies.

In Chapter 3 I explore the properties of galaxies in the local Universe as a function of morphology and highlight particularly interesting populations which are traditionally thought to be passive. The star-formation histories, dust content and environments of dusty ETGs and passive spirals are investigated. I compare these dusty populations to control samples to investigate how these galaxies are different to the general galaxy population.

High redshift SMGs are the most actively star-forming and dusty galaxies in the Universe, and are thought to be the progenitors of elliptical galaxies. Constraining the properties of SMGs is important for understanding the evolution of massive galaxies and galaxy evolution models in general. Using panchromatic data from the UV to the submillimetre, in Chapter 4 I explore the physical properties of a sample of $\sim 250\mu$m rest-frame selected SMGs. I then compare the SMGs to dusty galaxies at low redshift selected in a similar way, to investigate the differences in the dusty galaxy populations.

Previous surveys have found galaxies were significantly dustier at earlier times, but the cause of this evolution, and the origin of the dust, are hotly debated topics in astrophysics. I undertake chemical evolution modelling to explore the origin of dust in high redshift SMGs in Chapter 5.

The main conclusions are presented in Chapter 6, along with prospects for future work.

Chapter 2

Spectral energy distribution fitting

The physical properties of a galaxy are imprinted upon its spectral energy distribution (SED), which describes the energy emitted as a function of wavelength. These properties include the star-formation history (SFH), stellar mass, metallicity, and dust and gas content, which tell us about the evolution of a galaxy. The UV–NIR part of the SED is typically modelled using evolutionary population synthesis techniques (Tinsley & Gunn, 1976; Tinsley, 1978; Bruzual A., 1983; Charlot & Bruzual, 1991; Bruzual & Charlot, 1993, 2003; Bressan, Chiosi & Fagotto, 1994; Worthey, 1994; Fioc & Rocca-Volmerange, 1997; Maraston, 1998, 2005; Leitherer *et al.*, 1999; Vazdekis, 1999; Conroy, Gunn & White, 2009; Vazdekis *et al.*, 2010), often with a prescription for nebular emission (Leitherer *et al.*, 1999; Charlot & Longhetti, 2001; Groves *et al.*, 2008) and dust attenuation (e.g. Calzetti *et al.*, 2000; Charlot & Fall, 2000). Many models and templates exist for the infrared part of the SED. These range from simple models dependent on one parameter such as the FIR luminosity (Chary & Elbaz, 2001; Dale *et al.*, 2001; Dale & Helou, 2002; Rieke *et al.*, 2009), to complex models often involving radiative transfer, which account for a grain size distribution exposed to a variety of radiation fields (Desert, Boulanger & Puget, 1990; Draine & Li, 2007; Siebenmorgen & Krügel, 2007). Reviews of SED fitting methods are given in Walcher *et al.* (2011) and Conroy (2013).

The optical part of the SED is often modelled separately to the FIR. A self-consistent treatment of stellar emission and reprocessing by dust is only available using radiative transfer codes (e.g. Witt, Thronson & Capuano, 1992; Xilouris *et al.*, 1998; Popescu

et al., 2000; Baes *et al.*, 2011). These methods are computationally intensive and are not appropriate for studies of large galaxy samples. Furthermore, they often require detailed, spatially resolved observations which are only available for very nearby galaxies. Using physically-plausible assumptions about the distribution of stars and dust, the full SED can now be modelled self-consistently for statistically significant samples of galaxies (Devriendt, Guiderdoni & Sadat, 1999; Silva *et al.*, 1998; da Cunha, Charlot & Elbaz, 2008; Groves *et al.*, 2008; Noll *et al.*, 2009). A panchromatic SED fitting approach is desirable given the wealth of multiwavelength data available for the galaxies studied in this thesis.

2.1 Galaxy spectral energy distribution fitting with MAGPHYS

Throughout this thesis I use a modified version of the physically-motivated model of da Cunha, Charlot & Elbaz (2008, hereafter DCE08[1]) as a tool to recover the physical properties of the galaxy samples described in Chapters 3, 4 and 5. Whilst several multiwavelength SED fitting codes are now available, the MAGPHYS code is chosen because it can compute statistical constraints on physical parameters, using a simple, but physically motivated model. The code can be used to derive the properties of large samples of galaxies in a relatively short amount of time, compared to to full radiative transfer codes. Furthermore the model is easy to use, as it can simultaneously compute the stellar mass, star-formation rate (SFR) and dust mass for a galaxy.

In MAGPHYS, the energy from UV–optical radiation emitted by stellar populations is absorbed by dust, and this is matched to that re-radiated in the far-infrared (FIR). Spectral libraries of 50000 optical models with stochastic star-formation histories, and 50000 infrared models, are produced at the redshift of each galaxy in our sample, containing model parameters and synthetic photometry from the UV to the millimetre. The models are drawn at random from prior distributions, which define probability density distributions for parameters over a physically plausible range of values. The optical li-

[1]The da Cunha, Charlot & Elbaz (2008) models are publicly available as a user-friendly model package MAGPHYS at www.iap.fr/magphys/.

braries are produced using the spectral evolution of stellar populations calculated from the latest version of the population synthesis code of Bruzual & Charlot (2003). The stellar population models include a revised prescription for thermally-pulsing asymptotic giant branch (TP-AGB) stars from Marigo & Girardi (2007). A Chabrier (2003) Galactic-disk Initial Mass Function (IMF) is assumed. The libraries contain model spectra with a wide range of star-formation histories, metallicities and dust attenuations. The two-component dust model of Charlot & Fall (2000) is used to calculate the attenuation of starlight by dust, which accounts for the increased attenuation of stars in birth clouds compared to old stars in the ambient interstellar medium (ISM). The model assumes angle-averaged spectral properties and so does not include any spatial or dynamical information.

The infrared libraries contain SEDs comprised of four different temperature dust components, from which the dust mass ($M_{\rm d}$) is calculated. In stellar birth clouds, these components are polycyclic aromatic hydrocarbons (PAHs), hot dust (stochastically heated small grains with a temperature $130 - 250$ K), and warm dust in thermal equilibrium ($30-60$ K). In the diffuse ISM the relative fractions of these three dust components are fixed, but an additional cold dust component with an adjustable temperature between 15 and 25 K is added. A dust emissivity index (see Chapter 1.3.1) of $\beta = 1.5$ is assumed for warm dust, and $\beta = 2.0$ for cold dust. The prior distributions for the temperature of warm dust in birth clouds ($T_{\rm W}^{\rm BC}$), and the temperature of cold dust in the diffuse ISM ($T_{\rm C}^{\rm ISM}$) are flat, so that all temperatures within the bounds of the prior have equal probability in the model libraries.

The attenuated stellar emission and dust emission models in the two spectral libraries are combined using a simple energy balance argument, that the energy absorbed by dust in stellar birth clouds and the diffuse ISM are re-emitted by dust in the infrared. In practise, this means that each model in the optical library is matched to models in the infrared library which have the same fraction of total dust luminosity contributed by the diffuse ISM (f_{μ}), within a tolerance of 0.15, and are scaled to the total dust luminosity[2] $L_{\rm d}^{\rm tot}$. Statistical constraints on the various parameters of the model are derived using the Bayesian approach described in DCE08. Each observed galaxy SED is

[2]Integrated between 3 and 1000μm.

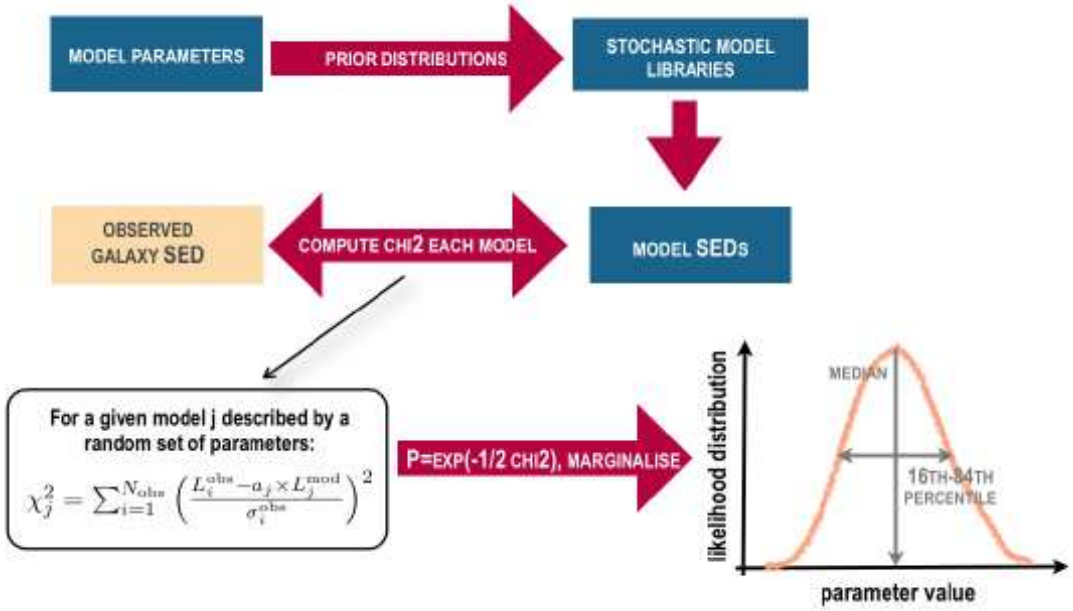

Figure 2.1: A flow chart showing the steps in the MAGPHYS code to fit multiwavelength spectral energy distributions and derive physical parameters. Figure credit: E. da Cunha and S. Charlot.

compared to a library of stochastic models which encompasses all plausible parameter combinations. For each galaxy, the marginalised likelihood distribution of any physical parameter is built by evaluating how well each model in the library can account for the observed properties of the galaxy (by computing the χ^2 goodness of fit). This method ensures that possible degeneracies between model parameters are included in the final probability density function (PDF) of each parameter. The effects of individual wavebands on the derived parameters are explored in DCE08, and Smith *et al.* (2012b), but I emphasise the importance of using the *Herschel* FIR-submillimetre data to sample the peak of the dust emission and the Rayleigh-Jeans slope in order to get reliable constraints on the dust mass and luminosity. A summary of the MAGPHYS SED fitting method is given in Fig. 2.1.

The MAGPHYS code is modified from the public version to take into account flux density upper limits in the χ^2 calculation to give additional constraints on physical parameters. When the model SED violates the upper limit, the photometry point is included in the χ^2 calculation and is weighted by the photometric error. If the upper limit is above the model SED, the upper limit does not contribute to the χ^2 value. Additionally, I modify the priors to take into account areas of parameter space which are not explored with the standard MAGPHYS libraries. This is important when studying a wide variety of galaxies from quiescent systems to highly obscured starburst galaxies.

The modified priors are described in the following Sections. Section 2.1.1 outlines the standard priors more applicable for low redshift galaxies and Section 2.1.2 describes the composite priors which better suit the high redshift SMGs (see Chapter 4).

An example best-fit SED and set of PDFs are shown in Fig. 2.2. The parameters of interest are f_{μ}, the fraction of total dust luminosity contributed by the diffuse ISM; $M_{*}/M_{\odot}$, stellar mass; $M_{\rm d}/M_{\odot}$, dust mass; $M_{\rm d}/M_{*}$, dust-to-stellar mass ratio; $L_{\rm d}^{\rm tot}/L_{\odot}$, dust luminosity; $T_{\rm C}^{\rm ISM}$/K, temperature of the cold diffuse ISM dust component; $T_{\rm W}^{\rm BC}$/K, temperature of the warm dust component in birth clouds; $\hat{\tau}_{V}$, total effective V-band optical depth seen by stars in birth clouds; $\hat{\tau}_{V}^{ISM}$, the V-band optical depth in the ambient ISM; $\psi/M_{\odot}yr^{-1}$, the SFR; and $\psi_{\rm S}/yr^{-1}$, specific star-formation rate (SSFR). For more details of the method I refer the reader to DCE08.

2.1.1 Standard priors

The 'standard' priors which are appropriate for low redshift galaxies are described in detail in DCE08; a summary is given here for illustration. The standard model libraries are used to derive the properties of low redshift dusty galaxies in Chapters 3 and 4. Here I highlight particular parameters which are different in the standard and modified libraries described in Section 2.1.2. From DCE08, the priors for $\hat{\tau}_{V}$ and $\hat{\tau}_{V}^{ISM}$, the V-band optical depth seen by stars in birth clouds and the ambient ISM, respectively, range from 0 to 6. This describes the full range of attenuations observed for normal low redshift galaxies (DCE08, and references within). The star-formation histories of galaxies are parametrised by an exponentially decreasing model of the form $\exp(-\gamma t)$, where γ is the star-formation time-scale parameter, which is distributed uniformly between 0 and 1. The time since the start of star formation in the galaxy ($t_{\rm form}$), is uniformly distributed between 0.1 and 13.5 Gyr. Bursts of star formation are superimposed at random times on the exponentially declining model, but with a probability that 50 per cent of galaxies experience a burst in the last 2 Gyr. The strength of the burst is defined as the mass of stars formed in the burst relative to the mass of stars formed in continuous star formation over the lifetime of the galaxy. This parameter has a range from 0.03 to 4.0 with logarithmic spacing. Moderately star-forming galaxies in the local Universe are assumed to have a fixed birth cloud timescale

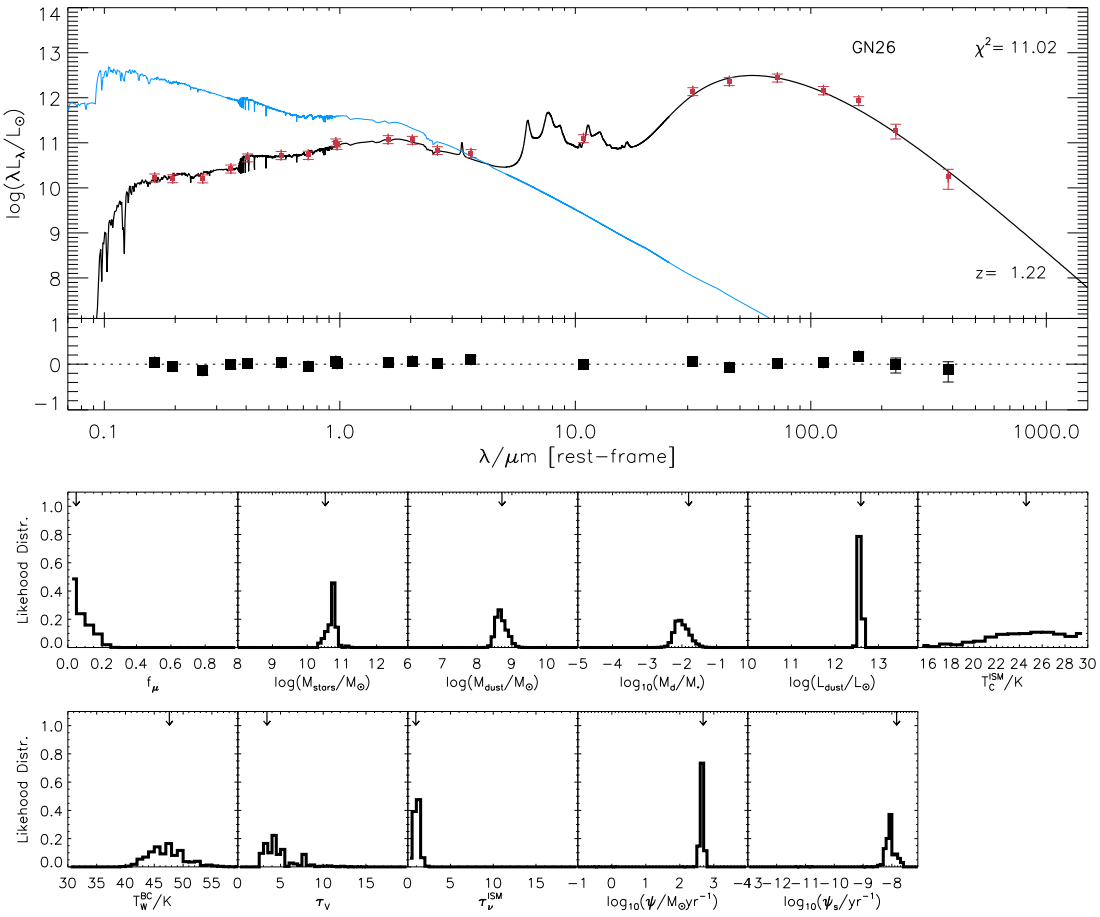

Figure 2.2: Top: Example best-fit rest-frame SED of a high-redshift submillimetre galaxy, with observed photometry (red points) from the rest-frame UV to the submillimetre. Errors on the photometry are described in Section 4.2.2. The black line is the best fit model SED and the blue line is the unattenuated optical model. **Bottom**: Probability density functions (PDFs) for each physical parameter are shown for this submillimetre galaxy, with the best-fit model values shown as arrows above each parameter PDF. The parameters are (from left to right): f_μ, the fraction of total dust luminosity contributed by the diffuse ISM; $M_*/M_\odot$, stellar mass; $M_{\rm d}/M_\odot$, dust mass; $M_{\rm d}/M_*$, dust-to-stellar mass ratio; $L_{\rm d}^{\rm tot}/L_\odot$, dust luminosity; $T_{\rm C}^{\rm ISM}$/K, temperature of the cold diffuse ISM dust component; $T_{\rm W}^{\rm BC}$/K, temperature of the warm dust component in birth clouds; $\hat{\tau}_V$, total effective V-band optical depth seen by stars in birth clouds; $\hat{\tau}_V^{ISM}$, the V-band optical depth in the ambient ISM; $\psi/M_\odot yr^{-1}$, the star-formation rate (SFR); and $\psi_{\rm S}/yr^{-1}$, the specific star-formation rate (SSFR). The SSFR and SFR are averaged over the last 10^7 years, although in this example the result is insensitive to changes in the timescale over which the SFR is averaged. The ranges of each panel reflect the width of the priors.

($t_{\rm BC}$) of 1×10^7 years, after which the young stars move from their birth clouds into the less obscured diffuse ISM.

2.1.2 Composite priors

In order to describe the SEDs of submillimetre selected galaxies at high redshift (see Chapter 4), I modify the standard priors which were calibrated for moderately star-forming systems. Recent studies have shown that the submillimetre galaxy (SMG)

population is a mix of strong starbursts and galaxies on the main-sequence of star formation (e.g. Magnelli *et al.*, 2012). I therefore need to modify the priors to accommodate a wider range of galaxy characteristics, and which have a much higher infrared luminosity and SSFR than most low-redshift galaxies. Furthermore, there is much discussion in the literature on whether SMGs are similar to local ULIRGs with a central starburst, or are have more extended star formation as observed in normal galaxies at low redshift (e.g. Tacconi *et al.*, 2008; Davé *et al.*, 2010; Hayward *et al.*, 2011; Targett *et al.*, 2012). In collaboration with E. da Cunha I created a modified set of priors, hereafter referred to as 'composite' priors, as they are a hybrid between the ULIRG priors described in da Cunha *et al.* (2010a) and the standard model libraries.

When fitting the SEDs of dusty high redshift galaxies with the standard priors, the $\hat{\tau}_V$ PDF frequently hits the upper end of the prior space. This suggests that the $\hat{\tau}_V$ prior in the standard libraries does not extend to sufficiently high values to fully describe the properties of SMGs. Furthermore, SMGs are known to be more obscured than local galaxies (Menéndez-Delmestre *et al.*, 2009). The $\hat{\tau}_V$ and $\hat{\tau}_V^{ISM}$ priors are modified to allow for higher optical depths so that they now range between 0 and 20. In order to account for the wide range of dust temperatures observed in SMGs, the temperature of the cold dust component is extended to have a range $15 - 30$ K. Since SMGs are thought to be experiencing strong starbursts, the burst strength is increased relative to the amount of continuous star formation to range between 0.1 and 100. I also adopt both exponentially increasing and decreasing star-formation rates by distributing the γ parameter between -1 and 1, as Maraston *et al.* (2010); Lee *et al.* (2010); Papovich *et al.* (2011) and Reddy *et al.* (2012) find that an exponentially increasing SFR is appropriate for some high-redshift galaxies. The star-formation time-scale parameter (γ) is constructed to have a Gaussian distribution, so that I do not include too many galaxies with negligible current star formation. Initial tests with these priors suggested that there were very few models which had a high enough SSFR to provide a good fit to the photometry of the SMGs. The minimum age of the galaxy is decreased from 0.1 to 0.01 Gyr in order to increase both the number of models with SSFR $\sim 1 \times 10^{-8}$ yr^{-1} and to extend the upper limit of the SSFR prior from 1.4×10^{-8} yr^{-1} to 1.4×10^{-7} yr^{-1}. da Cunha *et al.* (2010a) found that a birth clouds timescale ($t_{\rm BC}$) of 1×10^8 years was more appropriate for ULIRGs, which are more heavily obscured than normal star-

forming galaxies. Instead of fixing $t_{\rm BC}$ as in the standard libraries at 1×10^7 years, I let $t_{\rm BC}$ vary as a free parameter which is uniformly distributed in logarithmic space between 1×10^7 and 1×10^8 years. This accounts for the possibility of longer birth cloud lifetimes in gas-rich disks (Krumholz & Dekel, 2010).

To create the composite priors, the 50000 optical and 50000 infrared libraries are re-distributed in parameter space so that the number of libraries stays constant between the standard and composite priors. A summary of the relevant prior distributions is shown in Fig. 2.3. A comparison of the physical parameters of a sample of 23 SMGs (see Chapter 4) derived using the standard and composite priors is presented in the following Section.

2.2 Choice of priors

Figure 2.4 shows the parameter values derived using our composite libraries, and those using the standard MAGPHYS libraries. The median likelihood values of the dust-to-stellar mass ratio, dust luminosity and the cold dust temperature in the diffuse ISM are generally consistent (within the error given by the median 84th–16th percentile range of the sample) between the different prior libraries. Whilst the majority of the median likelihood stellar mass values are in good agreement, there is a slight tendency for the stellar masses to be lower when using the composite library. There is a small systematic offset in dust mass, with the standard libraries producing values which are larger by 0.2 dex, but values are typically within the median error range for this parameter. The warm dust temperature in the birth clouds also shows a small systematic offset, with the standard prior results being around 5 K warmer on average. However, the warm dust temperature is difficult to constrain, and the offset is in most cases within the median 1σ error for this parameter. When using the composite libraries there is a tendency for the optical depth in the birth clouds ($\hat{\tau}_V$) to be higher, but the majority of median likelihood values are consistent within the error range. The median likelihood values of the optical depth in the diffuse ISM ($\hat{\tau}_V^{ISM}$) are generally consistent between the standard and composite priors, although some values of $\hat{\tau}_V^{ISM}$ are lower when using the composite libraries.

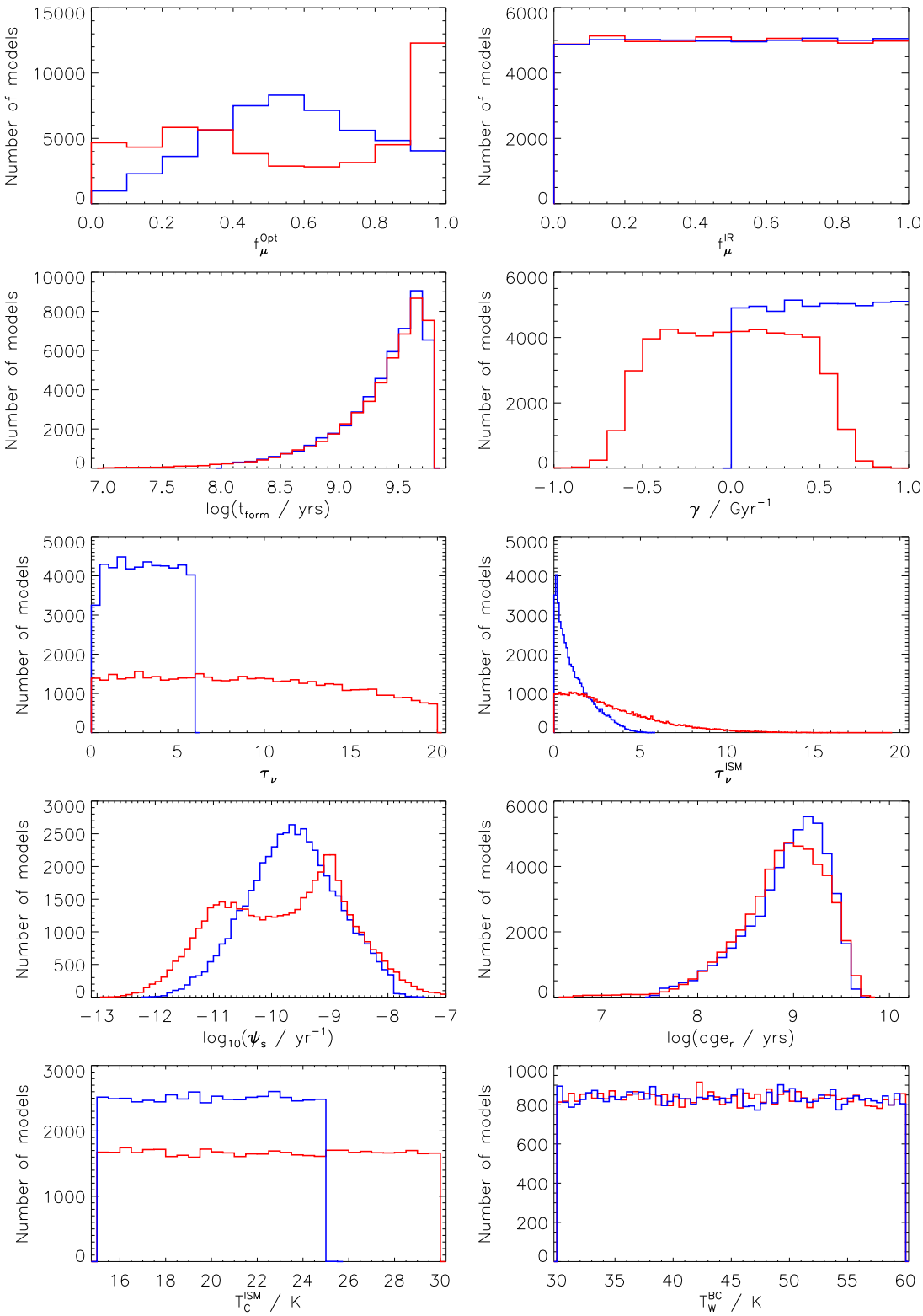

Figure 2.3: Comparison of the standard (blue histogram) and composite (red histogram) prior distributions for parameters relevant to this work. The panels are: f_μ^{Opt}, the fraction of total dust luminosity contributed by the diffuse ISM in the optical model; f_μ^{IR}, the fraction of total dust luminosity contributed by the diffuse ISM in the infrared model; $t_{\rm form}$, the time at which a model galaxy began forming stars; γ, the star-formation timescale; $\hat{\tau}_V$, total effective V-band optical depth seen by stars in birth clouds; $\hat{\tau}_V^{ISM}$, the V-band optical depth in the ambient ISM; $\psi_{\rm S}/yr^{-1}$, specific star-formation rate, $\mathrm{age_r}$, r-band light-weighted age; $T_{\rm C}^{\rm ISM}$/K, temperature of the cold diffuse ISM dust component; and $T_{\rm W}^{\rm BC}$/K, temperature of the warm dust component in birth clouds.

The SFR (averaged over the last 10^7 years) derived from the standard and composite priors are in general agreement, but there is a tendency for the composite SSFR to be higher than the standard SSFR. However, around 7/23 sources have SSFRs significantly higher than would be obtained using the standard priors. The results obtained for the SFR and SSFR averaged over the last 10^8 years show similar trends, with the composite SSFR and SFR slightly higher than the standard (S)SFR. However, the offset between composite and standard median likelihood values is larger than when using a shorter star-formation timescale. Since the galaxies using the composite libraries tend to have higher SSFRs, the median likelihood values of f_μ are consistently lower. This is because the composite libraries allow much stronger starbursts and younger ages in order to represent the properties of high redshift SMGs. This exercise highlights how the choice of prior can affect some parameters derived from broadband SED fitting. In the majority of cases the different priors do not change our conclusions in Chapter 4. Where the choice of prior influences our results this will be taken into account when interpreting our findings in the following Chapters.

2.3 Summary

In this Chapter I have outlined the method used to fit galaxy SEDs and derive physical properties for the samples examined in this thesis. I described the standard MAGPHYS priors, which are used to fit the SEDs of low redshift galaxies in Chapters 3 and 4. I also outlined the motivation for building a new set of priors to describe the properties of high-redshift dusty galaxies, which are described in Chapter 4. I then explored the differences in the derived physical properties when using two different sets of priors. For the majority of galaxies, median likelihood estimates of the parameters derived using the standard and composite priors show some scatter, but are generally consistent within the error given by the median 84th-16th percentile range of the sample. The fraction of total dust luminosity contributed by the diffuse ISM (f_μ), the SFR, and SSFR are the only parameters for which a minority of galaxies (7/23) show large departures from the one-to-one relation. This will be taken into account when interpreting our results in the following Chapters.

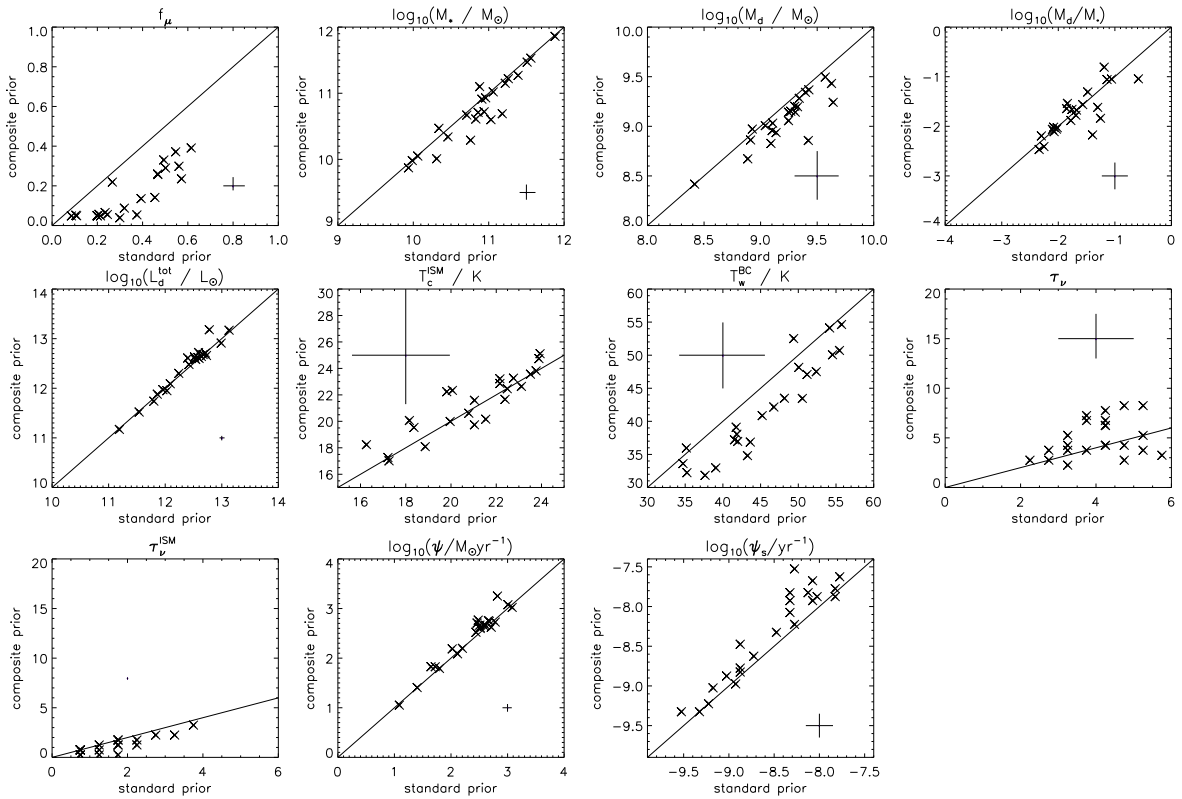

Figure 2.4: A comparison of different parameters using the standard MAGPHYS libraries and the new composite library for the 23 submillimetre galaxies in Chapter 4. Solid black lines show the one-to-one line for each parameter. The error bar indicates the median 84th-16th percentile range from the parameter PDF. The parameters shown are: f_μ, the fraction of total dust luminosity contributed by the diffuse ISM; $M_*/M_\odot$, stellar mass; $M_{\rm d}/M_\odot$, dust mass; $M_{\rm d}/M_*$, dust-to-stellar mass ratio; $L_{\rm d}^{\rm tot}/L_\odot$, dust luminosity; $\hat{\tau}_V$, total effective V-band optical depth seen by stars in birth clouds; $\hat{\tau}_V^{ISM}$, the V-band optical depth in the ambient ISM; $\psi/M_\odot yr^{-1}$, the star-formation rate (SFR); and $\psi_{\rm S}/yr^{-1}$, the specific star-formation rate averaged over the last 10^7 years.

Chapter 3

Dusty early-type galaxies and passive spirals

The work in this Chapter is published in Rowlands *et al.* (2012).

3.1 Introduction

It has long been known that there is a relationship between galaxy optical colour and morphology. Galaxies can be split into a red sequence and blue cloud (Tresse *et al.*, 1999; Strateva *et al.*, 2001; Blanton *et al.*, 2003; Baldry *et al.*, 2004; Bell *et al.*, 2004b). Red galaxies are generally passive early-type galaxies (ETGs, those that have elliptical or S0 morphology), but with $\sim 25\%$ being spirals which are red either due to dust or because they are passive (Driver *et al.*, 2006). Blue galaxies are actively star-forming and mostly of spiral or irregular morphology. The colour bimodality of galaxies is linked to their star-formation history (SFH), with the stellar population of galaxies transitioning from blue to red as their star formation ceases due to the removal or consumption of cold gas (e.g. Faber *et al.*, 2007; Hughes & Cortese, 2009). The injection of gas and dust via mergers may temporarily rejuvenate star formation, and so this evolution of colour can be reversed (Cortese & Hughes, 2009; Kannappan, Guie & Baker, 2009; Wei *et al.*, 2010). Such "rejuvenators" may have had substantially different star-formation histories from those which make up the majority of their morphologi-

cal type, and may provide insight into the evolutionary processes that shape galaxies today.

Massive ($> 10^{10}\mathrm{M}_{\odot}$) ETGs are traditionally thought to be "red and dead" (e.g. Temi, Brighenti & Mathews, 2009b), having formed most of their stellar mass at early epochs over a relatively short period of time (e.g. Cimatti *et al.*, 2004; Thomas *et al.*, 2005) and then evolved passively to their present state. Their optical light is dominated by old stellar populations; however, recent ultra-violet (UV) studies of large samples of ETGs have shown that many of these galaxies exhibit low to moderate levels of star formation (Yi *et al.*, 2005; Schawinski *et al.*, 2007b; Kaviraj *et al.*, 2007, 2008, 2011; Kaviraj, 2010). Studies of UV-optical colours suggest that at least $\sim$30% of UV-selected early-type galaxies at $z < 0.11$ have evidence of recent star formation within the last 1 Gyr (Kaviraj *et al.*, 2007); however, it is difficult to determine the contribution of UV flux from old stars.

Mergers are likely to trigger star formation, since a high incidence of ETGs with disturbed morphologies (18%) has been observed (Kaviraj, 2010), and these disturbed ETGs also have bluer $NUV - r$ colours than normal ETGs. The major merger rate at low and intermediate redshifts is thought to be too low to account for the number of galaxies which have disturbed morphologies (e.g. De Propris *et al.*, 2007, 2010; Lotz *et al.*, 2008), therefore Kaviraj *et al.* (2011) conclude that minor mergers are the most likely trigger of recent star formation in ETGs.

Although there is evidence for limited quantities of dust in ETGs, these galaxies are generally thought to be gas- and dust-poor, which gives an insight into their evolutionary state. UV starlight is preferentially absorbed and re-emitted by dust in the far-infrared (FIR) and submillimetre, so the presence of dust emission is often viewed as evidence for ongoing star formation (Kennicutt, 1998b), although dust can also be heated by the radiation field of an old stellar population. Evidence for dust in ETGs was first found in the optical (e.g. Hawarden *et al.*, 1981; Sadler & Gerhard, 1985; van Dokkum & Franx, 1995), yet it is difficult to estimate the total dust mass purely from optical observations. Warm dust (> 30K) was detected in 12% of local ETGs by *IRAS* (Bregman *et al.*, 1998), but *IRAS* was less sensitive to the cold dust component which dominates the dust mass in local galaxies (Dunne & Eales, 2001; Vlahakis, Dunne

& Eales, 2005; Smith *et al.*, 2012b). There have been few studies of ETGs at FIR–submillimetre wavelengths to date, since surveys conducted at these wavelengths have been limited in areal coverage. Consequently, studies of ETGs have been targeted observations of relatively small, and often biased, samples. Cold dust has been detected in ETGs through observations with *ISO*, SCUBA, *Spitzer*, and SHARC II (Temi *et al.* e.g. 2004; Leeuw *et al.* 2004; Vlahakis, Dunne & Eales 2005; Temi, Brighenti & Mathews 2007; Stickel, Klaas & Lemke 2007; Leeuw *et al.* 2008; Savoy, Welch & Fich 2009). Cold dust has also been observed by *Herschel* in 10 nearby ETGs (Skibba *et al.*, 2011), and in the Virgo cluster elliptical galaxy M86, which contains dust stripped from the nearby spiral NGC 4438 (Gomez *et al.*, 2010; Cortese *et al.*, 2010).

Conversely, spiral galaxies are generally rich in dust and gas, and make up the majority of the star-forming population. Their blue optical colours indicate young stellar populations, yet for some time optically red spirals with no spectroscopic evidence of star formation have been known to exist in the outskirts of clusters (van den Bergh, 1976; Poggianti *et al.*, 1999, 2004; Goto *et al.*, 2003). These spirals can be red due to dust obscuration, or because of an ageing stellar population (Wolf *et al.*, 2009). It is generally believed that passive red spirals have had their star formation quenched due to environmental effects, since they are found to mostly reside in intermediate density environments (Skibba *et al.*, 2009; Bamford *et al.*, 2009; Masters *et al.*, 2010b). The star-formation rate (SFR) was found to be lower for red spirals than blue spirals in all environments, which indicates that factors other than environment can truncate star formation in red spirals (Bamford *et al.*, 2009; Masters *et al.*, 2010b). The same authors also found that a large fraction of red spirals are massive ($> 10^{10}\,\mathrm{M}_{\odot}$), which may be linked to the quenching of star formation in red spirals.

An unprecedented view of dust in local galaxies can now be obtained from the *Herschel*-ATLAS survey (H-ATLAS, Eales *et al.* 2010a). The telescope observes at FIR-submillimetre wavelengths across the peak of the dust emission, making it an unbiased tracer of the dust mass in galaxies. In this chapter I examine the properties of galaxies detected in the H-ATLAS Science Demonstration Phase (SDP) field as a function of morphological type, and highlight interesting populations which do not conform to the usual trend of colour and morphology. In particular, I focus the analysis on the

properties of H-ATLAS ETGs and how these galaxies are different from optically selected ETGs, in addition to studying a population of dusty, passive spirals. I present the detection of the very dustiest ETGs in a large area blind submillimetre survey with *Herschel*, where the lack of pre-selection in other bands makes it the first unbiased survey for cold dust in ETGs. I adopt a cosmology with $\Omega_m = 0.27$, $\Omega_\Lambda = 0.73$ and $H_o = 71\,\mathrm{km\,s^{-1}\,Mpc^{-1}}$.

3.2 Observations and sample selection

The H-ATLAS (Eales *et al.*, 2010a) is a $\sim$570 deg^2 survey undertaken by the *Herschel Space Observatory* (Pilbratt *et al.*, 2010) at 100, 160, 250, 350 and 500μm to provide an unbiased view of the submillimetre Universe. Observations are carried out in parallel mode using the Photodetector Array Camera and Spectrometer (PACS; Poglitsch *et al.* 2010), and Spectral and Photometric Imaging Receiver (SPIRE; Griffin *et al.* 2010) instruments simultaneously. In this chapter, I use observations in the SDP field, with an area of $\sim$14 deg^2 centered on α=09^{h}05^{m}30.0^s, δ =00°30′00.0″ (J2000). Details of the map making can be found in Pascale (2011) and Ibar *et al.* (2010). A catalogue of $\geq 5\sigma$ detections in any of the 250, 350 and 500μm bands was produced (Rigby *et al.*, 2011) using the MAD-X algorithm (Maddox et al. in prep) and contains 6876 sources. The 5σ noise levels are 132, 126, 32, 36 and 45mJy per beam at 100, 160, 250, 350 and 500μm, respectively; the beam sizes are ~ 9, ~ 13, 18, 25 and 35 arcsec in these bands.

The H-ATLAS SDP field overlaps with that of the Galaxy And Mass Assembly (GAMA) survey (Driver *et al.*, 2011; Hill *et al.*, 2011; Robotham *et al.*, 2010; Baldry *et al.*, 2010; Hopkins *et al.*, 2013), which, when complete, will provide $\sim 350\,000$ spectra for galaxies at low redshifts over 6 regions, covering ~ 300 square degrees. The GAMA data comprise r-band defined aperture-matched photometry as described in Hill *et al.* (2011) from UV *GALEX* (Martin *et al.*, 2005; Morrissey *et al.*, 2007, Seibert et al. in prep.), optical $ugriz$ SDSS DR6 (Adelman-McCarthy *et al.*, 2008) and near-infrared $YJHK$ UKIDSS-LAS (Lawrence *et al.*, 2007) imaging. Spectroscopic redshifts and spectra from the AAOmega spectrograph are provided for $r_{\mathrm{Petro}} < 19.8$

or ($K_{\rm Kron} < 17.6$ and $r_{\rm modelmag} < 20.5$) or ($z_{\rm Kron} < 18.2$ and $r_{\rm modelmag} < 20.5$)[1] in the G12 field, and $r_{\rm Petro} < 19.4$ or ($K_{\rm Kron} < 17.6$ and $r_{\rm modelmag} < 20.5$) or ($z_{\rm Kron} < 18.2$ and $r_{\rm modelmag} < 20.5$) in G15 and G09 which includes the H-ATLAS SDP field.

A likelihood-ratio analysis (Sutherland & Saunders, 1992) is performed to match 250μm sources to SDSS DR7 (Abazajian *et al.*, 2009) sources with $r < 22.4$ within a 10″ radius (Smith *et al.*, 2011), and accounts for the possibility of the true counterpart being below the optical magnitude limit. The reliability of an association is defined as the probability that an optical source is associated with the submillimetre source. SDSS sources with reliability≥ 0.8 are considered to be likely matches to submillimetre sources. These are matched to GAMA survey data to provide spectra when available. There are 2423 reliable optical counterparts to H-ATLAS sources, with either photometric or spectroscopic redshifts. Around two-thirds of the objects without reliable optical counterparts are unidentified because their counterparts lie below the optical magnitude limit. These sources mostly reside at $z > 0.5$ (see Dunne *et al.* 2011). The remaining unidentified sources are believed to have a counterpart in the SDSS catalogue, but the correct counterpart cannot be identified in all cases due to near neighbours and the non-negligible probability of a background galaxy of the same magnitude being found up to 10″from a SPIRE source. Smith *et al.* (2011) estimate the completeness of the H-ATLAS sample as a function of redshift by calculating the total number of sources that would be expected to have a counterpart above the SDSS magnitude limit in H-ATLAS. I refer the reader to Smith *et al.* (2011) and Dunne *et al.* (2011) for further details. Smith *et al.* (2012b) find that at $z < 0.35$ the r-band selection does not bias our sample towards less obscured sources. Since the majority of our spirals and ETGs lie at redshifts less than this, our sample should be representative of the low-redshift galaxy population. Matches are also made to the *IRAS* (Moshir, Kopman & Conrow, 1992) and FIRST radio catalogues (Becker, White & Helfand, 1995) as described in Smith *et al.* (2011).

[1] $r_{\rm Petro}$ is the r-band Petrosian magnitude (Petrosian, 1976), which is measured using a circular aperture of twice the Petrosian radius, defined using the light profile of the galaxy (Blanton *et al.*, 2001; Yasuda *et al.*, 2001). $r_{\rm modelmag}$ is the SDSS r-band model magnitude, which is determined from the best fit of an exponential or de Vaucouleurs profile; further details are presented in Baldry *et al.* (2010).

3.2.1 Morphology

Morphological classification of sources was performed by eye using SDSS standard depth gri composite images by a collaborator (Kaviraj), and objects were assigned one of four categories: early-type, late-type, merger and unknown. The classification fractions are shown in Table 3.1. ETGs were identified by looking for a dominant bulge and a complete lack of spiral arms, and late-types were identified by the presence of spiral arms. Due to the shallow depth of the SDSS images, a distinction was not made between E and S0 types, however, it is possible that these populations may have different properties (e.g. Temi, Brighenti & Mathews, 2009a). The merger category contains systems of galaxies that are clearly interacting. Galaxies were classified as 'unknown' if it was impossible to assign a morphology, usually because the galaxy was too faint or small. This situation becomes more common as spatial resolution and signal-to-noise decrease at higher redshifts. It is possible that at low redshifts some of the unknown classifications are irregulars, which tend to have small angular size and are therefore difficult to identify. Additionally, very few H-ATLAS galaxies are low stellar mass objects, which is due to the flux limit in the submillimetre. Therefore the dearth of irregulars is likely to be a real effect and not an inability to classify them. Given the sample size, visual inspection is the preferred method to classify our galaxies into broad morphological classes. It has been shown that visual inspection is superior in identifying contaminants in samples of ETGs (e.g. face on spirals which have a dominant bulge but have weak spiral arms) than automated classification methods (Kaviraj *et al.*, 2007; Schawinski *et al.*, 2007b; Lintott *et al.*, 2008; Bamford *et al.*, 2009). Since I am interested in selecting spheroids, inclination is not an issue. It is possible that at higher redshifts Sa type galaxies with faint spiral arms not visible in the shallow imaging could be classified as ETGs.

3.2.1.1 H-ATLAS sample

We morphologically classify 1087 H-ATLAS sources which have reliability$\geq$0.8 of being associated with a SDSS source, and which have good quality spectroscopic redshifts (flagged with Z_QUALITY $(nQ) \geq 3$). Additionally, I require that sources are at a redshift of $z < 0.5$; above this redshift only a very small number of galaxies have

Table 3.1: Morphologies obtained by visual classification of 1087 H-ATLAS sources and 1052 control sample galaxies. The control sample galaxies are selected to have the same r-band magnitude and redshift distribution as those detected in H-ATLAS. The estimated detection fraction of galaxies in each morphological class is shown in the last row. These are estimated as explained in Section 3.2.1.2.

	Early-type	Late-type	Merger	Unknown
All (detected) 1087	44	496	23	524
	4.1%	45.6%	2.1%	48.2%
All (non-detected) 1052	233	378	22	419
	22.1%	35.8%	2.1%	39.8%
H-ATLAS detected fraction	5.5%	28.2%	25.0%	20.6%

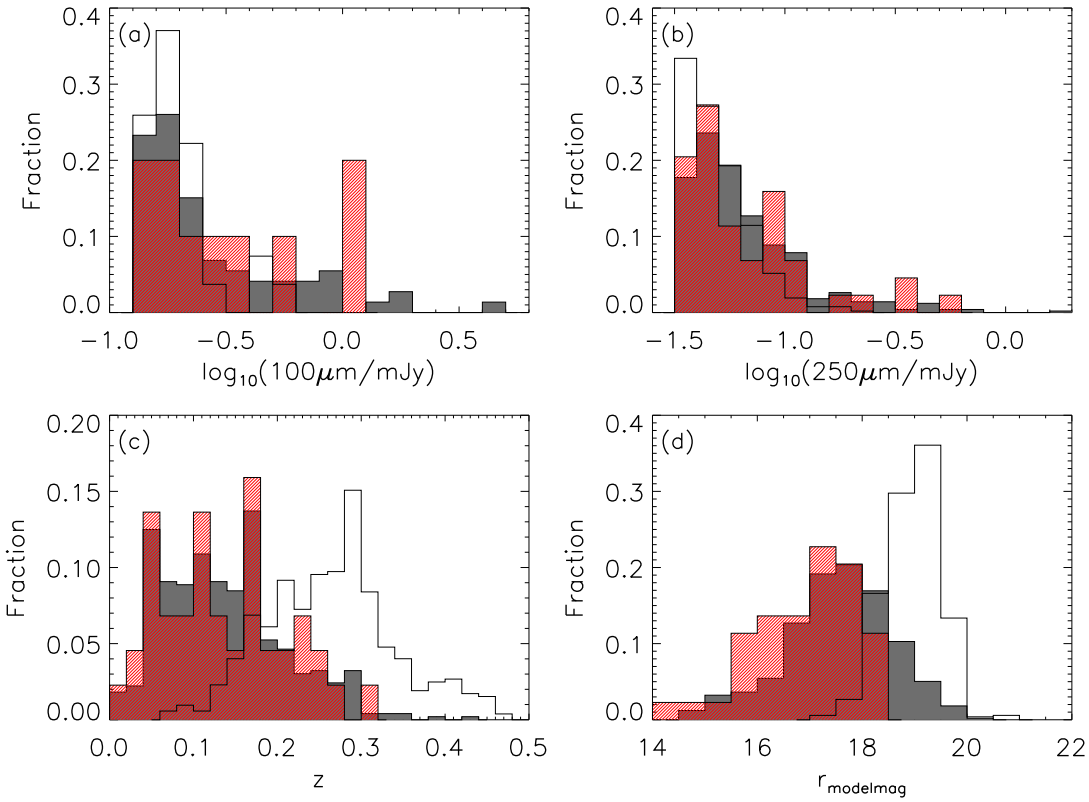

Figure 3.1: The distribution of $\geq 5\sigma$ 100μm (a) and 250μm point-source fluxes (b) are shown for the H-ATLAS morphologically classified sample. Spirals are shown as grey/filled, ETGs as red/hatched and unknown morphologies as an open histogram. It can be seen that the flux distributions are similar for each type of morphology. (c): Redshift distribution of our H-ATLAS sample for each morphological type. The ETGs and spirals have similar redshift distributions, but galaxies classified as unknown lie at much higher redshift on average. (d): The distribution of SDSS r-band model magnitudes for the same morphological classifications. Sources with unknown morphologies are fainter on average than those which are classified.

spectroscopic redshifts and will be difficult to classify. Two sources with stellar or QSO IDs were removed from the sample, as were the five sources identified as being lensed in Negrello *et al.* (2010). I calculate the number of false IDs expected in the classified sample from the sum of the probabilities of a false ID as $\sum(1-R)$, where R is the reliability. This indicates that 21 galaxies (2%) in our sample are likely to be false IDs. There are 115 and 199 sources which have PACS 100 and 160μm point-source detections at $\geq 5\sigma$, respectively. The selection effects arising from the PACS detections are discussed in Smith *et al.* (2012b), who found that the SED results in Section 3.3 are not significantly influenced by the inclusion of upper limits for PACS data in the majority of the sample. All sources have 250μm detections $\geq 5\sigma$ (which is a requirement for our sample selection), 272 sources have a $\geq 5\sigma$ detection at 350μm, and 138 sources have a $\geq 3\sigma$ detection at 500μm. The distribution of 100μm PACS and 250μm SPIRE detections is shown for each morphological type in Figures 3.1 (a) and (b).

Visual classifications revealed 44 galaxies as early-type (E or S0), with $0.01 < z < 0.32$. It can be seen from Table 3.1 that there are few ETGs in our sample compared to spirals, so it is evident that H-ATLAS preferentially selects spiral galaxies over ETGs. This is as expected since ETGs are generally passive and have little dust content. The late-type category in principle encompasses both spirals and irregular galaxies; however no irregular galaxies are found in our sample. This may be because these objects are difficult to classify at all but the very lowest redshifts, but H-ATLAS also does not detect many low optical luminosity (and therefore low mass) sources in the SDP field (Dunne *et al.*, 2011; Dariush *et al.*, 2011). The number of mergers in our classified sample is underestimated because the reliability≥ 0.8 criteria inherently assumes a 1:1 correspondence between optical and submillimetre sources (Sutherland & Saunders, 1992; Smith *et al.*, 2011). In the case of mergers there can be two optical sources close to the SPIRE position which both have a high likelihood of association but the probability (reliability) is split between the sources, sometimes reducing the reliability below our threshold of 0.8. The median redshifts of the ETGs and spirals in our sample are both ~ 0.13, and the redshift distribution is shown in Figure 3.1 (c). As galaxies become faint and small with increasing redshift, classification becomes difficult, and the unknown fraction increases significantly for $r_{\rm Petro} > 18.5$ (see Figure 3.1d). It

also seems easier to classify spirals than ETGs at fainter r-magnitudes. Morphological disturbances are observed in 13/44 ($30^{+8}_{-6}\%$) ETGs and 22/496 ($4 \pm 1\%$) spirals[2]. These disturbed galaxies show evidence of dust or tidal features which may be a sign of a recent merger. The number of disturbed sources is a lower limit since faint features may not be visible in standard depth SDSS images. Morphologically disturbed sources occupy a range of redshifts up to $z \sim 0.26$. A higher fraction of morphological disturbance is found in ETGs in our sample compared to Kaviraj (2010) who find 18% for a sample of optically selected ETGs (with $r < 16.5$ and $z < 0.05$).

To check our ETG classifications, I compare to those in the Galaxy Zoo sample (Lintott *et al.*, 2008, 2011), in which galaxies were visually classified by over 100,000 volunteers. Only the brighter members of our H-ATLAS sample ($r < 17.77$ and $z < 0.25$) overlap with Galaxy Zoo. Galaxies were classified as either elliptical[3], spiral, merger or 'don't know'. A galaxy is assigned one of these classifications if it has > 50 percent of the vote fraction. Debiased votes are used to account for the tendency for Galaxy Zoo classifiers to assign small or faint galaxies (usually at higher redshift due to a lack of resolution) to the 'elliptical' category. The debiasing procedure is described fully in Bamford *et al.* (2009); Lintott *et al.* (2011). There are 22 of our ETGs which have a match in Galaxy Zoo, 17/22 are classified as elliptical, 3/22 are classified as spiral, and 2 are ambiguous. The ETGs which are classified as spirals in Galaxy Zoo either have evidence of disturbed morphology which could have been mistaken for spiral structure, or have evidence of a disk yet no spiral arms. The majority our H-ATLAS ETGs which match with the Galaxy Zoo sample are classified as 'elliptical', and so our morphological classifications agree well with overlapping studies.

I also examine the Sérsic index (n) of our ETGs and spirals in Figure 3.2, to check that our morphological classifications are broadly consistent with what is expected from automated galaxy classification. This is accomplished by fitting single component Sérsic models to the light profile of the galaxy (Kelvin *et al.*, 2012). Generally, late-type galaxies have an exponential profile ($n = 1$), and ETGs have a de Vaucouleurs

[2]The errors are 1σ confidence intervals on a binomial population using a beta distribution, which is appropriate for small population numbers (Cameron, 2011).

[3]The 'elliptical' classification also contains the majority of S0 galaxies, as shown in Bamford *et al.* (2009).

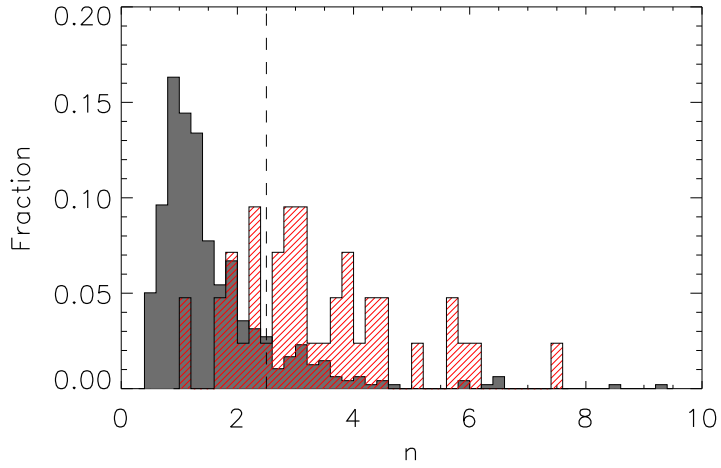

Figure 3.2: Sérsic index (n) distribution of the spirals (grey), and ETGs (red/hatched) in our H-ATLAS sample. The dashed line at $n = 2.5$ denotes the traditional cut between 'early-type' ($n > 2.5$) and 'late-type' ($n < 2.5$) (Bell *et al.*, 2004a), and gives an indication of the contamination that can occur in samples selected on Sérsic index.

profile ($n = 4$). As expected, our visually classified spirals have a very strong peak at $n = 1.3$, whereas the ETGs have a variety of Sersic in dices, but have a higher average n of 3.1. The wide range of Sérsic indices is because S0s are included in our early-type classification, which may have a substantial disk component. Although n broadly agrees with our visual morphologies, Sérsic index is not the ideal classification method, because a spiral with a bright nucleus may appear to have a high value of n and would be mis-classified as an ETG (e.g. Bamford *et al.*, 2009).

3.2.1.2 Control sample

In order to understand how the H-ATLAS and optically selected ETG populations differ, visual morphological classifications were obtained of a control sample drawn from the GAMA galaxy catalogue which overlaps with the H-ATLAS SDP field. Galaxies are required to be undetected in H-ATLAS and have good quality spectroscopic redshifts, and were chosen to have the same redshift and $r_{\rm Petro}$ -magnitude distribution $n(r, z)$ as our H-ATLAS detected, morphologically classified sample. This was accomplished by splitting the H-ATLAS sample into (r, z) bins, and randomly picking approximately the same number of galaxies in each bin from the GAMA catalogue, so that the control sample comprises 1052 galaxies. By selecting a control sample of galaxies which are matched in redshift to the H-ATLAS sample, selection effects are minimised.

The morphologies of the control sample are summarised in Table 3.1. It can be seen that there are many more ETGs compared to spirals in the optically selected sample than in the 250μm selected sample. To estimate the fraction of galaxies which are detected at the depth of H-ATLAS as a function of morphology, I pick a random sample of 1076 galaxies[4] from the GAMA catalogue in the SDP field, disregarding whether they are detected by *Herschel*. The selected galaxies follow the same $n(r, z)$ as our H-ATLAS detected and control samples. The random sampling is repeated 1000 times to estimate the average number of H-ATLAS detected and undetected galaxies. On average, 225 galaxies are in the H-ATLAS detected sample, and 11 of these are ETGs. There are 851 undetected galaxies, and from the control sample fractions 22% (188) of these are expected to be ETGs. Consequently, there are 199 ETGs in total in the random sample, so I estimate 5.5% of ETGs are detected in H-ATLAS compared to the total number of ETGs in the SDP field, for this $n(r, z)$. The detected fractions of other morphological types are presented in Table 3.1. Extrapolations of the control sample fractions cannot reliably be applied to the entire SDP field, since morphology is a function of both r and z, and the full (r, z) parameter space is not probed in this work.

3.2.1.3 Classification bias

Bamford *et al.* (2009) showed that in Galaxy Zoo the fraction of galaxies classified as 'elliptical' increases with redshift compared to spirals. This is because the spatial resolution and signal-to-noise decreases with redshift, so features such as spiral arms become invisible. Also, in Galaxy Zoo, images are presented to the classifier without any indication of angular scale, so distant, unresolved galaxies could have been classified as elliptical. I therefore check if this bias is present in our classifications. I show the classification fractions of our H-ATLAS sample in Figure 3.3, and there is no trend that more galaxies are classified as ETGs with increasing redshift. Indeed, fewer galaxies are classified as ETGs. This may be because unlike Galaxy Zoo volunteers,

[4]The random sample is chosen to be approximately the same size as the H-ATLAS detected sample, but 11 H-ATLAS galaxies are not in the GAMA survey region and lack $r_{\rm Petro}$-magnitude information. Therefore the size of the random sample is smaller than the H-ATLAS sample, but this should not affect any of our conclusions.

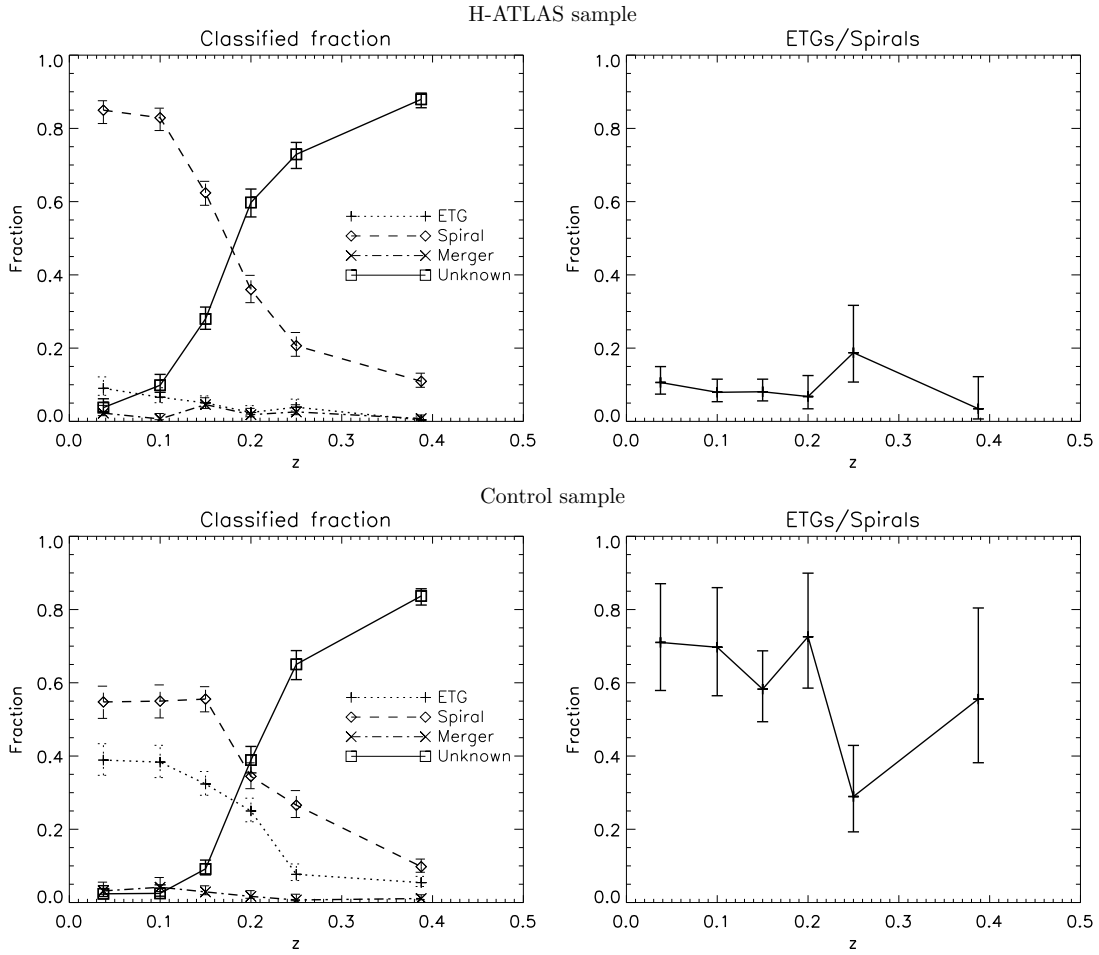

Figure 3.3: Morphological classification fractions as a function of redshift for the H-ATLAS detected sample (top) and the control sample (bottom). Errors bars are the 1σ confidence intervals for a binomial population, derived from a beta distribution (see Cameron 2011). Also shown is the ETG-to-spiral fraction for both samples, where error bars are the 1σ confidence intervals for a binomial distribution, using the approximation of Gehrels (1986). The ETG-to-spiral fraction does not increase with redshift, therefore I do not observe a bias towards classifying more ETGs as they become smaller and fainter.

our expert classifier recognises the limitations of the resolution of the image, and will classify an object as unknown instead of as an ETG.

3.2.2 SED fitting

Smith *et al.* (2012b) fit the UV-submillimetre SEDs of 1404 H-ATLAS galaxies with reliability > 0.8 of being associated with an optical counterpart in the SDSS r-band catalogue, and which have available multiwavelength photometry. Using the physically motivated method of da Cunha, Charlot & Elbaz (2008, hereafter DCE08) allows us to recover the physical properties of these galaxies. Further details of the method are described in Chapter 2.

An example best-fit SED and set of probability density functions (PDFs) are shown in Figure 2.2. The parameters of interest are f_{μ}, the fraction of total dust luminosity contributed by the diffuse ISM; $\hat{\tau}_V$, total effective V-band optical depth seen by stars in birth clouds; $M_*/M_{\odot}$, stellar mass; $L_{\rm d}^{\rm tot}/{\rm L}_{\odot}$, dust luminosity; $T_{\rm C}^{\rm ISM}$/K, temperature of the cold diffuse ISM dust component; $\hat{\tau}_V^{ISM}$, the V-band optical depth in the ambient ISM; $M_{\rm d}/{\rm M}_{\odot}$, dust mass; $\psi_{\rm S}/yr^{-1}$, specific star-formation rate (SSFR); $\psi/{\rm M}_{\odot}{\rm yr}^{-1}$, SFR; ${\rm t}_{\rm LB}$, time of last burst; ${\rm age}_{\rm r}$, r-band light-weighted age and $M_{\rm d}/M_*$, dust to stellar mass ratio. For more details of the method I refer the reader to DCE08.

3.3 Properties of ETGs compared to spirals

Here I explore the multiwavelength properties of our sample of morphologically classified spirals and ETGs detected in H-ATLAS. I present parameters derived from the SED fitting method as described in Section 2.1 for 42 of the 44 ETGs, and as a comparison I also explore the properties of 450 out of the 496 spiral galaxies in our sample. I present the SDSS images, best-fit SEDs and optical spectra of these ETGs in Figure A.1, and average physical properties in Table A.1. The galaxies excluded from our analysis do not have available aperture-matched GAMA photometry (2 ETGs, 17 spirals); additionally I reject 29 galaxies from our analysis which have poor quality SED fits with $\chi^2 > 30$. Our sample covers a range of redshifts, but since the median redshifts of the ETGs and spirals are approximately the same, differences between the samples due to evolution in the redshift range are likely to be small. Additionally, I have checked that the following trends are present if I look at galaxies at $z < 0.13$, and $z > 0.13$. I also observe similar results if I separate our successfully classified sample into 'early-type' ($n > 2.5$) and 'late-type' ($n < 2.5$) using Sérsic index.

3.3.1 SED parameters

In order to compare physical parameters for ETGs and spirals in our sample, I compute the average PDF for each parameter derived from our SED fitting. The average PDFs of ETGs (red) and spirals (black) are shown in Figure 3.4, and the mean values and errors are summarised in Table A.3. For each parameter, I use the first moment of the

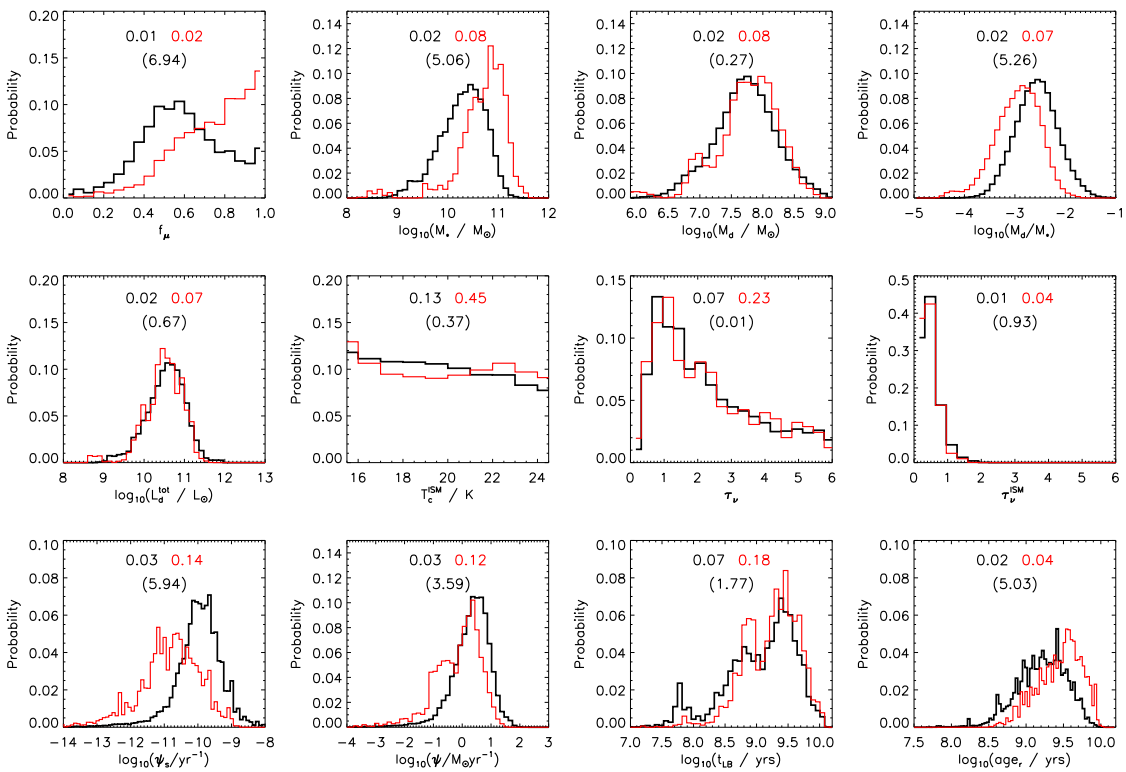

Figure 3.4: Average PDFs of the SED parameters of 42 dusty ETGs (red line) compared to 450 spirals (black line). The parameters are (from left to right): f_{μ} , the fraction of total dust luminosity contributed by the diffuse ISM; M_{*}, stellar mass; $M_{\rm d}$, dust mass; $M_{\rm d}/M_{*}$, dust to stellar mass ratio; $L_{\rm d}^{\rm tot}$, dust luminosity; $T_{\rm C}^{\rm ISM}$, temperature of the cold ISM dust component; $\hat{\tau}_{V}$, total effective V-band optical depth seen by stars in birth clouds; $\hat{\tau}_{V}^{ISM}$, the V-band optical depth in the ambient ISM; SSFR and SFR averaged over the last 10^{8} years; $\rm t_{LB}$, time of last burst; and $\rm age_{r}$, the r-band light-weighted age of the stellar population. The uncertainty on each distribution for ETGs and spirals is given by the error on the mean and is shown at the top of each histogram with corresponding colours, and the significance of the difference in the means in brackets. The errors for logarithmic parameters are in dex.

average PDF to estimate the mean of the population. I estimate the variance on the population mean as the second moment of the average PDF minus the mean squared. The error on the mean is simply the square root of the population variance, normalised by the number of galaxies in the sample. The significance of the difference in the means is shown in brackets in Figure 3.4. This is defined as the absolute difference of the two population means, normalised by the quadrature sum of the errors on the mean.

The ETGs have a mean f_μ of 0.74 ± 0.02, which is significantly higher than that of spirals which have a mean f_μ of 0.59 ± 0.01. This means that most of the FIR luminosity in ETGs is from dust in the diffuse ISM, which is mostly heated by old stellar populations (stars older than 10^7 years). Some ETGs have lower values of f_μ, indicating that more of the FIR luminosity comes from dust in birth clouds, which is heated by young stars and implies ongoing star formation. The ETGs in our sample are more massive than spirals, with ETGs having a mean stellar mass (M_*) of $(4.9^{+1.0}_{-0.8}) \times 10^{10}$ $\mathrm{M}_\odot$ compared to M_* of $(1.9 \pm 0.1) \times 10^{10}\,\mathrm{M}_\odot$ for spirals. ETGs have approximately the same mean dust mass (M_d) and dust luminosity ($L_\mathrm{d}^\mathrm{tot}$) as spirals, although the mean ratio of dust to stellar mass (M_d/M_*) for ETGs is lower than that for spirals in our sample by 0.38 dex, meaning that ETGs are dust deficient for their stellar mass compared to spirals. Our median M_d/M_* value for ETGs is $(1.6 \pm 0.1) \times 10^{-3}$, which is larger than the average found by Skibba *et al.* (2011) of 1.7×10^{-4} for 10 ETGs. In order to contain enough dust to be detected in H-ATLAS, galaxies which have low M_d/M_* need to be more massive in general, which may explain why ETGs have a higher M_* on average than spirals in our sample. I find a mean dust mass of $(5.5^{+1.1}_{-0.9}) \times 10^7\,\mathrm{M}_\odot$ for the sample of ETGs, which is larger than the highest dust masses found in some previous studies of ETGs e.g. Temi *et al.* (2004) found $10^5 - 10^7\,\mathrm{M}_\odot$, which is similar to the dust masses found in ETGs with optical dust lanes (Kaviraj *et al.*, 2012) (although these are likely to be underestimated by the use of *IRAS* data - this issue will be addressed in future work.) Our mean dust mass is consistent with Vlahakis, Dunne & Eales (2005) who found dust masses greater than $10^7\,\mathrm{M}_\odot$ for 6 elliptical galaxies from an optically selected sample observed with SCUBA. The dust mass inferred for the SCUBA ellipticals may include contamination from synchrotron radiation, but for the sample of ETGs studied here, I find that synchrotron radiation is negligible compared

to thermal emission from dust (see Section 3.5.3). I find no significant difference in the $T_{\rm C}^{\rm ISM}$of the spirals and ETGs, and find a wide range of values for the dust temperature. The total effective V-band optical depth seen by stars ($\hat{\tau}_V$, $\hat{\tau}_V^{ISM}$) is approximately the same for ETGs and spirals. This shows that ETGs have approximately the same attenuation as spiral galaxies (though with rather large uncertainties).

3.3.2 Star-formation histories

I investigate the SFH of our galaxies by examining the SFR, (ψ) and SSFR, ($\psi_{\rm S}$, defined as ψ/M_*) averaged over the last 10^8 years. These parameters are derived from the SED fitting as described in Section 2.1. The model SFHs are described by a continuous exponentially decreasing star-formation rate, with superimposed randomly distributed bursts of star formation (Kauffmann *et al.*, 2003a) lasting between 3×10^7 and 3×10^8 years. These bursts occur with equal probability throughout the lifetime of the galaxy. The probability is set such that 50 percent of the galaxies in the library have undergone a burst of star formation in the last 2 Gyr. The amplitude of the burst (ratio of mass formed in the burst to mass formed in continuous star formation over the lifetime of the galaxy) is distributed between 0.03 and 4.0 with logarithmic spacing. For further details of the models, and the effects of model assumptions on derived parameters I refer the reader to Kauffmann *et al.* (2003a) and DCE08.

The mean SFR for ETGs is $0.7 \pm 0.2\,{\rm M}_\odot{\rm yr}^{-1}$, with a range of $0.04 - 12.4\,{\rm M}_\odot{\rm yr}^{-1}$. It is interesting to note that the distribution of ETG SFRs in Figure 3.4 shows signs of bimodality. Our range of SFRs is comparable to that found for optically blue ETGs by Schawinski *et al.* (2009), who find SFRs of $0.5 - 50\,{\rm M}_\odot{\rm yr}^{-1}$ using a range of indicators (Hα luminosity, u-band light, infrared luminosity from *IRAS*). H-ATLAS ETG SFRs are also larger than those found in recent studies of ETGs in the SAURON sample, which is a representative sample of local ETGs located in clusters and field environments (de Zeeuw *et al.*, 2002). Temi, Brighenti & Mathews (2009a) find that the SFR of SAURON S0s as estimated from 24μm luminosity is $0.02 - 0.2\,{\rm M}_\odot{\rm yr}^{-1}$, and Shapiro *et al.* (2010) calculated the SFR in the SAURON sample from non-stellar 8μm emission, and this was found to be $< 0.4\,{\rm M}_\odot{\rm yr}^{-1}$. These findings of low level star formation in the SAURON galaxies can possibly be explained by the optical selection,

which is not biased towards highly star-forming galaxies. This is in contrast to the H-ATLAS sample which selects the dustiest ETGs, and therefore the highest SFRs. Additionally, the SAURON measurements only give the obscured SFR, and may not be representative of the total SFR of the galaxy.

SSFR is defined as the star-formation rate per unit stellar mass and measures the star-formation efficiency of a galaxy. Figure 3.4 shows that the mean SSFR averaged over the last 10^8 years for ETGs ($1.4^{+0.5}_{-0.3} \times 10^{-11}\mathrm{yr}^{-1}$) is lower than that of spirals ($1.0 \pm 0.7 \times 10^{-10}\mathrm{yr}^{-1}$). This trend is insensitive to changes in the timescale over which the SSFR is averaged. There is, however, a wide range of SSFR and 17 percent of ETGs have a SSFR greater than the mean of the spiral sample.

In Figure 3.5 (a), I show a plot of dust mass versus SFR for spirals and ETGs in our sample. It can be seen that galaxies with the highest dust mass also have a high SFR. This trend is expected since both dust mass and SFR will depend on the total stellar mass of a galaxy. I can remove this trend by dividing by stellar mass and so I plot M_d/M_* vs. SSFR in Figure 3.5 (b). As was found in da Cunha *et al.* (2010b), there is a strong correlation between these two parameters. It can be seen that typically the ETGs have lower SSFR and M_d/M_* than spirals. There are some spirals with very low SSFR and M_d/M_* , which are discussed in Section 3.4.

I can use the results of our SED fitting to see if star formation is dominated by a recent burst or continuous star formation using the model parameter describing the time of last burst ($\mathrm{t_{LB}}$). Although there is a large uncertainty on this parameter, our results are still useful for a statistical comparison of two populations. As shown in Figure 3.4, ~ 76 percent of our ETGs have not had a burst of star formation in the last 10^9 years, and have therefore not formed a substantial fraction of their mass in recent bursts. It seems that most of our sample have residual star formation left over from the last major burst. Kauffmann *et al.* (2003b) find that galaxies with $M_* > 10^{10}\,\mathrm{M}_\odot$ typically have not had recent bursts of star formation, which may explain why our generally high mass ETG sample shows few recent bursts. The time since the last burst can also be characterised by the age of the young stellar population, parametrised in our models by the r-band light-weighted age ($\mathrm{age_r}$). It is found that the mean stellar population age of the ETGs is 2.8 ± 0.3 Gyr, which is older than that found for the spirals of 1.6 ± 0.1 Gyr.

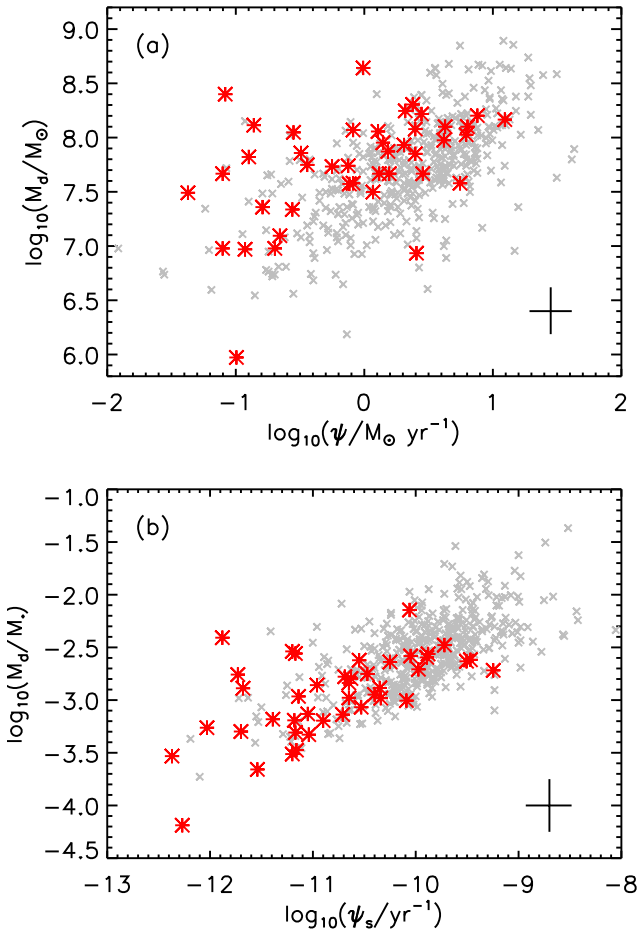

Figure 3.5: (a): $M_{\rm d}$ vs. SFR of the ETGs (large red stars) compared to the spiral galaxies (small grey crosses). **(b):** $M_{\rm d}/M_*$ vs. SSFR of the ETGs compared to the spiral galaxies. The error bars indicate the median 1σ uncertainty on a data point.

This is consistent with the general picture that ETGs are older than spirals. I note that 3/10 ETGs with bursts of star formation in the last 1 Gyr show disturbed morphologies, so galaxy interactions may be the cause of the burst. It is possible that more ETGs in this sample are disturbed at a level which is not detected in the shallow imaging that is available. Without deeper imaging, conclusions cannot be drawn about whether there is a correlation between morphological disturbance and recent star formation in this sample.

3.3.3 Comparison of broadband photometric and spectroscopic star formation parameters

SFH parameters are traditionally measured using spectroscopic information, whereas I used broadband data, so there may be a large uncertainty on some parameters. Walcher *et al.* (2008) explored degeneracies in the SFH parameters from broadband photometry using similar stellar population models to those in this work, and found that M_*, $\mathrm{age_r}$ and ψ_S are well determined. Wild *et al.* (2009) classify galaxies into star-forming galaxies and quiescent galaxies using broadband and spectroscopic data, and found a good agreement between these two classification methods. They also find the time of last burst derived from broadband SED fitting agrees with that derived from spectroscopy.

To investigate whether fitting SEDs to broadband photometry can accurately describe the SFHs of our galaxies, I stack spectra of ETGs and spirals together in bins of SSFR and r-band weighted age to look for trends in spectral features. The spectra are shifted to rest wavelength and resampled onto a common wavelength array. The spectra are normalised to the median of the spectrum, and then combined using the median of the spectra in each bin. Spectra which show signs of AGN (see Section 3.5), or have anomalous effects such as bad sky subtraction or fibre fringing (Colless *et al.*, 2001) have been removed. It can be seen from Figure 3.6 that as expected, the galaxies with the highest SSFR show signatures of star formation such as strong Hα and [OIII] and [OII] emission lines. Going from high to low SSFR, the strength of the emission lines decrease; the same trends are found for age, with older stellar populations showing minimal signs of star formation.

3.3.4 UV–Optical Colours

Galaxy colour is often used as a proxy for the age of a stellar population, with red galaxies assumed to be old due to a lack of UV emission from young stars. This simple interpretation can become complicated, with young star-forming galaxies appearing red due to dust obscuration, and old galaxies appearing blue due to contamination of

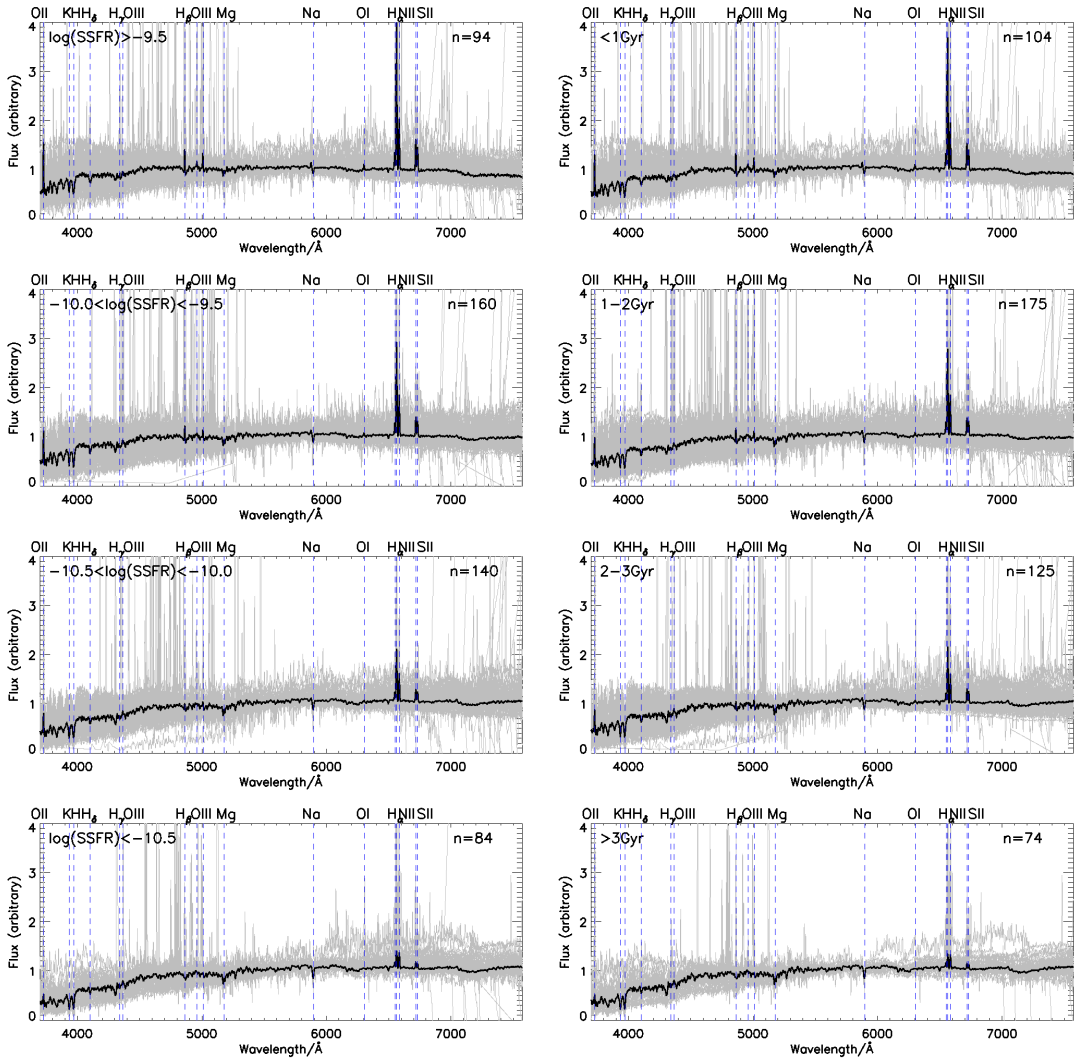

Figure 3.6: Stacked spectra in bins of SSFR (left) and stellar population age (right). The bins are arranged from high SSFR/young stellar population (top) to low SSFR/old stellar population (bottom). The grey area shows the normalised, individual spectra, and the thick black line is the median of these spectra, smoothed by a boxcar of 5Å. Prominent emission lines are shown by the blue dashed lines. The number of spectra in each stack is indicated in each panel.

the UV light by horizontal branch stars.[5] (O'Connell, 1999; Yi *et al.*, 2005; Kaviraj *et al.*, 2009). Dariush *et al.* (2011) separate red and blue galaxies in the H-ATLAS sample at $NUV - r = 4.5$ by fitting double Gaussians to the colour distribution. They found that *Herschel* preferentially selects blue galaxies, and that 90 percent of H-ATLAS sources with red colours are not old/passive[6] but have their light attenuated by dust. I examine the $NUV - r$ colours of our morphologically-selected galaxies using

[5]UV contamination from old stars is unlikely to be a concern, since our sample does not contain giant elliptical galaxies (Yi, Demarque & Oemler, 1997), and UV flux from old stars is likely to be swamped by that produced by young stars (Kaviraj *et al.*, 2011).

[6]Dariush *et al.* (2011) define 'passive' systems as galaxies which have red colours ($NUV-r > 4.5$), after correcting for dust obscuration.

aperture matched *GALEX* UV and GAMA optical photometry in Figure 3.7. Rest-frame photometry is calculated using K-CORRECT.V4.2 (Blanton & Roweis, 2007), and is corrected for galactic extinction using the reddening data of Schlegel, Finkbeiner & Davis (1998). Overall, 93 percent of ETGs have available NUV photometry. For sources which have a $< 5\sigma$ NUV detection [7], I compute lower limits for the colours. The mean error in the $NUV - r$ colour is 0.08 magnitudes.

Using the colour cut of Dariush *et al.* (2011) at $NUV - r = 4.5$ in Figure 3.7 (a), I find the ETGs have a range of colours, with 24 'blue' and 15 'red' ETGs. Many exist in the transition region between the red sequence and blue cloud. The SSFR of each galaxy is represented by the colour of each point, and a correlation with $NUV - r$ colour is observed. As expected, blue galaxies tend to have a higher SSFR, and red galaxies a lower SSFR, although with some exceptions. In Figure 3.7 (b) there is a wide range in the colours of both morphological types, although the median $NUV - r$ colour for the spirals is bluer than that of the ETGs. This trend is expected since spirals have more of their stellar population dominated by young stars.

The red ETGs generally have low SSFR, but still contain an appreciable amount of dust. These sources have high f_μ values which indicate the dust in these sources is predominantly heated by an older stellar population, which gives rise to the red colour of these galaxies. These objects are observed at a time when their star formation has mostly ceased, either because they have used up all their gas, or because star formation has been quenched by some process. Their dust has not yet been destroyed by sputtering and shocks from type Ia SNe, which is discussed in Rowlands *et al.* (2012)[8].

The ETGs which show signs of morphological disturbance (denoted by filled circles in Figure 3.7 a) have a range of colours. A Kolmogorov-Smirnov (K-S) test gives a probability of 0.14 of the colours of disturbed and non-disturbed ETGs being drawn from the same distribution; however, the difference is not significantly different (1.1σ). In contrast, Kaviraj (2010) find that peculiar ETGs have significantly bluer $NUV - r$ colours than relaxed ETGs. There is also a small population of 15 spirals with $NUV - r > 4.5$, and these are discussed in the following section.

[7] corresponding to $NUV > 23.0$ in the AB magnitude system after galactic extinction correction.

[8] An investigation of the origin of dust in ETGs was undertaken in Rowlands *et al.* (2012), but is not included in the thesis as the work was primarily done by a collaborator, H. Gomez.

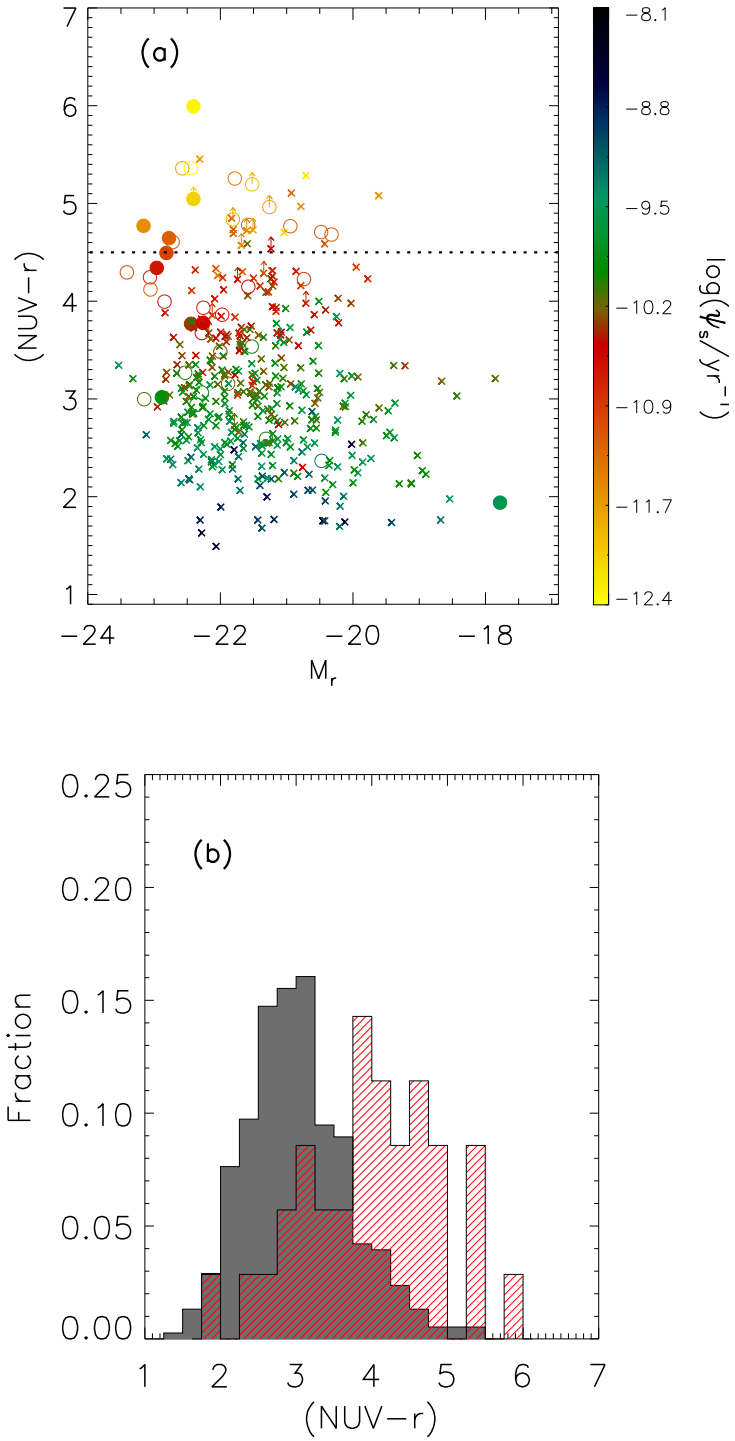

Figure 3.7: (a): UV-optical colour magnitude diagram, colour coded according to SSFR. Circles are ETGs, crosses are spirals, filled circles indicate that the ETG is morphologically disturbed. The dashed line shows the separation between 'blue' and'red' as defined in Dariush *et al.* (2011). Lower limits are shown for galaxies which do not have a $\geq 5\sigma$ NUV detection. **(b)**: The distribution of $(NUV - r)$ colours for the ETGs (red/hatched) and spirals (grey) which have a $\geq 5\sigma$ NUV detection.

3.4 Passive and Red Spirals

There has been much discussion in the literature about whether the red colour of some spirals is due to dust extinction or an old stellar population (Wolf, Gray & Meisenheimer 2005; Wolf *et al.* 2009; Masters *et al.* 2010b). Wolf *et al.* (2009) find optically red spirals have a lower SFR than blue spirals, but also contain large amounts of dust which obscures star formation. This may be due to the inclusion of edge-on spirals in their sample, which would inherently have a higher dust extinction because the central dust lane is oriented along the line-of-sight.

Of the 15 red ($NUV - r > 4.5$) spirals in our sample, only two have moderate levels of star formation with SSFR$\geq 10^{-11}\mathrm{yr}^{-1}$. The majority of the red spirals have SSFR much lower than this. By selecting spirals with SSFR$< 10^{-11}\mathrm{yr}^{-1}$ I explore the properties of the 19 (~ 5%) most passive galaxies in our spiral sample. I note that this is different from the 'passive' definition used by Dariush *et al.* (2011), which was based on dust-corrected UV-optical colour. The error on the SSFR for some passive spirals is large (up to $^{+0.7}_{-1.4}$dex), meaning that some passive spirals could plausibly have SSFR$> 10^{-11}\mathrm{yr}^{-1}$, however, the mean of the average SSFR PDF is $(2.6^{+1.3}_{-0.9}) \times 10^{-12}\mathrm{yr}^{-1}$. As a population, I can regard the average SSFR of passive spirals as being significantly (9.3σ) different from those of normal spirals (which have a mean of $(1.2 \pm 0.1) \times 10^{-10}\mathrm{yr}^{-1}$). SDSS images, best-fit SEDs and optical spectra of the passive spirals are presented in Figure A.2.

These spirals have $NUV - r$ colours ranging from 4.3 to 5.5, although there are 2/19 spirals for which NUV magnitudes are not measured due to the source being in close proximity to a bright star. I find 13/17 passive spirals are 'red', and 3/17 are 'blue', with one passive spiral having ambiguous colour due to an upper limit on the NUV magnitude. The majority of the passive spirals are not found at the extremes of the colour distribution, and lie in the green valley. This indicates that the passive spirals may be undergoing quenching of their star formation, and may be transitioning from the blue cloud to the red sequence.

3.4.1 Properties of passive spirals

A comparison of average PDFs derived from the SED fitting for 19 passive and 431 normal (SSFR $> 10^{-11}\mathrm{yr}^{-1}$) spirals is shown in Figure 3.8. The physical properties of the individual passive spirals derived from the SED fitting are presented in Table A.2, and the mean physical properties of the population are summarised in Table A.3. The passive spirals have a high mean f_{μ} of 0.87 ± 0.02, indicating that the majority of the dust luminosity is produced in the diffuse ISM, and powered mostly by old stellar populations. The distribution of V-band optical depths in the passive and normal spirals is similar, which argues against the passive spirals being red due to higher dust obscuration. The differences found in opacity between our passive spirals and the Wolf *et al.* (2009) red spirals (which have twice the dust extinction of blue spirals) may be because I only examine passive spirals, and they select their sample of red spirals on the basis of optical colour alone. As I have shown in Section 3.3.4, red colour does not necessarily mean that galaxies are passive.

The mean M_* of the passive spirals is $(4.2^{+0.7}_{-0.6}) \times 10^{10}\,\mathrm{M}_{\odot}$, in comparison to that of the normal spiral population which has a mean of $(1.9 \pm 0.1) \times 10^{10}\,\mathrm{M}_{\odot}$. I find 95 percent of the passive spirals are massive with $M_* > 10^{10}\,\mathrm{M}_{\odot}$. This could be a selection bias in that dust can only be detected in the most massive passive spirals as their M_{d}/M_* ratios are much lower than the normal spiral population. Alternatively, Masters *et al.* (2010b) found that in their sample almost all red spirals were massive ($M_* > 10^{10}\,\mathrm{M}_{\odot}$). Figure 3.8 shows that the passive spirals in our sample have much older stellar populations than the normal spiral population. This is consistent with Masters *et al.* (2010b), who found red, face-on spirals have older stellar populations than blue spirals, and are not post-starburst objects. This suggests our spirals have not stopped forming stars recently, and may have low SSFR because they have used up most of their gas. This implies that, under some circumstances, spirals can retain their spiral appearance for a few Gyr following the cessation of their star formation (e.g. Bekki, Couch & Shioya, 2002). This interpretation is supported by the time of last burst, for which I find a mean of $1.8^{+0.5}_{-0.4}$ Gyr for the passive spiral sample.

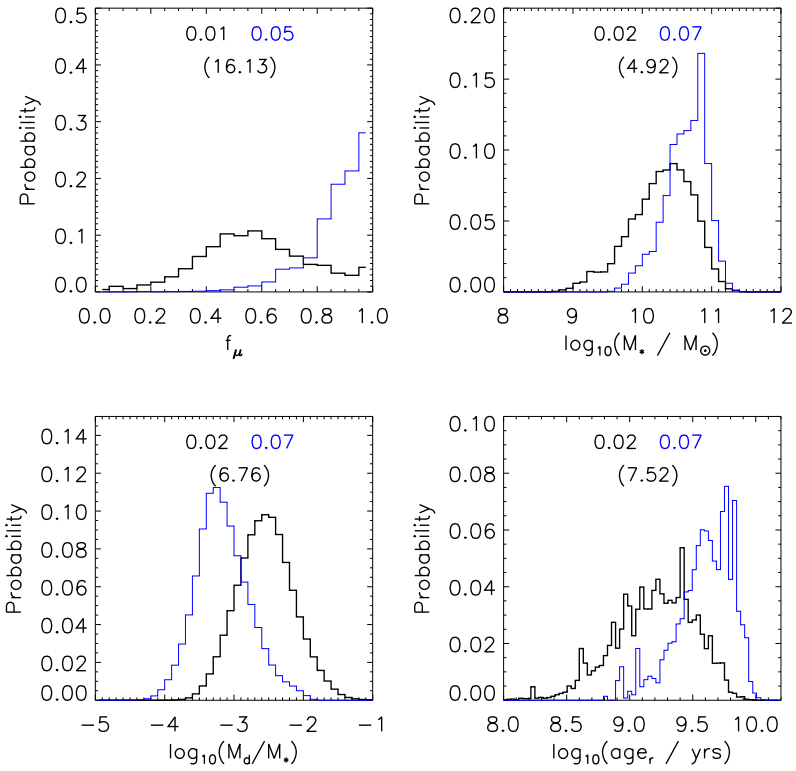

Figure 3.8: Average PDFs of the SED parameters of 19 passive spirals (SSFR$<10^{-11}\mathrm{yr}^{-1}$) (blue line) compared to 431 normal spirals with SSFR$\geq 10^{-11}\mathrm{yr}^{-1}$ (black line). The parameters are (from left to right): f_μ , the fraction of total dust luminosity contributed by the diffuse ISM; M_*, stellar mass; M_d/M_* , dust to stellar mass ratio; and $\mathrm{age_r}$, the r-band light-weighted age of the stellar population. The uncertainty on each distribution for ETGs and spirals is given by the error on the mean and is shown at the top of each histogram with corresponding colours, and the significance of the difference in the means in brackets. The errors for logarithmic parameters are in dex.

3.4.2 Inclination effects

Our sample of passive spirals is separated from the other morphologically-classified spirals on the basis of our SED fitting results, which uses an 'angle-averaged' approach. Results may be biased for sources with high inclinations (da Cunha *et al.*, 2010b), so I calculate the inclination of our passive spirals to check that there is not a high fraction of edge-on galaxies in our sample. The minor-to-major observed axis ratio b/a of the SDSS g-band isophote at 25 mag arcsec^{-2} can be used to determine inclination. A ratio of b/a of $\sim$1 indicates that a galaxy is face-on, b/a decreases as the galaxy inclination becomes edge-on. The observed axial ratio b/a can be converted into an inclination using the relation (as used in Masters *et al.*, 2010a)

$$\cos^2 i = \frac{(b/a)^2 - q^2}{1 - q^2}, \tag{3.1}$$

where q is the intrinsic axial ratio that would be measured for an edge-on galaxy ($i = 90°$). An estimate of q can be obtained from the observed distribution of axial ratios for SDSS galaxies with different values of the parameter f_{Dev} (Stoughton, 2002). This SDSS parameter describes the fraction of the galaxy light which is fit by a de Vaucouleurs profile (the other fraction of the luminosity is fit by an exponential profile), and gives information about the bulge-to-disk ratio. I adopt the relation found in Masters *et al.* (2010a) $q = 0.12 + 0.10 \times f_{Dev}$, and use the g-band defined f_{Dev}. The inclinations are listed in Table 3.2. Assuming that galaxies appear approximately edge-on for $i > 75°$, then a random sample of inclinations would lead to 17 percent of galaxies appearing edge-on. I find that 5/19 of our passive spirals have an edge-on inclination, and so within 2σ binomial errors our sample is consistent with a random distribution of inclinations. da Cunha *et al.* (2010b) show that the SSFR derived from SED fitting may be biased low for high inclinations ($b/a < 0.4$, corresponding to $i > 67°$). However, the SSFR of these passive spirals are sufficiently low that after accounting for this small bias the majority of these galaxies would still be regarded as passive.

I conclude that most of the 'passive' spirals are red because they harbour old stellar populations, not because of increased amounts of dust which obscures star formation. This agrees with the findings of Masters *et al.* (2010b), who find that red spirals have similar dust content (measured from Balmer decrements) to blue spirals at the same stellar mass.

3.5 Star-formation and AGN fractions

3.5.1 Emission line diagnostics

I use optical emission line ratios plotted on a BPT diagram (Baldwin, Phillips & Terlevich, 1981) to characterise the AGN activity in our H-ATLAS ETGs and spirals. Line ratios and equivalent widths (EWs) are derived from the SDSS MPA-JHU cata-

Table 3.2: Inclinations (i) in degrees of the 19 passive spirals in our sample. The *Herschel* SDP ID is given in column 1, b/a is the minor to major observed axis ratio of the SDSS g-band isophote at 25 mag arcsec^{-2}, f_{Dev} is an SDSS parameter which is the fraction of the galaxy fit by a de Vaucouleurs profile, q is the intrinsic axial ratio that would be measured for $i = 90°$.

SDP ID	b/a	f_{Dev}	q	i
SDP.30	0.87	0.70	0.19	29.9
SDP.77	0.95	0.82	0.20	17.9
SDP.143	0.33	1.00	0.22	75.1
SDP.271	0.24	0.27	0.15	79.2
SDP.372	0.32	0.98	0.22	76.1
SDP.1544	0.78	1.00	0.22	40.0
SDP.1773	0.32	0.94	0.21	75.9
SDP.1888	0.51	0.40	0.16	60.3
SDP.2547	0.43	0.01	0.12	65.6
SDP.2612	0.31	0.00	0.12	73.1
SDP.3578	0.28	0.56	0.18	77.4
SDP.3935	0.58	0.98	0.22	56.4
SDP.4548	0.36	0.51	0.17	71.4
SDP.4639	0.73	0.02	0.12	43.9
SDP.4859	0.43	0.59	0.18	66.8
SDP.4964	0.64	0.35	0.16	51.3
SDP.5108	0.49	0.47	0.17	61.8
SDP.5226	0.62	0.95	0.22	53.4
SDP.7324	0.38	1.00	0.22	71.3

logue[9] (Tremonti *et al.*, 2004) and the GAMA survey (Driver *et al.*, 2011). I regard a line detection as $> 3\sigma$ above the continuum, but lines affected by sky emission or fibre fringing are not used. For line fluxes derived from the SDSS sample, corrections are made for stellar continuum absorption by subtracting a stellar population model from the spectrum, and measuring emission lines from the residual (Tremonti *et al.*, 2004). Where line fluxes are derived from GAMA measurements, a correction of 1.3Å for stellar absorption is applied to the EW of the Hα and Hβ emission lines (Hopkins *et al.*, 2003; Gunawardhana *et al.*, 2011; Wijesinghe *et al.*, 2011). Gunawardhana *et al.* (2011) found for Hα lines with log(Hα EW)< 0.9 there was a difference of more than 5% in EW when a range of absorption corrections from $0.7 - 1.3$Å was applied. Some of our sources are below log(Hα EW)< 0.9, but our results are unchanged if this range of absorption corrections are used. In the cases where there are multiple measurements of the same galaxy, I take the signal–to–noise weighted mean of the line fluxes.

[9] http://www.mpa-garching.mpg.de/SDSS/DR7/

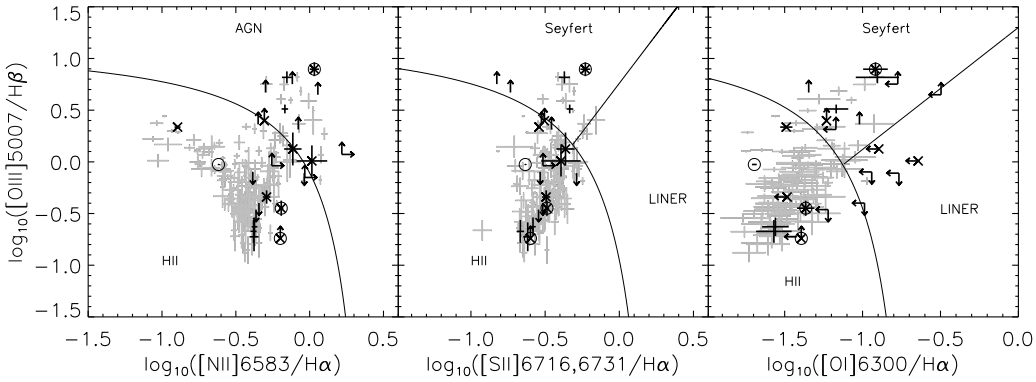

Figure 3.9: BPT diagram showing H-ATLAS spirals (grey) and ETGs (black) with all four lines in each diagram detected at $> 3\sigma$, with error bars shown. Those below the curved line are classified as star-forming, those above the curved line are classified as AGN. Upper limits are shown for the ETGs where at least two emission lines are detected. ETGs which have radio emission (Section 3.5.3) are marked with a circle, and disturbed morphologies with a diagonal cross.

I plot the [OIII]/Hβ line ratio as a function of the [NII]/Hα, [SII]/Hα and [OI]/Hα line ratios in Figure 3.9 for spirals and ETGs. I classify objects as AGN or star-forming first from the [OI]/Hα diagram, since [OI] is the most sensitive to the presence of an AGN. If the galaxy is not present in the [OI] diagram, I use the [SII]/Hα diagram, and finally the [NII]/Hα diagram. On all diagrams, galaxies that lie above the curved line are classified as AGN (Kewley *et al.*, 2001), and galaxies below the line are star-forming. Low signal-to-noise [OIII] and Hβ lines mean that some sources cannot be located on the BPT diagram. In these cases, a source is classified as an AGN if [NII]/H$\alpha \geq 0.2$. In many ETGs, fewer than four of the required emission lines are detected, so upper limits are utilised to locate the galaxy on the BPT diagram where at least two lines are present[10]. I present the classification fractions of ETGs in Table 3.3; more than half of ETGs are star-forming, but 45 percent of ETGs cannot be classified due to their weak emission lines. For comparison, spiral galaxies are plotted on Figure 3.9 in grey, and are mostly classified as star-forming.

In a sample of optically selected ETGs, Schawinski *et al.* (2007b) found 61% are star-forming, and 39% are AGN dominated, which is similar to the fractions in our H-ATLAS sample. Since the AGN fraction is consistent with that from an optically-

[10]In the case where there is Hβ absorption, the Hβ flux is not measured in the GAMA spectra, so 3σ upper limits are used. Assuming a flat continuum, I estimate the area under a Gaussian line in pixels ($Npix$) with FWHM equal to the instrumental resolution of 3.5Å, and estimate the error on this line given the mean noise in the spectrum (σ) as $\sqrt{Npix} \times \sigma$.

Table 3.3: Emission line classifications of H-ATLAS ETGs which can be unambiguously classified on the BPT diagram. These fractions do not include galaxies which cannot be classified into either category, which comprises 45 percent of the sample. Ambiguous classifications result from one or more weak emission lines not detected at $> 3\sigma$, or measurements affected by skylines. The errors are 1σ confidence intervals on a binomial population using a beta distribution, which is appropriate for small population numbers (Cameron, 2011).

Classification	Number	ETG Percentage
ETGs	23	100%
Star-forming	13 ± 2	$57^{+9}_{-10}\%$
AGN	10 ± 2	$43^{+10}_{-9}\%$

selected sample, this would suggest there is no link between the presence of AGN and dust emission, although it is interesting to note that there are few Low-Ionisation Nuclear Emission-Line Region (LINER) type galaxies in our sample (although some galaxies with upper limits may fall into this category). The lack of LINERs in our sample may be because they are dust poor (Kauffmann *et al.*, 2003b; Kewley *et al.*, 2006), and so there may be a bias against detecting LINERS in H-ATLAS, although a larger sample of galaxies is needed to confirm this.

AGN emission is not accounted for in the SED fitting, so galaxies with AGN may be poorly described by the MAGPHYS models. For the ETGs which host AGN, their SEDs look similar in the optical to those which are classified as star-forming. Kauffmann *et al.* (2003b) find that the optical spectra of type-2 AGN have a small fraction of their optical light from non-stellar sources, and are very similar to spectra of non-AGN host galaxies, except for emission lines. Since our physical properties are determined from broadband fitting and not from line strengths, properties derived from broadband optical data should not be affected by the presence of a type-2 AGN. Since Hatzminaoglou *et al.* (2010) find no difference between the FIR/submillimetre colours of star-forming and AGN galaxies; the FIR is insensitive to presence of AGN and therefore will not produce a bias in SED parameters.

3.5.2 Hα equivalent widths

I present the Hα EW distribution of our ETGs in comparison to spirals in Figure 3.10. For the ETGs there is a range in EW from 0–109Å with a median of 8.7Å, which

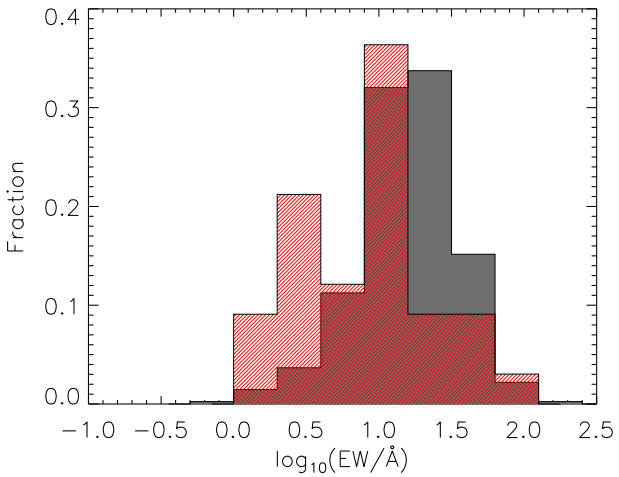

Figure 3.10: Hα EW (corrected for stellar absorption) of spiral galaxies (grey) and ETGs (red/hatched) which have $\geq 3\sigma$ Hα detections. A K-S test shows that the ETGs have a probability of 1.7×10^{-4} of being drawn from the same distribution as the spirals. Therefore the Hα EWs of ETGs and spirals are not drawn from the same underlying distribution.

is lower than the median for the spirals in our sample (16.4Å). The median value for the spirals is similar to that found for field galaxies by Tresse *et al.* (1999). It is not unsurprising that the EW of ETGs is less than that of spirals, but nonetheless some EWs are substantial and indicate ongoing star formation (consistent with the broad-band SED fitting). The range of Hα EWs in ETGs are comparable to those found by Schawinski *et al.* (2009), who found EWs up to 85Å in their blue ETG sample. Fukugita *et al.* (2004) found that visually-classified ETGs (with $r < 15.9$ and $z \lesssim 0.12$) have a similar Hα EW range as our sample, with 19 out of 420 E/S0s with Hα EW > 10Å (which represents star-forming galaxies in the Fukugita *et al.* (2004) sample). In our sample, a much larger fraction (31 percent) of our ETGs have Hα EW > 10Å, which is unsurprising given our FIR selection.

3.5.3 Radio detections

Another indicator of star formation and AGN activity is radio emission. Smith *et al.* (2011) computed the statistical probability of a chance alignment between radio and H-ATLAS sources using the frequentist technique of Downes *et al.* (1986), which used a method to determine the most likely radio counterpart by choosing the source with the lowest probability P of being a chance alignment. ETGs are cross-matched with the FIRST radio catalogue in Smith *et al.* (2011), with 5/42 ETGs having radio counter-

Table 3.4: q_{IR} values for the 5/42 *Herschel* ETGs with reliable radio counterparts and SED fits. Errors are propagated from the 1σ error on TIR and the local noise estimate at the source position measured in mJy. $F_{\rm int}$ is the integrated flux density at 1.4 GHz in mJy. P is the probability of a chance alignment of the submillimetre and the radio source as computed in Smith *et al.* (2011).

Name	SDP ID	P	$F_{\rm int}$	q_{IR}
J091205.8+002656	SDP.15	0.014	4.25	2.53 ± 0.15
J090352.0-005353	SDP.45	0.048	0.98	2.59 ± 0.17
J090718.9-005210	SDP.350	0.148	1.18	2.58 ± 0.18
J090752.3+012945	SDP.1027	0.083	2.14	1.68 ± 0.41
J085947.9-002143	SDP.6427	0.077	8.62	0.86 ± 0.56

parts with $P < 0.2$, and so are considered to be likely associations. The radio emission may indicate the presence of an AGN and/or star formation, so I compute the ratio of the bolometric IR flux to the 1.4 GHz radio flux ($q_{\rm IR}$) using the method of Helou, Soifer & Rowan-Robinson (1985), see also Bell (2003); $q_{\rm IR}$ is defined as

$$q_{\rm IR} = \log_{10}\left(\frac{\rm TIR}{3.75 \times 10^{12} {\rm W\,m^{-2}}}\right) - \log_{10}\left(\frac{S_{1.4\,{\rm GHz}}}{\rm W\,m^{-2}\,Hz^{-1}}\right), \qquad (3.2)$$

where $S_{1.4\,{\rm GHz}}$ is the rest-frame 1.4 GHz k-corrected flux density and TIR is the total infrared luminosity ($L_{\rm d}^{\rm tot}$), which is integrated between $3 - 1000\mu$m.

The $q_{\rm IR}$ values for the ETGs are presented in Table 3.4. Three ETGs have q_{IR} values which are consistent with the median $q_{IR} = 2.64 \pm 0.02$ for 162 star-forming galaxies in Bell (2003). I find two ETGs have $q_{\rm IR}$ values which are significantly lower than that for star formation, which suggests the presence of a radio-loud AGN in these galaxies. To rule out synchrotron contamination of the 500μm flux, I extrapolate the 1.4 GHz radio flux to 500μm using a power law with a spectral slope α. Assuming $\alpha = -0.8$ the synchrotron emission at this wavelength is negligible compared to the dust emission measured at 500μm.

It is interesting to note the classifications of ETGs using emission line ratios are consistent with those from radio emission. The three ETGs with radio emission consistent with star formation also have some of the bluest optical colours and largest Hα EWs. For the ETGs which are classified as AGN using radio emission, one (SDP.6427) is classified as an AGN using emission lines. The other (SDP.1027) is likely to be an AGN from its line emission, although it has insufficient signal–to–noise to confirm this.

3.5.4 Passive spirals

In most cases the spectra of the passive spirals show little or no Hα emission and a strong 4000Å break (see Figure A.2), indicating low SFR and an old stellar population. Strong sodium and magnesium absorption is often observed in the spectra, which can indicate the presence of an old stellar population or high metallicity. Only 4/19 passive spirals have sufficiently strong emission lines such that they can be located on a BPT diagram, and all of these are classified as AGN. This may be because AGN are more common in massive galaxies (Kauffmann *et al.*, 2003b), although Masters *et al.* (2010b) found that red face-on spirals have a higher AGN fraction than blue face-on spirals. The lack of emission lines in the majority of the sample is consistent with their being selected as passive in terms of star formation, and also indicates a lack of AGN activity. This agrees with radio data, as there are no matches for these sources in the FIRST radio catalogue.

3.6 Environment of Herschel detected sources

The environment of ETGs and spirals is examined by computing the local density around each one (Brough et al. in prep). To define the local density, a volume limited sample of galaxies is used with $M_r < -20$ and $z < 0.18$. The density Σ_N in Mpc^{-2} is computed as

$$\Sigma_N = \frac{N}{\pi d_N^2}, \tag{3.3}$$

where d_N is the projected comoving distance to the Nth nearest neighbour within $\pm 1000 \mathrm{kms}^{-1}$, and $N = 5$. Densities are computed for all H-ATLAS galaxies which have $r_{Petro} \leq 19.4$, and have good quality spectroscopic redshifts with $0.01 < z < 0.18$, which is the limit defined by the absolute magnitude limit of the sample.

3.6.1 H-ATLAS ETGs

Using these criteria densities are measured for 30 ETGs and 354 spirals detected in H-ATLAS, which are compared in Figure 3.11. The densities for ETGs and spirals both range from void to group environments (Baldry *et al.*, 2006), with most galaxies residing in field environments. There are few H-ATLAS galaxies in group/cluster environments, so our galaxies do not sample the full range of densities in the SDP field, which range from ~ 0.01 to 100 galaxies Mpc^{-2}. From the morphology-density relation (Dressler, 1980), spirals are more numerous in low density environments, and ETGs generally reside in high density environments. However, a K-S test reveals there is no significant difference between the densities of spirals and ETGs detected in H-ATLAS. This is consistent with the findings of Dariush *et al.* (2011), who found that the detection rate of H-ATLAS galaxies split into blue and red colours does not depend on environment. Young *et al.* (2011) observed a volume-limited sample of ETGs and found a statistically weak dependence of molecular CO (which is often associated with star formation) on local galaxy density, where CO detections were only marginally lower in the cluster environment compared to the field. Conversely, blue ETGs have been found in lower density environments than red ETGs (Schawinski *et al.*, 2007a; Bamford *et al.*, 2009), although these studies sampled both field and cluster environments. Kannappan, Guie & Baker (2009) found that intermediate mass ETGs are common in low density environments, and suggest that they may be undergoing disk re-growth.

It is possible that the range of environments probed is too small to see a significant difference in the densities of H-ATLAS sources as a function of morphology. The full H-ATLAS data set will encompass the Coma cluster and many other rich Abell clusters and will allow a more in depth investigation of environmental effects. Since some of the H-ATLAS galaxies are in low density regions, it is possible that our measure of environment does not always reflect the true local density, and instead traces inter-halo distances.

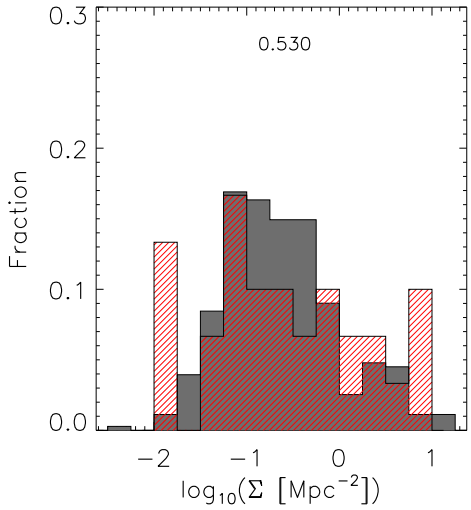

Figure 3.11: Comparison of densities for H-ATLAS spirals (grey) and ETGs (red/hatched). A K-S test (shown at top of histogram) shows that the null hypothesis cannot be rejected, therefore the samples are likely to be drawn from the same distribution.

3.6.2 Passive spirals

It is thought that passive spirals have had their star formation quenched as a result of galaxy interactions with the intra-cluster medium. This can remove gas from the outer halo, which stops the supply of fuel for star formation in the disk (e.g. Bekki, Couch & Shioya, 2002; Wolf *et al.*, 2009). I use the local density estimates to test for any environmental differences between our passive and normal spirals. Densities can be measured for 17/19 passive spirals. Figure 3.12 shows that passive spirals in our sample mostly inhabit low density environments with a median density of 0.28 galaxies Mpc^{-2}, which is slightly higher than the median density of normal spirals (0.19 galaxies Mpc^{-2}). A K-S test shows that the distributions of densities of passive and normal spirals are not significantly different, although this may be due to our small sample size. Our median density is different from Masters *et al.* (2010b) who found the red, face-on spiral fraction peaks at $1\,\mathrm{Mpc}^{-2}$, and Bamford *et al.* (2009) who found that the density of red spirals peaks at $6\,\mathrm{Mpc}^{-2}$. While 19% of their red spirals are found at densities $< 1\,\mathrm{Mpc}^{-2}$, I find that 71% of our passive spirals lie at densities lower than this. The differences in these fractions may be due to selection effects, since the Bamford and Masters samples are selected to be 'red', rather than 'passive', and also because our H-ATLAS spirals are in low density environments. Our sample shows that it is possible to have passive spirals at low densities. I conclude that environment is

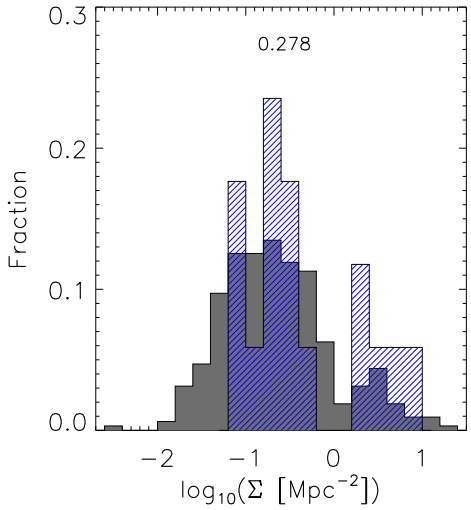

Figure 3.12: Environment of passive spirals with SSFR$< 10^{-11}\mathrm{yr}^{-1}$ detected in H-ATLAS (blue), compared to normal spirals with SSFR$> 10^{-11}\mathrm{yr}^{-1}$ (grey). A K-S test shows a high probability (shown at top of histogram) that both samples are drawn from the same distribution.

not the only factor influencing whether galaxies are passive, and the processes which turn spirals passive occur at both high and low densities.

3.7 Properties of non-detected ETGs

I have identified a population of ETGs with substantial dust masses, some of which are actively star-forming. In order to understand how this population is different from optically-selected ETGs, I compare to a control sample of morphologically-classified galaxies in the SDP field. The control sample is chosen to have the same $n(r, z)$ as the H-ATLAS sample, and are not detected in H-ATLAS. The selection method for this sample is described in Section 3.2.1.2.

3.7.1 Dust masses

The control sample is comprised of galaxies which are not detected in the submillimetre. I can, however, investigate the average dust mass of optically-selected ETGs with stacking techniques. The stacking was performed on background-subtracted, unfiltered SPIRE maps by N. Bourne. All detected SPIRE sources are subtracted from the map, so that that the stack is not contaminated by sources outside our sample. Stacking is

performed at the positions of the ETGs in the control sample, using the same method as Bourne *et al.* (2012). Assuming all galaxies are unresolved point sources, for each source a cut-out of the map is convolved with a point spread function (PSF) centred on the optical position, which is interpolated to the same pixel grid as the data map. The flux of blended sources is shared out as described in the appendix of Bourne *et al.* (2012), but the effect of blending is negligible in this sparsely distributed sample, so double-counting of flux does not affect the stacked values. This method is effectively similar to stacking in a PSF-filtered map. The background level is estimated by stacking at random positions and this is subtracted from the stacked flux. The median value in the stack is used in order to avoid bias from outliers. Following the same method as Bourne *et al.* (2012), the 1σ error on the median is estimated from the distribution of values in the stack as described by Gott *et al.* (2001). This error estimate automatically takes into account both the measurement error, which reduces as the square root of the number of objects stacked, and the intrinsic spread of fluxes within the stack. By stacking on the positions of 233 ETGs in the control sample, I find median fluxes of 2.9 ± 0.5mJy at 250μm (5.8σ), 0.8 ± 0.6mJy at 350μm and -0.6 ± 0.6mJy at 500μm. The 250μm flux is consistent with the typical fluxes of the optically red galaxies in Bourne *et al.* (2012).

To obtain the median stacked dust mass, I calculate the dust mass of each object in the sample from its measured flux in Jy and its redshift, using equation 3.4. Again, the error is calculated from the distribution of dust mass values in the stack using the Gott *et al.* (2001) method.

$$M_{\rm d} = \frac{S_{250}\, D_L^2 K}{\kappa_d(\nu)\, B(\nu,\, T_{\rm d})(1+z)}. \tag{3.4}$$

S_{250} is the observed 250μm flux, D_L is the luminosity distance at redshift z, $B(\nu,\, T_{\rm d})$ is the value of the Planck function at 250μm for a dust temperature $T_{\rm d}$, and the dust mass opacity coefficient $\kappa_d(\nu)$ is $0.89{\rm m}^2{\rm kg}^{-1}$ (following Dunne *et al.* 2011). K is the k-correction, which is given by

$$K = \left(\frac{\nu_{\rm o}}{\nu_{\rm e}}\right)^{3+\beta} \frac{e^{h\nu_{\rm e}/kT_{\rm iso}} - 1}{e^{h\nu_{\rm o}/kT_{\rm iso}} - 1}, \tag{3.5}$$

where $\nu_{\rm o}$ is the observed frequency at 250μm, $\nu_{\rm e}$ is the emitted frequency and $T_{\rm iso}$ is the isothermal temperature of a greybody model normalised to recover the stacked flux at 250μm. I assume a dust emissivity index $\beta = 2.0$ and $T_{\rm iso} = 18.5$ K, which adequately describes the SEDs of optically selected galaxies (Bourne *et al.*, 2012).

Assuming a realistic range of temperatures for ETGs of 25–15 K[11] (Temi *et al.*, 2004; Leeuw *et al.*, 2004; Smith *et al.*, 2012c), I find median dust masses in the range $(0.8 - 4.0) \times 10^6\,{\rm M}_{\odot}$. The dust masses of the control sample ETGs are more than an order of magnitude smaller than the dust masses of the H-ATLAS ETGs, indicating that the 250μm selected ETGs are indeed much dustier than the average optically-selected ETG.

3.7.2 Star formation histories and optical colours

I use the same technique as described in Section 2.1 to fit the multiwavelength SEDs of the 1052 control sample galaxies, using 5σ upper limits for the FIR–submillimetre fluxes. I reject 27 ETGs and spirals which have poor quality SED fits with $\chi^2 > 30$. Although the parameters derived from the FIR-submillimetre region of the SED are only constrained by the UV–NIR data, I can put similar constraints on SFH parameters as for the 250μm selected sample, as most of the constraint for SFH parameters comes from the UV–NIR photometry. A summary of the parameters derived from the mean PDFs is provided in Table A.3. Stellar mass is one of the main drivers of galaxy properties, so it is important to check that the M_* distributions are the same for the H-ATLAS detected and control ETGs. If this is the case then physical properties can be compared without a dependence on galaxy mass. Figure 3.13 shows the stacked PDFs of the stellar mass distributions for H-ATLAS and control ETGs are not significantly different, since the control sample is selected to have the same r, z distribution. The range of $M_{\rm d}/M_*$ for the control ETGs is $(1.4 - 6.8) \times 10^{-5}$ for 25–15 K dust, and, on average, the mean SSFR of the control ETGs is 1.1 dex lower than that of H-

[11]Higher dust temperatures have been found in some studies of ETGs (e.g. Savoy, Welch & Fich, 2009; Skibba *et al.*, 2011), but these used $\beta = 1.5$ which results in a higher dust temperature ($\sim 3-4$ K) being calculated (Bendo *et al.*, 2003). Accounting for this difference in β, these studies yield dust temperatures which are consistent with our range of adopted values.

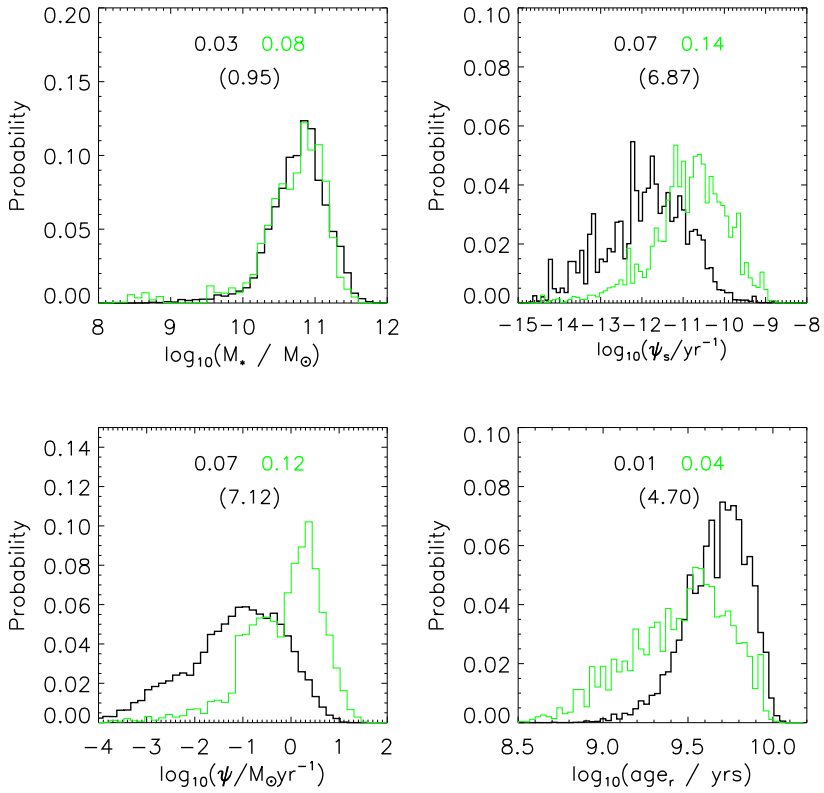

Figure 3.13: Average PDFs of the SED parameters of 42 detected ETGs (green line) compared to 222 control ETGs (black line). The parameters are (from left to right): M_*, stellar mass; ψ_S/yr^{-1}, SSFR; $\psi/\mathrm{M}_\odot\,\mathrm{yr}^{-1}$, SFR; and $\mathrm{age_r}$, the r-band light-weighted age of the stellar population. The uncertainty on each distribution for ETGs and spirals is given by the error on the mean and is shown at the top of each histogram with corresponding colours, and the significance of the difference in the means in brackets. The errors for logarithmic parameters are in dex.

ATLAS ETGs. A similar trend is found when comparing the mean SFR of the ETGs. For our control ETGs the mean r-band light-weighted age of the stellar population is 4.6 ± 0.1 Gyr, which is 1.8 Gyr older than the H-ATLAS sample of ETGs.

The $NUV - r$ colours of the control ETGs are computed as in Section 3.3.4, and are compared to the H-ATLAS ETGs on a colour–magnitude diagram in Figure 3.14 (a). These cover approximately the same range in M_r by design. The distribution of colours are shown in Figure 3.14 (b); the control ETGs are on average 1.0 magnitude redder than the H-ATLAS detected ETGs. Since the control ETGs are not detected in H-ATLAS these galaxies are less obscured by dust, with colours dominated by stellar population age rather than obscuration. The colour difference between detected and control ETGs is therefore intrinsic. A handful of control ETGs have very blue $NUV-r$ colours, but the dust masses of these star-forming galaxies may not be high enough to be detected by H-ATLAS. Alternatively, there could have been a failure in matching

the optical counterpart and submillimetre source, which is a possibility for 7 of the control ETGs, (of which 3 are 'blue'). These, however, have a very small reliability of association as determined in Smith *et al.* (2011).

3.7.3 Environments of Herschel non-detected sources

I compare the environments of control sample ETGs and spirals in Figure 3.15, with densities as calculated in Section 3.6. As expected, on average the median density of control ETGs is higher than that of the spirals, and in contrast to the H-ATLAS ETGs and spirals, a K-S test shows a low probability of the control ETGs and spirals being drawn from the same distribution.

To see how the environments of the detected ETGs are different from those in the control sample, I compare the densities in Figure 3.16 (a), and find they are different at only the 1.8σ level. There is some indication that H-ATLAS ETGs are in lower density environments than optically-selected ETGs, but a larger sample size is needed to confirm this. A comparison of the detected and control spirals using a K-S test in Figure 3.16 (b) shows that the null hypothesis cannot be rejected, therefore the environments of the detected and control ETGs are drawn from the same distribution. The similarity of the distributions suggests that environment does not explain the differences between the H-ATLAS detected and control sample ETGs, however, small sample statistics combined with a small range of environments currently limits the strength of our findings.

3.8 Conclusions

I have presented the properties of a 250μm selected sample of 44 early-type galaxies and 496 spiral galaxies in the 14 square degree *Herschel*-ATLAS science demonstration phase field. Both samples have panchromatic photometry from the rest-frame UV to the submillimetre, which allowed me to fit SEDs to derive statistical constraints on galaxy physical parameters using an energy balance technique. I then examined the properties of H-ATLAS galaxies as a function of morphological type. I also compared

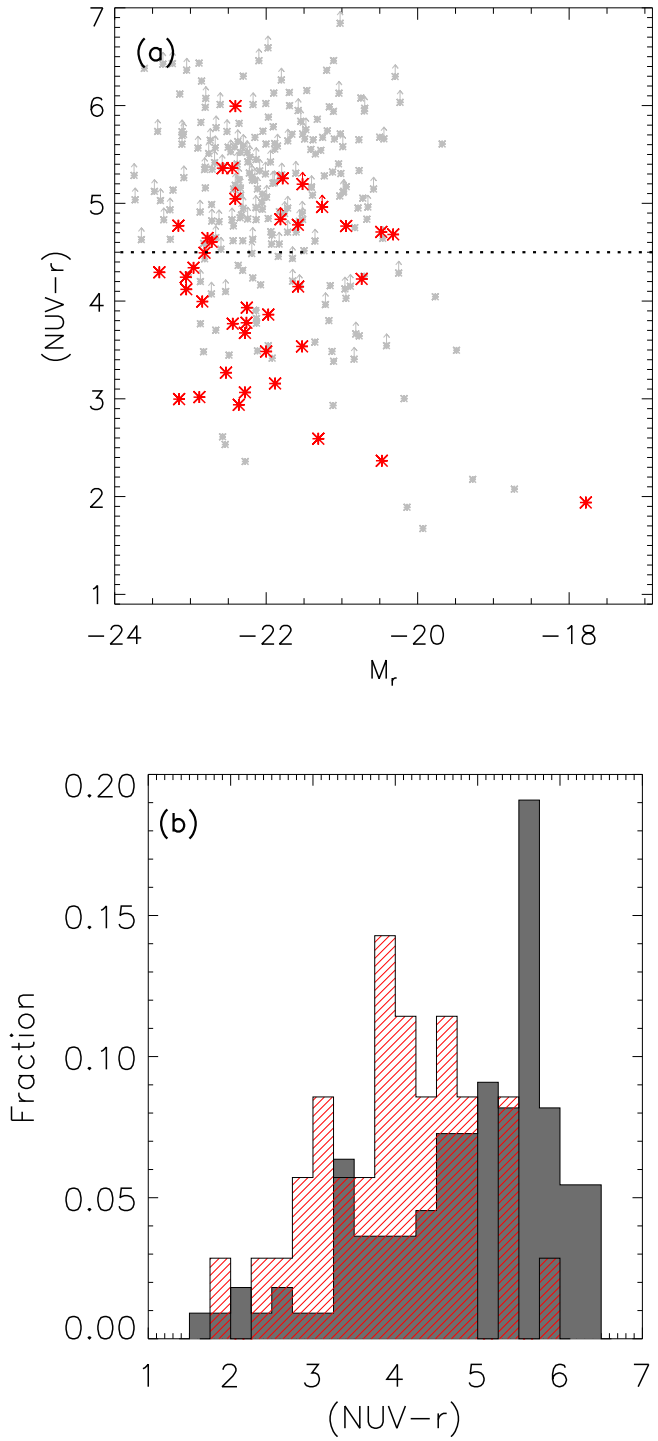

Figure 3.14: (a): UV-optical colour magnitude diagram for H-ATLAS detected (red stars) and control ETGs (grey crosses). Lower limits are shown for galaxies which do not have a $\geq 5\sigma$ NUV detection. **(b)**: Comparison of the $NUV - r$ colours for the detected ETGs (red/hatched) and control ETGs (grey/filled) which have a $\geq 5\sigma$ NUV detection.

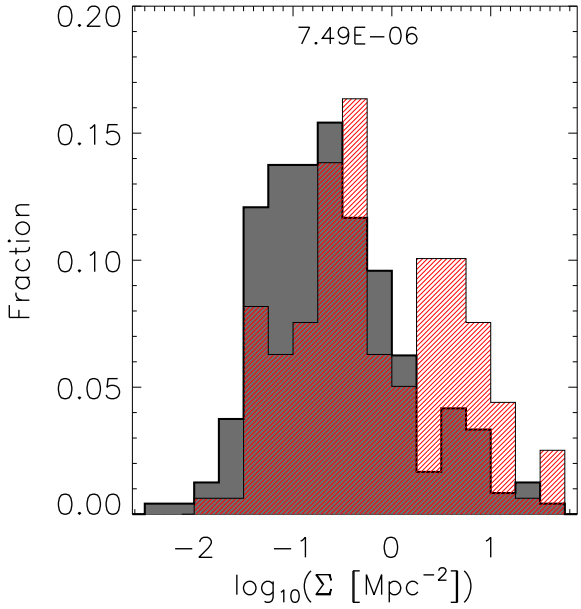

Figure 3.15: Comparison of densities for control sample ETGs (red/hatched) and spirals (grey). As expected, the spirals have a lower median density than the ETGs. A K-S test shows a low probability (shown at top of histogram) of the samples of ETGs and spirals being drawn from the same distribution.

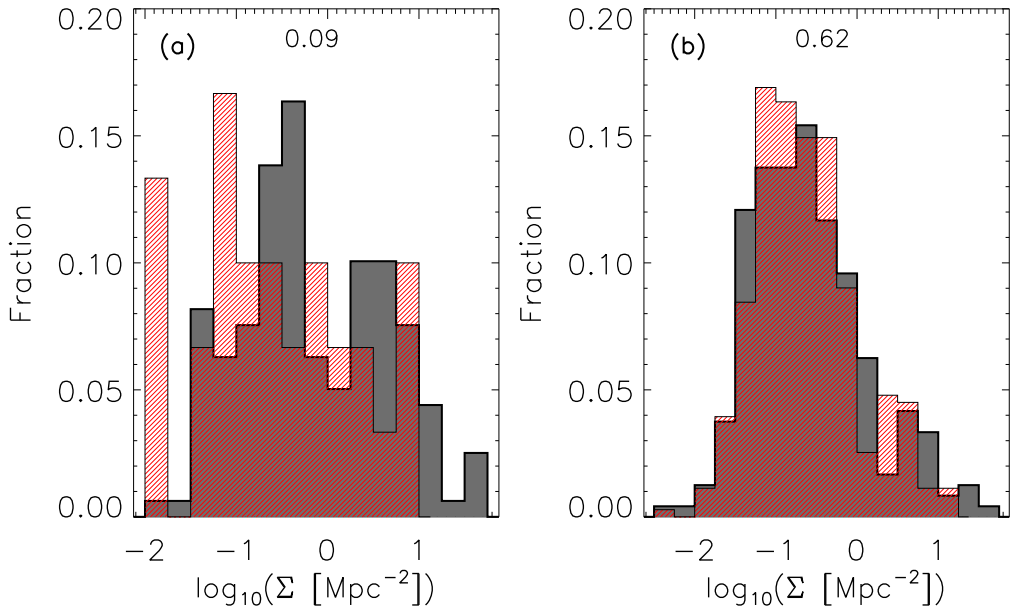

Figure 3.16: Comparison of environments between H-ATLAS detected (red/hatched) and control ETGs (a) and H-ATLAS and control spirals (b). For the detected and control ETGs a K-S test shows the two distributions have a low probability (shown at top of histogram) of being drawn from the same distribution, although this is only significant at the 1.8σ level. A K-S test of the environments of the control and H-ATLAS spirals shows that they are likely to be drawn from the same distribution.

to a control sample of galaxies selected in the optical to have the same redshift and r-band magnitude distribution as the H-ATLAS sample. Our main results are as follows.

- ETGs detected by *Herschel* are atypical compared to optically selected ETGs. A significant mass of dust is detected in H-ATLAS ETGs, with a mean of $5.5 \times 10^7\,\mathrm{M}_\odot$. Through stacking I find that dust masses are an order of magnitude lower than optically selected ETGs of a similar stellar mass.

- Only a small fraction of H-ATLAS ETGs (24 percent) have evidence for a recent burst of star formation within the past Gyr. Some of these galaxies may have had star formation triggered as a result of an interaction, indicated by disturbed morphologies in 31 percent of the sample, although not all disturbed sources show signs of a recent burst. The majority of ETGs have residual low-level star formation left over from the last burst a few Gyrs ago, and their optical colours suggest they exist in the transition region between the blue cloud and the red sequence.

- I find that the control ETGs have lower SSFRs and older stellar population ages than H-ATLAS ETGs, which is consistent with the red UV-optical colours of the control ETGs. It is possible that the dust content may therefore be related to the time of the last major star formation episode several Gyrs ago.

- No significant difference is found in the environments of H-ATLAS and control ETGs, although this may be due to small sample size. Environment does not seem to influence whether an ETG is dusty at the moderate-low densities probed in this study. Additionally, H-ATLAS ETGs are not found to reside in high density environments.

- I examine the properties of passive spirals in our sample which have low SSFR $< 10^{-11}\mathrm{yr}^{-1}$, but still contain significant dust mass. They have larger M_* and lower M_d/M_* than 'normal' spirals, and are red in colour, which is due to an old stellar population, and not due to increased dust reddening. It is possible that these passive spirals have simply run out of gas to fuel star formation, or their star formation has been quenched by some process in the low density environment in which they reside.

Herschel can probe the dust content of different types of galaxies over a wide range of redshifts. The full coverage of the H-ATLAS survey will allow further investigation of dusty galaxy populations, with far larger numbers of ETGs and passive spirals. This will improve our understanding of objects which are transitioning between the blue and red sequence, either through rejuvenated star formation, or through the cessation of star formation as the supply of gas ends.

Chapter 4

Dust in galaxies at high and low redshift

4.1 Introduction

The first blind submillimetre surveys discovered a population of luminous ($L_{\rm IR} \sim 10^{12}\,{\rm L}_{\odot}$), highly star-forming ($100 - 1000\,{\rm M}_{\odot}{\rm yr}^{-1}$), dusty galaxies at high redshift (Smail, Ivison & Blain, 1997; Hughes *et al.*, 1998; Barger *et al.*, 1998; Eales *et al.*, 1999). These submillimetre galaxies (SMGs) are thought to be undergoing intense, obscured starbursts (Greve *et al.*, 2005; Alexander *et al.*, 2005; Tacconi *et al.*, 2006; Pope *et al.*, 2008), which may be driven by gas-rich major mergers (e.g. Tacconi *et al.*, 2008; Engel *et al.*, 2010; Wang *et al.*, 2011; Riechers *et al.*, 2011), or streams of cold gas (Dekel *et al.*, 2009; Davé *et al.*, 2010; van de Voort *et al.*, 2011). Measurements of the stellar masses, star-formation histories and clustering properties of SMGs indicate that they may be the progenitors of massive elliptical galaxies observed in the local Universe (Eales *et al.*, 1999; Blain *et al.*, 2002; Chapman *et al.*, 2005; Swinbank *et al.*, 2006; Hainline *et al.*, 2011; Hickox *et al.*, 2012). Due to their extreme far-infrared (FIR) luminosities, it was proposed that SMGs were the high-redshift analogues of local ultra-luminous infrared galaxies (ULIRGs), which are undergoing major mergers. Evidence is now emerging that the SMG population is a mix of mergers and massive star-forming galaxies (Davé *et al.*, 2010; Hayward *et al.*, 2011; Targett *et al.*, 2012; Magnelli *et al.*, 2012), with the most luminous SMGs ($L_{\rm IR} \sim 10^{13}\,{\rm L}_{\odot}$) being ma-

jor mergers and lower luminosity SMGs being consistent with turbulent, star-forming disks. There are, however, still considerable uncertainties in the physical properties of SMGs (e.g. Michałowski, Hjorth & Watson, 2010; Michałowski *et al.*, 2012; Hainline *et al.*, 2011), which affects our view of how SMGs fit into the general picture of galaxy evolution.

SMGs have traditionally been found to reside at $z \sim 2 - 2.5$ (Chapman *et al.*, 2005; Lapi *et al.*, 2011; Wardlow *et al.*, 2011), partly due to the effect of the negative k-correction, which allows galaxies which are bright at 850μm to be detected across a large range in redshift (Blain *et al.*, 2002, see also Chapter 1.3.2). Due to the long integration times required to survey a large area of sky at 850μm, submillimetre survey volumes at low redshift have until recently been relatively small, leading to difficulties in obtaining a representative sample of dusty galaxies in the local Universe. With the launch of the *Herschel Space Observatory* (Pilbratt *et al.*, 2010), we can now get an unprecedented view of dust in local galaxies. The telescope observes at FIR–submillimetre wavelengths across the peak of the dust emission, making it an unbiased tracer of the dust mass in galaxies. The *Herschel* Astrophysical TeraHertz Large Area Survey (H-ATLAS, Eales *et al.* 2010a) is the largest area survey carried out with *Herschel* and has allowed us to quantify the amount of dust in galaxies in the local Universe. By studying galaxies detected at 250μm, Smith *et al.* (2012b) found an average dust mass of $9.1 \times 10^7\,\mathrm{M}_\odot$ in local ($z < 0.35$) dusty galaxies. Furthermore, the dust mass in galaxies is found to increase by a factor of $3 - 4$ between $0 < z < 0.3$ (Dunne *et al.*, 2011; Bourne *et al.*, 2012), which may be linked to higher gas fractions in galaxies at earlier epochs (Geach *et al.*, 2011; Tacconi *et al.*, 2012; Combes *et al.*, 2013).

In this Chapter I investigate the physical properties of dusty galaxies over a wide range in cosmic time. I describe the sample selection of high and low redshift dusty galaxies in Section 4.2. Using the multiwavelength SED fitting code MAGPHYS (see Chapter 2), I derive the physical parameters of high and low redshift dusty galaxies. A comparison of the dusty galaxy populations are presented in Section 4.4. The conclusions are presented in Section 4.5. I adopt a cosmology with $\Omega_m = 0.27$, $\Omega_\Lambda = 0.73$ and $H_o = 71\,\mathrm{km\,s^{-1}\,Mpc^{-1}}$.

4.2 Sample selection

In order to investigate the physical properties of dusty galaxies over a range of redshifts, I construct a sample selected at $\sim 250\mu$m rest-frame wavelength. This comprises panchromatic data of low redshift galaxies from the H-ATLAS Phase 1 catalogue, and a sample of high redshift SMGs presented in Magnelli *et al.* (2012).

4.2.1 Low redshift sample

To select a sample of low redshift dusty galaxies, I make use of the observations in the *Herschel*-ATLAS Phase 1 field, which has similar characteristics to the SDP field as described in Chapter 3.2. The Phase 1 field is centered on the Galaxy And Mass Assembly (GAMA) 9, 12 and 15 hr equatorial fields (Driver *et al.*, 2011), and covers an area of $\sim$161 deg^2 (~ 12 times the area of the SDP field). In a way similar to that detailed in Chapter 3.2, a catalogue of $\geq 5\sigma$ detections in any of the 250, 350 and 500μm bands was produced (Rigby *et al.*, 2011, Rigby et al. in prep., Valiante et al. in prep.) using the MAD-X algorithm (Maddox et al. in prep). PACS flux densities were measured for sources with SDSS r-band isophotal major axis (isoA) $< 30''$ by placing circular apertures at the SPIRE positions[1]. A catalogue of 109231 sources were detected at $> 5\sigma$ at 250μm, with 100, 160, 250, 350 and 500μm fluxes measured at the 250μm source position. Similar to Chapter 3.2, the 5σ noise levels are 130, 130, 30, 37 and 41mJy per beam at 100, 160, 250, 350 and 500μm, respectively. The identification of optical counterparts to SPIRE sources is performed using a likelihood-ratio analysis as described in Chapter 3.2.

4.2.2 High redshift sample

High redshift galaxies are present in the H-ATLAS data (Amblard *et al.*, 2010; Smith *et al.*, 2011), however, the identification of secure optical counterparts to these submillimetre sources is hampered by the relatively shallow ancillary optical imaging. I

[1]For sources with isoA $> 30''$, reliable PACS flux densities cannot be obtained due to high-pass filtering in the maps. This issue will be rectified in the public data release.

therefore rely on publicly available measurements of submillimetre-detected galaxies with robust optical counterparts and spectroscopic redshifts in the literature. I utilise a sample of SMGs detected in blank field (sub)millimetre surveys ($850 - 1200\mu$m) which have robust counterparts identified with deep radio, interferometric submillimetre and/or mid-infrared (MIR) imaging in Magnelli *et al.* (2012, hereafter M12). The SMGs are located in fields which have excellent multiwavelength coverage (GOODS-N, GOODS-S, COSMOS and Lockman Hole), which is required in order to derive statistical constraints on galaxy physical properties using SED fitting. In M12 the submillimetre counterparts were matched within $3''$ to *Spitzer* Multiband Imaging Photometer (MIPS; Rieke *et al.* 2004) 24μm positions associated with PACS and SPIRE data at 70μm, 100μm, 160μm, 250μm, 350μm and 500μm from the PACS Evolutionary Probe (PEP; Lutz *et al.* 2011) and *Herschel* Multi-tiered Extragalactic Survey (HerMES; Oliver *et al.* 2012). The reduction of the HerMES maps is described in Smith *et al.* (2012a), and cross-identifications of 24μm and SPIRE sources were performed in Roseboom *et al.* (2010). The PACS and SPIRE fluxes of the sources were extracted by fitting a point spread function (PSF) at the 24μm position, which allows the flux of blended FIR sources to be recovered. Additionally, the inherent association of a SPIRE source with a more accurate 24μm position allows for relatively easy identification of multiwavelength counterparts.

M12 present photometry for 61 galaxies, however, I only consider the 46 SMGs which are unlensed. This is because the uncertainty in the magnification and source reconstruction could affect the photometry and therefore introduce systematics into physical parameters derived from the SED fitting. I also conservatively exclude 6/46 sources listed in M12 which have multiple robust counterparts to the submillimetre source. These systems are thought to be interacting, so the submillimetre emission is thought to originate from both sources and there is no way to quantify the individual contribution of each counterpart to the submillimetre emission. I also only consider galaxies which have a $> 3\sigma$ detection above the confusion limit in at least one of the SPIRE bands; this criterion excludes four galaxies in the GOODS-N field.

I match the counterpart positions presented in M12 to ancillary optical–MIR data using a $1''$ search radius for optical data and a $2''$ search radius for *Spitzer* Infrared Array

Camera (IRAC; Fazio *et al.* 2004) data. I only include a galaxy counterpart in the sample if it has IRAC data (as 24μm detected galaxies are expected to also have IRAC data). In the COSMOS field I use the broad band ($u^*, B_J, g^+, V_J, r^+, i^+, z^+, J, K$), medium band ($IA427$, $IA464$, $IA484$, $IA505$, $IA527$, $IA574$, $IA624$, $IA679$, $IA709$, $IA738$, $IA767$, $IA827$) and narrow band ($NB711, NB816$) photometry as presented in Ilbert *et al.* (2009) and Salvato *et al.* (2009). The public *Spitzer* IRAC photometry was retrieved from the COSMOS archive[2]. The GOODS-N multiwavelength catalogue is briefly described in Berta *et al.* (2010, 2011) and includes PSF-matched photometry from *HST* ACS $bviz$ (version 1.0), FLAMINGOS JHK[3] and IRAC 3.6, 4.5, 5.8, 8.0μm obtained with the ConvPhot code (Grazian *et al.*, 2006). Spectroscopic redshifts from Barger, Cowie & Wang (2008) were added, as well as the associated *GALEX*, U-band, radio and X-ray fluxes. Deep CFHT WirCAM K_s band photometry was taken from Wang *et al.* (2010) and 24 and 70μm MIPS data are from Magnelli *et al.* (2011). In GOODS-S I use the compilation of photometry for SMGs presented in Wardlow *et al.* (2011) from the MUSYC (Gawiser *et al.*, 2006; Taylor *et al.*, 2009), IRAC photometry from SIMPLE (Damen *et al.*, 2011) and GOODS/VIMOS U-band data from Nonino *et al.* (2009), in addition to deep J and K_s imaging. In the Lockman Hole I use the photometry described in Fotopoulou *et al.* (2012), which comprises UV data from *GALEX*, Large Binocular Telescope (U, B, V, Y, z') and Subaru (R_c, I_c, z') photometry, J and K photometry from UKIRT and MIR data from IRAC. Across all fields I find six sources which were included in M12 do not have optical matches within $1''$. I follow the recommendations in each catalogue and apply the relevant offsets to correct all of the photometry to total magnitudes. Additionally, I have removed any spurious or problematic photometry, including COSMOS medium band photometry where I suspect that strong nebular emission lines contribute significantly to the flux. Deboosted millimetre photometry is provided for some sources in M12 where available. The final sample comprises 30 SMGs with robust counterparts and panchromatic data from the rest-frame UV to the submillimetre.

In order to account for additional uncertainties, for example, in deriving total flux

[2]http://irsa.ipac.caltech.edu/data/COSMOS/

[3]The KPNO 4m FLAMINGOS data were kindly provided by Mark Dickinson, Kyoungsoo Lee and the GOODS team.

measurements and photometric calibration for the wide array of multiwavelength data, I add in quadrature a calibration error to the catalogue photometric errors. For optical, near-infrared (NIR), MIR and FIR bands I add in quadrature 20 per cent of the flux. I add 30 per cent of the flux in quadrature to (sub)millimetre ($\geq 850\mu$m) photometric errors to account for calibration errors and the uncertainty in deboosting the fluxes. For sources which are not detected, I set the fluxes to upper limits as detailed in the respective catalogues.

4.3 SED fitting

The wealth of multiwavelength coverage for the sample of dusty galaxies allows us to derive physical properties using SED fitting techniques. Due to a lack of FIR data, studies of SMGs have often derived dust luminosities and star-formation rates based upon fitting SEDs to 850μm photometry alone. The availability of *Herschel* data across the peak of the dust emission provides better constraints on the dust luminosity and temperature.

I use the method described in Chapter 2 to fit the SEDs of my galaxies and derive physical properties. The low redshift galaxy SEDs are fit using the standard priors, and the high redshift galaxy SEDs are fit using both the standard and composite priors as described in Chapter 2. Throughout this Chapter I primarily report the results using the composite priors, as these model libraries explore a wider parameter space than the standard MAGPHYS libraries. As I find that the majority of SMGs are adequately described by both the standard and composite priors, I also explore the results derived using the standard priors in cases where the choice of prior influences the results. A comparison of the physical parameters derived using the standard and composite priors is presented in Chapter 2.2 and a summary is provided in Table 4.1. In most cases I find that the use of the composite priors do not significantly change the conclusions.

As a summary, the parameters of interest derived from the SED fitting are f_{μ}, the fraction of total dust luminosity contributed by the diffuse ISM; $M_*/\mathrm{M}_{\odot}$, stellar mass; $M_{\mathrm{d}}/\mathrm{M}_{\odot}$, dust mass; M_{d}/M_*, dust to stellar mass ratio; $L_{\mathrm{d}}^{\mathrm{tot}}/\mathrm{L}_{\odot}$, dust luminosity; $T_{\mathrm{C}}^{\mathrm{ISM}}$/K, temperature of the cold diffuse ISM dust component; $T_{\mathrm{W}}^{\mathrm{BC}}$/K, temperature

of the warm dust component in birth clouds; $\hat{\tau}_V$, total effective V-band optical depth seen by stars in birth clouds; $\hat{\tau}_V^{ISM}$, the V-band optical depth in the ambient ISM; $\psi_{\rm S}/yr^{-1}$, specific star-formation rate (SSFR); $\psi/{\rm M}_{\odot}{\rm yr}^{-1}$, and the star-formation rate (SFR) averaged over the last 10^7 years. For more details of the method I refer the reader to DCE08.

4.4 Results

The SEDs for the 30 high redshift galaxies are shown in Fig. B.1. After examining the SEDs, I exclude 7/30 SMGs from the following analysis where useful constraints on galaxy physical parameters cannot be obtained due to anomalous photometric data, where the spectroscopic redshift is incorrect, the wrong counterpart could be matched to the submillimetre source or where the photometry is contaminated by a strong AGN (identified via clear power-law emission in the NIR). I retain weak AGN (AzLOCK.1, AzLOCK.10, LOCK850.15) in the sample as their SEDs are not significantly affected by excess emission. I exclude LOCK850.17 because there is a large discrepancy between the photometric and spectroscopic redshift. This was also noted in Dye *et al.* (2008), who propose that the spectroscopic redshift is from a background source blended with a foreground galaxy which dominates the flux measurements. COSLA-155R1K, LESS017, LESS018 and LOCK850.03 are also not well described by the model SEDs due to problems with the photometry. In the case of LESS017 the FIR–submillimetre photometry appears offset in wavelength from the best-fit model, which indicates that there may be an error in the redshift for this source, or the optical counterpart to the submillimetre source has been incorrectly identified. Furthermore, I exclude AzTECJ100019+023206 and LOCK850.04 as these galaxies have significant AGN contribution to their SEDs, although the inclusion of these sources would not significantly change the conclusions, as discussed in Section 4.4.2. The high redshift final sample comprises 23 galaxies with $0.47 < z < 5.31$.

To create a low redshift comparison sample, using the standard MAGPHYS priors, I fit the UV–millimetre SEDs of 18934 low redshift ($z < 0.5$) H-ATLAS galaxies. These sources have a reliability > 0.8 of being associated with an optical counterpart in the

SDSS r-band catalogue, and which have available multiwavelength photometry (see also Smith *et al.*, 2012b). To ensure that I only include galaxies which have good photometry, I reject 4261 galaxies which have less than 1 per cent chance that their photometry is well described by the best-fit model SED (see Smith *et al.* 2012b for details). Galaxies which are excluded from the sample have problems with photometry or AGN contamination, similar to the issues encountered in the high redshift sample. The rejected fraction from the low redshift sample (23%) is comparable to the high redshift rejected fraction (23%).

In this study I use the 14672 galaxies which have a greater than 99 per cent chance that their photometry is well described by the best-fit SED model. The low redshift H-ATLAS sample is dominated by galaxies with lower stellar mass than the SMGs. In order to compare the two dusty galaxy samples, I construct a sample of low redshift H-ATLAS galaxies which are matched in stellar mass to the SMGs. This was accomplished by splitting the SMG sample into median-likelihood stellar mass bins of 0.2 dex width and randomly picking galaxies in the same stellar mass bin from the H-ATLAS sample, so that both distributions match. Since the H-ATLAS sample is much larger than the SMG sample, I pick 17 times the number of galaxies in each SMG bin from the H-ATLAS sample, in order to achieve better sample statistics. If I attempt to increase the size of the low redshift sample by more than 17 times then my ability to match the distributions in stellar mass becomes worse at the high mass end. I note that there is a lack of H-ATLAS galaxies with the very highest stellar masses, therefore I cannot exactly match the stellar mass distribution at $\mathrm{M}_{*} > 10^{11.4}\,\mathrm{M}_{\odot}$. The low redshift mass-matched sample comprises 374 galaxies. In total 17 galaxies are missing from the highest stellar mass bin centred on $10^{11.9}\,\mathrm{M}_{\odot}$, which comprises 4% of the low redshift stellar mass-matched sample. The final $\sim 250\mu$m rest-frame selected sample comprises 23 high redshift galaxies ($\overline{z} = 1.94$) and 374 dusty galaxies at low redshift ($\overline{z} = 0.25$) of a similar stellar mass to the high redshift sample. The redshift distribution of the samples are shown in Fig. 4.1.

To compare the physical parameters of the high and low redshift dusty populations, I compute the average probability density function (PDF) of parameters derived from the SED fitting, which are shown in Fig. 4.2. For each parameter, I use the first moment

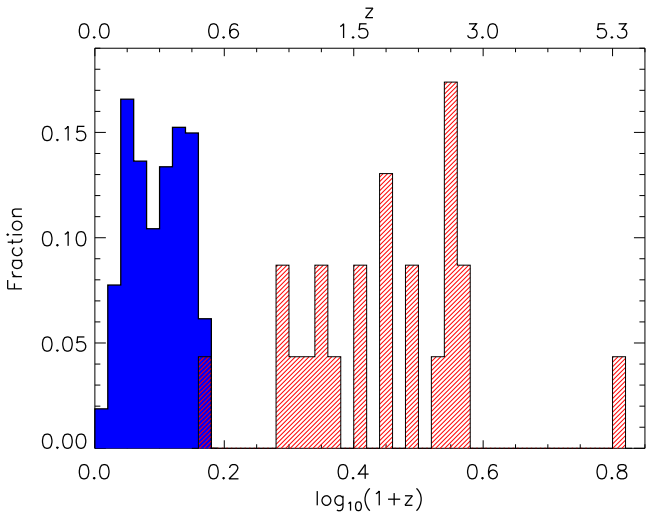

Figure 4.1: Redshift distribution of the low redshift H-ATLAS sample (blue solid histogram) and the high redshift submillimetre galaxies (red hatched histogram).

of the average PDF to estimate the mean of the population. I can estimate the variance on the population mean as the second moment of the average PDF minus the mean squared. The error on the mean is simply the square root of the population variance, normalised by the number of galaxies in the sample. The mean values and errors on each PDF for the high and low redshift samples are summarised in Table 4.1, including parameters for the SMGs derived using both standard and composite priors.

The selection effects in the high redshift sample are rather complex due to the nature of the multiwavelength data, and are discussed in M12. Quantitative comparisons between the high and low redshift samples should therefore be interpreted within the selection functions of the samples. A larger sample of high redshift galaxies encompassing less massive and FIR luminous systems would better allow us to assess the evolution of physical properties of the typical galaxy population from high to low redshift.

4.4.1 Comparison of parameters for high and low redshift populations

I first compare f_μ, the fraction of total dust luminosity contributed by the diffuse ISM for the low and high redshift redshift samples, as shown in panel (a) of Fig. 4.2. When considering the composite priors, the high redshift SMG sample has on average a significantly lower value of f_μ than dusty galaxies of similar stellar mass at low redshift.

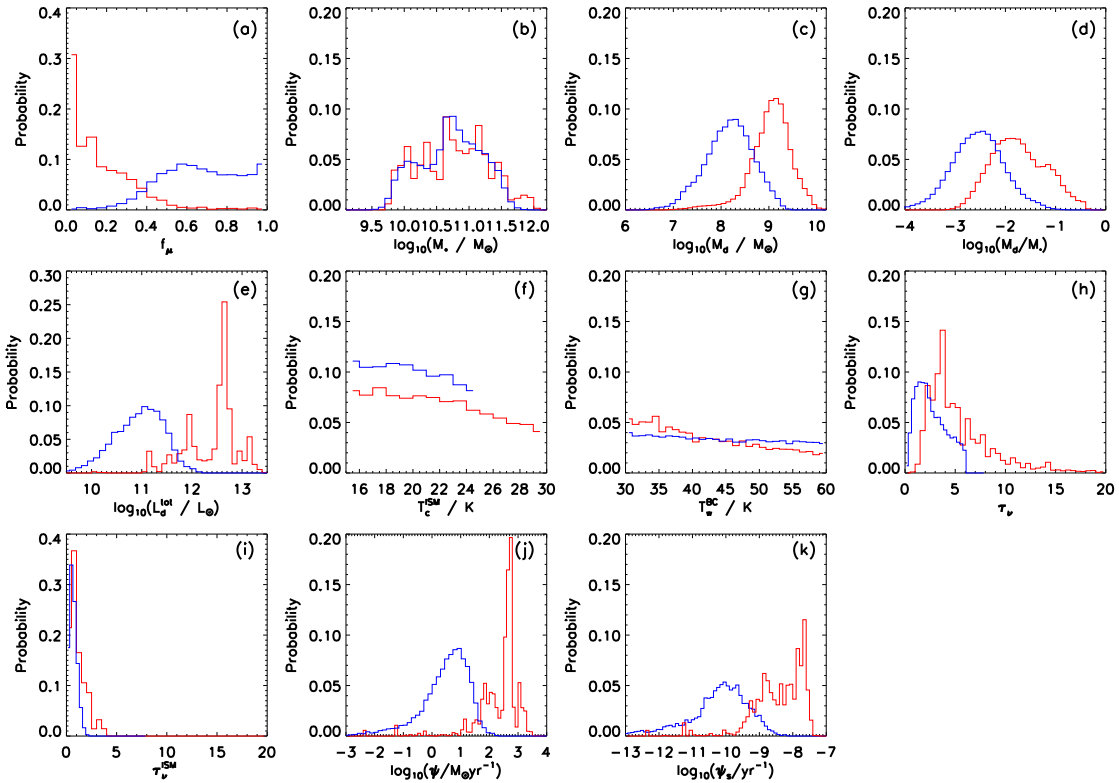

Figure 4.2: Stacked probability density functions (PDFs) of the low redshift (blue) and high redshift (red) samples. The parameters are (from left to right): f_μ, the fraction of total dust luminosity contributed by the diffuse ISM; $M_*/\mathrm{M}_\odot$, stellar mass; $M_\mathrm{d}/\mathrm{M}_\odot$, dust mass; M_d/M_*, dust to stellar mass ratio; $L_\mathrm{d}^\mathrm{tot}/\mathrm{L}_\odot$, dust luminosity; $T_\mathrm{C}^\mathrm{ISM}/\mathrm{K}$, temperature of the cold diffuse ISM dust component; $T_\mathrm{W}^\mathrm{BC}/\mathrm{K}$, temperature of the warm dust component in birth clouds; $\hat{\tau}_V$, total effective V-band optical depth seen by stars in birth clouds; $\hat{\tau}_V^{ISM}$, the V-band optical depth in the ambient ISM; ψ_S/yr^{-1}, specific star-formation rate (SSFR); $\psi/\mathrm{M}_\odot\mathrm{yr}^{-1}$, and the star-formation rate (SFR) averaged over the last 10^7 years. The ranges of each panel reflect the width of the priors. The cold dust temperature for the low redshift sample is restricted to $15-25\mathrm{K}$ and so does not sample the high temperatures allowed in the high redshift prior space. The justification of the choice of cold dust temperature prior is examined in da Cunha *et al.* (2010a); Smith *et al.* (2012b).

Table 4.1: Summary of mean physical properties derived from stacking of probability density functions (PDFs) for the different galaxy populations studied in this Chapter. For each parameter, I use the first moment of the average PDF to estimate the mean of the population. I can estimate the variance on the population mean as the second moment of the average PDF minus the mean squared. The error on the mean is simply the square root of the population variance, normalised by the number of galaxies in the sample. The parameters are: f_{μ} , the fraction of total dust luminosity contributed by the diffuse ISM; $M_{*}/\mathrm{M}_{\odot}$, stellar mass; $M_{\mathrm{d}}/\mathrm{M}_{\odot}$, dust mass; M_{d}/M_{*} , dust to stellar mass ratio; $L_{\mathrm{d}}^{\mathrm{tot}}/\mathrm{L}_{\odot}$, dust luminosity; $T_{\mathrm{C}}^{\mathrm{ISM}}$/K, temperature of the cold diffuse ISM dust component; $T_{\mathrm{W}}^{\mathrm{BC}}$/K, temperature of the warm dust component in birth clouds; $\hat{\tau}_{V}$, total effective V-band optical depth seen by stars in birth clouds; $\hat{\tau}_{V}^{ISM}$, the V-band optical depth in the ambient ISM; $\psi^{7}/\mathrm{M}_{\odot}\mathrm{yr}^{-1}$, the star-formation rate (SFR) averaged over the last 10^{7} years; ${\psi_{\mathrm{S}}}^{7}/yr^{-1}$, specific star-formation rate (SSFR) averaged over the last 10^{7} years; $\psi^{8}/\mathrm{M}_{\odot}\mathrm{yr}^{-1}$, the SFR averaged over the last 10^{8} years; and ${\psi_{\mathrm{S}}}^{8}/yr^{-1}$, the SSFR averaged over the last 10^{8} years.

Parameter	Low redshift sample (standard prior)	SMG sample (composite prior)	SMG sample (standard prior)
f_{μ}	0.68 ± 0.01	0.17 ± 0.02	0.34 ± 0.03
$\log_{10}(M_{*})$	10.71 ± 0.02	10.76 ± 0.11	10.88 ± 0.11
$\log_{10}(M_{\mathrm{d}})$	8.19 ± 0.03	9.03 ± 0.09	9.20 ± 0.08
$\log_{10}(M_{\mathrm{d}}/M_{*})$	-2.52 ± 0.03	-1.73 ± 0.11	-1.68 ± 0.11
$\log_{10}(L_{\mathrm{d}}^{\mathrm{tot}})$	10.94 ± 0.02	12.40 ± 0.10	12.34 ± 0.10
$T_{\mathrm{C}}^{\mathrm{ISM}}$	19.6 ± 0.1	21.7 ± 0.9	20.8 ± 0.6
$T_{\mathrm{W}}^{\mathrm{BC}}$	44.4 ± 0.4	42.3 ± 1.8	45.7 ± 1.8
$\hat{\tau}_{V}$	2.65 ± 0.08	5.42 ± 0.69	4.10 ± 0.26
$\hat{\tau}_{V}^{ISM}$	0.68 ± 0.02	1.11 ± 0.17	1.48 ± 0.17
$\log_{10}(\psi^{7})$	0.43 ± 0.04	2.34 ± 0.17	2.33 ± 0.11
$\log_{10}({\psi_{\mathrm{S}}}^{7})$	-10.23 ± 0.05	-8.43 ± 0.17	-8.54 ± 0.11
$\log_{10}(\psi^{8})$	0.48 ± 0.04	2.38 ± 0.11	2.08 ± 0.09
$\log_{10}({\psi_{\mathrm{S}}}^{8})$	-10.30 ± 0.05	-8.39 ± 0.12	-8.80 ± 0.09

This means that most of the dust luminosity in SMGs is contributed by the birth clouds, which are mostly heated by young stars with ages $< 10^{7}$ years. If the standard priors are used, the values of f_{μ} tend to be higher (see Chapter 2.2) but I still conclude that the majority of the SMGs have $f_{\mu} < 0.5$. Therefore, the dust luminosity in most SMGs is dominated by the birth cloud component.

In panel (b) I show the average PDF of the stellar masses of the SMGs and the low redshift sample, which are selected to have the same stellar mass distribution. I find a mean stellar mass of $5.8^{+1.6}_{-1.3}\times10^{10}\,\mathrm{M}_{\odot}$ for the high redshift sample, in agreement with M12 and Hainline *et al.* (2011).

In Fig. 4.2 panel (c) I find the SMG sample has a mean dust mass of $1.1^{+0.2}_{-0.2}\times10^{9}\,\mathrm{M}_{\odot}$, in agreement with other studies of SMGs (Santini *et al.*, 2010; Michałowski, Hjorth & Watson, 2010; Magdis *et al.*, 2012). The dust mass of the SMGs are significantly

higher than 250μm rest-frame selected galaxies of a similar stellar mass at low redshift, which have a mean dust mass of $(1.4 \pm 0.1) \times 10^8\,\mathrm{M}_\odot$. Furthermore, there is a distinct lack of galaxies in the low redshift sample with dust masses as large as the dustiest SMGs ($M_\mathrm{d} > 2.5 \times 10^9\,\mathrm{M}_\odot$). This suggests that there may be strong evolution in the dust content of massive, dusty galaxies with redshift, in agreement with Dunne & Eales (2001); Dunne, Eales & Edmunds (2003); Eales *et al.* (2010b); Dunne *et al.* (2011); Bourne *et al.* (2012); Symeonidis *et al.* (2013). The M_d/M_* values of SMGs in panel (d) typically range from 0.01 to 1×10^{-3}, with a mean of $0.019^{+0.005}_{-0.004}$, which is similar to the M_d/M_* values of SMGs in Santini *et al.* (2010). Santini *et al.* (2010) found that SMGs have a factor of 30 higher M_d/M_* values compared to a sample of normal spirals from SINGS, whereas I find the SMGs in my sample are only a factor of 7 more dusty relative to their stellar mass compared to low redshift dusty galaxies. This disparity may be because Santini *et al.* (2010) compare to a representative sample of local spirals, whereas the low redshift sample is selected on dust mass and therefore will include dustier galaxies. In Fig. 4.2 panel (e) the dust luminosities of the low and high redshift dusty galaxy samples are significantly different, as the mean of the low redshift sample is $8.3^{+0.5}_{-0.5} \times 10^{10}\mathrm{L}_\odot$, whereas the high redshift sample has an average dust luminosity around a factor of 30 higher. The integrated infrared luminosity of the high redshift sample ($2.5^{+0.7}_{-0.5} \times 10^{12}\mathrm{L}_\odot$) is in good agreement with that found in Hilton *et al.* (2012) for massive ($6.3 \times 10^{10}\,\mathrm{M}_\odot$), dusty galaxies at $z \sim 2$. This shows that dusty galaxies at high redshift are more luminous in the FIR compared to dusty galaxies of a similar stellar mass at low redshift.

In panel (f) I observe no significant difference in the $T_\mathrm{C}^\mathrm{ISM}$of the SMGs and low redshift dusty galaxies, and find a wide range of values for the cold dust temperature in both samples. Examination of individual galaxy PDFs shows that I can often only place weak constraints on the cold dust temperature component in SMGs, even in the case where there is good photometric coverage of the dust peak. This may be because in SMGs the dust luminosity is dominated by the birth cloud component, which makes it difficult to constrain the cold dust temperature in the diffuse ISM. The stacked PDF of $T_\mathrm{C}^\mathrm{ISM}$rises towards the cold end of the prior for both the low and high redshift dusty galaxy samples, with no clear peak in temperature. Smith *et al.* (2012b) found that the median cold dust temperature of the H-ATLAS sample was 20 K, although this

could only be determined for sources with PACS photometry which allows the peak of the dust SED to be sampled. The stacked PDF for $T_{\rm W}^{\rm BC}$in panel (g) also has no clear peak, but shows a slight rise towards 30 K. Examination of individual galaxy PDFs shows that I can often obtain some constraint on the temperature of warm dust in birth clouds. When averaged over the whole SMG sample, the wide range of $T_{\rm W}^{\rm BC}$values result in a flat stacked PDF. The $T_{\rm W}^{\rm BC}$PDF is flat for the low redshift sample because there is insufficient data shortward of the dust peak to constrain the warm dust temperature. As shown in panels (h) and (i), the total effective V-band optical depth seen by stars in birth clouds ($\hat{\tau}_V$), and in the ISM ($\hat{\tau}_V^{ISM}$), is significantly higher for the SMG sample compared to low redshift dusty galaxies. These results are consistent with other studies which find that SMGs are very obscured compared to local galaxies (Menéndez-Delmestre *et al.*, 2009).

Fig. 4.2 (j) shows that the mean SFR of the high redshift sample (averaged over the last 10^7 years) is $220^{+100}_{-70}\,{\rm M}_\odot\,{\rm yr}^{-1}$, in agreement with other recent studies of similar high redshift dusty galaxy samples (Banerji *et al.*, 2011; Hilton *et al.*, 2012; Lo Faro *et al.*, 2013; Casey *et al.*, 2013). The average SMG SFR is consistent with those of normal, massive ($10^{11}\,{\rm M}_\odot$) galaxies at $z \sim 2$. I note that because I exclude SMGs where the submillimetre emission may originate from multiple sources, the sample may be biased against systems undergoing major mergers, which tend to have the highest SFRs. The average SFR of the SMGs is around 70 times greater than the mean SFR of the low redshift sample, which has an average SFR of $3 \pm 1\,{\rm M}_\odot{\rm yr}^{-1}$. Dusty galaxies at high redshift are therefore forming more stars than dusty galaxies of a similar stellar mass at low redshift, which is consistent with the general picture of galaxy evolution. The lack of highly star-forming galaxies in the low redshift sample is not a volume effect, as the co-moving volume probed by the H-ATLAS Phase 1 data is $1.1 \times 10^8\,{\rm Mpc}^3$, which is comparable to the co-moving volume covered by the combined SPIRE survey areas of GOODS-N, GOODS-S, COSMOS and Lockman Hole ($1.4 \times 10^8\,{\rm Mpc}^3$).

The mean SSFR of the SMG sample in Fig. 4.2 (k) is $3.7^{+1.8}_{-1.2} \times 10^{-9}\,{\rm yr}^{-1}$, which implies a doubling time of $\sim 270\,{\rm Myr}$, similar to the gas consumption timescale of SMGs from Tacconi *et al.* (2008). The average SSFR of the SMGs is around 60 times greater than the mean SSFR of the low redshift sample, which has an average SSFR

of $5.9^{+0.7}_{-0.6} \times 10^{-11}\,\mathrm{yr}^{-1}$. I note that choosing the standard MAGPHYS priors causes a reduction in the SFR and SSFR for eight of the SMGs (see Fig. 2.4). The difference in the stacked PDFs when using the composite and standard priors for the SFR and SSFR averaged over the last 10^7 years are only 0.01 and 0.12 dex, respectively, which is within the 1σ error on the parameter PDFs. When using the composite priors these results are not sensitive to the timescale over which the (S)SFR is averaged. When using the standard priors, the mean (S)SFR is ~ 0.25 dex lower when using a longer star-formation timescale of 10^8 years, compared to 10^7 years. However, the choice of prior or star-formation timescale does not change the conclusion that dusty galaxies at high redshift are forming more stars than dusty galaxies of a similar stellar mass at low redshift.

4.4.2 AGN

Evidence from X-ray emission suggests that the majority of SMGs host an AGN (Alexander *et al.*, 2005), although it has been found that the FIR luminosity of SMGs is dominated by starburst activity (Hatziminaoglou *et al.*, 2010; Pozzi *et al.*, 2012). Some SMGs in the sample show excess emission in the rest-frame NIR, which is due to hot dust originating either from an obscured AGN, or possibly from small, hot dust grains in star-forming regions (Hainline *et al.*, 2009, 2011). For galaxies which have small power-law contributions to the NIR, Hainline *et al.* (2011) estimate that the median stellar mass could be overestimated by around 10 per cent, under the assumption that all of the NIR luminosity is from stars. Since the MAGPHYS SED models do not include a prescription for AGN emission, the inclusion of photometric bands which are contaminated with power-law emission can cause the photometry to be poorly described by the model SEDs. As excess NIR emission can cause the stellar mass to be overestimated, other parameters such as the SFR and f_μ could also be affected. In order to test this, I use the Ivison *et al.* (2004) $S_{24}/S_{8.0} - S_{8.0}/S_{4.5}$ diagram and the colour cut $S_{8.0}/S_{4.5} > 1.65$ (for $1 < z < 4$ galaxies) from Coppin *et al.* (2010) to select SMGs which have power-law emission in the NIR. I find 3/23 galaxies have power-law emission in the NIR (AzLOCK.01, AzLOCK.10 and LOCK850.15). I include one galaxy from the original sample of 30 SMGs which was excluded from the

main results because of strong AGN emission (LOCK850.04). I do not include the AGN source AzTECJ100019+023206, as the poor quality optical photometry does not allow us to judge the effectiveness of the power-law subtraction method.

I quantify the effect of AGN contamination on the derived physical parameters in the most power-law dominated galaxies in the high redshift sample. Following the method in Hainline *et al.* (2011), I subtract from the optical photometry a power law parametrised by $f_\lambda \propto \lambda^\alpha$, with both $\alpha = 2$ and 3. I assume the power law has a maximal contribution at 8μm (observed frame), so the power law is normalised to the 8μm data point. I then subtract in increments of $0.1\times$ the maximum power-law fraction from all photometry shortwards of 8μm to account for possible hot dust emission from either an AGN or star formation. When the power-law fraction is large the optical emission can be over-subtracted, therefore I set flux density values to an upper limit at the value of the power law. I perform MAGPHYS SED fitting at each increment to determine the galaxy physical parameters. The power-law contribution is determined as the combination of power law and SED fit which results in the best-fitting SED. Since the AGN contribution to the rest-frame MIR fluxes are not known, I include data with $5 < \lambda_{\rm rest} < 30\mu$m as an upper limit in the SED fitting procedure. I assume that photometry longwards of rest-frame 30μm has a negligible contribution from AGN emission (Netzer *et al.*, 2007; Pozzi *et al.*, 2012). Some sources such as AzLOCK.1 and LOCK850.04 show a clear preference for an $\alpha = 3$ power-law slope, as a shallower power-law slope of $\alpha = 2$ over-subtracts the optical emission. The $\alpha = 2$ slope results in poor-quality SED fits to the subtracted photometry, therefore for AzLOCK.1 and LOCK850.04 I only consider the results from the $\alpha = 3$ power-law slope. For the majority of sources the choice of an $\alpha = 2$ or $\alpha = 3$ power-law slope does not produce significantly different results. The change in stellar mass for individual galaxies ranges from 0.24 dex larger to 0.17 dex smaller. The stellar mass changes by slightly more than the error represented by the 84th–16th percentile range on each individual galaxy PDF (on average ± 0.11 dex). We find that the median-likelihood f_μ, SFR, SSFR, and $\hat{\tau}_V$ do not change substantially when I account for the emission from a power law in the rest-frame optical–NIR. The changes observed in the parameters are typically within the error represented by the 84th–16th percentile range on each individual galaxy PDF. For the galaxies which are not classified as having power-

law emission in the Ivison *et al.* (2004) diagram, we find that subtraction of a small power-law component from the photometry does not result in significant changes to physical parameters. The galaxies with power-law emission comprise a small minority of the SMG sample. I therefore conclude that the changes in the median-likelihood parameters due to power-law emission are therefore negligible for the SMG sample.

4.4.3 Correlations between star formation and dust content in galaxies

The mass of dust and star formation are closely linked in galaxies, and this has been shown to be due to an evolutionary sequence (da Cunha *et al.*, 2010b), where galaxies with high (S)SFR produce copious amounts of dust. As the gas supply is consumed by star formation, the (S)SFR drops and the dust mass decreases as supernova shocks and astration destroy dust grains in the galaxy. To place SMGs and low redshift dusty galaxies in their evolutionary context, in Fig. 4.3 (a) I show the dust mass as a function of SFR. The SMGs have dust masses which are much higher than the majority of the low redshift sample, yet there are a small number of galaxies at low redshift which have dust masses comparable to the SMGs. The lack of very dusty galaxies at low redshift suggests evolution in the dust content of massive galaxies between $0 < z < 3$. One clear trend is that the SMGs have star-formation rates which are higher by 1–2 orders of magnitude compared to the low redshift dusty galaxies. Similarly, a trend between dust attenuation and SFR, and an increase in SFR towards higher redshifts was also found by Sobral *et al.* (2012) and Roseboom *et al.* (2012). There is a dearth of highly star-forming galaxies in the low redshift sample, however, this is not a volume effect. The co-moving number density of SMGs with a SFR greater than the mean of the SMG PDF ($\psi > 220\,\mathrm{M_{\odot}yr^{-1}}$) is $1.1 \times 10^{-7}\,\mathrm{Mpc^{-3}}$, whereas the co-moving number density of galaxies above the average SMG SFR at $z < 0.5$ is smaller ($1.8 \times 10^{-8}\,\mathrm{Mpc^{-3}}$). Since I only consider SMGs in the sample with good SED fits and available multiwavelength data, the co-moving number density of highly star-forming SMGs is a lower limit. Galaxies with such high SFRs are rare in the low redshift Universe, so there is a substantial evolution in the SFR in dusty galaxies from low to high redshift. The increase in star-formation rate could be due to galaxies at high redshift having larger gas fractions (Geach *et al.*, 2011; Tacconi *et al.*, 2012; Combes

et al., 2013). Alternatively, the SMG sample may have a larger fraction of interactions and mergers relative to the low redshift sample, which can cause increases in the SFR and dust luminosity in galaxies (Georgakakis, Forbes & Norris, 2000; Xilouris *et al.*, 2004; Lanz *et al.*, 2013).

In Fig. 4.3 (b) I plot $M_{\rm d}/M_*$ as a function of SSFR. The addition of SMGs allows us to extend my investigation of the $M_{\rm d}/M_*$ –SSFR relation to higher redshifts, beyond that studied in da Cunha *et al.* (2010b) and Smith *et al.* (2012b). The high redshift galaxies typically occupy the high SSFR end of the low redshift relation, which means that these galaxies are at an earlier stage of evolution compared to the low redshift dusty galaxies of a similar stellar mass. A few SMGs at the lowest redshifts lie in the same part of parameter space as the low redshift sources. This indicates that these galaxies may be more evolved than the majority of SMGs, and are more similar to low redshift dusty galaxies.

In Fig. 4.3 (c) I plot SSFR and $M_{\rm d}/\psi$, which is closely linked to the dust-to-gas ratio (da Cunha *et al.*, 2010b) via the Schmidt-Kennicutt law. The high redshift galaxies lie along the relation defined by the low redshift H-ATLAS sample, but have considerably lower $M_{\rm d}/\psi$ values than the low redshift dusty galaxies. This suggests that SMGs are more gas-rich than low redshift dusty galaxies of a similar stellar mass. This is consistent with observations of evolution in the gas fractions in galaxies from $z = 0-2$ (Geach *et al.*, 2011; Tacconi *et al.*, 2012; Combes *et al.*, 2013).

4.4.4 The nature of star formation in SMGs

Clues to the stellar mass build-up of galaxies can be found via the relatively tight correlation between stellar mass and SSFR, known as the "main sequence". The slope of the main sequence has been found to be approximately constant for $0 < z < 3$ (although this is sensitive to survey selection effects, see Dunne *et al.* 2009, and references within), but with the normalisation increasing a factor of 20–30 in the range $0 < z < 2$ (Noeske *et al.*, 2007; Elbaz *et al.*, 2007; Daddi *et al.*, 2007; Dunne *et al.*, 2009; Rodighiero *et al.*, 2010; Whitaker *et al.*, 2012). Galaxies which lie on the main sequence of star formation are thought to be secularly evolving, with starbursts lying above the main sequence. Due to their high inferred SFRs, studies have found SMGs

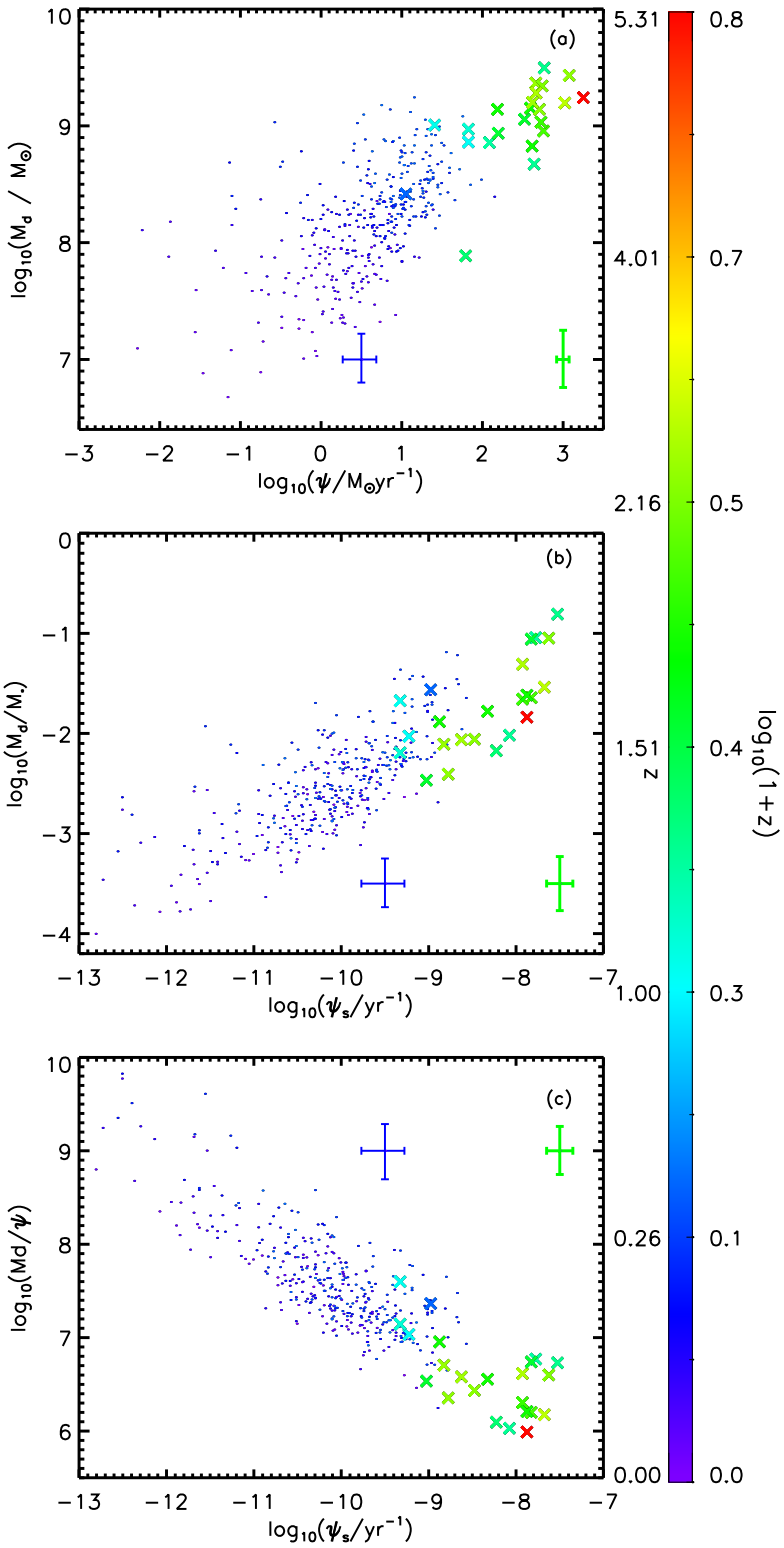

Figure 4.3: (a) The relation between dust mass and SFR, dust-to-stellar mass ratio and SSFR (b), and (c) dust mass/SFR and SSFR for the low and high redshift samples (dots and crosses, respectively). The SFR and SSFR are averaged over the last 10^7 years. Points are coloured by redshift, showing that SMGs are dustier, forming more stars and have lower dust-to-gas ratios than dusty galaxies of a similar stellar mass at low redshift. The error bars indicate the median 84th–16th percentile range from each individual parameter PDF; the thin and thick error bars correspond to the low redshift H-ATLAS and high redshift SMG samples, respectively.

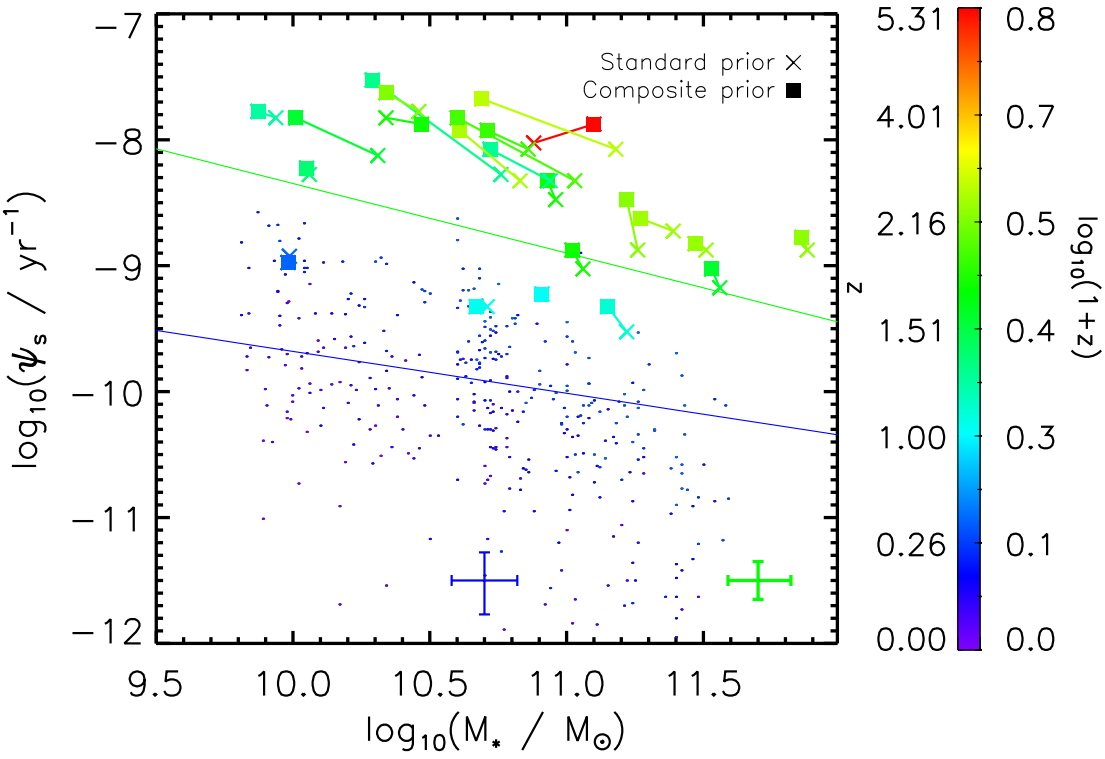

Figure 4.4: The relation between stellar mass and SSFR (averaged over the last 10^7 years) for the high redshift sample (large points), with the low redshift H-ATLAS sample shown for reference (small points); points are coloured by redshift. The SSFR and stellar mass derived from the SED fitting using the composite priors are shown as filled points and crosses show the parameters derived using the standard priors. The main sequence of star-forming galaxies is shown at $z = 0.25$ and $z = 1.94$ (the mean redshifts of the low and high redshift samples) derived from Whitaker *et al.* (2012). The colours of the main sequence lines correspond to the redshift colour bar. The typical scatter around the main sequence from Whitaker *et al.* (2012) is 0.34 dex, and is independent of redshift. The error bars indicate the median 84th–16th percentile range from each individual parameter PDF; the blue (thin) and green (thick) error bars correspond to the low and high redshift samples, respectively.

to lie above the main sequence of star formation, (Daddi *et al.*, 2009; Genzel *et al.*, 2010), which leads to the idea that these systems are major-merger driven starbursts.

To determine which SMGs are starbursts, I compare the SSFR and stellar mass of each galaxy to the position of the main sequence at the galaxy redshift. The star forming main sequence is derived using the redshift-dependent parametrisation in Whitaker *et al.* (2012). I define a starburst as a galaxy with a SSFR $4\times$ higher than the main sequence at a given stellar mass and redshift (Rodighiero *et al.*, 2011). In Fig. 4.4, the low redshift dusty galaxy population are mostly star-forming galaxies with SSFRs consistent with the main sequence at $0 < z < 0.5$. Only $\sim 7\%$ of the sample are classified as starbursts. However, at high stellar masses there are a significant number of dusty galaxies below the main sequence. These galaxies may be similar to the dusty

early-type galaxies and passive spirals investigated in Rowlands *et al.* (2012). The galaxies below the main sequence may be in the process of shutting down their star formation, but still harbour a substantial amount of dust. A much higher fraction of high redshift dusty galaxies are starbursts, with 10/23 (43%) of SMGs lying above the main sequence at a given redshift (using the composite priors). This supports the idea that the SMG population is a mix of massive star-forming disks and starbursting merger-driven systems (Hayward *et al.*, 2011; Magnelli *et al.*, 2012). It is interesting to note that using the composite priors increases the stellar mass and SSFR of the SMGs relative to the standard priors, which results in galaxies moving to the top left in Fig. 4.4, with the exception of the very high redshift SMG at $z = 5.31$. Using the stellar mass and SSFR values derived using the standard priors I find 8/23 (35%) of SMGs are starbursts. Using the standard priors results in marginally fewer starbursts compared to the results derived using the composite priors. However, since the difference between the two priors shifts galaxies in SSFR–M_* space approximately parallel to the main sequence, the choice of prior does not significantly change our conclusions that the SMG population is a mix of normal galaxies and starbursts.

There is, however, some disagreement over the interpretation of the location of SMGs on the SSFR–M_* plane. Casey *et al.* (2013) found that when using the dust-corrected UV derived SFR, the majority of SMGs lie on the main sequence, but the SFR derived from the FIR luminosity is larger by a factor ~ 13. This means that the choice of SFR indicator changes our view of SMGs as existing on the main sequence or undergoing a starburst. The difference in SFR may be because the dust correction in the UV is underestimated, as this is often based on extinction in normal galaxies which are less obscured than SMGs. Alternatively, the SFR derived from the infrared luminosity may be overestimated if young stars are assumed to be the only dust heating mechanism. In this work, and in Lo Faro *et al.* (2013), it is found that in some SMGs there is a non-negligible contribution to the infrared luminosity from the diffuse ISM, which is mainly heated by old stars (Bendo *et al.*, 2012; Groves *et al.*, 2012). Therefore, when determining the SFR, careful consideration of the full SED is needed. It has been suggested that mergers do not cause a significant enhancement in the SSFR of SMGs (Hayward *et al.*, 2011) and so merging SMGs are observed to be on the main sequence. Further investigation of large samples of SMGs with well constrained phys-

ical parameters are needed in order to understand how SMGs are related to the general galaxy population. Using the analysis of the full galaxy SED, I conclude that the SMG population is a mix of main sequence and starburst systems.

4.5 Conclusions

I have presented the physical properties of a rest-frame 250μm selected sample of massive, dusty galaxies, in the range $0 < z < 5.3$. The sample consists of 23 high redshift SMGs from Magnelli *et al.* (2012) and 374 dusty galaxies at $z < 0.5$ from the *Herschel*-ATLAS, selected to have a similar stellar mass to the SMGs. Both samples have panchromatic photometry from the rest-frame UV to the submillimetre, which allowed me to fit SEDs to derive statistical constraints on galaxy physical parameters using an energy balance technique. I compared the physical properties of the high and low redshift samples and found significant differences in the dusty galaxy populations. My main results are as follows:

- The sample of SMGs have an average SFR of $220^{+100}_{-70}\,\mathrm{M_{\odot}yr^{-1}}$, and harbour a substantial mass of dust ($1.1^{+0.2}_{-0.2} \times 10^{9}\,\mathrm{M_{\odot}}$), compared to $(1.4 \pm 0.1) \times 10^{8}\,\mathrm{M_{\odot}}$ for low redshift dusty galaxies. I find SMGs have significantly higher SFRs, dust masses and obscuration than $z < 0.5$ dusty galaxies selected to have a similar stellar mass. The differences between the high and low redshift dusty galaxy populations may be driven by an increase in the gas fraction at higher redshifts.

- From my SED analysis I find that a large fraction of the dust luminosity in SMGs originates from star-forming regions, whereas at lower redshifts the dust luminosity is dominated by the diffuse ISM.

- Around 40 per cent of the SMGs lie above the main sequence of star formation at a given redshift. This supports the idea that the SMG population is a mix of massive secularly evolving galaxies and starbursting, possibly merger-driven systems.

The origin of dust in high redshift SMGs is explored in Chapter 5.

Chapter 5

The origin of dust in submillimetre galaxies

5.1 Introduction

The dominant origin of dust in the local Universe is thought to be the stellar winds of low–intermediate mass stars (LIMS) in the asymptotic giant branch (AGB) phase of evolution (Ferrarotti & Gail, 2006). Recent work has revealed a *'dust budget crisis'*, whereby the mass of dust observed in galaxies at low redshift (Matsuura *et al.*, 2009; Dunne *et al.*, 2011; Rowlands *et al.*, 2012) and at high redshift (Michałowski, Watson & Hjorth, 2010; Gall, Andersen & Hjorth, 2011) cannot entirely be accounted for by stellar mass loss from LIMS. At $z > 5$ there is speculation about the source of dust, as there is not enough time for LIMS to evolve to their dust producing phase ($\sim 0.5 - 1$ Gyr). It has been proposed that supernovae are prolific dust producers at early times (Morgan & Edmunds, 2003; Nozawa *et al.*, 2003; Dunne *et al.*, 2003a, 2009; Gall, Hjorth & Andersen, 2011), as supernovae can produce dust on timescales much shorter than that taken for LIMS to reach the AGB phase. Dust has been detected in supernova remnants (Dunne *et al.*, 2003a; Krause *et al.*, 2004; Sugerman *et al.*, 2006; Gomez *et al.*, 2009; Rho *et al.*, 2008; Barlow *et al.*, 2010; Matsuura *et al.*, 2011; Temim *et al.*, 2012; Gomez *et al.*, 2012b), although evidence for large quantities of dust remains controversial. Furthermore, the mass of dust which survives the supernova shocks is highly uncertain (Kozasa *et al.*, 2009; Jones & Nuth, 2011). Alternatively,

significant dust grain growth may occur in the ISM at both high redshift (Michałowski, Watson & Hjorth, 2010; Hirashita & Kuo, 2011), and at low redshift (Dwek, Galliano & Jones, 2007; Dunne *et al.*, 2011; Inoue, 2012; Kuo & Hirashita, 2012; Mattsson, Andersen & Munkhammar, 2012), which could make up the shortfall in the dust budget of galaxies.

In order to investigate the origin of dust in high redshift galaxies, in this Chapter I compare the observed dust masses of the 23 SMGs investigated in Chapter 4 to predictions from a modified version of the chemical evolution model of ME03. In Section 5.2 I describe the chemical evolution model and the modifications that I have made. By considering dust sources from LIMS and supernovae in Section 5.3 I present my investigations into the origin of dust in a closed box model. I also consider the effects of dust destruction and grain growth on the dust mass of SMGs. In reality, as galaxies are unlikely to be closed systems, I then investigate models with inflows and outflow of gas. Finally, I consider the effect of a top heavy initial mass function (IMF) on the properties of SMGs.

5.2 Description of the model

In order to investigate the origin of dust in high redshift galaxies, I compare the observed dust masses of the 23 SMGs investigated in Chapter 4 to predictions from a modified version of the chemical evolution model of ME03. The model has a basis similar to chemical evolution codes in the literature (Tinsley, 1980; Pagel, 1997; Dwek, 1998; Calura, Pipino & Matteucci, 2008). By relaxing the instantaneous recycling approximation to account for the lifetimes of stars of different masses, the model tracks the build-up of heavy elements over time produced by LIMS and supernovae. Given an input SFH, gas is converted into stars over time, assuming an IMF. Heavy elements are produced by both LIMS and supernovae, with a fraction of metals turned into dust. The majority of the SMGs are at $z < 4$, which gives enough time for LIMS to evolve to their AGB phase and contribute to the dust budget. I therefore consider both supernova and LIMS as dust sources.

For completeness, I will now describe in detail the chemical evolution equations in the

model. The total mass of the system is

$$M = g + s, \tag{5.1}$$

where g is the gas mass and s is the stellar mass. The gas mass changes with time as described in Eq. 5.2, as gas is depleted by the SFR, $\psi(t)$, and returned to the ISM as stars die, $e(t)$.

$$\frac{dg}{dt} = -\psi(t) + e(t) + I(t) - O(t) \tag{5.2}$$

The first two terms in Eq. 5.2 on their own describe a closed box system. The last two terms are added to describe an open box scenario with an inflow and outflow of gas. I is the inflow rate and O is outflow rate. Both are parametrised as a fraction of the instantaneous SFR. Assuming that mass loss occurs suddenly at the end of stellar evolution, the ejected mass, $e(t)$ from stars is

$$e(t) = \int_{m_{\tau_m}}^{m_U} \left[m - m_R(m)\right] \psi(t - \tau_m)\phi(m)dm, \tag{5.3}$$

and the remnant mass is

$$m_R(m) = \begin{cases} 0.11m + 0.45 & \text{if } m \leq 6.8\,\mathrm{M}_\odot \\ 1.5 & \text{if } m > 6.8\,\mathrm{M}_\odot \end{cases},$$

(Iben & Tutukov, 1984), where τ_m is the stellar lifetime of a star of a mass m from Schaller *et al.* (1992), $m_U = 100\,\mathrm{M}_\odot$ and m_{τ_m} is the stellar mass of a star whose age is that of the system. A star formed at $t - \tau_m$ has died at time τ_m.

For self-consistency with my SED fitting method I adopt a Chabrier (2003) IMF, unless stated otherwise. This takes the form:

$$\phi_{\mathrm{Chabrier}}(m) = \begin{cases} 0.85e^{-\frac{(\log(m)-\log(m_c))^2}{2\sigma^2}} & \text{if } m \leq 1\,\mathrm{M}_\odot \\ 0.24\,m^{-1.3} & \text{if } m > 1\,\mathrm{M}_\odot \end{cases},$$

where $m_c = 0.079$ and $\sigma = 0.69$. The IMF is normalised to 1 in the mass range $0.1 - 100\,\mathrm{M}_\odot$. I note that the choice of a Chabrier IMF results in higher dust production than other IMFs such as Scalo and Salpeter, as fewer stars with $m < 1\,\mathrm{M}_\odot$ are produced which lock up gas and metals for timescales of the order of the Hubble time.

The evolution of the mass of metals in the ISM (Zg) is described by

$$\frac{d(Zg)}{dt} = -Z(t)\psi(t) + e_z(t) + Z_I I(t) - Z_O O(t). \tag{5.4}$$

The first term of Eq. 5.4 describes the mass of metals locked up in stars, and the second term describes the metals returned to the ISM via stars as described in Eq.5.5. Together these two terms describe the evolution of metals in a closed box system. Note that the metals include the heavy elements in both the gas-phase and in dust. The third term of Eq. 5.4 describes an inflow of gas with metallicity Z_I at a rate I. The fourth term of Eq. 5.4 describes an outflow of gas with metallicity Z_O at a rate O. In the model I assume that the gas and metals in the ISM are well mixed, and so the outflow removes gas at ambient metallicity $Z_O = Z$. I assume that inflows deliver unenriched gas with $Z_I = 0$. The mass of heavy elements ejected by stars at the end of their lives is described by

$$e_z(t) = \int_{m_{\tau_m}}^{m_U} \big([m - m_R(m)]\, Z(t-\tau_m) + m p_z\big)\psi(t-\tau_m)\phi(m)dm. \quad (5.5)$$

where mp_z is the yield of heavy elements from a star of initial mass m and metallicity Z, interpolated from Maeder (1992) for massive stars, and from Marigo (2000) for LIMS. The integrated yield (p_z) is defined as the mass fraction of stars formed in the mass range $m_1 - m_2$ which are expelled as heavy elements z in Eq. 5.6. Further details are given in ME03.

$$p_z = \int_{m_1}^{m_2} m p_z(m)\phi(m)dm \quad (5.6)$$

The evolution of dust mass (yg) with time is described by

$$\begin{aligned}\frac{d(yg)}{dt} = & \int_{m_{\tau_m}}^{m_U} \big([m - m_R(m)]\, Z(t-\tau_m)\chi_2 + m p_z \chi_1\big)\psi(t-\tau_m)\phi(m)dm \\ & - y\psi(t) - yg\delta_{dest}(t) + yg\delta_{grow}(t) \\ & + y_I I(t) - y_O O(t). \end{aligned} \quad (5.7)$$

The first term describes the dust injected into the ISM by LIMS, the second term accounts for dust produced by supernovae and massive stars with $m > 8\,\mathrm{M}_\odot$, and the third term accounts for dust lost in forming stars (astration).

The dust condensation efficiencies, χ_1 (Eq. 5.8) and χ_2 (Eq. 5.9), describe the fraction of heavy elements which are incorporated into dust for newly synthesised elements (e.g. in supernovae), and pre-existing heavy elements (e.g. in stellar winds), respectively. The dust condensation efficiency $\chi_1 \sim 0.22$ (depending on the progenitor mass), and $\chi_2 = 0.45$, following Edmunds (2001) and ME03.

$$\chi_1 = \frac{\text{Mass of dust formed in ejecta}}{\text{Mass of freshly formed heavy elements in ejecta}} \tag{5.8}$$

$$\chi_2 = \frac{\text{Mass of dust formed in stellar winds}}{\text{Mass of heavy elements in stellar winds}} \tag{5.9}$$

The dust condensation efficiencies for LIMS are taken from ME03, who predicted $(1 - 2000) \times 10^{-5}\,\mathrm{M}_{\odot}$ of dust per LIMS, depending on the initial stellar mass and metallicity. The dust yields from Type II supernovae are taken from Todini & Ferrara (2001, hereafter TF01) following ME03, who predicted $\sim 0.1 - 1.0\,\mathrm{M}_{\odot}$ of dust per supernova, depending on the progenitor mass and metallicity. Current observations of Galactic supernova remnants generally have not detected as much dust as TF01 predict with (unambiguous) detections of warm dust averaging $\sim 0.1\,\mathrm{M}_{\odot}$ (Rho *et al.*, 2009; Barlow *et al.*, 2010; Gomez *et al.*, 2012a). Indirect (or more ambiguous) evidence suggests there may be a massive colder population of dust ($T_d \sim 20\,\mathrm{K}$) in supernova remnants (e.g. Dunne *et al.*, 2003b; Gomez *et al.*, 2009; Dunne *et al.*, 2009; Matsuura *et al.*, 2011) but in many cases, resolution and Galactic cirrus make these observations difficult to interpret. The yields from TF01 are therefore extremely optimistic, even more so when combined with the large uncertainty on how much dust formed in the ejecta will survive the passage through the shockfronts (e.g. Bianchi, Schneider & Valiante, 2009). I do not include dust produced by Type Ia supernovae, as these events are not thought to contribute a significant mass of dust to the ISM (Gomez *et al.*, 2012a).

Dust is thought to be removed from the ISM by the sputtering and shattering of dust grains by supernova shocks (e.g. McKee, 1989). Dust destruction is accounted for in Eq. 5.7 by the term $yg\delta_{dest}(t)$. Following Dwek, Galliano & Jones (2007) the dust destruction timescale is described by Eq. 5.10

$$\tau_{\mathrm{des}} = \frac{g}{m_{\mathrm{ISM}} R_{\mathrm{SN}}(t)}, \tag{5.10}$$

therefore $\delta = \tau_{\mathrm{des}}^{-1}$ in Eq. 5.7. The gas mass is g and $m_{\mathrm{ISM}}$is the effective mass of dust cleared by each SN event, which is taken to be $1000\,\mathrm{M}_{\odot}$. R_{SN} is the SN rate:

$$R_{\mathrm{SN}}(t) = \int_{8\mathrm{M}_{\odot}}^{40\mathrm{M}_{\odot}} \phi(m)\psi(t - \tau_m)dm. \tag{5.11}$$

Estimates of how much dust survives the supernova shockwaves are highly uncertain, and Dwek, Galliano & Jones (2007) propose that $m_{\rm ISM}$ may be as low as $100\,{\rm M}_{\odot}$ if dust destruction is inefficient in high redshift galaxies.

Dust grain cores are predicted to accrete atoms in the cold, dense regions of the ISM (Dwek & Scalo, 1980b; Tielens, 1998; Zhukovska, Gail & Trieloff, 2008; Draine, 2009; Jones & Nuth, 2011). Considering the shortfall in stellar dust sources, dust grain growth may be a significant contributor to the dust budget in galaxies (e.g. Draine, 2009; Pipino *et al.*, 2010; Gall, Hjorth & Andersen, 2011; Kuo & Hirashita, 2012). I include grain growth in the model following the prescription of Mattsson, Andersen & Munkhammar (2012), where the rate of grain growth is proportional to the mass of metals and the SFR, which is linked to the fraction of the ISM in the molecular phase where dust grains may grow.

Following Mattsson, Andersen & Munkhammar (2012), the timescale for mantle growth in the ISM is given by

$$\tau_{\rm grow} = \tau_o \left(1 - \frac{Z_d}{Z}\right)^{-1}, \tag{5.12}$$

$$\tau_o^{-1} = \frac{\epsilon Z}{g} \times \psi, \tag{5.13}$$

where g is the gas mass, Z_d is the dust-to-gas ratio, Z is the metallicity (ratio of metal mass to gas mass), ψ is the SFR and ϵ is an efficiency parameter. In order to obtain a minimum $\tau_{\rm grow} \sim (4-9) \times 10^7$ years in the fiducial models in line with expected grain growth timescales (Zhukovska, Gail & Trieloff, 2008; Mattsson, Andersen & Munkhammar, 2012), I set $\epsilon = 500$. If the value of ϵ is lower, then the grain growth timescale is longer, but since the dust mass in many of the SMGs becomes limited by the mass in metals long before the end of the SFH, decreasing ϵ by a factor of a few has negligible impact on the final dust mass.

The last two terms in Eq. 5.7 account for the change in dust mass via inflows with dust mass fraction y_I, and dust lost from the ISM due to outflows with dust mass fraction y_O. In the models $y_I = 0$ for inflows of pristine gas. Assuming the gas, metals and dust are well mixed in the ISM, I set $y_O = y$ so the outflowing dust mass fraction is

equal to the ambient value at time t.

The main difference between this work and the ME03 model is that instead of parametrising the SFR as proportional to the gas mass which decreases smoothly with time, I allow a more complex SFH. This allows us to implement physically realistic SFHs with bursts of variable strength and duration, and with an underlying SFH which can be either exponentially rising or declining. The detailed treatment of the lifetimes of stars of different stellar masses is important for SMGs, which may have bursts of star formation which occur on short timescales. In this work I use the best-fit SFH derived from the SED of each SMG in Chapter 4, which are shown in Fig. 5.1. The use of MAGPHYS SFHs allows us to carry out chemical evolution modelling which is self-consistent with the SED fitting method. My method is a significant improvement over chemical evolution codes which use arbitrary SFHs which may not be appropriate for the galaxies which are being studied.

Figure 5.1 shows that the SMG sample has a variety of best-fit SFHs, with some galaxies having a recent burst of star formation which produces a significant fraction of its stellar mass, or a smooth (either exponentially declining or increasing) SFH with a high sustained SFR over time. I note that because of degeneracies between parameters in the SFH such as γ, which parametrises the continuous underlying SFR, and the timing and strength of bursts, the best-fit SFH may not be the actual galaxy SFH. The adopted SFH, however, gives a physically plausible and self-consistent representation of the SFH which I can use as an input to my chemical evolution models.

In the first instance I consider a closed box model, assuming no inflow or outflow of gas or metals. The initial gas mass is two times the best-fit stellar mass derived from the SED fitting, such that $\sim 50\%$ of the total galaxy mass is in stars at the end of the SFH. I use the best-fit MAGPHYS stellar mass to be consistent with the best-fit SFH. The initial gas masses are therefore tuned to reproduce the observed gas fractions of SMGs ($\sim 40-60\%$, Tacconi *et al.* 2008). I then use my model to go beyond the simple closed box model by including the effects of inflows and outflows on the gas, heavy elements and dust. I also explore the effect of dust destruction and grain growth on the dust mass.

I also explore the changes in dust mass where I vary key parameters such as the SFH

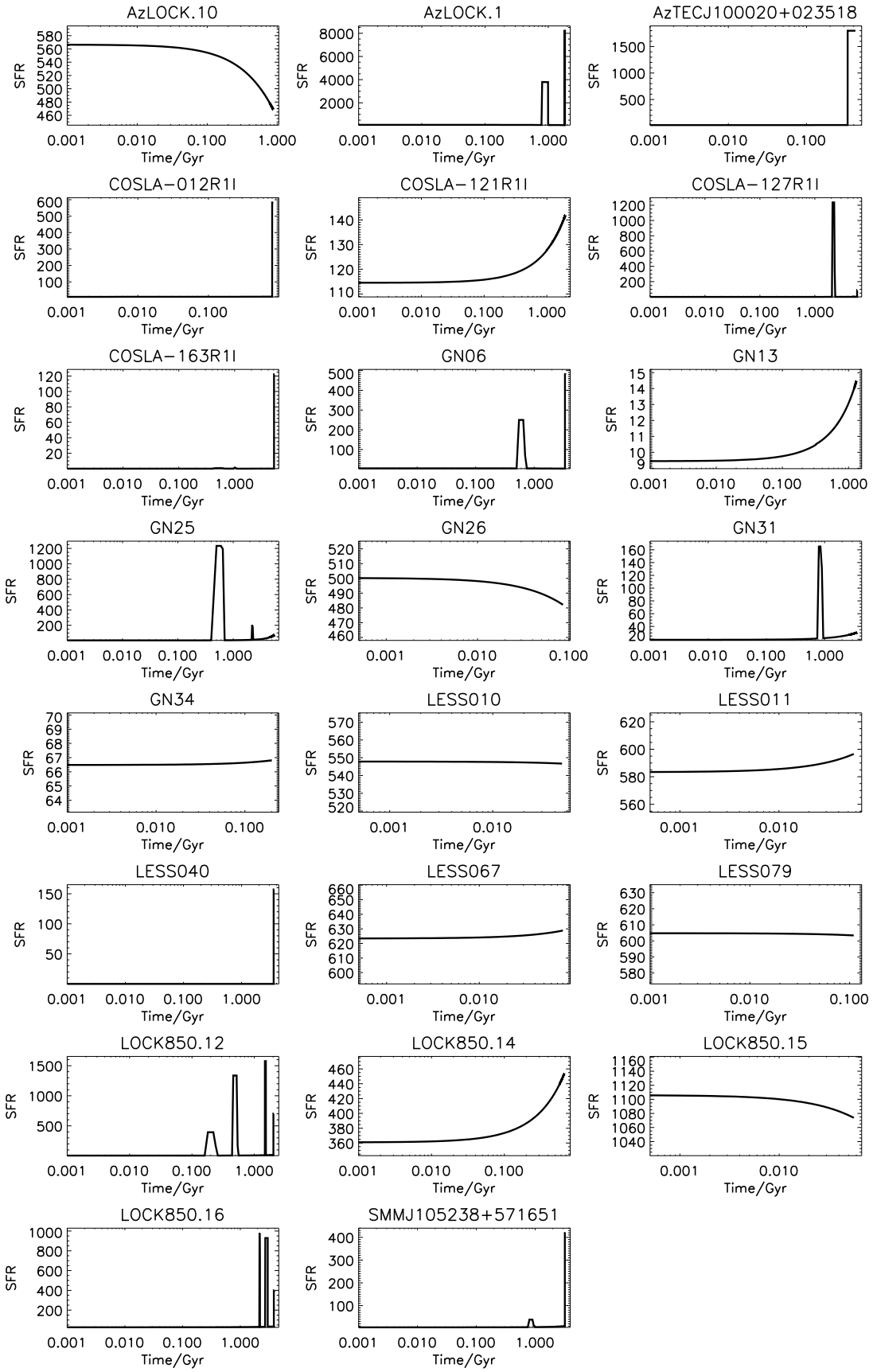

Figure 5.1: Best-fit star-formation histories of the submillimetre galaxies derived from the MAGPHYS SED fitting in Chapter 4.

and IMF using three fiducial models. These models represent the range of SFHs in the MAGPHYS models of SMGs. The fiducial models are parametrised by an exponentially declining (initial SFR of $150\,\mathrm{M_{\odot}yr^{-1}}$), exponentially increasing (final SFR of $150\,\mathrm{M_{\odot}yr^{-1}}$) and constant SFH of $150\,\mathrm{M_{\odot}yr^{-1}}$, with an initial gas mass set to the median initial gas mass of the SMG sample ($1.05 \times 10^{11}\,\mathrm{M_{\odot}}$). The exponentially declining, increasing and constant SFH reach the mean stellar mass of the SMG sample ($5.8^{+1.6}_{-1.3} \times 10^{10}\,\mathrm{M_{\odot}}$) at 1.09, 0.64 and 0.54 Gyr, respectively. At these times there is a factor of two variation in the dust masses produced using the different fiducial models. This means that variations between different SFHs can cause a small change in the final dust masses derived from the chemical evolution models.

5.3 Comparison of SMGs to chemical evolution models

In a closed box model, the average final gas mass of the SMGs ($5.2 \times 10^{10}\,\mathrm{M_{\odot}}$) is in agreement with observations (Bothwell *et al.*, 2013). Furthermore, by design, the final stellar masses are in excellent agreement with the best-fit stellar masses derived from the SED fitting.

5.3.1 Dust production by LIMS

In the first instance I consider dust production from LIMS only, with no dust destruction. A summary of the results derived from the different chemical evolution models considered in this work are given in Table 5.1. The build-up of dust and stellar mass over time for different chemical evolution models is shown for each individual SMG in Fig. 5.2, with the dust produced by LIMS only indicated by the solid black line. The delay between the onset of star formation (as traced by the build-up of stellar mass shown as the solid grey line) and dust production by LIMS is evident in these plots, as the first LIMS die and produce dust after a few hundred Myr. In Fig. 5.3 (a) I show the median likelihood dust mass and SFR of the SMGs derived from the SED fitting, and the final dust mass derived from the chemical evolution modelling. The dust masses calculated from the chemical evolution model with dust from LIMS only fall far short of the observed dust masses for the majority of SMGs. On average for the SMG sam-

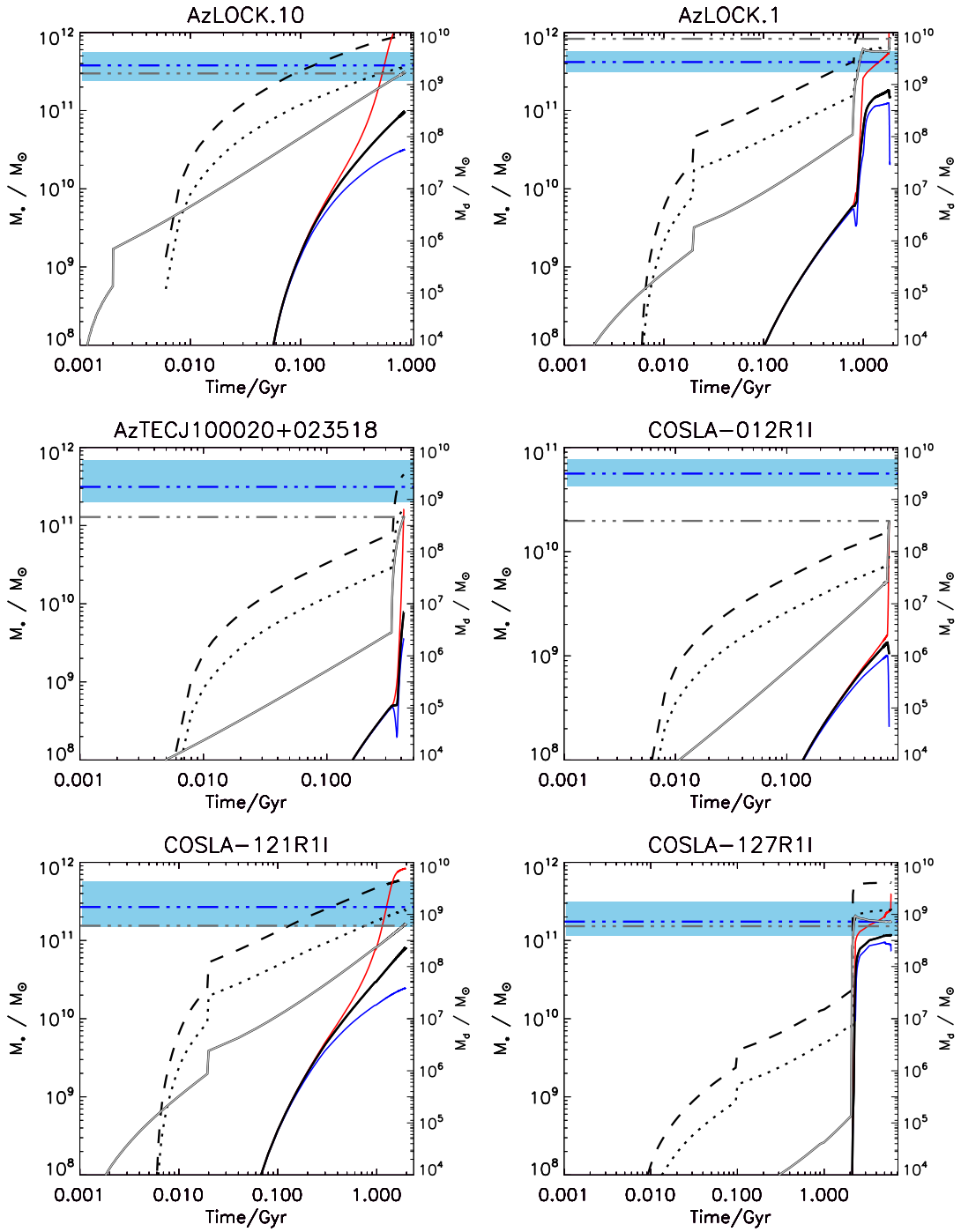

Figure 5.2: The stellar and dust mass evolution over time derived from chemical evolution modelling for the sample of 23 SMGs with good SED fits (see Chapter 4). The stellar mass growth from the input MAGPHYS SFH is represented by the grey line and corresponds to the left axis. All of the other lines represent different dust models and correspond to the right axis. The black solid line is the dust mass produced by low–intermediate mass stars (LIMS) only, the black dotted line is LIMS and supernova dust, and the black dashed line is LIMS and maximal supernova dust production. The red line represents the dust mass in a model where dust is produced by LIMS and grain growth, and the blue line shows the dust mass if dust produced by LIMS is destroyed by supernova shocks. At early times, dust destruction and grain growth models have a dust mass track similar to that with dust from LIMS only. Horizontal dot-dashed grey and blue lines represent the observed best-fit stellar masses and median-likelihood dust masses, respectively, with the blue shaded region indicating the 84th–16th percentile range from the SED fitting.

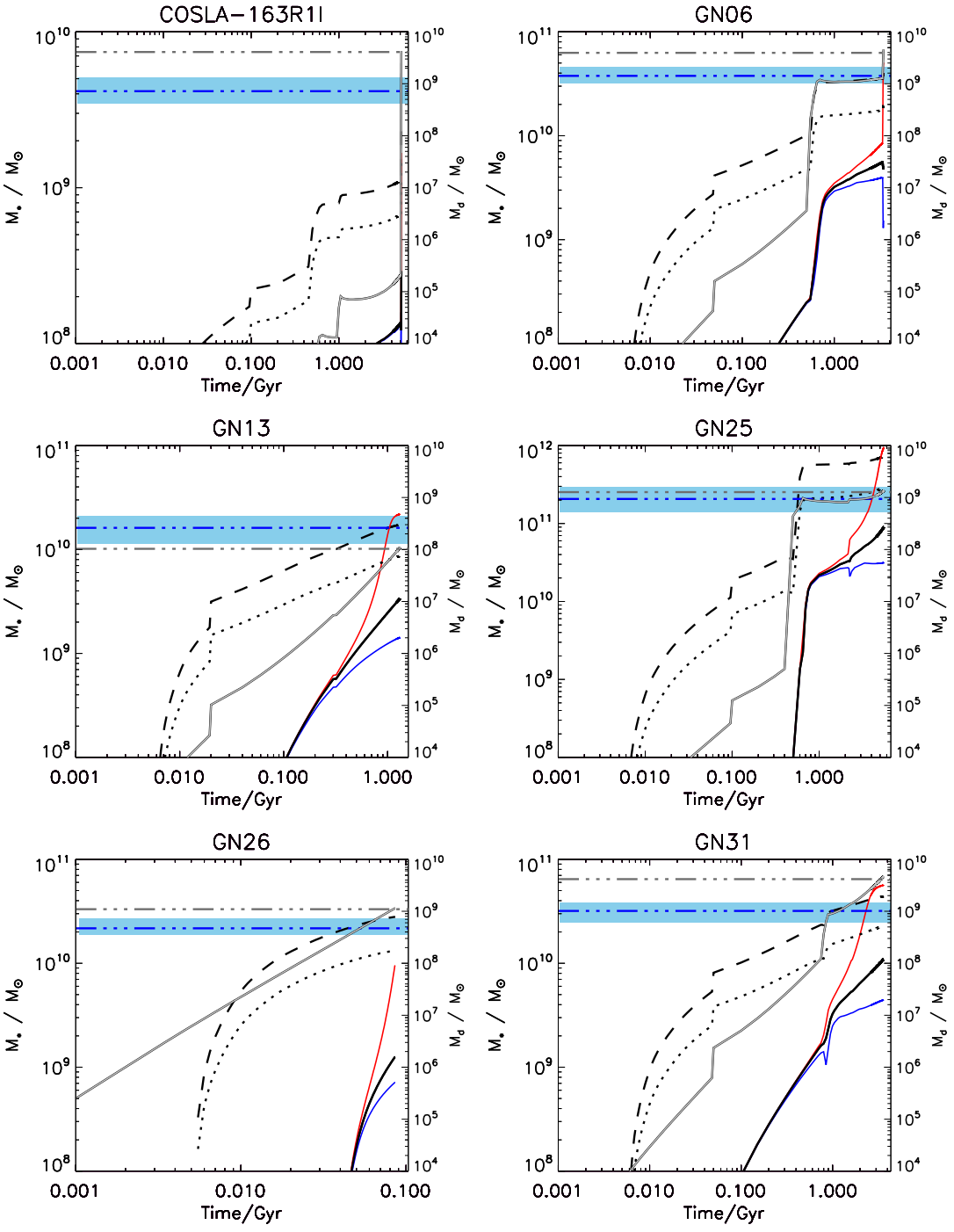

Fig. 5.2 *continued*

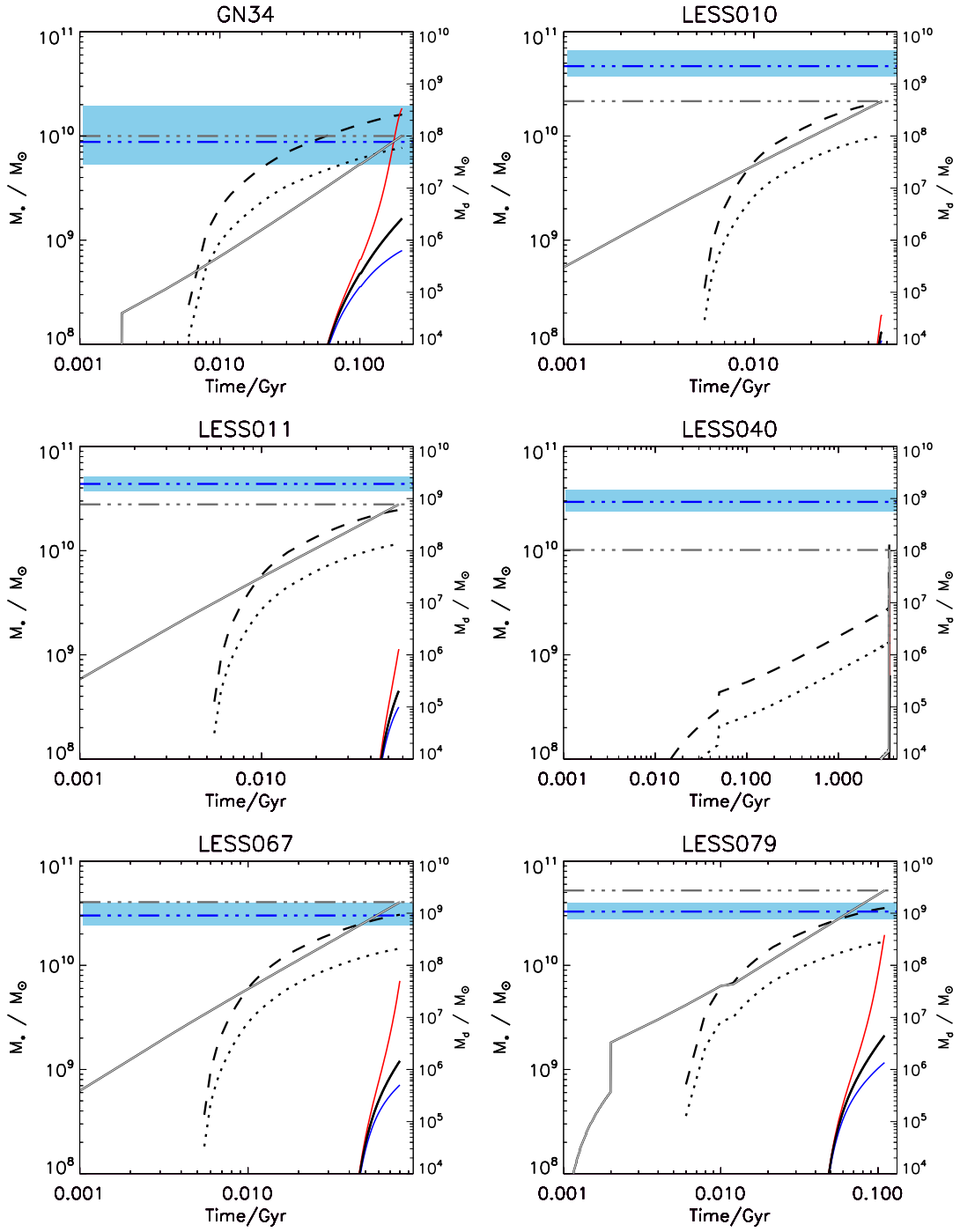

Fig. 5.2 *continued*

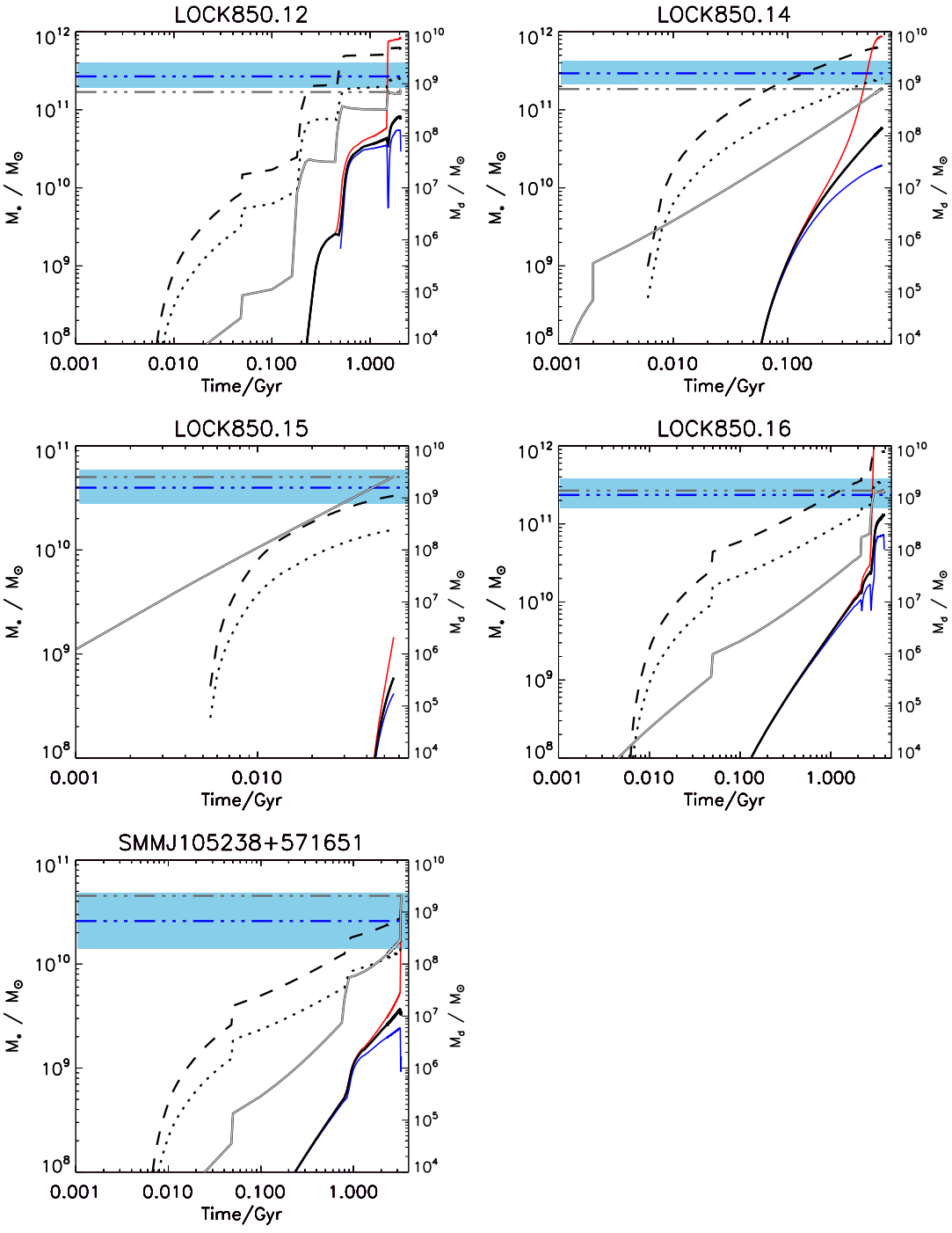

Fig. 5.2 *continued*

ple, the theoretical dust masses are $1.1 \times 10^7\,\mathrm{M}_\odot$, which is a factor 100 lower than the average observed dust mass in the SMG sample ($1.1 \times 10^9\,\mathrm{M}_\odot$). This indicates that the majority of dust in SMGs must come from a source other than LIMS. I find that my closed box chemical evolution models predict high metallicities with a median of $2.3\,\mathrm{Z}_\odot$[1]; this will be discussed later in Section 5.3.5. The median fraction of metals in the ISM in the form of dust in this model is 0.6%.

The mass of dust in each galaxy is sensitive to the gas mass. Increasing the initial gas mass in each galaxy by a factor of two to $2.09 \times 10^{11}\,\mathrm{M}_\odot$ (compared to the original value of $1.05 \times 10^{11}\,\mathrm{M}_\odot$), results in a decrease in the median final dust mass by a factor of 1.6 to $7.2 \times 10^6\,\mathrm{M}_\odot$ (compared to the original value of $1.1 \times 10^7\,\mathrm{M}_\odot$). The median final metallicity is $1.0\,\mathrm{Z}_\odot$,which is closer to observed metallcities of SMGs, see Section 5.3.5. The metallicity and the dust mass (as this is linked to the metallicity) are decreased compared to the original model because the same mass of stars enriches a larger mass of gas. The stellar mass is unchanged as this is set by the SFH, resulting in a final gas fraction of 0.75 on average. However, such large gas fractions in SMGs are not supported by observations.

5.3.2 Dust production via supernovae

If I include dust production from both supernovae and LIMS, dust builds up more rapidly in SMGs as there is a delay of only tens of Myrs between the highest mass stars forming and evolving to the supernova phase. This is evident in Fig. 5.2, as the dust produced by both supernovae and LIMS (dotted black line) closely tracks the stellar mass build-up over time, with bursts of star formation resulting in an almost instantaneous increase in the dust mass. Dust from supernovae accounts for more than an order of magnitude increase in the dust mass of SMGs (a median of $2.8 \times 10^8\,\mathrm{M}_\odot$) compared to the dust mass from LIMS only ($1.1 \times 10^7\,\mathrm{M}_\odot$). The observed dust mass can therefore be accounted for in around 40% of the SMG sample. The median metallicity of the SMGs in this model is the same as with LIMS only ($2.3\,\mathrm{Z}_\odot$), however, due to the inclusion of supernova dust, the median fraction of metals in the ISM in the form of dust is higher (14%). In Fig. 5.3 (b) it can be seen that the predicted

[1]Adopting $\mathrm{Z}_\odot = 0.019$ as solar metallicity.

dust mass for 60% of the sample falls short of the observed dust mass, which indicates additional sources of dust, or higher supernova dust yields are required. It is also evident from Fig. 5.3 that dust production from LIMS and supernovae are needed in order to produce enough dust to match the observed dust masses of the low redshift galaxies. This will be explored further in future work.

In Fig 5.3 (c) I consider the extreme case of maximal dust production from supernovae, such that all metals are incorporated into dust. Sufficiently high dust masses are achieved (a median of $1.3 \times 10^9\,\mathrm{M}_\odot$) that can account for all of the observed dust in SMGs, and in some cases the dust mass is overproduced (see the black dashed lines in Fig. 5.2). The median fraction of metals in the ISM in the form of dust is 59%, similar to that found in Gall, Andersen & Hjorth (2011). It is unlikely, however, that additional dust is contributed by supernovae, as the theoretical supernova dust yields from TF01 are considered optimistic and exceed the dust mass observed in supernova remnants. This means that a significant mass of dust probably comes from grain growth in the dense regions of the ISM, which is explored in Section 5.3.4.

5.3.3 Dust destruction

Dust is thought to be removed from the ISM by the sputtering and shattering of dust grains by supernova shocks (McKee, 1989). I include dust destruction in the model proportional to the supernova rate, following Dwek, Galliano & Jones (2007). The blue line in Fig. 5.2 shows that with dust from LIMS only, dust destruction on average lowers the dust mass by a factor of 6 if supernovae are efficient in clearing the surrounding ISM of dust, with $m_{\mathrm{ISM}} = 1000\,\mathrm{M}_\odot$ of ISM cleared of dust by each supernova event. This value is similar to the maximum dust destruction case in Gall, Andersen & Hjorth (2011) of $m_{\mathrm{ISM}} = 800\,\mathrm{M}_\odot$. If dust is produced by LIMS and supernovae, then the increase in dust mass is approximately cancelled out by the dust destroyed by supernovae, thereby resulting in a median dust mass of $3.4 \times 10^7\,\mathrm{M}_\odot$, similar to that with dust production from LIMS only ($1.1 \times 10^7\,\mathrm{M}_\odot$).

Table 5.1: Summary of the properties derived from different chemical evolution models for 23 SMGs, which have a mean dust mass of $1.1^{+0.2}_{-0.2} \times 10^9\,\mathrm{M}_\odot$. The properties are: the final gas mass ($M_{\rm gas}/\mathrm{M}_\odot$), metallicity ($Z$; the ratio of metal mass to gas mass), the dust mass ($M_{\rm dust}/\mathrm{M}_\odot$), and the dust-to-metal mass ratio ($M_{\rm dust}/M_Z$). For each model, the first line gives the median value from the chemical evolution modelling for the 23 SMGs, and the values in brackets on the second line is the range of values in the sample.

Model	$M_{\rm gas}/\mathrm{M}_\odot$	Z	$M_{\rm dust}/\mathrm{M}_\odot$	$M_{\rm dust}/M_Z$
LIMS dust only	5.2×10^{10} $(7.3 \times 10^9 - 8.4 \times 10^{11})$	0.043 $(0.034 - 0.056)$	1.1×10^7 $(1.7 \times 10^4 - 6.0 \times 10^8)$	0.006 $(2.3 \times 10^{-5} - 0.055)$
LIMS+supernova dust	5.2×10^{10} $(7.3 \times 10^9 - 8.4 \times 10^{11})$	0.043 $(0.034 - 0.056)$	2.8×10^8 $(3.8 \times 10^7 - 5.8 \times 10^9)$	0.14 $(0.13 - 0.17)$
LIMS+maximal supernova dust	5.2×10^{10} $(7.3 \times 10^9 - 8.4 \times 10^{11})$	0.043 $(0.034 - 0.056)$	1.3×10^9 $(1.7 \times 10^8 - 2.8 \times 10^{10})$	0.59 $(0.57 - 0.60)$
LIMS only+destruction ($m_{\rm ISM} = 1000\,\mathrm{M}_\odot$)	5.2×10^{10} $(7.3 \times 10^9 - 8.4 \times 10^{11})$	0.043 $(0.034 - 0.056)$	2.0×10^6 $(1.2 \times 10^4 - 2.0 \times 10^8)$	8.6×10^{-4} $(1.5 \times 10^{-5} - 0.028)$
LIMS only+destruction ($m_{\rm ISM} = 100\ \mathrm{M}_\odot$)	5.2×10^{10} $(7.3 \times 10^9 - 8.4 \times 10^{11})$	0.043 $(0.034 - 0.056)$	8.0×10^6 $(1.6 \times 10^4 - 4.0 \times 10^8)$	0.0048 $(2.2 \times 10^{-5} - 0.051)$
LIMS+supernova dust+destruction ($m_{\rm ISM} = 1000\ \mathrm{M}_\odot$)	5.2×10^{10} $(7.3 \times 10^9 - 8.4 \times 10^{11})$	0.043 $(0.034 - 0.056)$	3.5×10^7 $(4.7 \times 10^6 - 4.4 \times 10^8)$	0.017 $(0.011 - 0.034)$
LIMS+supernova dust+destruction ($m_{\rm ISM} = 100\ \mathrm{M}_\odot$)	5.2×10^{10} $(7.3 \times 10^9 - 8.4 \times 10^{11})$	0.043 $(0.034 - 0.056)$	1.9×10^8 $(2.6 \times 10^7 - 6.0 \times 10^8)$	0.092 $(2.3 \times 10^{-5} - 0.055)$
LIMS+graingrowth	5.2×10^{10} $(7.3 \times 10^9 - 8.4 \times 10^{11})$	0.043 $(0.034 - 0.056)$	6.6×10^8 $(1.7 \times 10^4 - 3.6 \times 10^9)$	0.79 $(4.8 \times 10^{-5} - 0.96)$
LIMS only+destruction+graingrowth ($m_{\rm ISM} = 1000\,\mathrm{M}_\odot$)	5.2×10^{10} $(7.3 \times 10^9 - 8.4 \times 10^{11})$	0.043 $(0.034 - 0.056)$	1.8×10^8 $(2.2 \times 10^4 - 4.6 \times 10^9)$	0.080 $(2.9 \times 10^{-5} - 0.50)$
LIMS inflow ($I = 1\times$ SFR)	1.2×10^{11} $(1.7 \times 10^{10} - 2.2 \times 10^{12})$	0.022 $(0.018 - 0.026)$	9.0×10^6 $(1.6 \times 10^4 - 5.2 \times 10^8)$	0.0053 $(1.8 \times 10^{-5} - 0.022)$
LIMS inflow ($I = 2\times$ SFR)	1.8×10^{11} $(2.6 \times 10^{10} - 3.2 \times 10^{12})$	0.015 $(0.013 - 0.016)$	7.5×10^6 $(1.4 \times 10^4 - 4.6 \times 10^8)$	0.0046 $(1.5 \times 10^{-5} - 0.016)$
LIMS outflow ($O = 1\times$ SFR)	3.0×10^8 $(1.4 \times 10^7 - 7.0 \times 10^{10})$	0.088 $(0.0 - 0.88)$	3.2×10^3 $(0.0 - 2.9 \times 10^6)$	3.7×10^{-4} $(0.0 - 0.040)$
LIMS dust only ($2\times$ initial gas mass)	1.6×10^{11} $(2.2 \times 10^{10} - 2.5 \times 10^{12})$	0.020 $(0.016 - 0.025)$	7.2×10^6 $(8.5 \times 10^3 - 3.9 \times 10^8)$	0.0035 $(8.1 \times 10^{-6} - 0.016)$

It is possible, however, that supernova shocks are less efficient at destroying dust, particularly if the dust is shielded in cold, dense regions of the ISM. Lower dust destruction rates have been suggested by Dwek, Galliano & Jones (2007), Dwek *et al.* (2011) and Gall, Andersen & Hjorth (2011), who struggle to produce the dust masses of high redshift galaxies with efficient dust destruction. Since the ISM properties of high redshift SMGs are not well known, there are large uncertainties about the effectiveness of dust destruction in the ISM. Dwek, Galliano & Jones (2007) and Gall, Andersen & Hjorth (2011) suggest that $m_{\rm ISM} = 100\,{\rm M}_{\odot}$ may be more appropriate in high redshift galaxies. In the models with $m_{\rm ISM} = 100\,{\rm M}_{\odot}$, less efficient dust destruction on average lowers the dust mass by a factor of 1.4 and 1.5 for models with dust produced by LIMS only, and LIMS and supernovae, respectively.

5.3.4 Grain growth

Dust grain cores are predicted to accrete atoms in the cold, dense regions of the ISM (Dwek & Scalo, 1980b; Tielens, 1998; Zhukovska, Gail & Trieloff, 2008; Draine, 2009; Jones & Nuth, 2011). Considering the shortfall in stellar dust sources, dust grain growth may be a significant contributor to the dust budget in galaxies (e.g. Draine, 2009; Michałowski *et al.*, 2010; Pipino *et al.*, 2010; Gall, Hjorth & Andersen, 2011; Kuo & Hirashita, 2012). The prescription for grain growth is described in Eq. 5.13, following Mattsson, Andersen & Munkhammar (2012).

The effect of grain growth (with no dust destruction) on the dust mass is shown in Fig. 5.2 by the solid red line. In Fig 5.3 I find that grain growth on average increases the dust mass by a factor 60 to $6.6 \times 10^8\,{\rm M}_{\odot}$, compared to dust production from LIMS only ($1.1 \times 10^7\,{\rm M}_{\odot}$). Grain growth can make up the shortfall in the predicted dust masses compared to LIMS dust for 50% of SMGs in the sample. This indicates that a small contribution from supernova dust is required in some SMGs. Yet, in some cases, the dust mass rapidly approaches the metal mass, with a median value of 79% of the metals in the ISM in the form of dust, which may be unrealistic. In some cases the grain growth overpredicts the dust mass in SMGs, therefore conversion of nearly all the metals into dust is not always required.

If efficient dust destruction is included along with grain growth, then the dust produced

is not enough to account for the dust masses observed in SMGs, with the median dust mass reaching $1.8 \times 10^8\,\mathrm{M}_\odot$ (c.f. $1.1 \times 10^7\,\mathrm{M}_\odot$ from LIMS only). For the SMGs whose predicted dust masses fall short of the observed value, it is possible that dust destruction is less efficient, or a contribution from supernovae to the dust budget is needed. Whilst there are considerable uncertainties in the sources of dust production and destruction in galaxies, I can conclude that LIMS cannot be the only source of dust in SMGs. The majority of dust must be produced by a combination of supernova dust and grain growth, in order to explain the observed dust masses of SMGs.

5.3.5 Inflows

The closed box model is the simplest approach to chemical evolution, and gives the most optimistic view of metal and dust build up in galaxies (Edmunds & Eales, 1998). In reality, galaxies are unlikely to be closed systems, (e.g. see Erb 2008). For example, the well known G-Dwarf problem requires infall of material in the Milky Way (e.g. van den Bergh, 1962; Searle & Sargent, 1972; Pagel & Patchett, 1975; Tinsley, 1980). Gallazzi *et al.* (2005) suggest that in galaxies at a fixed gas-phase oxygen abundance, the wide range in stellar metallicity suggests that inflows and outflows of gas are important in the chemical evolution of galaxies.

Inflows of cold gas are essential ingredients in galaxy formation simulations at high redshift (e.g. Dekel *et al.*, 2009). Although there is limited direct observational evidence for gas inflows, recent studies have suggested inflows of gas are required in order to sustain the SFRs observed in galaxies at high redshift (Giavalisco *et al.*, 2011; Reddy *et al.*, 2012; Tacconi *et al.*, 2012). I find that my closed box chemical evolution models predict high metallicities with a median of $2.3\,\mathrm{Z}_\odot$, at odds with some observations of SMGs. Although supersolar metallicities have been measured in some SMGs (Tecza *et al.*, 2004), high redshift ULIRGs (Kawara *et al.*, 2010), and QSOs (e.g. D'Odorico *et al.*, 2004), other studies typically find that SMGs have solar or subsolar metallicities (Swinbank *et al.*, 2004; Banerji *et al.*, 2011; Nagao *et al.*, 2012). It may be possible that since SMGs are very obscured, the optical emission lines used to measure metallicites only probe the outer parts of galaxies, which may be less enriched (Santini *et al.*, 2010). If SMGs have sub-solar metallicities this suggests that inflows

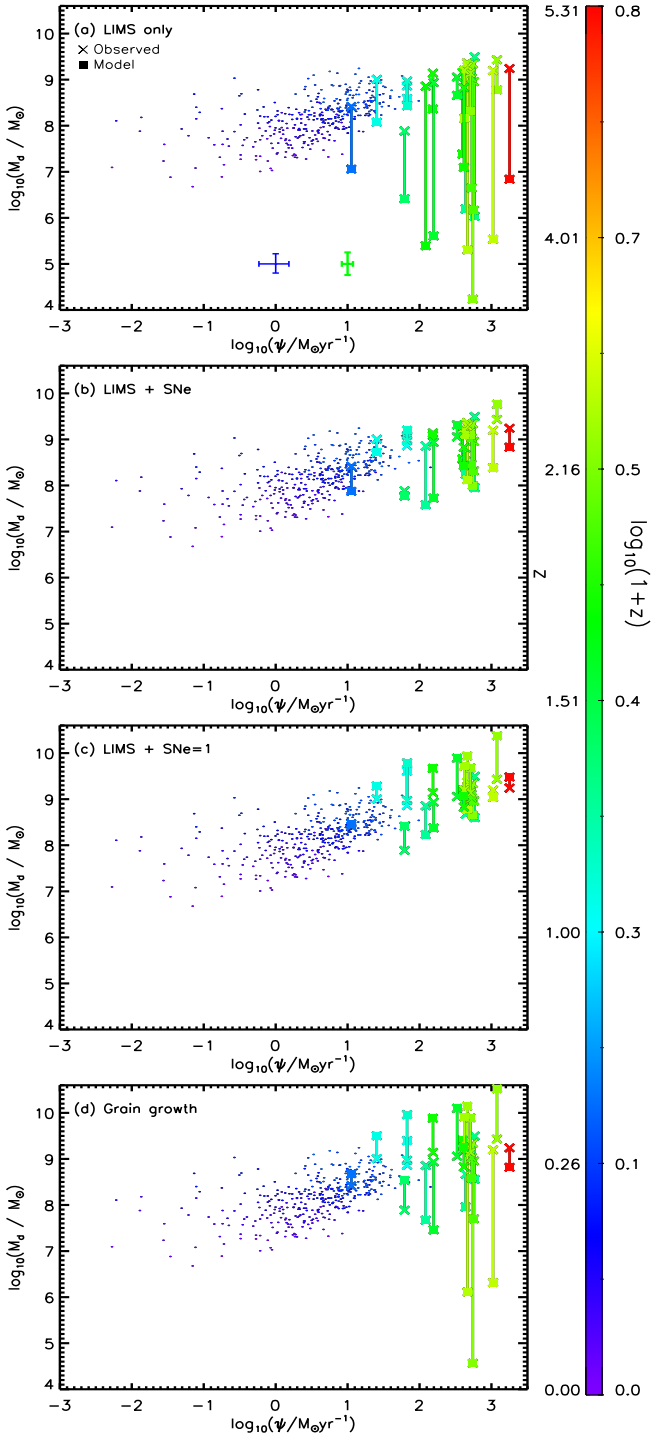

Figure 5.3: The relation between the SFR (averaged over the last 10^7 years) and observed dust mass for the high redshift SMGs (crosses) and dust masses derived from the chemical evolution model (squares), assuming no dust destruction. Dust is produced in panel (a) by low–intermediate mass stars (LIMS) only, LIMS and supernovae (b), LIMS and maximal dust production by supernovae (c), and by LIMS and grain growth (d). Lines link the observed dust mass in each SMG to the dust mass predicted from the chemical evolution model to indicate the shortfall in dust production. As a reference the low redshift H-ATLAS sample are shown as dots, with all points coloured by redshift. Chemical evolution modelling of the low redshift dusty galaxies is investigated in Dunne *et al.* (2011) and Gomez et al. (in prep), and so is not performed in this work. The error bars indicate the median 84th–16th percentile range from each individual parameter PDF; the thin and thick error bars correspond to the low redshift H-ATLAS and high redshift SMG samples in Chapter 4, respectively.

of metal-poor gas are needed to dilute the metal-rich gas to lower metallicity.

In the chemical evolution model I assume that an inflow delivers un-enriched gas to the galaxy at a rate proportional to the SFR. I adopt the same initial gas mass as for the closed box model to provide a consistent comparison, although this results in a final gas mass which is larger than that observed in SMGs. In galaxies, inflows decrease the metallicity and dust mass (Edmunds, 1990; Edmunds & Eales, 1998), as the enriched gas is diluted by the unenriched inflow. I find that an inflow rate equal to the SFR throughout the lifetime of each SMG is sufficient to reduce the median metallicity of the SMG sample to $1.1\,\mathrm{Z}_{\odot}$. Inflow rates of the order of the SFR are consistent with the semi-analytic model of Dutton, van den Bosch & Dekel (2010) and the simple analytic model of Erb (2008), who find that the rate-of-change of the gas mass (inflow-outflow) is in a steady state with the SFR.

If SMGs have sub-solar metallicities, then inflows of greater than 1 times the SFR is needed. These inflow rates are consistent with the results of Reddy *et al.* (2012), who find that at redshifts $\gtrsim 2-3$ the gas accretion rate is larger than the SFR. Similarly, Papovich *et al.* (2011) find that at $z > 4$ the gas accretion rate is equal to, or can exceed the SFR. An inflow rate of two times the SFR results in a median metallicity of $0.8\,\mathrm{Z}_{\odot}$ for the 23 SMGs. Inflows of $2\times$ the SFR reduce the dust mass by a factor 1.5 on average, requiring a larger contribution of supernova dust or grain growth to the dust budget than is needed with a closed box model.

However, such high inflow rates are not supported by simulations. van de Voort *et al.* (2011) estimate the cold and warm gas accretion onto halos using hydrodynamical simulations. For a typical SMG halo mass of $\mathrm{M}_H = 10^{12.8}\,\mathrm{M}_{\odot}$ (Hickox *et al.*, 2012) at $z = 2$, it is estimated that $176\,\mathrm{M}_{\odot}\mathrm{yr}^{-1}$ of cold gas is accreted onto the halo, although only $88\,\mathrm{M}_{\odot}\mathrm{yr}^{-1}$ in total reaches the galaxy. Of this, $40\,\mathrm{M}_{\odot}\mathrm{yr}^{-1}$ is from hot gas, of which 25% will cool to form stars, and $48\,\mathrm{M}_{\odot}\mathrm{yr}^{-1}$ is from cold gas. This means that at $z = 2$ there is $58\,\mathrm{M}_{\odot}\mathrm{yr}^{-1}$ of gas accreted. This accretion rate is similar to that found in Kereš *et al.* (2005) for $10^{13}\,\mathrm{M}_{\odot}$ halos in smoothed particle hydrodynamics simulations of $60\,\mathrm{M}_{\odot}\mathrm{yr}^{-1}$ of hot gas at $z = 2$, rising to $150\,\mathrm{M}_{\odot}\mathrm{yr}^{-1}$ at $z = 3$. The accretion rates in simulations are therefore lower than than those implied by the chemical evolution models. In summary, if SMGs have sub-solar metallicities, inflows of 1–2 times the

SFR are needed. Whilst there is indirect observational support from some studies of high redshift galaxies, simulations do not support high inflow rates. If SMGs do not have gas inflow rates comparable to the SFR, this implies that SMG gas-phase metallicities are super-solar. At present, the uncertainties in the measured metallicities of SMGs do not allow us to choose between models which have different gas inflow rates.

5.3.6 Outflows

Outflows of gas are thought to be common in actively star-forming galaxies at all epochs (Heckman *et al.*, 2000; Weiner *et al.*, 2009; Rubin *et al.*, 2010; Diamond-Stanic *et al.*, 2012), and may be either driven by stars (stellar winds and supernovae), or by AGN. Significant outflows of enriched material are implied by the results of Ménard *et al.* (2010), who found evidence for dust in galaxy halos, with a mass comparable to that of dust in the disk. Outflows of dust in nearby starburst galaxies were observed by Alton, Davies & Bianchi (1999). Furthermore, Erb *et al.* (2006) suggest that the mass–metallicity relation at $z \sim 2$ is modulated by metal-rich outflows from galaxies, with rates of up to four times the SFR. Outflows could therefore be responsible for the metal enrichment of the IGM. Large outflow rates are also indicated by Dunne *et al.* (2011), who find that chemical evolution models with outflows of four times the SFR best describe the evolution of the dust mass function of H-ATLAS galaxies at $0 < z < 0.5$. Sturm *et al.* (2011) find evidence of outflows in local ULIRGs of the order of $1\times$ the SFR in starburst dominated galaxies, and outflows of $4 - 20\times$ the SFR in AGN dominated ULIRGs. Outflows have been observed in SMGs with velocities of up to $1000\,\mathrm{kms}^{-1}$ (Banerji *et al.*, 2011; Harrison *et al.*, 2012).

I investigate the effect of outflows of enriched gas on the dust mass in the SMG sample. In the chemical evolution model I assume that the gas and dust in the ISM are well mixed, and that outflows remove enriched gas (including heavy elements and dust), from the galaxy at a rate proportional to the SFR. Outflows significantly reduce the dust mass in a galaxy, which further increases the tension between the observed and predicted dust masses in SMGs. Furthermore, outflows of the order of the SFR significantly reduce the gas available for star formation, such that most of the SMGs in the

sample rapidly deplete their gas supply. This does not allow enough time for dust to build up if it is produced by LIMS only. As the majority of SMGs run out of gas before the end of their SFH, this means that the stellar mass is not high enough to match observations. This indicates that in the case of long-lived outflows, higher SFRs are needed in order to build-up sufficient stellar mass.

In order for SMGs to retain a substantial gas mass, either a larger initial gas mass is required, or significant inflows of gas are needed. However, this would reduce the dust mass further. The high outflow rates seen in AGN and starbursts are likely to be short-lived, therefore the gas mass may not be substantially depleted by outflows. In outflow models, the metallicity is higher compared to the closed box model. This is because there is less gas in the system, but this continues to be enriched by star formation, so the metal mass increases relative to the gas mass. Since outflows driven by star formation or AGN are likely to be short-lived, this may allow the metallicity of the galaxy to remain within observational limits. It is also possible that both inflows and outflows occur simultaneously (Sakamoto *et al.*, 2013), or in short succession (Dalcanton, 2007), which would allow the predicted metallicity to match observed values in SMGs.

5.3.7 Variations in the IMF

The IMF has been found by many studies to be invariant with time and location (see the review in Bastian, Covey & Meyer, 2010), although theoretical studies predict that the IMF should vary, albeit weakly (Narayanan & Davé, 2012, and references therein). Semi-analytic models have required a top-heavy IMF in order to predict the observed number counts of SMGs (Baugh *et al.*, 2005; González *et al.*, 2011). However, more recent work by Hayward *et al.* (2013) found that a top-heavy IMF in a semi-empirical model of galaxy formation overpredicts the number counts of SMGs. Many studies have suggested that the IMF may become top-heavy under certain conditions, for example in starbursts (Dabringhausen, Kroupa & Baumgardt, 2009; Papadopoulos *et al.*, 2011; Kroupa, 2012), where birth clouds are likely in a cosmic ray dominated heating regime. Gunawardhana *et al.* (2011) found a strong relationship between SFR and IMF slope, such that galaxies with higher SFRs form more massive stars. Dwek

et al. (2011) found that a top heavy IMF best reproduced the observed dust mass in the submillimetre galaxy AzTEC3 (AzTECJ100020+023518 in my sample of SMGs).

To investigate the sensitivity of the dust mass to the IMF, I increase the power law slope of the Chabrier IMF from -1.3 to -0.8, but leave the low mass end unchanged. If dust is produced by LIMS only, then a top heavy IMF does not increase the dust mass enough to account for the observed dust masses of SMGs. Using the three fiducial models which represent the range of SFHs of SMGs (see Section 5.2), I find that a slope of -0.8 allows us to reproduce the average observed SMG dust masses ($1.1 \times 10^9\,\mathrm{M}_\odot$) at a time of 0.5 Gyr after the onset of star formation, if dust production from both LIMS and supernovae are considered. With a top heavy IMF the metallicity is also higher, which is hard to reconcile with observations unless significant inflows of pristine gas occur. A top heavy IMF implies that the dust destruction rate due to supernovae will be higher (Gall, Andersen & Hjorth, 2011). Therefore, the increase in the dust mass from LIMS and supernovae with destruction ($m_{\mathrm{ISM}} = 1000\,\mathrm{M}_\odot$) achieved by making the IMF top heavy is only a factor of 1.7 compared to a Chabrier IMF with the same dust sources and destruction (at a time of 0.5 Gyr after the onset of star formation). Invoking a top heavy IMF with minimal dust destruction can solve the dust budget crisis in SMGs, but given the uncertainties involved this does not provide unequivocal evidence for a top heavy IMF.

5.4 Conclusions

Using a chemical evolution model with physically-motivated, complex SFHs I investigated the origin of dust in high redshift SMGs. My main results are as follows:

- Using my chemical evolution model I find that dust produced only by low–intermediate mass stars (LIMS) falls a factor 100 short of the observed dust masses of SMGs ($1.1 \times 10^9\,\mathrm{M}_\odot$). Adding an extra source of dust from supernovae can account for the dust mass in SMGs in 40% of cases. Even after accounting for dust produced by supernovae, the remaining deficit in the dust mass budget suggests that higher supernova yields, and/or substantial grain growth are required in order for the dust mass predicted by the chemical evolution models

to match observations.

- The efficient destruction of dust grains by supernova shocks on average decreases the dust mass from LIMS by a factor of six. Additional sources of dust would be required in order to account for the additional shortfall of dust in SMGs caused by dust destruction. Alternatively, dust destruction may be less efficient if dust grains are shielded from supernova shocks in dense regions of the ISM, or if the ISM is inhomogeneous in density.

- The metallicity in the closed box model on average reaches $2.3\,Z_{\odot}$, which is larger than the metallicity measured in some SMGs. This implies that inflows of pristine gas are required in order to reduce the metallicity to observed values. However, inflows reduce the dust mass, which worsens the discrepancy between model and observed dust masses.

- Outflows of enriched gas rapidly deplete the gas reservoir, which prevents a sufficient build-up of dust and stellar mass in the SMGs. If the metallicity of SMGs is to remain below solar, this indicates that outflows must be short lived, or must occur simultaneously with inflows of unenriched gas.

- With minimal dust destruction I found that a top heavy IMF with dust produced by both LIMS and supernovae can produce the average dust mass observed in SMGs. Yet, given the uncertainties involved (e.g. in the dust destruction rate and metallicity in SMGs) this does not provide unequivocal evidence for a top heavy IMF in dusty high redshift galaxies.

In summary, the high dust masses observed in SMGs at high redshift are difficult to reconcile with conventional dust sources. However, this issue is not limited to high redshift, as similar problems are encountered with low redshift dusty galaxies, which will be explored in future work.

Chapter 6

Conclusions

6.1 Summary of the thesis

Our understanding of the build-up of stellar mass in galaxies via star formation from far-infrared (FIR) and submillimetre observations has grown considerably over the last 30 years. Until recently, FIR–submillimetre studies of galaxies were limited to relatively small samples, and were often biased towards the most luminous and highly star-forming galaxies at high and low redshifts. Observations of normal galaxies in the local Universe were limited to targeted studies, making a truly unbiased survey of dust and obscured star formation impossible. With *Herschel*, we now have a complete census of the dusty galaxy population. In this thesis I have shown that dusty galaxies are a diverse population, both morphologically and in star-formation activity. Dusty galaxies comprise both spirals and early-types, and range from quiescent systems to starburst galaxies. I have used data from the largest area *Herschel* surveys, in combination with a wealth of multiwavelength data, to study the statistical properties of dusty galaxies throughout cosmic time.

In this thesis I used a panchromatic approach, utilising data from the UV to the submillimetre to study galaxy evolution. I have demonstrated the utility and power of multiwavelength SED fitting to derive statistical constraints on the physical properties of large galaxy samples. I used the physically-motivated model of da Cunha, Charlot & Elbaz (2008, MAGPHYS), to provide a self-consistent treatment of stellar emission

which is reprocessed by dust in the far-infrared. In Chapters 3 and 4 I used the standard MAGPHYS priors to fit the SEDs of low redshift galaxies. In Chapter 2 I also outlined the motivation for building a new set of priors to describe the properties of high-redshift dusty galaxies, which were described in Chapter 4. I then explored the differences in the derived physical properties using two different sets of priors, which highlights how the choice of prior can affect some parameters derived from broadband SED fitting. For the majority of galaxies, median likelihood estimates of the parameters derived using the standard and composite priors show some scatter, but are generally consistent within the parameter uncertainties for the sample. A minority of galaxies showed large departures from the one-to-one relation for a few parameters such as star-formation rate. This does not change our conclusions in Chapter 4.

In Chapter 3 I presented the properties of a 250μm selected sample of galaxies according to their morphology. Using the large area ($\sim$14 deg^2) of the first *Herschel*-ATLAS (H-ATLAS) data release, I showed that the dusty galaxy population is not solely comprised of spirals but also includes a rare population of dusty early-type galaxies (ETGs). These dusty ETGs comprise only 5.5% of the general ETG population within the redshift and r-band selection function of H-ATLAS. This is contrary to the traditional idea that ETGs are 'red and dead', having formed most of their stellar mass at early epochs over a short period of time. Although there is some evidence for gas and dust in ETGs, studies have been limited to small and often biased samples. I have shown in the first unbiased survey of dust in the local Universe that a small minority of dusty ETGs harbour on average $5.5 \times 10^7\,\mathrm{M}_\odot$ of dust, which is comparable to that of some spiral galaxies in our sample.

In order to see how dusty ETGs are different to the general ETG population, I compared to a control sample of optically-selected ETGs, which were not detected at 250μm. H-ATLAS ETGs inhabit a range of environments, and I find no environmental difference between the ETG and spiral populations, or between H-ATLAS and the control samples. ETGs detected in H-ATLAS tend to be bluer and younger than those which are optically selected. The H-ATLAS ETGs have, on average, more than an order of magnitude more dust than non-detected ETGs, for which I inferred a median dust mass through stacking. Since only a small fraction of ETGs have dust masses as

large as those detected in H-ATLAS, it could be that our sample represents a short-lived phase in the evolution of some ETGs, for example following a star-formation episode as the result of a delivery of gas via a merger or accretion event.

In Chapter 3 I also explored the properties of the most passive spiral galaxies in our sample, which have old stellar populations yet still contain considerable amounts of dust. These have lower dust-to-stellar mass ratios and older ages but appear to inhabit similar environments to more actively star-forming spirals. It is possible that these passive spirals have run out of gas to fuel star formation, or that their star formation has been quenched by some process in the low density environment in which they reside.

In Chapter 4 I examined the physical properties of a rest-frame 250μm selected sample of massive, dusty galaxies over a large range in cosmic time ($0 < z < 5.3$). Whilst the sample size of high redshift ($z \sim 2$) submillimetre galaxies (SMGs) is relatively small, the excellent multiwavelength coverage from the rest-frame UV to the submillimetre, including coverage of the peak of the dust emission, allowed me to derive statistical constraints on galaxy physical parameters. I compared the SMGs to a sample of low redshift $z < 0.5$ dusty galaxies selected to have a similar stellar mass, which provides a large low-redshift benchmark comparison sample to SMGs. I found high redshift dusty galaxies have significantly higher star-formation rates and dust masses than $z < 0.5$ dusty galaxies selected to have a similar stellar mass. Galaxies which are as highly star forming and dusty as those at $z \sim 2$ are rare in the local Universe. I found that the fraction of dusty starburst galaxies at low redshift (7 per cent) is much smaller than that of dusty starbursts at high redshift. The differences between the high and low redshift dusty galaxy populations may be driven by an increase in the gas fraction at higher redshifts (Geach *et al.*, 2011; Tacconi *et al.*, 2012; Combes *et al.*, 2013). To determine the mode of star formation in the high redshift dusty galaxy sample, I examined where each galaxy lies relative to the main sequence of star formation at a given redshift. My results support the idea that the most dusty galaxies at high redshift are a heterogeneous population (Davé *et al.*, 2010; Hayward *et al.*, 2011; Targett *et al.*, 2012; Magnelli *et al.*, 2012; Symeonidis *et al.*, 2013), with around 60% of our sample consistent with secular evolution, and the other 40% of galaxies are starbursting, possibly merger-

driven systems. Further insights into the properties of high redshift dusty galaxies will be gained from the investigation of larger samples which encompass lower stellar masses and infrared luminosities more typical of the high redshift galaxy population.

The origin of dust in galaxies at both low and high redshifts presents a challenge to current theories of galaxy evolution. Recent work has revealed a *'dust budget crisis'*, whereby the mass of dust observed in galaxies at low redshift (Matsuura *et al.*, 2009; Dunne *et al.*, 2011; Rowlands *et al.*, 2012) and at high redshift (Michałowski, Watson & Hjorth, 2010; Gall, Andersen & Hjorth, 2011) cannot be accounted for by stellar mass loss from low–intermediate mass stars (LIMS). In Chapter 5 I tackled this challenge using chemical evolution modelling of the high redshift SMGs discussed in Chapter 4, with a detailed treatment of their SFHs and the dust sources and sinks in galaxies. I implemented modifications to an existing chemical evolution code (Morgan & Edmunds, 2003) so that the SFHs of galaxies are treated self-consistently in both the SED fitting and theoretical modelling of the build-up of dust over time.

Starting with the most simple model, in a closed box scenario I modelled the dust produced in SMGs by LIMS, which is the dominant source of dust in the local Universe. I showed that dust from LIMS only is inadequate (by a factor of 100) at producing the large dust masses of high redshift dusty galaxies ($1.1 \times 10^9\,\mathrm{M}_\odot$ on average). To increase the dust mass in SMGs, I added dust produced by supernovae to the model, using theoretical dust yields and assuming no dust destruction by supernova shocks. The dust produced by LIMS and supernovae can account for the observed dust mass in 40% of SMGs in my sample. It is important to realise that the theoretical dust yields from supernovae are optimistic, which often exceed the dust mass observed in supernova remnants. Furthermore, the mass of dust which is destroyed by supernova shocks is highly uncertain, but if dust is destroyed efficiently this worsens the discrepancy between the model and observed dust masses by a factor of $6 - 8$. It is therefore possible that dust destruction is inefficient in SMGs. The uncertainty in supernova yields, dust destruction rates and the remaining deficit in the dust mass budget for 60% of SMGs, suggests that additional sources of dust such as grain growth must be considered. Dust produced by LIMS and grain growth can account for the dust in SMGs. However, this presents the problem that a large fraction of metals ($> 50\%$) are in the form of dust.

The metallicity in the closed box model on average reaches $2.3\,Z_{\odot}$, which is higher than the sub-solar metallicity measured in some SMGs. This implies that inflows of pristine gas with a rate of $1-2\times$ the SFR are required in order to reduce the metallicity to observed values. Whilst there is indirect observational support of inflows with $1-2\times$ the SFR from some studies of high redshift galaxies (Papovich *et al.*, 2011; Giavalisco *et al.*, 2011; Reddy *et al.*, 2012; Tacconi *et al.*, 2012), simulations do not predict such high inflow rates (Kereš *et al.*, 2005; van de Voort *et al.*, 2011). Although inflows can solve issues related to metallicity, inflows reduce the mass of dust in galaxies, which exacerbates the problems of producing enough dust in SMGs.

Gas outflows are thought to be ubiquitous in actively star-forming galaxies at all epochs (e.g. Heckman *et al.*, 2000; Erb, 2008; Weiner *et al.*, 2009; Rubin *et al.*, 2010). It is therefore important to assess the impact of outflows on the dust and gas masses of SMGs. If outflows occur at a rate comparable to the SFR, this quickly exhausts the gas supply and severely limits the mass of dust formed in SMGs. This means that outflows must occur at a rate much lower than the SFR or only for a short period of time (e.g. during a starburst or AGN event) or concurrently with gas inflows. Investigations into the effect of simultaneous inflows and outflows on the gas and dust masses, and a more realistic treatment of the time dependence of gas flows, would benefit my modelling of SMGs.

One other possible solution to solving the dust budget crisis is to invoke a top heavy IMF. With minimal dust destruction I found that a top heavy IMF with dust produced by both LIMS and supernovae can produce the average dust mass observed in SMGs. Yet, given the uncertainties involved (e.g. in the dust destruction rate and metallicity in SMGs) this does not provide unequivocal evidence for a top heavy IMF in dusty high redshift galaxies.

In Chapter 5 I investigated the build-up of dust in SMGs with chemical evolution models of increasing complexity. It is clear that a significant mass of dust must be from supernovae and/or grain growth; however, the origin of dust in SMGs remains uncertain. Reducing the uncertainties of supernova yields and the physical properties of SMGs such as the SFH and metallicity through further observations would allow me to better constrain the mechanisms of dust production.

6.2 Future work

Herschel is in the last days of its mission but has provided a wealth of data which will continue to advance astronomy for many years. In addition to the SCUBA-2 Legacy Survey and high resolution millimetre observations from ALMA, *Herschel* will allow us to study the dust and gas properties of galaxies over the last 13 billion years of cosmic time. FIR–submillimetre observations are extremely useful for constraining the star formation and ISM properties of galaxies, especially when combined with multiwavelength observations from current optical-NIR surveys such as CANDELS, and forthcoming observations with the *James Webb Space Telescope* (JWST). This will allow us to study the co-evolution of stars and the ISM of galaxies from the epoch of reionisation, during the peak of star formation in the Universe to the present day.

The unique sample of 44 dusty ETGs studied in Chapter 3 revealed interesting results, but the work would benefit from a larger sample size. Steps toward this have been undertaken by Agius *et al.* (2013), who studied the properties of 220 ETGs at $0.013 < z < 0.06$ detected in H-ATLAS. Dust comprises only a small fraction of the ISM in galaxies. Hydrogen makes up the bulk of the ISM and provides the fuel for future generations of stars. In order to improve our understanding of objects which are transitioning between the blue cloud and the red sequence, observations of the molecular gas content of dusty ETGs and passive spirals studied in Chapter 3 would be beneficial. I have recently obtained CO(2-1) and CO(1-0) observations of a small number of ETGs with visible dust lanes, which revealed that these galaxies harbour large gas masses, which may be delivered by minor mergers. However, observations of a larger sample of dusty ETGs, including those without dust lanes are needed in order to investigate the origin of gas and dust in the general ETG population. This would allow me to test a possible link between the presence of gas and dust in ETGs and morphological disturbances as a result of recent (minor) mergers. My work could also be improved with deeper optical imaging, which would allow me to better examine the morphologies of dusty ETGs.

Now that the H-ATLAS survey is complete, large numbers of ETGs across a wide variety of environments can be studied. The environmental density probed in Chapter 3 using the the first data release from H-ATLAS was relatively small, and did not contain

many dense clusters. Whilst *Herschel* has already uncovered a relatively small number of dusty ETGs in the Virgo cluster (Smith *et al.*, 2012c; di Serego Alighieri *et al.*, 2013), studies of larger samples in different environments are needed. Investigations of the dust and gas content of ETGs in denser environments such as the Coma cluster and comparison to the field, will reveal more clearly how the cold ISM content of ETGs depends on environment.

The results presented in Chapter 4 support the idea that rest-frame 250μm selected high redshift galaxies are much dustier and more highly star forming than 250μm selected galaxies of a similar stellar mass at low redshift. This work could be improved by including larger samples of dusty galaxies at high redshift from HerMES. This would allow me to explore the multiwavelength properties of less massive, and less FIR luminous galaxies which are more typical of normal galaxies. I can therefore better define the evolutionary trends in dust mass and SFR with redshift, and minimise and quantify the selection effects in my sample. Deep multiwavelength imaging in HerMES fields would allow me to fully characterise the SFHs and morphologies of dusty galaxies at different redshifts. Since the dust content in galaxies is tightly linked to the gas mass, it is possible that changes in the gas content of galaxies (and therefore star-formation rate) is responsible for the dust mass evolution. Observations of cold gas in galaxies are therefore of paramount importance in order to test this hypothesis.

One limitation of most current FIR-submillimetre data is the relatively large beam size of 10–20$''$. Although the use of radio and 24μm data has been successful at identifying multiwavelength counterparts to submillimetre galaxies, this is a challenging task. This issue can be solved using high resolution ($< 2''$) millimetre imaging from ALMA to provide accurate positional information for SMGs, therefore allowing the unambiguous identification of multiwavelength counterparts. Most importantly, ALMA will be able to directly probe the gas properties of galaxies at all redshifts in unprecedented detail.

Work is also being undertaken to extend the chemical evolution modelling in Chapter 5 to dusty galaxies at low redshift (Gomez et al. in prep). One of the variables in the chemical evolution modelling is the SFH of each galaxy. To overcome this uncertainty I will apply the chemical evolution models to post-starburst galaxies in the

local Universe, where the SFH is well known from spectroscopy. This will allow me to determine the connection between stellar population age and dust content in galaxies which have recently undergone a starburst as a result of a merger. By comparing my measurements of age and dust mass to models I can put constraints on the mechanisms of dust production and the life cycle of dust in galaxies.

Using the full H-ATLAS data set it will be possible to observe how the dust mass varies as a function of time since a merger began. Observations of the cold gas will allow me to gain an insight into how the gas and dust properties are different in merging galaxies compared to secularly-evolving spiral galaxies. An understanding of the gas and dust characteristics of mergers will provide a local benchmark for comparison to hydrodynamical merger simulations, and also to studies at high redshift, where mergers may be more common. This will allow me to quantify the importance of different evolutionary stages to the chemical enrichment of galaxies at different epochs.

The multiwavelength data from *Herschel* and ALMA, and forthcoming observatories such as as JWST, SPICA and the SKA, will significantly increase our knowledge of the physical properties of galaxy populations. These data, combined with models and simulations will contribute to our understanding of the co-evolution of stars and the ISM in galaxies. This will allow us to trace the growth of galaxies from clouds of gas in dark matter halos to the diverse structures we see in the Universe today.

Appendices

Appendices

Appendix A

Dusty ETGs and passive spirals

A.1 Early-type galaxies

The following table shows the physical properties of the 42 dusty ETGs derived from the SED fitting in Chapter 3. The figures show the SDSS gri postage stamp image, the SED fit and the optical spectrum from either SDSS or the GAMA survey.

Table A.1: Properties of ETGs derived from SED fitting. The columns are (from left to right): ID, SDP ID, redshift, SDSS RA, SDSS DEC, 250μm flux in Jy, f_μ, the fraction of total dust luminosity contributed by the diffuse ISM; $\hat{\tau}_V$, total effective V-band optical depth seen by stars in birth clouds; $M_*/\mathrm{M}_\odot$, log(stellar mass); $L_\mathrm{d}^\mathrm{tot}/\mathrm{L}_\odot$, log(dust luminosity); $T_\mathrm{C}^\mathrm{ISM}$/K, temperature of the cold ISM dust component; $\hat{\tau}_V^{ISM}$, the V-band optical depth in the ambient ISM. $M_\mathrm{d}/\mathrm{M}_\odot$, log(dust mass); ψ_S/yr^{-1}, log(SSFR); $\psi/\mathrm{M}_\odot\mathrm{yr}-1$, log(SFR), $\mathrm{t_{LB}}$, log(time of last burst); $\mathrm{age_r}$, log(r-band light-weighted age of the stellar population), rest-frame $NUV-r$ colour (Section 3.3.4), density (Σ/galaxies Mpc^{-2}, see Section 3.6) Hα EW/Å(corrected for stellar absorption of 1.3Å if $>3\sigma$ detection). * indicates morphological disturbance.

ID	SDP ID	z	RA	DEC	F_{250}	f_μ	$\hat{\tau}_V$	M_*	$L_\mathrm{d}^\mathrm{tot}$	$T_\mathrm{C}^\mathrm{ISM}$	$\hat{\tau}_V^{ISM}$	M_d	ψ_S	ψ	$\mathrm{t_{LB}}$	$\mathrm{age_r}$	$NUV-r$	Σ	Hα EW
J091205.8+002656	15*	0.05	138.024	0.449	0.38	0.50	3.60	10.20	11.00	24.1	1.27	7.58	-9.47	0.74	9.04	9.08	–	2.92	27.54
J091448.7-003533	35*	0.05	138.704	-0.592	0.25	0.73	2.31	10.45	10.44	21.5	0.69	7.50	-10.40	0.07	9.38	9.52	–	1.02	8.39
J090352.0-005353	45*	0.10	135.967	-0.898	0.20	0.73	2.20	10.96	11.00	22.2	0.64	7.97	-10.34	0.62	9.25	9.41	3.77	0.06	14.87
J091051.1+020121	128	0.05	137.714	2.022	0.11	0.58	1.71	9.87	10.00	15.7	0.46	7.74	-10.06	-0.13	9.05	9.29	2.59	0.46	12.63
J090234.3+012518	159	0.12	135.643	1.421	0.11	0.93	3.02	10.96	10.72	22.9	0.88	7.75	-11.39	-0.44	9.31	9.67	5.25	1.08	5.24
J090647.7+011555	186	0.15	136.699	1.265	0.10	0.57	2.53	10.50	10.91	20.4	0.48	8.03	-9.72	0.79	8.69	9.00	3.07	0.08	24.35
J090101.2-005541	273	0.09	135.256	-0.929	0.09	0.68	1.10	10.82	10.36	19.0	0.21	7.67	-10.71	0.12	9.33	9.51	3.93	0.01	5.01
J090238.7+013253	311	0.12	135.661	1.548	0.09	0.68	2.44	10.38	10.78	23.0	0.82	7.67	-9.97	0.46	8.61	9.11	3.54	0.63	39.30
J090223.1+010709	328*	0.20	135.597	1.120	0.09	0.83	2.08	11.02	11.04	20.8	0.60	8.22	-10.63	0.44	8.90	9.31	4.34	–	8.87
J090718.9-005210	350	0.06	136.829	-0.869	0.09	0.36	1.33	9.65	10.55	24.1	0.50	6.93	-9.25	0.41	8.80	8.92	2.37	0.01	109.07
J091332.4+000631	366*	0.23	138.386	0.108	0.08	0.93	3.65	10.88	11.13	23.7	0.84	8.07	-10.96	-0.09	8.78	9.00	4.49	–	14.76
J091023.1+014023	370	0.14	137.596	1.673	0.08	0.95	3.68	10.82	10.46	15.7	0.71	8.40	-11.88	-1.08	9.48	9.80	>5.19	0.07	0.48

Table A.1 – *Continued*

ID	SDP ID	z	RA	DEC	F_{250}	f_{μ}	$\hat{\tau}_V$	M_*	$L_{\rm d}^{\rm tot}$	$T_{\rm C}^{\rm ISM}$	$\hat{\tau}_V^{ISM}$	$M_{\rm d}$	$\psi_{\rm S}$	ψ	$t_{\rm LB}$	$age_{\rm r}$	$NUV-r$	Σ	Hα EW
J090952.3-003019	451	0.05	137.468	-0.505	0.09	0.90	1.86	10.28	9.93	22.4	0.56	6.97	-11.17	-0.93	9.35	9.65	4.68	0.01	12.69
J085915.7+002329	457*	0.01	134.815	0.392	0.09	0.30	0.67	8.62	8.76	18.3	0.14	5.97	-9.51	-1.00	9.16	9.28	1.94	–	45.87
J090551.5+010752	628*	0.05	136.465	1.131	0.07	0.92	1.08	11.18	9.94	21.7	0.12	6.98	-12.27	-1.10	9.57	9.92	5.99	0.17	1.70
J090522.1-005925	786	0.10	136.343	-0.991	0.08	0.80	1.58	10.91	10.40	20.3	0.26	7.57	-11.04	-0.12	9.41	9.60	–	0.08	1.59
J090752.3+012945	1027	0.10	136.968	1.496	0.07	0.80	1.28	11.06	10.36	20.3	0.20	7.58	-11.16	-0.09	9.52	9.67	4.61	3.24	1.39
J085852.1+010624	1278	0.12	134.718	1.106	0.06	0.63	1.14	10.60	10.35	17.4	0.20	7.87	-10.47	0.18	8.86	9.24	3.67	0.50	2.21
J091037.8+015654	1372*	0.23	137.658	1.949	0.06	0.55	2.41	10.76	10.99	19.4	0.37	8.20	-9.88	0.88	8.77	9.05	3.02	–	32.32
J090929.3+020327	1409	0.15	137.373	2.057	0.06	0.92	1.85	11.17	10.49	19.4	0.31	7.86	-11.70	-0.49	9.36	9.67	5.36	0.26	1.30
J090618.0-002455	1955*	0.17	136.575	-0.415	0.05	0.66	2.30	10.92	10.68	20.1	0.38	7.85	-10.53	0.40	9.40	9.51	3.78	0.28	3.49
J090259.5+020046	2025	0.07	135.747	2.012	0.05	0.85	2.12	10.34	9.87	18.5	0.45	7.36	-11.14	-0.79	9.53	9.74	4.71	0.08	8.11
J085934.1+003629	2311*	0.26	134.892	0.608	0.05	0.90	2.02	11.20	10.81	16.3	0.47	8.64	-11.20	-0.01	9.27	9.61	4.64	–	2.47
J085842.0+010956	2364	0.12	134.677	1.166	0.06	0.86	1.49	10.96	10.42	19.5	0.36	7.73	-11.18	-0.25	9.31	9.58	4.12	0.67	3.55
J085944.2+011708	2702	0.16	134.933	1.285	0.05	0.94	2.18	10.88	10.43	17.2	0.52	8.11	-11.73	-0.86	9.37	9.66	> 4.84	0.59	1.78
J090634.8+020752	2853	0.25	136.645	2.132	0.04	0.82	1.14	11.39	10.88	19.0	0.31	8.25	-11.05	0.32	9.46	9.59	4.29	–	2.37
J090210.6+004805	2945	0.20	135.545	0.802	0.05	0.46	1.51	10.70	10.88	18.3	0.32	8.10	-9.89	0.80	9.46	9.27	2.94	–	9.97
J085727.4+010847	2959	0.07	134.364	1.146	0.05	0.78	1.51	10.30	9.84	20.1	0.31	7.09	-10.90	-0.66	9.48	9.63	4.23	2.80	5.19
J091359.4+000909	3005	0.17	138.498	0.152	0.04	0.92	1.95	10.58	10.41	17.5	0.55	8.05	-11.17	-0.55	8.91	9.38	4.78	6.02	1.30

Table A.1 – *Continued*

ID	SDP ID	z	RA	DEC	F_{250}	f_{μ}	$\hat{\tau}_V$	M_*	$L_{\rm d}^{\rm tot}$	$T_{\rm C}^{\rm ISM}$	$\hat{\tau}_V^{ISM}$	$M_{\rm d}$	$\psi_{\rm S}$	ψ	$t_{\rm LB}$	$age_{\rm r}$	$NUV-r$	Σ	Hα EW
J090236.7+011909	3252	0.09	135.653	1.320	0.06	0.95	1.58	11.03	10.14	19.7	0.19	7.49	-12.37	-1.37	9.47	9.77	5.36	0.17	0.38
J090849.5-001846	3321	0.22	137.208	-0.313	0.04	0.72	1.62	11.07	10.76	19.1	0.32	8.08	-10.65	0.40	9.39	9.50	4.00	–	2.46
J091435.2-003919	3549	0.32	138.648	-0.655	0.04	0.54	1.72	11.19	11.24	21.5	0.43	8.17	-10.09	1.09	9.41	9.36	3.00	–	6.21
J091409.6+000439	3702	0.16	138.541	0.078	0.04	0.74	2.20	10.69	10.49	17.4	0.51	8.06	-10.55	0.11	9.15	9.45	4.15	6.99	3.99
J090938.9-005753	3834	0.13	137.412	-0.966	0.04	0.94	2.16	10.56	10.22	18.8	0.50	7.67	-11.68	-1.10	9.10	9.48	> 4.96	0.04	1.30
J091315.8+004445	5088	0.23	138.315	0.746	0.04	0.71	1.56	11.05	10.68	16.9	0.22	8.31	-10.69	0.38	8.95	9.30	4.24	–	19.50
J090936.0+023324	5311	0.16	137.399	2.557	0.04	0.66	1.38	10.58	10.48	19.9	0.31	7.67	-10.35	0.19	9.28	9.41	3.48	7.44	15.18
J091054.2+005454	5382	0.16	137.726	0.916	0.04	0.69	1.68	10.80	10.48	17.6	0.33	7.95	-10.65	0.14	9.48	9.55	3.86	0.22	3.55
J091143.5+012053	5489	0.07	137.932	1.349	0.04	0.82	1.81	10.49	9.83	20.9	0.26	6.98	-11.20	-0.70	9.38	9.62	4.77	0.04	2.70
J090310.3+014233	6310	0.16	135.793	1.709	0.04	0.57	1.71	10.57	10.48	17.3	0.28	7.93	-10.25	0.31	9.45	9.47	3.16	0.11	8.74
J085916.4+005218	6337	0.24	134.819	0.873	0.04	0.59	1.68	10.66	10.80	18.6	0.32	8.10	-10.05	0.63	8.78	9.09	3.27	–	8.75
J085947.9-002143	6427*	0.12	134.95	-0.363	0.05	0.87	1.65	11.00	10.16	21.2	0.18	7.34	-11.54	-0.56	9.47	9.65	4.77	0.01	12.04
J090413.9-004405	6640*	0.20	136.058	-0.734	0.04	0.94	1.97	11.10	10.52	20.0	0.37	7.82	-12.03	-0.90	9.33	9.63	> 5.05	–	2.60

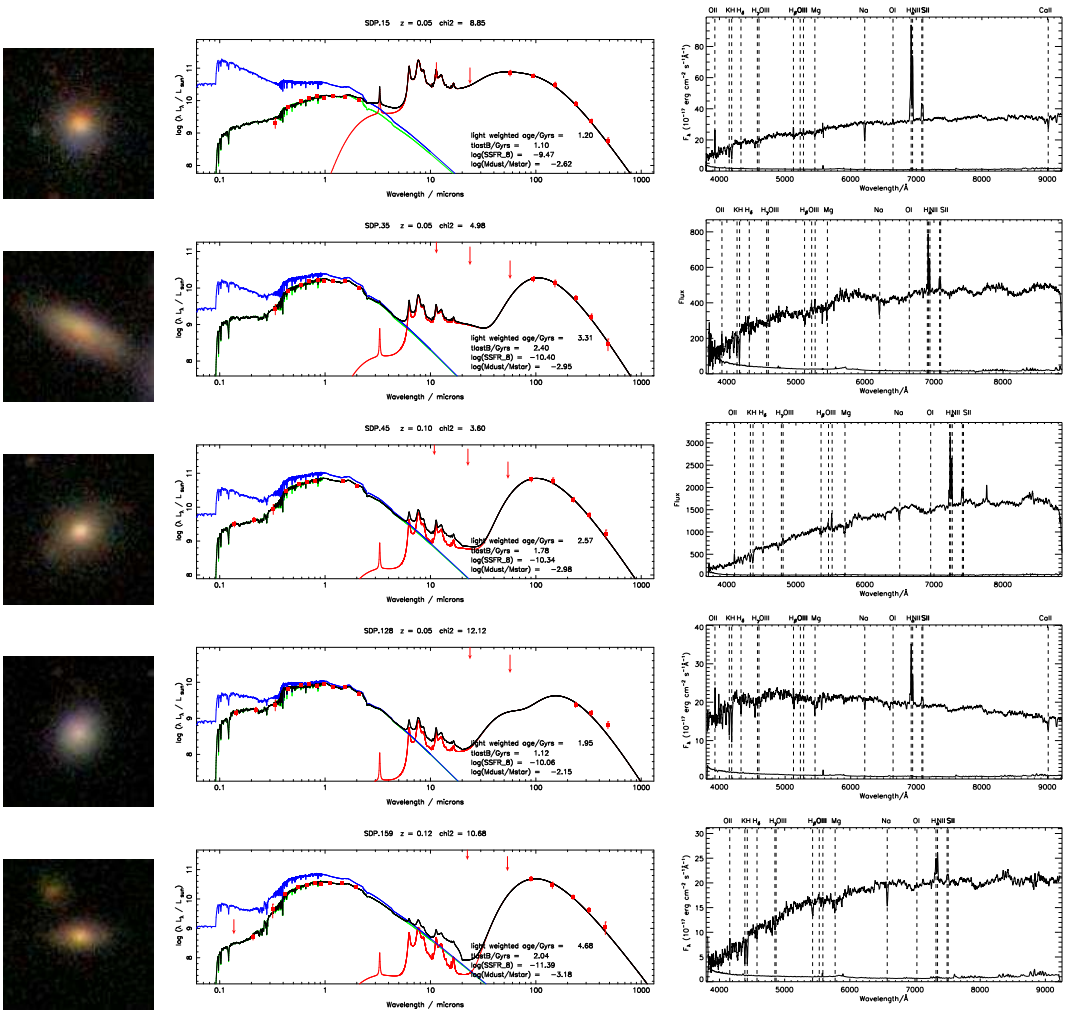

Figure A.1: Optical images, multiwavelength SEDs and optical spectra of the 42 ETGs in Chapter 3. Images are 30” on a side. The rest-frame SEDs of each ETG are shown, where red points are the observed photometry, with 5σ upper limits shown as arrows. Errors on the photometry are described in Smith *et al.* (2012b). The black line is the total best fit model, the green line is the attenuated optical model, the blue line is the unattenuated optical model, the red line is the infrared model. Spectra are from SDSS and GAMA, and the standard deviation in the spectra is also shown. The spectra have been smoothed by a boxcar of 8 pixels. Some spectra (SDP.3834) show an effect known as fibre fringing (Colless *et al.*, 2001), and were excluded from any spectral analysis.

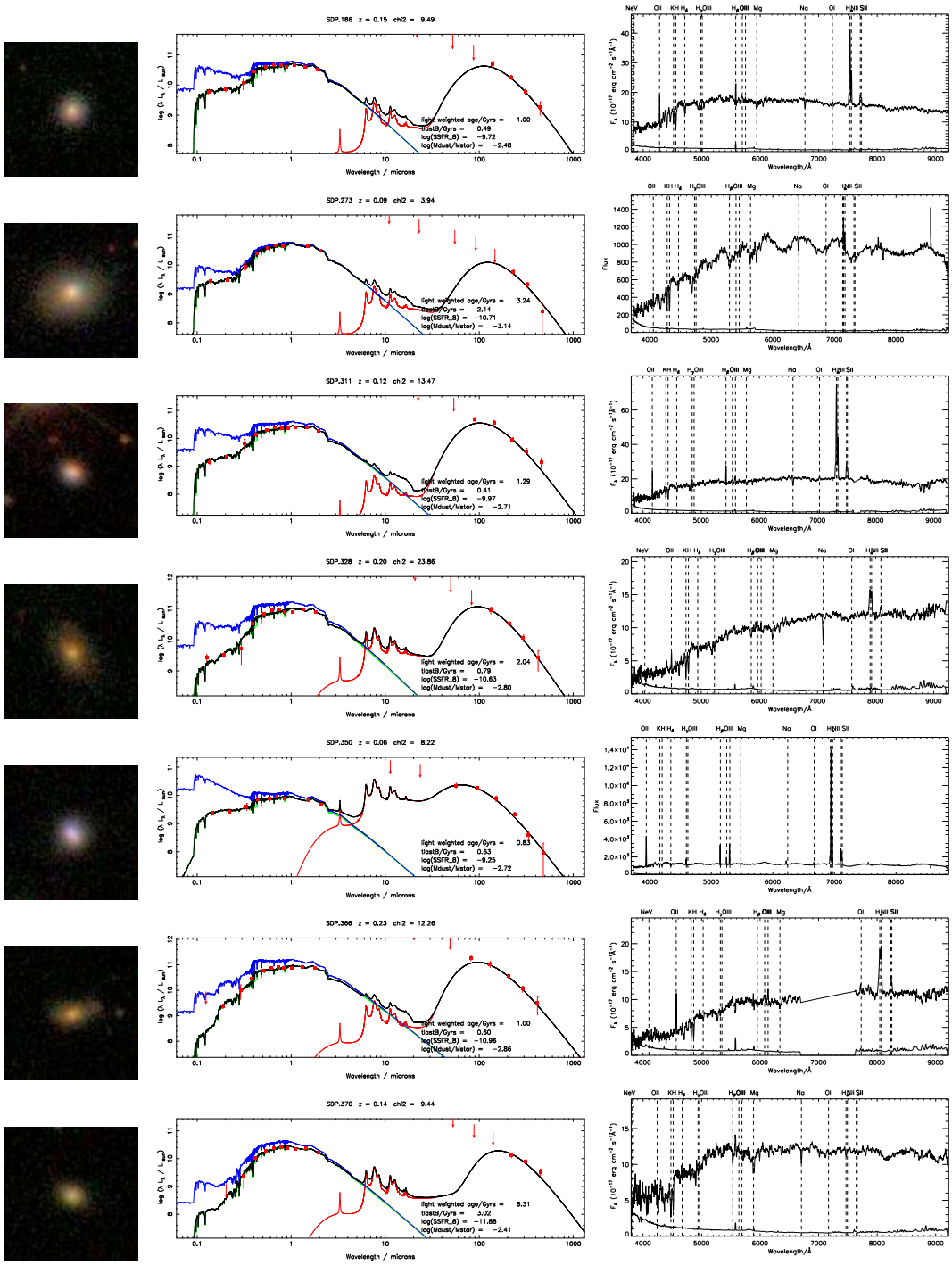
SDP.186 z = 0.15 chi2 = 9.49
light weighted age/Gyrs = 1.00
tlastB/Gyrs = 0.49
log(SSFR_8) = −9.72
log(Mdust/Mstar) = −2.48
SDP.273 z = 0.09 chi2 = 3.94
light weighted age/Gyrs = 3.24
tlastB/Gyrs = 2.14
log(SSFR_8) = −10.71
log(Mdust/Mstar) = −3.14
SDP.311 z = 0.12 chi2 = 13.47
light weighted age/Gyrs = 1.29
tlastB/Gyrs = 0.41
log(SSFR_8) = −9.97
log(Mdust/Mstar) = −2.71
SDP.328 z = 0.20 chi2 = 23.86
light weighted age/Gyrs = 2.04
tlastB/Gyrs = 0.79
log(SSFR_8) = −10.63
log(Mdust/Mstar) = −2.80
SDP.350 z = 0.06 chi2 = 8.22
light weighted age/Gyrs = 0.83
tlastB/Gyrs = 0.63
log(SSFR_8) = −9.25
log(Mdust/Mstar) = −2.72
SDP.366 z = 0.23 chi2 = 12.26
light weighted age/Gyrs = 1.00
tlastB/Gyrs = 0.60
log(SSFR_8) = −10.96
log(Mdust/Mstar) = −2.86
SDP.370 z = 0.14 chi2 = 9.44
light weighted age/Gyrs = 6.31
tlastB/Gyrs = 3.02
log(SSFR_8) = −11.88
log(Mdust/Mstar) = −2.41
Wavelength / microns
Wavelength/Å
Flux

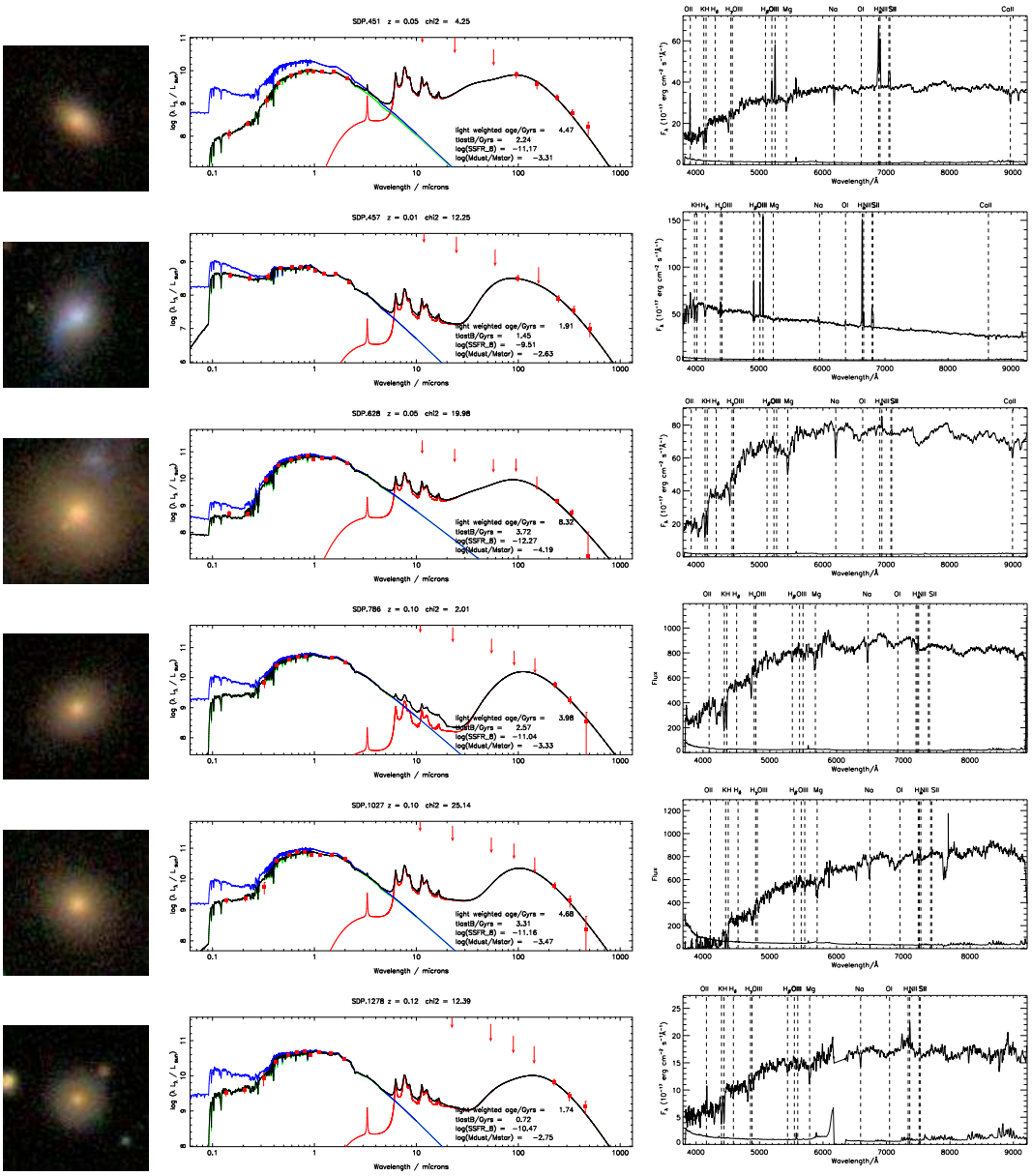
SDP.451 z = 0.05 chi2 = 4.25
light weighted age/Gyrs = 4.47
tlastB/Gyrs = 2.24
log(SSFR_8) = −11.17
log(Mdust/Mstar) = −3.31
SDP.457 z = 0.01 chi2 = 12.25
light weighted age/Gyrs = 1.91
tlastB/Gyrs = 1.45
log(SSFR_8) = −9.51
log(Mdust/Mstar) = −2.63
SDP.628 z = 0.05 chi2 = 19.98
light weighted age/Gyrs = 8.32
tlastB/Gyrs = 3.72
log(SSFR_8) = −12.27
log(Mdust/Mstar) = −4.19
SDP.786 z = 0.10 chi2 = 2.01
light weighted age/Gyrs = 3.98
tlastB/Gyrs = 2.57
log(SSFR_8) = −11.04
log(Mdust/Mstar) = −3.33
SDP.1027 z = 0.10 chi2 = 25.14
light weighted age/Gyrs = 4.68
tlastB/Gyrs = 3.31
log(SSFR_8) = −11.16
log(Mdust/Mstar) = −3.47
SDP.1278 z = 0.12 chi2 = 12.39
light weighted age/Gyrs = 1.74
tlastB/Gyrs = 0.72
log(SSFR_8) = −10.47
log(Mdust/Mstar) = −2.75
Wavelength / microns
Wavelength/Å
Flux

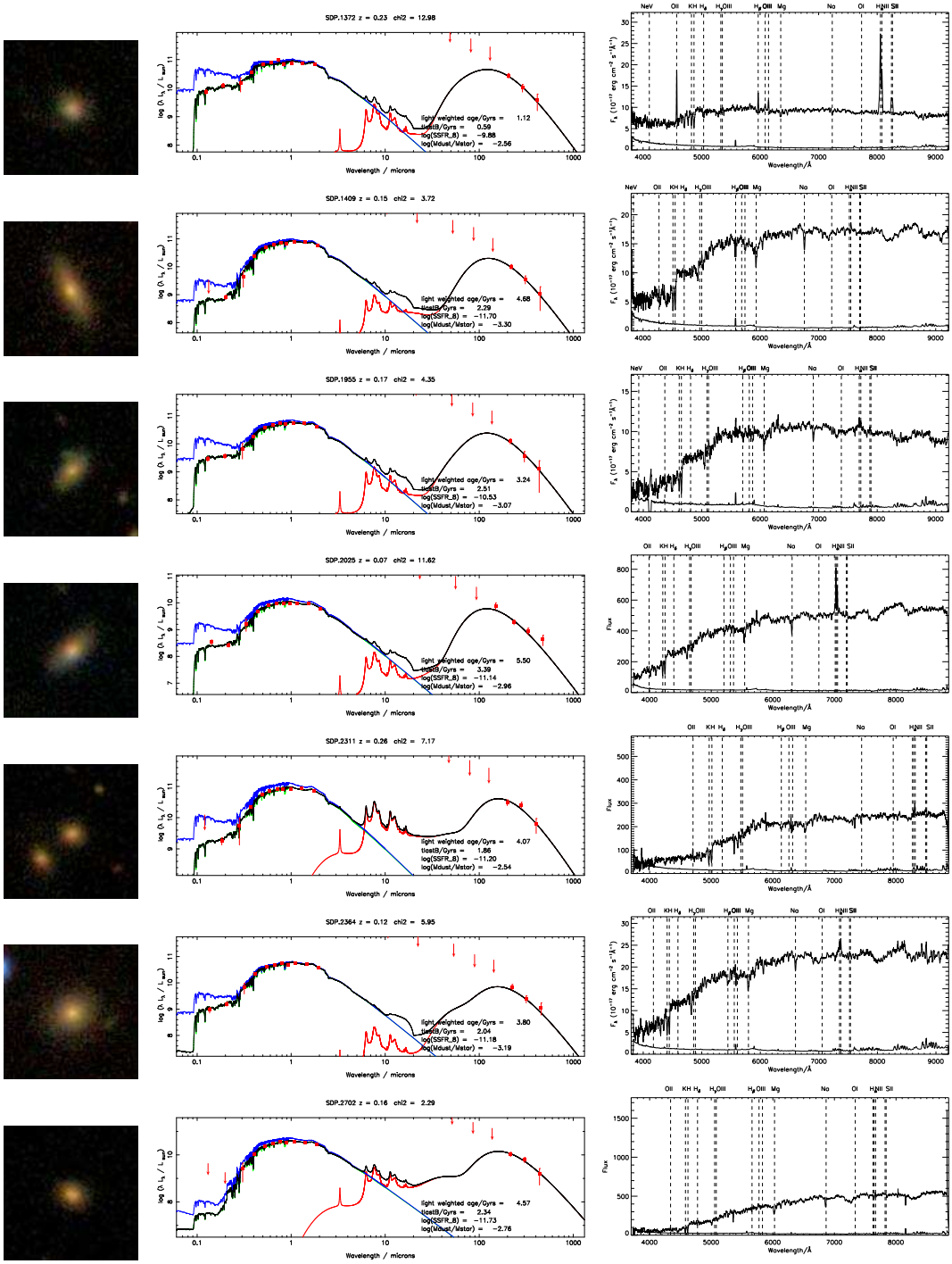
SDP.1372 z = 0.23 chi2 = 12.98
light weighted age/Gyrs = 1.12
tlastB/Gyrs = 0.59
log(SSFR_8) = −9.88
log(Mdust/Mstar) = −2.56
SDP.1409 z = 0.15 chi2 = 3.72
light weighted age/Gyrs = 4.68
tlastB/Gyrs = 2.29
log(SSFR_8) = −11.70
log(Mdust/Mstar) = −3.30
SDP.1955 z = 0.17 chi2 = 4.35
light weighted age/Gyrs = 3.24
tlastB/Gyrs = 2.51
log(SSFR_8) = −10.53
log(Mdust/Mstar) = −3.07
SDP.2025 z = 0.07 chi2 = 11.62
light weighted age/Gyrs = 5.50
tlastB/Gyrs = 3.39
log(SSFR_8) = −11.14
log(Mdust/Mstar) = −2.96
SDP.2311 z = 0.26 chi2 = 7.17
light weighted age/Gyrs = 4.07
tlastB/Gyrs = 1.86
log(SSFR_8) = −11.20
log(Mdust/Mstar) = −2.54
SDP.2364 z = 0.12 chi2 = 5.95
light weighted age/Gyrs = 3.80
tlastB/Gyrs = 2.04
log(SSFR_8) = −11.18
log(Mdust/Mstar) = −3.19
SDP.2702 z = 0.16 chi2 = 2.29
light weighted age/Gyrs = 4.57
tlastB/Gyrs = 2.34
log(SSFR_8) = −11.73
log(Mdust/Mstar) = −2.76
Wavelength / microns
Wavelength/Å
Flux

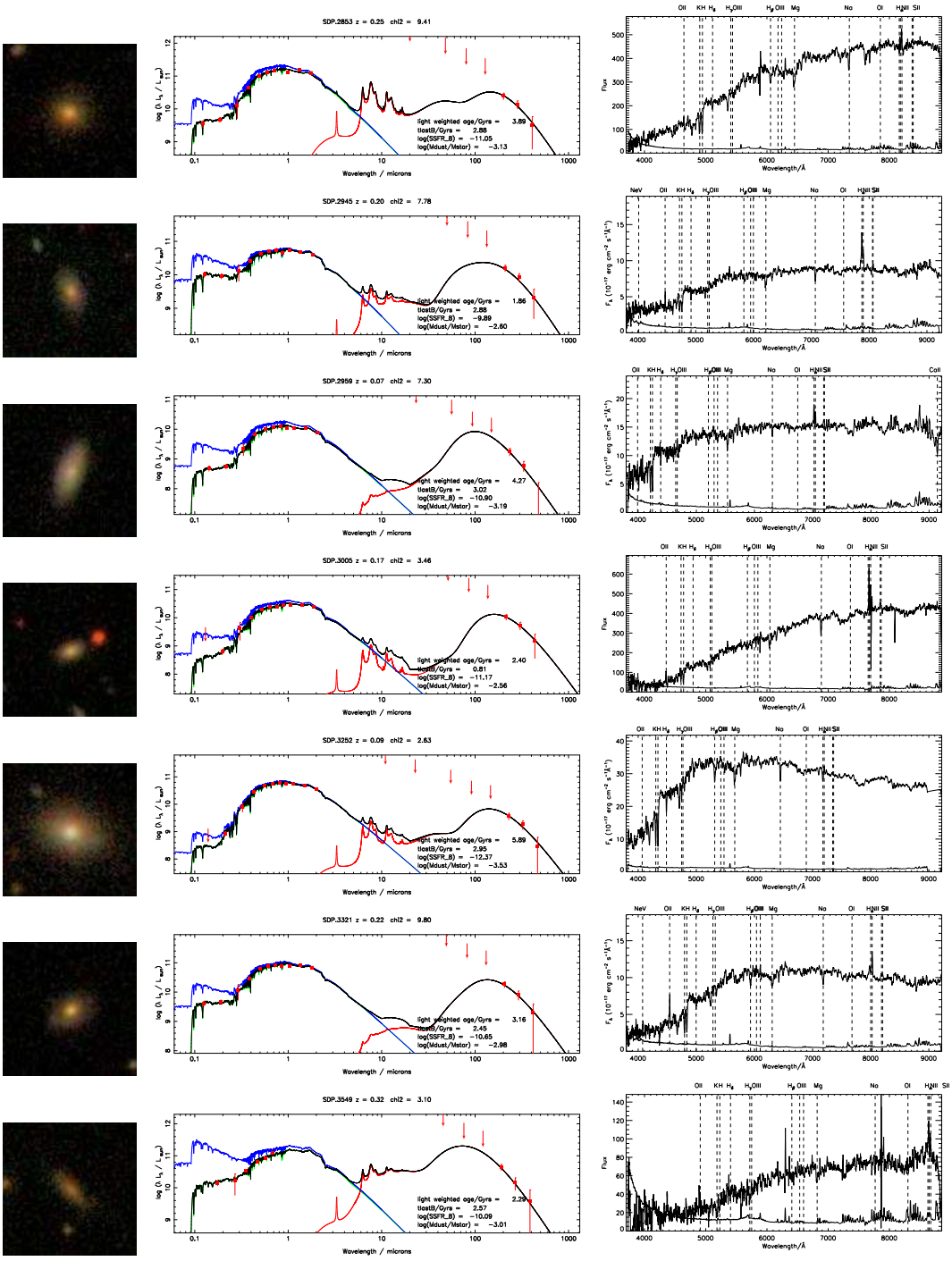
SDP.2853 z = 0.25 chi2 = 9.41
light weighted age/Gyrs = 3.89
tlostB/Gyrs = 2.86
log(SSFR_8) = −11.05
log(Mdust/Mstar) = −3.13
SDP.2945 z = 0.20 chi2 = 7.78
light weighted age/Gyrs = 1.86
tlostB/Gyrs = 2.88
log(SSFR_8) = −9.89
log(Mdust/Mstar) = −2.60
SDP.2959 z = 0.07 chi2 = 7.30
light weighted age/Gyrs = 4.27
tlostB/Gyrs = 3.02
log(SSFR_8) = −10.90
log(Mdust/Mstar) = −3.19
SDP.3005 z = 0.17 chi2 = 3.46
light weighted age/Gyrs = 2.40
tlostB/Gyrs = 0.81
log(SSFR_8) = −11.17
log(Mdust/Mstar) = −2.56
SDP.3252 z = 0.09 chi2 = 2.63
light weighted age/Gyrs = 5.89
tlostB/Gyrs = 2.95
log(SSFR_8) = −12.37
log(Mdust/Mstar) = −3.53
SDP.3321 z = 0.22 chi2 = 9.80
light weighted age/Gyrs = 3.16
tlostB/Gyrs = 2.45
log(SSFR_8) = −10.65
log(Mdust/Mstar) = −2.98
SDP.3549 z = 0.32 chi2 = 3.10
light weighted age/Gyrs = 2.29
tlostB/Gyrs = 2.57
log(SSFR_8) = −10.09
log(Mdust/Mstar) = −3.01
Wavelength / microns
Wavelength/Å
Flux

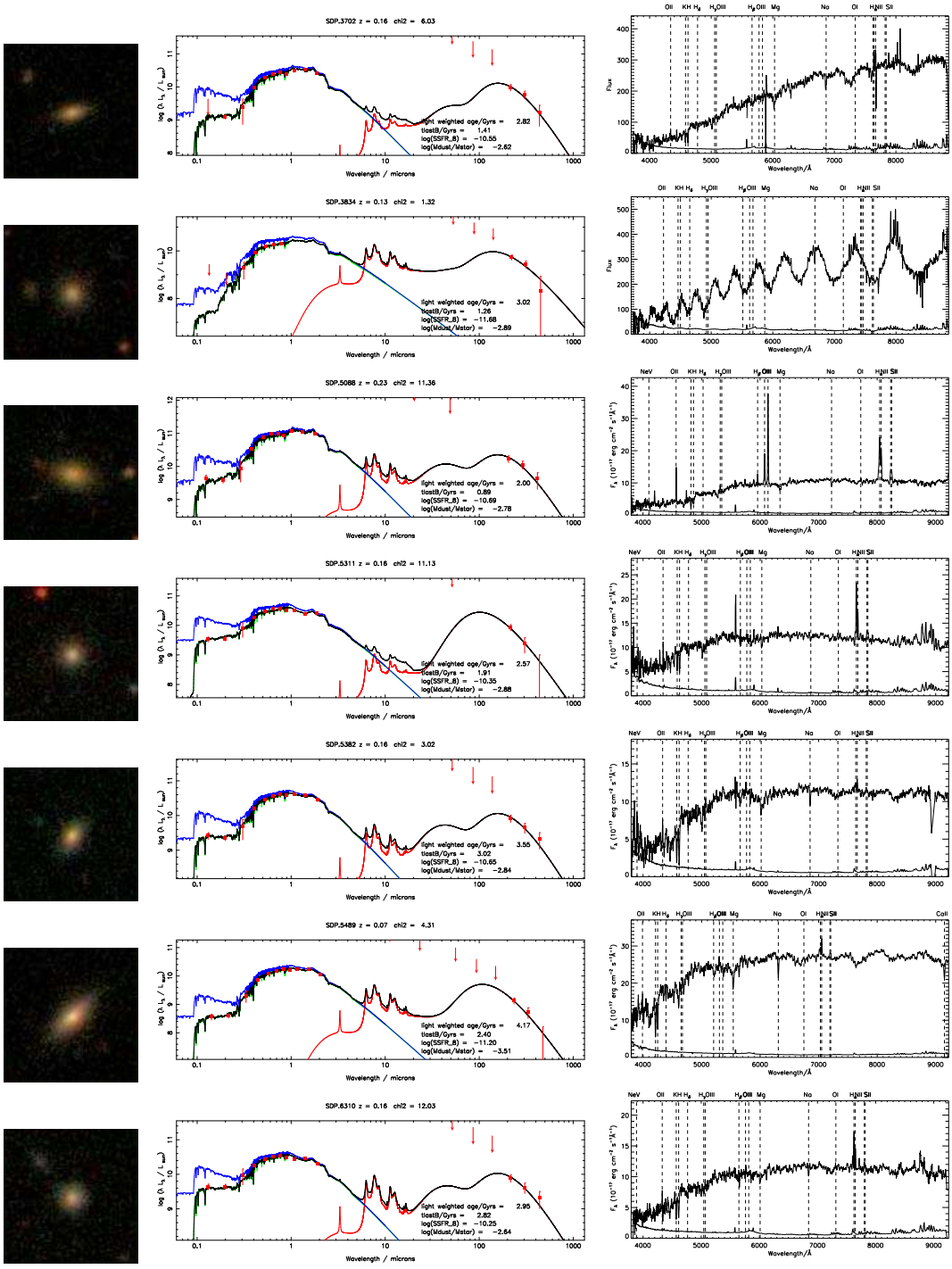
SDP.3702 z = 0.16 chi2 = 6.03
light weighted age/Gyrs = 2.82
tlastB/Gyrs = 1.41
log(SSFR_8) = −10.55
log(Mdust/Mstar) = −2.62
SDP.3834 z = 0.13 chi2 = 1.32
light weighted age/Gyrs = 3.02
tlastB/Gyrs = 1.26
log(SSFR_8) = −11.68
log(Mdust/Mstar) = −2.89
SDP.5088 z = 0.23 chi2 = 11.36
light weighted age/Gyrs = 2.06
tlastB/Gyrs = 0.89
log(SSFR_8) = −10.69
log(Mdust/Mstar) = −2.78
SDP.5311 z = 0.16 chi2 = 11.13
light weighted age/Gyrs = 2.57
tlastB/Gyrs = 1.91
log(SSFR_8) = −10.35
log(Mdust/Mstar) = −2.88
SDP.5382 z = 0.16 chi2 = 3.02
light weighted age/Gyrs = 3.55
tlastB/Gyrs = 3.02
log(SSFR_8) = −10.65
log(Mdust/Mstar) = −2.84
SDP.5489 z = 0.07 chi2 = 4.31
light weighted age/Gyrs = 4.17
tlastB/Gyrs = 2.40
log(SSFR_8) = −11.20
log(Mdust/Mstar) = −3.51
SDP.6310 z = 0.16 chi2 = 12.03
light weighted age/Gyrs = 2.95
tlastB/Gyrs = 2.82
log(SSFR_8) = −10.25
log(Mdust/Mstar) = −2.64
Wavelength / microns
Wavelength/Å
Flux

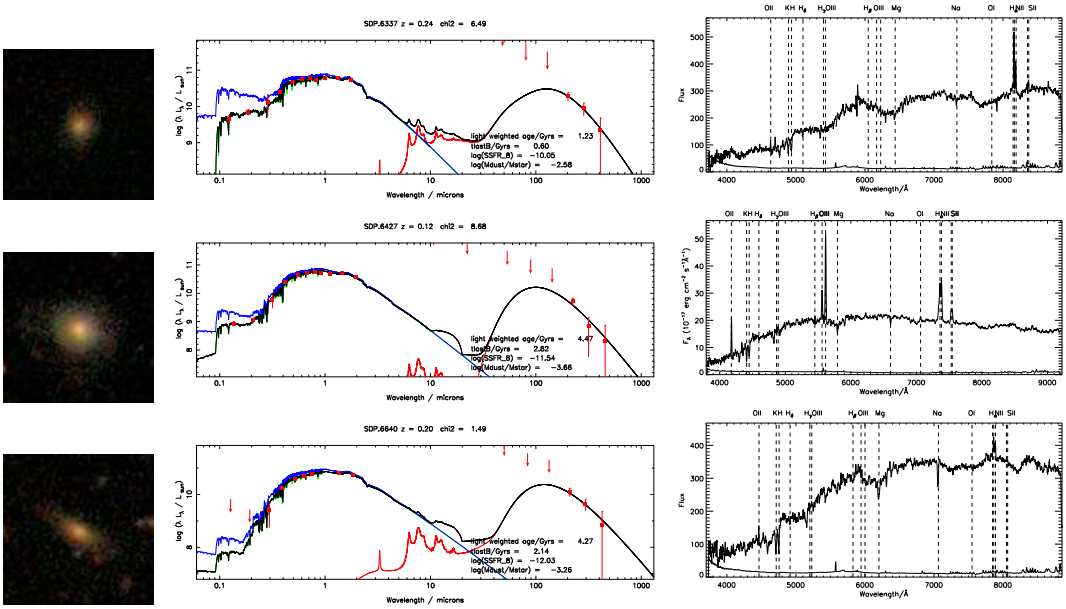
SDP.6337 z = 0.24 chi2 = 6.49
light weighted age/Gyrs = 1.23
tlastB/Gyrs = 0.60
log(SSFR_8) = −10.05
log(Mdust/Mstar) = −2.58
Wavelength / microns
OII KH Hδ H20III Hβ OIII Mg No OI H2NII SII
Flux
Wavelength/Å
SDP.6427 z = 0.12 chi2 = 8.68
light weighted age/Gyrs = 4.47
tlastB/Gyrs = 2.82
log(SSFR_8) = −11.54
log(Mdust/Mstar) = −3.66
Wavelength / microns
OII KH Hδ H20III Hβ OIII Mg No OI H2NII SII
Wavelength/Å
SDP.6640 z = 0.20 chi2 = 1.49
light weighted age/Gyrs = 4.27
tlastB/Gyrs = 2.14
log(SSFR_8) = −12.03
log(Mdust/Mstar) = −3.26
Wavelength / microns
OII KH Hδ H20III Hβ OIII Mg No OI H2NII SII
Flux
Wavelength/Å

A.2 Passive spirals

The following table shows the physical properties of the 19 passive spirals derived from the SED fitting in Chapter 3. The figures show the SDSS gri postage stamp image, the SED fit and the optical spectrum from either SDSS or the GAMA survey.

Table A.2: Properties of passive spirals in Chapter 3 derived from SED fitting. The columns are (from left to right): ID, SDP ID, redshift, SDSS RA, SDSS DEC, 250μm flux in Jy, f_μ , the fraction of total dust luminosity contributed by the diffuse ISM; $\hat{\tau}_V$, total effective V-band optical depth seen by stars in birth clouds; $M_*/\mathrm{M}_\odot$, log(stellar mass); $L_\mathrm{d}^\mathrm{tot}/\mathrm{L}_\odot$, log(dust luminosity); $T_\mathrm{C}^\mathrm{ISM}$/K, temperature of the cold ISM dust component; $\hat{\tau}_V^{ISM}$, the V-band optical depth in the ambient ISM. $M_\mathrm{d}/\mathrm{M}_\odot$, log(dust mass); ψ_S/yr^{-1}, log(SSFR); $\psi/\mathrm{M}_\odot\mathrm{yr}{-}1$, log(SFR), $\mathrm{t_{LB}}$, log(time of last burst); $\mathrm{age_r}$, log(r-band light-weighted age of the stellar population), rest-frame $NUV-r$ colour (Section 3.3.4), density (Σ/galaxies Mpc^{-2}, see Section 3.6) Hα EW/Å(corrected for stellar absorption of 1.3Å if $>3\sigma$ detection).

ID	SDP ID	z	RA	DEC	F_{250}	f_μ	$\hat{\tau}_V$	M_*	$L_\mathrm{d}^\mathrm{tot}$	$T_\mathrm{C}^\mathrm{ISM}$	$\hat{\tau}_V^{ISM}$	M_d	ψ_S	ψ	$\mathrm{t_{LB}}$	$\mathrm{age_r}$	$NUV{-}r$	Σ	Hα EW
J085828.5+003814	30	0.05	134.619	0.637	0.28	0.87	4.22	10.84	10.39	21.7	0.45	7.50	-11.17	-0.30	9.57	9.77	4.73	0.39	14.77
J090038.0+012810	77	0.05	135.158	1.470	0.19	0.79	1.44	10.86	10.04	17.5	0.17	7.64	-11.14	-0.31	9.39	9.83	4.33	0.19	1.00
J085946.7-000020	143	0.05	134.945	-0.006	0.15	0.85	1.80	10.78	10.15	19.5	0.26	7.45	-11.22	-0.48	9.41	9.65	4.69	0.39	0.57
J090911.8+000029	271	0.08	137.299	0.008	0.12	0.90	2.04	10.53	10.16	18.3	0.52	7.66	-11.25	-0.72	9.18	9.53	5.11	0.18	2.45
J090648.9-005059	372	0.16	136.704	-0.850	0.09	0.94	2.05	11.02	10.73	19.9	0.56	8.05	-11.63	-0.56	9.08	9.45	5.45	0.08	6.06
J090312.4-004509	1544	0.05	135.803	-0.753	0.09	0.67	1.62	10.69	9.88	18.5	0.13	7.23	-11.11	-0.40	9.56	9.73	4.30	–	0.62
J090944.5+022100	1773	0.05	137.435	2.350	0.06	0.94	1.57	10.50	9.78	22.7	0.25	6.76	-12.10	-1.57	8.93	9.62	4.70	0.56	1.63
J090622.3+010014	1888	0.07	136.593	1.004	0.06	0.85	1.13	10.50	9.87	19.8	0.19	7.15	-11.29	-0.76	9.42	9.73	–	0.08	1.01
J085827.1+010426	2547	0.07	134.613	1.074	0.05	0.95	1.66	10.34	9.61	19.8	0.27	6.98	-12.19	-1.91	9.44	9.71	5.29	6.78	2.01
J090543.6+010754	2612	0.05	136.432	1.132	0.05	0.92	2.00	9.94	9.45	20.3	0.40	6.74	-11.53	-1.56	9.19	9.56	5.08	0.22	4.25
J090547.8+001136	3578	0.16	136.450	0.193	0.04	0.92	2.24	10.95	10.48	20.0	0.56	7.78	-11.55	-0.58	9.36	9.63	>4.57	0.14	1.64
J091311.5+001619	3935	0.17	138.299	0.274	0.04	0.94	2.44	10.71	10.27	18.9	0.46	7.72	-11.72	-1.07	9.36	9.69	>4.73	0.28	69.03
J085738.2+010740	4548	0.07	134.410	1.128	0.04	0.91	1.72	10.36	9.72	20.6	0.28	6.96	-11.56	-1.21	9.20	9.58	4.97	4.37	4.65
J090646.2-004453	4639	0.16	136.693	-0.749	0.04	0.85	1.51	10.99	10.48	21.2	0.30	7.57	-11.21	-0.17	9.48	9.73	–	0.17	1.30
J091144.5+012952	4859	0.17	137.936	1.499	0.04	0.88	2.57	10.85	10.59	21.4	0.79	7.70	-11.04	-0.21	9.32	9.59	>4.29	2.22	2.05
J090013.7+004139	4964	0.24	135.057	0.693	0.04	0.94	2.33	10.49	10.48	17.6	0.48	8.15	-11.41	-0.93	8.70	9.05	4.26	–	9.60
J090707.3+000805	5108	0.10	136.78	0.135	0.04	0.88	2.00	10.21	9.88	18.1	0.47	7.41	-11.13	-0.90	9.13	9.52	4.59	0.09	17.53
J091230.6-005442	5226	0.16	138.128	-0.913	0.04	0.91	2.07	10.75	10.40	19.3	0.44	7.79	-11.26	-0.50	9.10	9.49	4.85	3.12	1.30
J085934.4-000456	7324	0.17	134.895	-0.082	0.03	0.92	1.97	10.73	10.28	19.6	0.43	7.65	-11.50	-0.75	9.24	9.56	>4.72	2.12	2.55

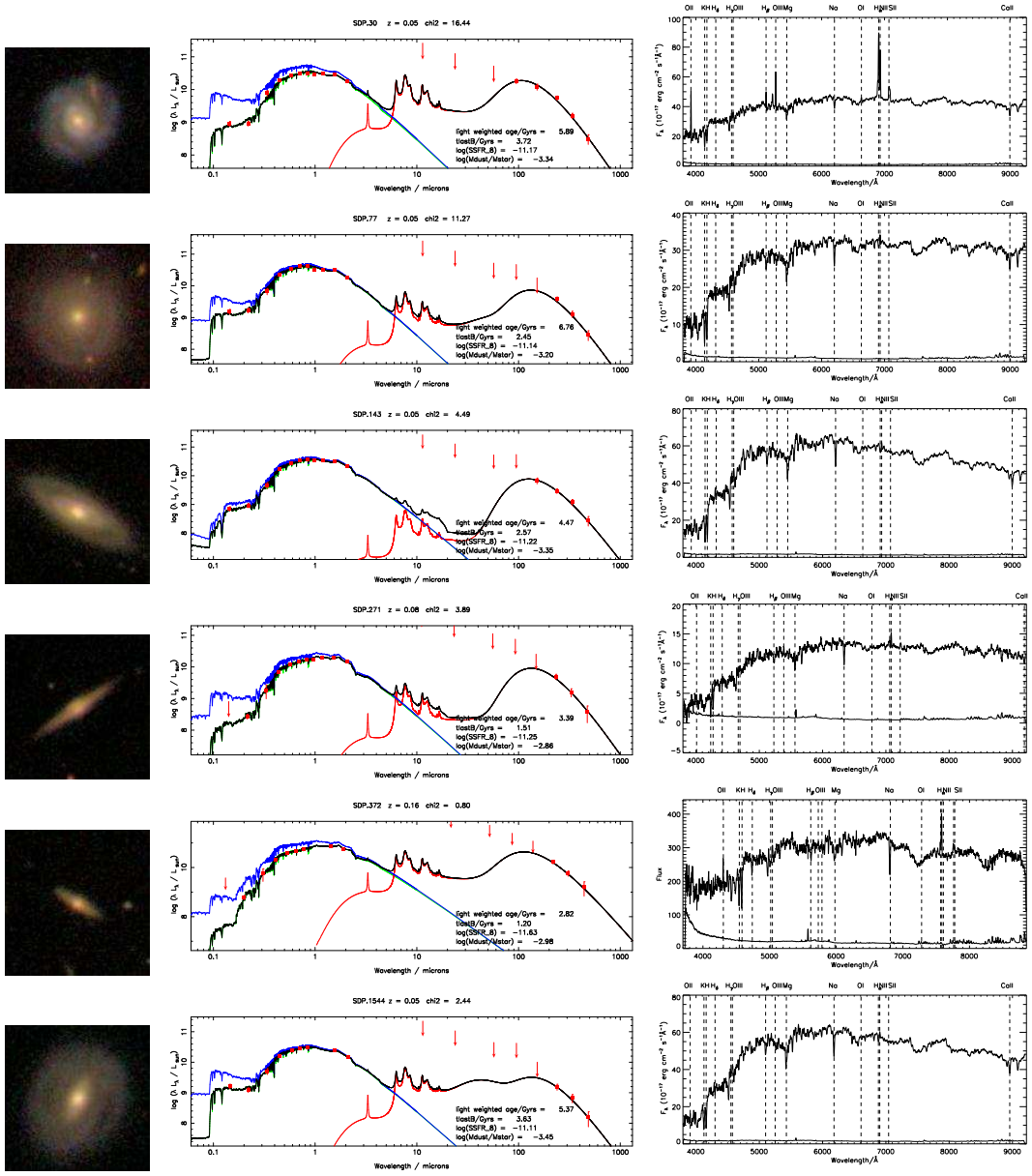

Figure A.2: Optical images, multiwavelength SEDs and optical spectra of the 19 passive spirals in our sample. Images are 40” on a side. The rest-frame SEDs of each passive spiral are shown, where red points are the observed photometry, with 5σ upper limits shown as arrows. Errors on the photometry are described in Smith *et al.* (2012b). The black line is the total best fit SED model, the green line is the attenuated optical model, the blue line is the unattenuated optical model, the red line is the infrared model. Spectra are from SDSS and GAMA, and the standard deviation in the spectra is also shown. The spectra have been smoothed by a boxcar of 8 pixels. Some spectra (SDP.4639) show an effect known as fibre fringing (Colless *et al.*, 2001), and were excluded from any spectral analysis.

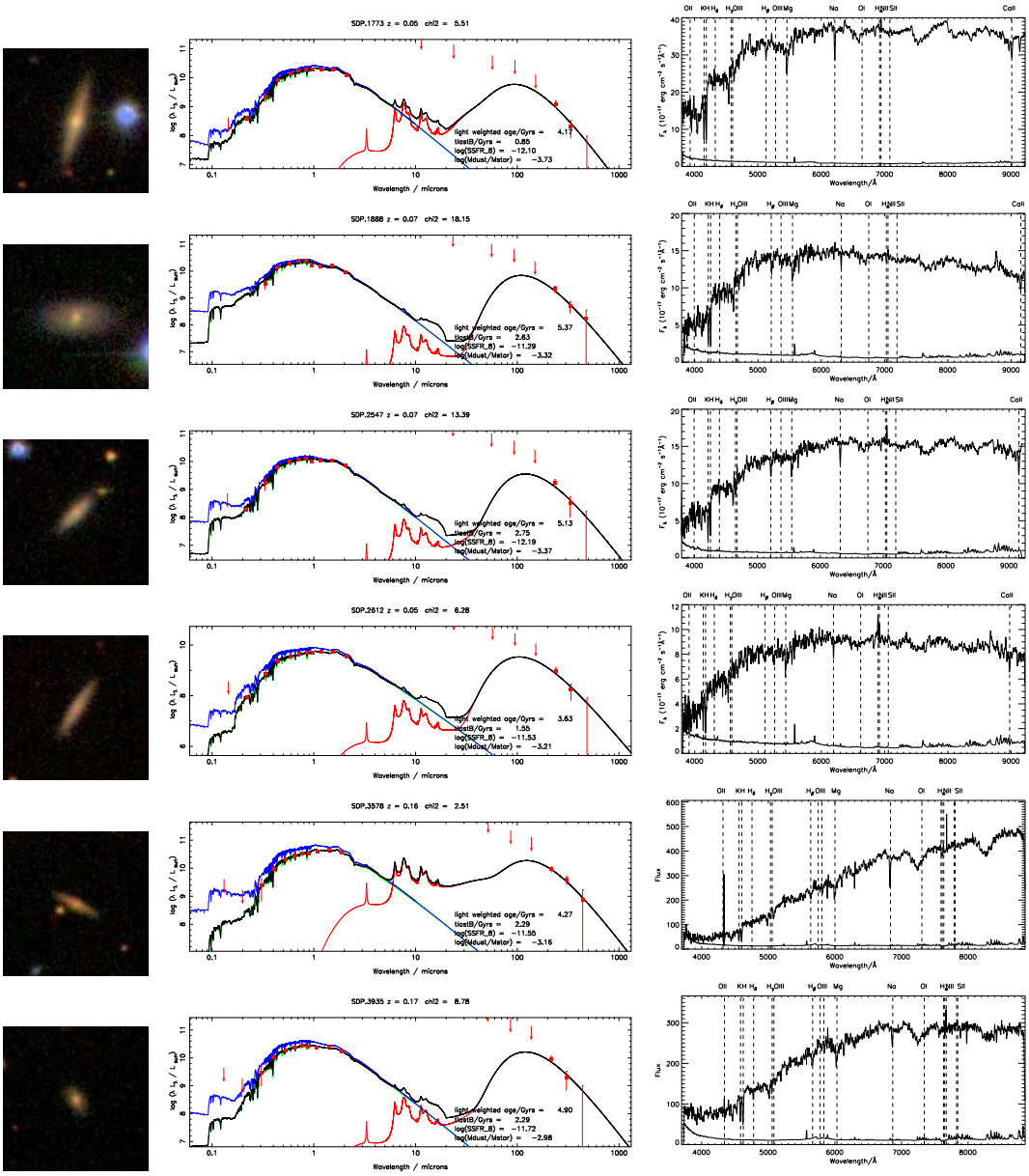
SDP.1773 z = 0.05 chi2 = 5.51
light weighted age/Gyrs = 4.17
tlastB/Gyrs = 0.85
log(SSFR_8) = −12.10
log(Mdust/Mstar) = −3.73
SDP.1888 z = 0.07 chi2 = 18.15
light weighted age/Gyrs = 5.37
tlastB/Gyrs = 2.63
log(SSFR_8) = −11.29
log(Mdust/Mstar) = −3.32
SDP.2547 z = 0.07 chi2 = 13.39
light weighted age/Gyrs = 5.13
tlastB/Gyrs = 2.75
log(SSFR_8) = −12.19
log(Mdust/Mstar) = −3.37
SDP.2612 z = 0.05 chi2 = 6.28
light weighted age/Gyrs = 3.63
tlastB/Gyrs = 1.55
log(SSFR_8) = −11.53
log(Mdust/Mstar) = −3.21
SDP.3578 z = 0.16 chi2 = 2.51
light weighted age/Gyrs = 4.27
tlastB/Gyrs = 2.29
log(SSFR_8) = −11.55
log(Mdust/Mstar) = −3.16
SDP.3935 z = 0.17 chi2 = 8.78
light weighted age/Gyrs = 4.90
tlastB/Gyrs = 2.29
log(SSFR_8) = −11.72
log(Mdust/Mstar) = −2.98
Wavelength / microns
Wavelength/Å
Flux

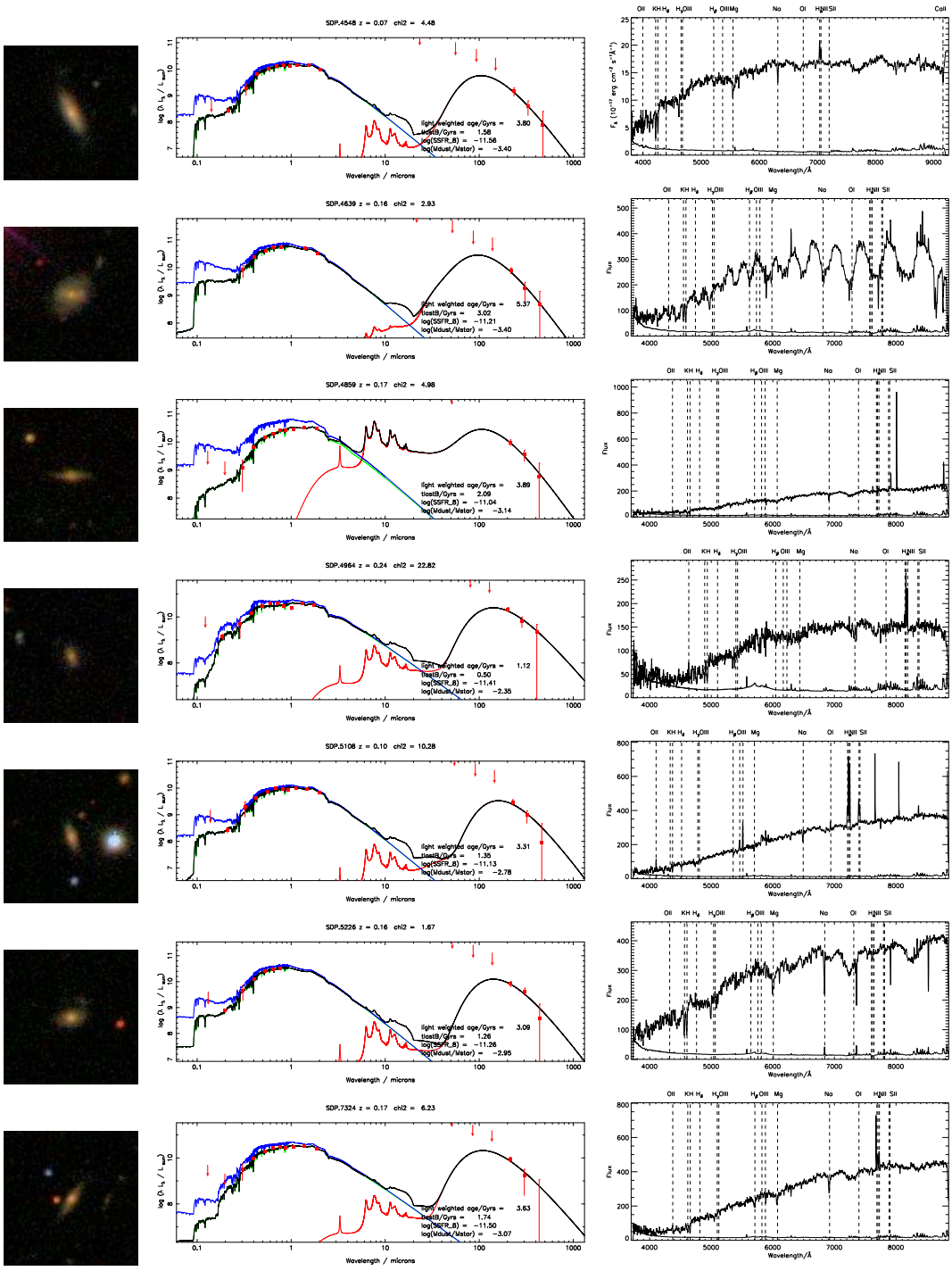
SDP.4548 z = 0.07 chi2 = 4.48
light weighted age/Gyrs = 3.80
tlast8/Gyrs = 1.58
log(SSFR_8) = −11.56
log(Mdust/Mstar) = −3.40
SDP.4639 z = 0.16 chi2 = 2.93
light weighted age/Gyrs = 5.37
tlast8/Gyrs = 3.02
log(SSFR_8) = −11.21
log(Mdust/Mstar) = −3.40
SDP.4859 z = 0.17 chi2 = 4.98
light weighted age/Gyrs = 3.89
tlast8/Gyrs = 2.09
log(SSFR_8) = −11.04
log(Mdust/Mstar) = −3.14
SDP.4964 z = 0.24 chi2 = 22.82
light weighted age/Gyrs = 1.12
tlast8/Gyrs = 0.50
log(SSFR_8) = −11.41
log(Mdust/Mstar) = −2.35
SDP.5108 z = 0.10 chi2 = 10.28
light weighted age/Gyrs = 3.31
tlast8/Gyrs = 1.35
log(SSFR_8) = −11.13
log(Mdust/Mstar) = −2.78
SDP.5226 z = 0.16 chi2 = 1.67
light weighted age/Gyrs = 3.09
tlast8/Gyrs = 1.26
log(SSFR_8) = −11.26
log(Mdust/Mstar) = −2.95
SDP.7324 z = 0.17 chi2 = 6.23
light weighted age/Gyrs = 3.63
tlast8/Gyrs = 1.74
log(SSFR_8) = −11.50
log(Mdust/Mstar) = −3.07
Wavelength / microns
Wavelength/Å
Flux

A.3 Summary of mean physical properties

The following table summarises the mean physical properties derived from stacking of PDFs for the different populations studied in Chapter 3.

Table A.3: Summary of mean physical properties derived from stacking of PDFs for the different populations studied in Chapter 3. The parameters are: f_μ, the fraction of total dust luminosity contributed by the diffuse ISM; $M_*/\mathrm{M}_\odot$, log(stellar mass); $M_\mathrm{d}/\mathrm{M}_\odot$, log(dust mass); M_d/M_*, log(dust to stellar mass ratio); $L_\mathrm{d}^\mathrm{tot}/\mathrm{L}_\odot$, log(dust luminosity); $T_\mathrm{C}^\mathrm{ISM}$/K, temperature of the cold ISM dust component; $\hat{\tau}_V$, total effective V-band optical depth seen by stars in birth clouds; $\hat{\tau}_V^{ISM}$, the V-band optical depth in the ambient ISM, $\psi_\mathrm{S}/\mathrm{yr}^{-1}$, log(SSFR); $\psi/\mathrm{M}_\odot\mathrm{yr}^{-1}$, log(SFR), $\mathrm{t_{LB}}$, log(time of last burst); $\mathrm{age_r}$, log(r-band light-weighted age of the stellar population). For each parameter, we use the first moment of the average PDF to estimate the mean for the population. We can estimate the variance on the population mean as the second moment of the average PDF minus the mean squared, divided by the number of galaxies in the sample. The error on the mean is simply the square root of the population variance. The errors for logarithmic parameters are in dex. The mean parameters from the infrared part of the SED and energy balance parameters are not determined for the control sample, since we only have constraints from upper limits on the FIR-submillimetre flux.

Parameter	H-ATLAS spiral	H-ATLAS ETG	Normal spiral	Passive spiral	Control spiral	Control ETG
f_μ	0.59 ± 0.01	0.74 ± 0.02	0.58 ± 0.01	0.87 ± 0.02	–	–
$\log M_*$	10.29 ± 0.02	10.69 ± 0.08	10.27 ± 0.02	10.62 ± 0.07	10.15 ± 0.03	10.77 ± 0.03
$\log M_\mathrm{d}$	7.72 ± 0.02	7.74 ± 0.08	7.73 ± 0.02	7.47 ± 0.10	–	–
$\log M_\mathrm{d}/M_*$	-2.57 ± 0.02	-2.95 ± 0.07	-2.54 ± 0.02	-3.16 ± 0.09	–	–
$\log L_\mathrm{d}^\mathrm{tot}$	10.53 ± 0.02	10.48 ± 0.07	10.55 ± 0.02	10.14 ± 0.09	–	–
$T_\mathrm{C}^\mathrm{ISM}$	19.7 ± 0.1	19.8 ± 0.5	19.7 ± 0.1	19.8 ± 0.6	–	–
$\hat{\tau}_V$	2.28 ± 0.07	2.28 ± 0.23	2.28 ± 0.07	2.34 ± 0.37	1.66 ± 0.08	1.61 ± 0.10
$\hat{\tau}_V^{ISM}$	0.47 ± 0.01	0.43 ± 0.04	0.48 ± 0.02	0.41 ± 0.05	0.24 ± 0.01	0.20 ± 0.01
$\log\psi_\mathrm{S}$	-9.99 ± 0.03	-10.85 ± 0.14	-9.92 ± 0.03	-11.59 ± 0.18	-10.58 ± 0.07	-11.92 ± 0.07
$\log\psi$	0.30 ± 0.03	-0.16 ± 0.12	0.36 ± 0.03	-0.97 ± 0.19	-0.43 ± 0.05	-1.16 ± 0.07
$\log\mathrm{t_{LB}}$	8.70 ± 0.07	9.04 ± 0.18	8.68 ± 0.08	9.26 ± 0.10	8.87 ± 0.07	9.39 ± 0.03
$\log\mathrm{age_r}$	9.21 ± 0.02	9.45 ± 0.05	9.19 ± 0.02	9.59 ± 0.05	9.32 ± 0.02	9.67 ± 0.01

Appendix B

The SEDs of high redshift submillimetre galaxies

B.1 SED fits

Here I present the panchromatic SED fits for the sample of 30 submillimetre galaxies studied in Chapter 4, using the composite MAGPHYS libraries described in Chapter 2.

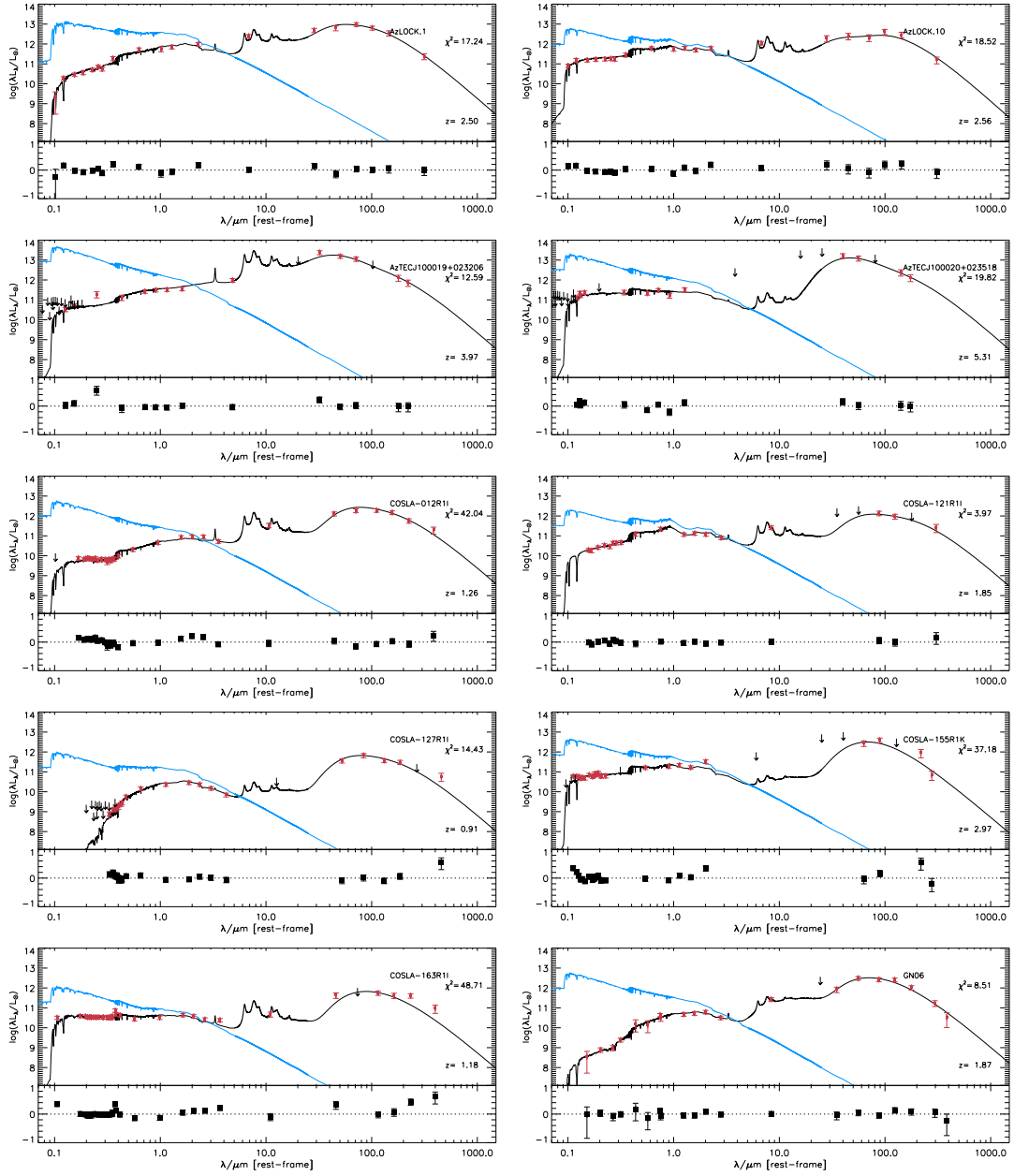

Figure B.1: Multiwavelength SEDs of the 30 submillimetre galaxies in my sample (including seven sources rejected due to bad fits), with observed photometry (red points) from the rest-frame UV to the submillimetre. Upper limits are shown as arrows and errors on the photometry are described in Section 4.2.2. The black line is the best-fit model SED and the blue line is the unattenuated optical model. The residuals of the fit are shown in the panel below each SED.

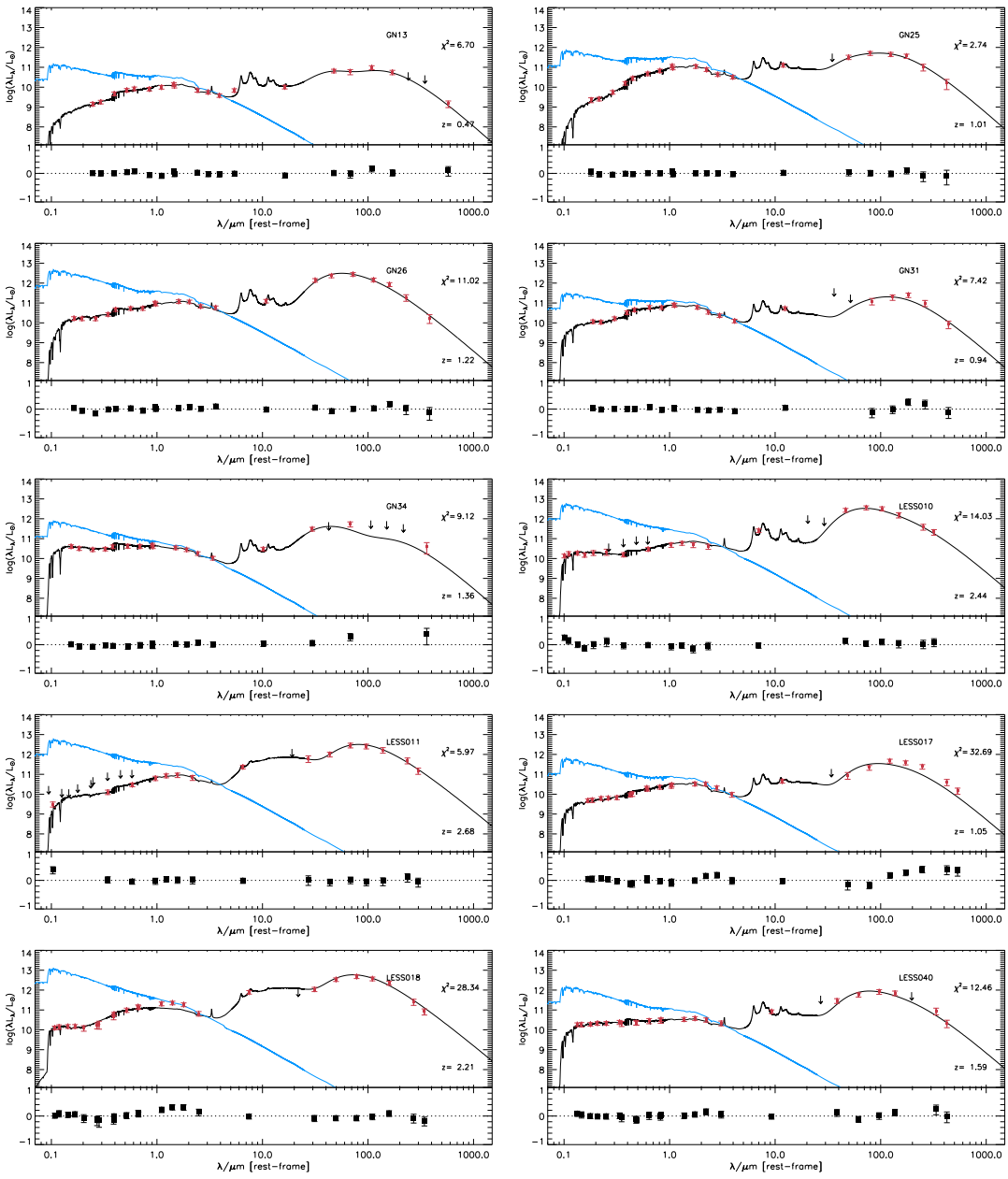

Figure B.1 – *continued*

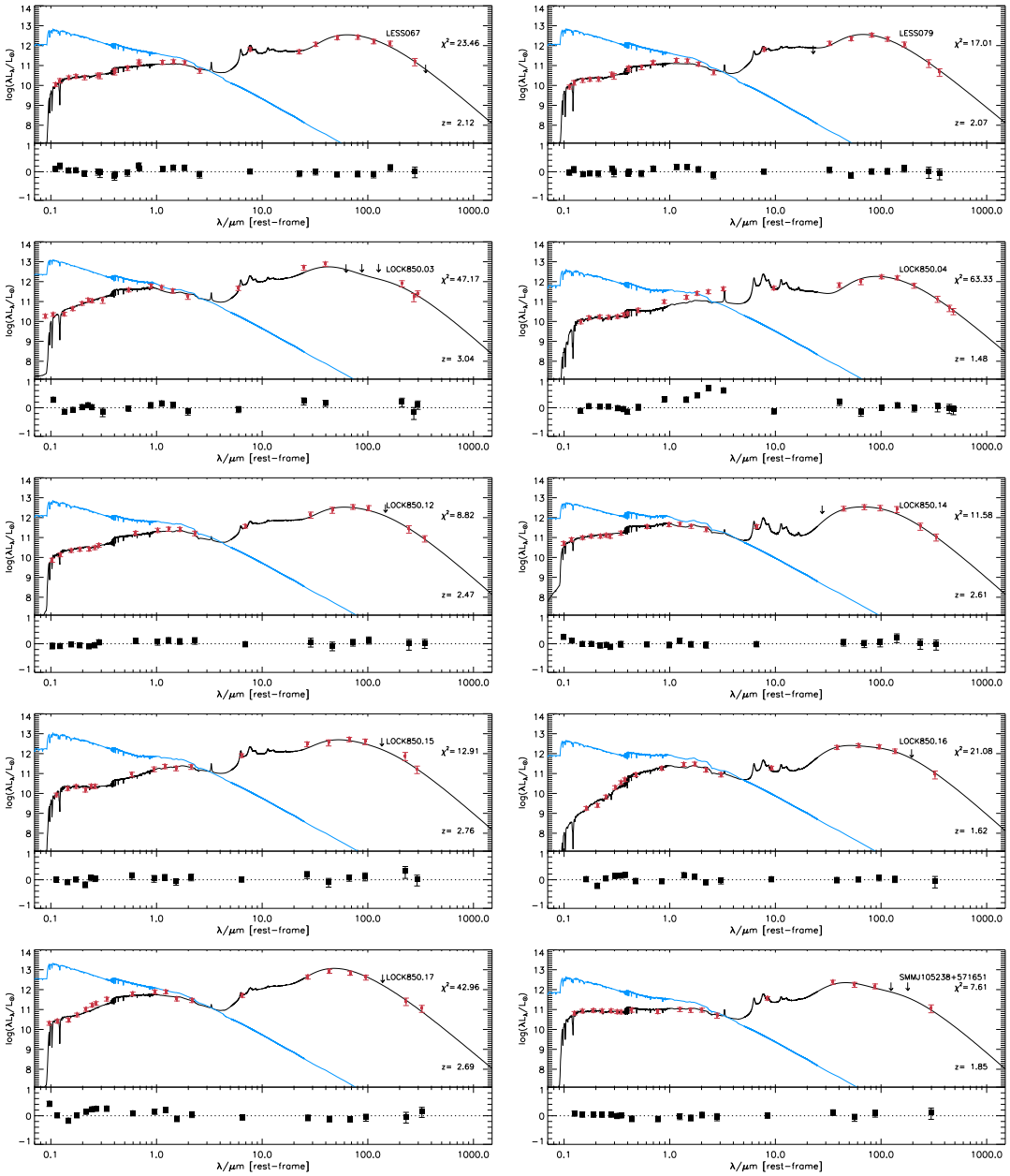

Figure B.1 – *continued*

Bibliography

Abazajian K. N. *et al.*, 2009. ApJS, **182**, 543.

Adelman-McCarthy J. K. *et al.*, 2008. ApJS, **175**, 297.

Agius N. K. *et al.*, 2013. *ArXiv:1302.4276*.

Alexander D. M., Bauer F. E., Chapman S. C., Smail I., Blain A. W., Brandt W. N., Ivison R. J., 2005. ApJ, **632**, 736.

Alton P. B., Davies J. I., Bianchi S., 1999. A&A, **343**, 51.

Alton P. B., Bianchi S., Rand R. J., Xilouris E. M., Davies J. I., Trewhella M., 1998. ApJ, **507**, L125.

Amblard A. *et al.*, 2010. A&A, **518**, L9.

Armus L., Heckman T., Miley G., 1987. AJ, **94**, 831.

Baes M., Verstappen J., De Looze I., Fritz J., Saftly W., Vidal Pérez E., Stalevski M., Valcke S., 2011. ApJS, **196**, 22.

Baldry I. K., Glazebrook K., Brinkmann J., Ivezić Ž., Lupton R. H., Nichol R. C., Szalay A. S., 2004. ApJ, **600**, 681.

Baldry I. K., Balogh M. L., Bower R. G., Glazebrook K., Nichol R. C., Bamford S. P., Budavari T., 2006. MNRAS, **373**, 469.

Baldry I. K. *et al.*, 2010. MNRAS, **404**, 86.

Baldwin J. A., Phillips M. M., Terlevich R., 1981. PASP, **93**, 5.

Bamford S. P. *et al.*, 2009. MNRAS, **393**, 1324.

Banerji M., Chapman S. C., Smail I., Alaghband-Zadeh S., Swinbank A. M., Dunlop J. S., Ivison R. J., Blain A. W., 2011. MNRAS, **418**, 1071.

Barger A. J., Cowie L. L., Wang W.-H., 2008. ApJ, **689**, 687.

Barger A. J., Cowie L. L., Sanders D. B., Fulton E., Taniguchi Y., Sato Y., Kawara K., Okuda H., 1998. Nature, **394**, 248.

Barlow M. J. *et al.*, 2010. A&A, **518**, L138+.

Barnes J. E., Hernquist L., 1992. ARA&A, **30**, 705.

Bastian N., Covey K. R., Meyer M. R., 2010. ARA&A, **48**, 339.

Baugh C. M. *et al.*, 2005. MNRAS, **356**, 1191.

Becker R. H., White R. L., Helfand D. J., 1995. ApJ, **450**, 559.

Bekki K., Couch W. J., Shioya Y., 2002. ApJ, **577**, 651.

Bell E. F. *et al.*, 2004a. ApJ, **600**, L11.

Bell E. F. *et al.*, 2004b. ApJ, **608**, 752.

Bell E. F., 2003. ApJ, **586**, 794.

Bendo G. J. *et al.*, 2003. AJ, **125**, 2361.

Bendo G. J. *et al.*, 2012. MNRAS, **419**, 1833.

Berta S. *et al.*, 2010. A&A, **518**, L30.

Berta S. *et al.*, 2011. A&A, **532**, A49.

Bianchi S., Alton P. B., Davies J. I., Trewhella M., 1998. MNRAS, **298**, L49.

Bianchi S., Schneider R., Valiante R., 2009. In: *Cosmic Dust - Near and Far*, 65, eds Henning T., Grün E., Steinacker J.

Blain A. W., Smail I., Ivison R. J., Kneib J., Frayer D. T., 2002. Phys. Rep., **369**, 111.

Blanton M. R., Roweis S., 2007. AJ, **133**, 734.

Blanton M. R. *et al.*, 2001. AJ, **121**, 2358.

Blanton M. R. *et al.*, 2003. ApJ, **594**, 186.

Bothwell M. S. *et al.*, 2013. MNRAS, **429**, 3047.

Bourne N. *et al.*, 2012. MNRAS, **421**, 3027.

Bouwens R. J., Illingworth G. D., Franx M., Ford H., 2007. ApJ, **670**, 928.

Bouwens R. J. *et al.*, 2009. ApJ, **705**, 936.

Bouwens R. J. *et al.*, 2011. ApJ, **737**, 90.

Bregman J. N., Snider B. A., Grego L., Cox C. V., 1998. ApJ, **499**, 670.

Bressan A., Chiosi C., Fagotto F., 1994. ApJS, **94**, 63.

Bruzual A. G., Charlot S., 1993. ApJ, **405**, 538.

Bruzual G., Charlot S., 2003. MNRAS, **344**, 1000.

Bruzual A. G., 1983. ApJ, **273**, 105.

Buat V. *et al.*, 2005. ApJ, **619**, L51.

Buat V., 2002. Ap&SS, **281**, 129.

Buta R. J., 2011. *ArXiv:1102.0550*.

Calura F., Pipino A., Matteucci F., 2008. A&A, **479**, 669.

Calzetti D., Armus L., Bohlin R. C., Kinney A. L., Koornneef J., Storchi-Bergmann T., 2000. ApJ, **533**, 682.

Calzetti D., Kinney A. L., Storchi-Bergmann T., 1994. ApJ, **429**, 582.

Calzetti D., 2012. *ArXiv:1208.2997*.

Cameron E., 2011. PASA, **28**, 128.

Cappellari M. *et al.*, 2011. MNRAS, **416**, 1680.

Cardelli J. A., Clayton G. C., Mathis J. S., 1989. ApJ, **345**, 245.

Casey C. M. *et al.*, 2013. *ArXiv:1302.2619*.

Chabrier G., 2003. PASP, **115**, 763.

Chapman S. C., Blain A. W., Smail I., Ivison R. J., 2005. ApJ, **622**, 772.

Charlot S., Bruzual A. G., 1991. ApJ, **367**, 126.

Charlot S., Fall S. M., 2000. ApJ, **539**, 718.

Charlot S., Longhetti M., 2001. MNRAS, **323**, 887.

Chary R., Elbaz D., 2001. ApJ, **556**, 562.

Cimatti A. *et al.*, 2004. Nature, **430**, 184.

Colless M. *et al.*, 2001. MNRAS, **328**, 1039.

Combes F., García-Burillo S., Braine J., Schinnerer E., Walter F., Colina L., 2013. A&A, **550**, A41.

Combes F., Young L. M., Bureau M., 2007. MNRAS, **377**, 1795.

Conroy C., Gunn J. E., White M., 2009. ApJ, **699**, 486.

Conroy C., 2013. *ArXiv:1301.7095*.

Coppin K. *et al.*, 2006. MNRAS, **372**, 1621.

Coppin K. *et al.*, 2010. ApJ, **713**, 503.

Cortese L., Hughes T. M., 2009. MNRAS, **400**, 1225.

Cortese L. *et al.*, 2006. ApJ, **637**, 242.

Cortese L., Boselli A., Franzetti P., Decarli R., Gavazzi G., Boissier S., Buat V., 2008. MNRAS, **386**, 1157.

Cortese L. *et al.*, 2010. A&A, **518**, L63+.

Cucciati O. *et al.*, 2012. A&A, **539**, A31.

da Cunha E., Charlot S., Elbaz D., 2008. MNRAS, **388**, 1595.

da Cunha E., Charmandaris V., Díaz-Santos T., Armus L., Marshall J. A., Elbaz D., 2010a. A&A, **523**, A78.

da Cunha E., Eminian C., Charlot S., Blaizot J., 2010b. MNRAS, **403**, 1894.

Dabringhausen J., Kroupa P., Baumgardt H., 2009. MNRAS, **394**, 1529.

Daddi E. *et al.*, 2007. ApJ, **670**, 156.

Daddi E. *et al.*, 2009. ApJ, **694**, 1517.

Dalcanton J. J., 2007. ApJ, **658**, 941.

Dale D. A., Helou G., 2002. ApJ, **576**, 159.

Dale D. A., Helou G., Contursi A., Silbermann N. A., Kolhatkar S., 2001. ApJ, **549**, 215.

Damen M. *et al.*, 2011. ApJ, **727**, 1.

Dariush A. *et al.*, 2011. MNRAS, **418**, 64.

Davé R., Finlator K., Oppenheimer B. D., Fardal M., Katz N., Kereš D., Weinberg D. H., 2010. MNRAS, **404**, 1355.

de Graauw T. *et al.*, 2010. A&A, **518**, L6.

De Propris R., Conselice C. J., Liske J., Driver S. P., Patton D. R., Graham A. W., Allen P. D., 2007. ApJ, **666**, 212.

De Propris R. *et al.*, 2010. AJ, **139**, 794.

de Vaucouleurs G., 1959. *Handbuch der Physik*, **53**, 275.

de Vaucouleurs G., 1974. In: *The Formation and Dynamics of Galaxies*, p. 1, ed. Shakeshaft J. R.

de Zeeuw P. T. *et al.*, 2002. MNRAS, **329**, 513.

Dekel A., Birnboim Y., Engel G., Freundlich J., Goerdt T., Mumcuoglu M., Neistein E., Pichon C., Teyssier R., Zinger E., 2009. Nature, **457**, 451.

Desert F.-X., Boulanger F., Puget J. L., 1990. A&A, **237**, 215.

Devriendt J. E. G., Guiderdoni B., Sadat R., 1999. A&A, **350**, 381.

di Serego Alighieri S. *et al.*, 2013. *ArXiv:1301.2160*.

Diamond-Stanic A. M., Moustakas J., Tremonti C. A., Coil A. L., Hickox R. C., Robaina A. R., Rudnick G. H., Sell P. H., 2012. ApJ, **755**, L26.

D'Odorico V., Cristiani S., Romano D., Granato G. L., Danese L., 2004. MNRAS, **351**, 976.

Donas J., Deharveng J. M., 1984. A&A, **140**, 325.

Downes A. J. B., Peacock J. A., Savage A., Carrie D. R., 1986. MNRAS, **218**, 31.

Draine B. T., Li A., 2007. ApJ, **657**, 810.

Draine B. T., 2009. In: *Cosmic Dust - Near and Far*, p. 453, ed. T. Henning, E. Grün, & J. Steinacker.

Draine B. T., 2011. *Physics of the Interstellar and Intergalactic Medium*.

Dressler A., 1980. ApJ, **236**, 351.

Driver S. P. *et al.*, 2006. MNRAS, **368**, 414.

Driver S. P. *et al.*, 2011. MNRAS, **413**, 971.

Dunlop J., 2001. In: *Deep Millimeter Surveys: Implications for Galaxy Formation and Evolution*, 11, eds Lowenthal J. D., Hughes D. H.

Dunne L., Eales S. A., 2001. MNRAS, **327**, 697.

Dunne L., Eales S. A., Edmunds M. G., 2003. MNRAS, **341**, 589.

Dunne L., Eales S., Edmunds M., Ivison R., Alexander P., Clements D. L., 2000. MNRAS, **315**, 115.

Dunne L., Eales S., Ivison R., Morgan H., Edmunds M., 2003a. Nature, **424**, 285.

Dunne L., Eales S., Ivison R., Morgan H., Edmunds M., 2003b. Nature, **424**, 285.

Dunne L. *et al.*, 2009. MNRAS, **394**, 1307.

Dunne L. *et al.*, 2011. MNRAS, **417**, 1510.

Dutton A. A., van den Bosch F. C., Dekel A., 2010. MNRAS, **405**, 1690.

Dwek E., Scalo J. M., 1980a. ApJ, **239**, 193.

Dwek E., Scalo J. M., 1980b. ApJ, **239**, 193.

Dwek E. *et al.*, 1998. ApJ, **508**, 106.

Dwek E. *et al.*, 2011. ApJ, **738**, 36.

Dwek E., Galliano F., Jones A. P., 2007. ApJ, **662**, 927.

Dwek E., 1998. ApJ, **501**, 643.

Dye S. *et al.*, 2008. MNRAS, **386**, 1107.

Eales S., Lilly S., Gear W., Dunne L., Bond J. R., Hammer F., Le Fèvre O., Crampton D., 1999. ApJ, **515**, 518.

Eales S. *et al.*, 2010a. PASP, **122**, 499.

Eales S. A. *et al.*, 2010b. A&A, **518**, L23.

Edmunds M. G., Eales S. A., 1998. MNRAS, **299**, L29.

Edmunds M. G., 1990. MNRAS, **246**, 678.

Edmunds M. G., 2001. MNRAS, **328**, 223.

Elbaz D. *et al.*, 2007. A&A, **468**, 33.

Elvis M., Marengo M., Karovska M., 2002. ApJ, **567**, L107.

Engel H. *et al.*, 2010. ApJ, **724**, 233.

Erb D. K., Shapley A. E., Pettini M., Steidel C. C., Reddy N. A., Adelberger K. L., 2006. ApJ, **644**, 813.

Erb D. K., 2008. ApJ, **674**, 151.

Faber S. M. *et al.*, 2007. ApJ, **665**, 265.

Fazio G. G. *et al.*, 2004. ApJS, **154**, 10.

Ferrarotti A. S., Gail H.-P., 2006. A&A, **447**, 553.

Fioc M., Rocca-Volmerange B., 1997. A&A, **326**, 950.

Fixsen D. J., Dwek E., Mather J. C., Bennett C. L., Shafer R. A., 1998. ApJ, **508**, 123.

Fontanot F., De Lucia G., Monaco P., Somerville R. S., Santini P., 2009. MNRAS, **397**, 1776.

Fotopoulou S. *et al.*, 2012. ApJS, **198**, 1.

Fukugita M., Nakamura O., Turner E. L., Helmboldt J., Nichol R. C., 2004. ApJ, **601**, L127.

Gall C., Andersen A. C., Hjorth J., 2011. A&A, **528**, A13.

Gall C., Hjorth J., Andersen A. C., 2011. A&A Rev., **19**, 43.

Gallazzi A., Charlot S., Brinchmann J., White S. D. M., Tremonti C. A., 2005. MNRAS, **362**, 41.

Gallazzi A., Brinchmann J., Charlot S., White S. D. M., 2008. MNRAS, **383**, 1439.

Gawiser E. *et al.*, 2006. ApJS, **162**, 1.

Geach J. E., Smail I., Moran S. M., MacArthur L. A., Lagos C. d. P., Edge A. C., 2011. ApJ, **730**, L19.

Gehrels N., 1986. ApJ, **303**, 336.

Genzel R. *et al.*, 1998. ApJ, **498**, 579.

Genzel R. *et al.*, 2010. MNRAS, **407**, 2091.

Georgakakis A., Forbes D. A., Norris R. P., 2000. MNRAS, **318**, 124.

Giavalisco M. *et al.*, 2004. ApJ, **600**, L93.

Giavalisco M. *et al.*, 2011. ApJ, **743**, 95.

Gomez H. L. *et al.*, 2009. MNRAS, **397**, 1621.

Gomez H. L. *et al.*, 2010. A&A, **518**, L45+.

Gomez H. L. *et al.*, 2012a. MNRAS, **420**, 3557.

Gomez H. L. *et al.*, 2012b. ApJ, **760**, 96.

González J. E., Lacey C. G., Baugh C. M., Frenk C. S., 2011. MNRAS, **413**, 749.

Gordon K. D., Clayton G. C., Misselt K. A., Landolt A. U., Wolff M. J., 2003. ApJ, **594**, 279.

Goto T., Yamauchi C., Fujita Y., Okamura S., Sekiguchi M., Smail I., Bernardi M., Gomez P. L., 2003. MNRAS, **346**, 601.

Gott, III J. R., Vogeley M. S., Podariu S., Ratra B., 2001. ApJ, **549**, 1.

Grazian A. *et al.*, 2006. A&A, **449**, 951.

Greve T. R., Ivison R. J., Bertoldi F., Stevens J. A., Dunlop J. S., Lutz D., Carilli C. L., 2004. MNRAS, **354**, 779.

Greve T. R. *et al.*, 2005. MNRAS, **359**, 1165.

Griffin M. J. *et al.*, 2010. A&A, **518**, L3.

Groves B., Dopita M. A., Sutherland R. S., Kewley L. J., Fischera J., Leitherer C., Brandl B., van Breugel W., 2008. ApJS, **176**, 438.

Groves B. *et al.*, 2012. MNRAS, **426**, 892.

Guilloteau S. *et al.*, 1992. A&A, **262**, 624.

Gunawardhana M. L. P. *et al.*, 2011. MNRAS, **415**, 1647.

Gunn J. E., Gott, III J. R., 1972. ApJ, **176**, 1.

Hainline L. J., Blain A. W., Smail I., Frayer D. T., Chapman S. C., Ivison R. J., Alexander D. M., 2009. ApJ, **699**, 1610.

Hainline L. J., Blain A. W., Smail I., Alexander D. M., Armus L., Chapman S. C., Ivison R. J., 2011. ApJ, **740**, 96.

Häring N., Rix H.-W., 2004. ApJ, **604**, L89.

Harrison C. M. *et al.*, 2012. MNRAS, **426**, 1073.

Hatziminaoglou E. *et al.*, 2010. A&A, **518**, L33+.

Hawarden T. G., Longmore A. J., Tritton S. B., Elson R. A. W., Corwin, Jr. H. G., 1981. MNRAS, **196**, 747.

Hayward C. C., Kereš D., Jonsson P., Narayanan D., Cox T. J., Hernquist L., 2011. ApJ, **743**, 159.

Hayward C. C., Narayanan D., Kereš D., Jonsson P., Hopkins P. F., Cox T. J., Hernquist L., 2013. MNRAS, **428**, 2529.

Heavens A., Panter B., Jimenez R., Dunlop J., 2004. Nature, **428**, 625.

Heckman T. M., Lehnert M. D., Strickland D. K., Armus L., 2000. ApJS, **129**, 493.

Helou G., Soifer B. T., Rowan-Robinson M., 1985. ApJ, **298**, L7.

Hickox R. C. *et al.*, 2012. MNRAS.

Hill D. T. *et al.*, 2011. MNRAS, **412**, 765.

Hilton M. *et al.*, 2012. MNRAS, **425**, 540.

Hirashita H., Kuo T.-M., 2011. MNRAS, **416**, 1340.

Ho P. T. P., Moran J. M., Lo K. Y., 2004. ApJ, **616**, L1.

Holland W. S. *et al.*, 1999. MNRAS, **303**, 659.

Hopkins A. M. *et al.*, 2003. ApJ, **599**, 971.

Hopkins A. M. *et al.*, 2013. MNRAS.

Hubble E. P., 1926. ApJ, **64**, 321.

Hughes T. M., Cortese L., 2009. MNRAS, **396**, L41.

Hughes D. H. *et al.*, 1998. Nature, **394**, 241.

Ibar E. *et al.*, 2010. MNRAS, **409**, 38.

Iben, Jr. I., Tutukov A. V., 1984. ApJS, **54**, 335.

Ilbert O. *et al.*, 2009. ApJ, **690**, 1236.

Inoue A. K., 2012. *ArXiv:1202.2932*.

Ivison R. J. *et al.*, 2004. ApJS, **154**, 124.

Johnson B. D. *et al.*, 2007. ApJS, **173**, 392.

Jones A. P., Nuth J. A., 2011. A&A, **530**, A44.

Jones A. P., 2004. In: *Astrophysics of Dust*, 347, eds Witt A. N., Clayton G. C., Draine B. T.

Kannappan S. J., Guie J. M., Baker A. J., 2009. AJ, **138**, 579.

Kauffmann G. *et al.*, 2003a. MNRAS, **341**, 54.

Kauffmann G. *et al.*, 2003b. MNRAS, **346**, 1055.

Kaviraj S. *et al.*, 2007. ApJS, **173**, 619.

Kaviraj S. *et al.*, 2008. MNRAS, **388**, 67.

Kaviraj S., Peirani S., Khochfar S., Silk J., Kay S., 2009. MNRAS, **394**, 1713.

Kaviraj S., Tan K.-M., Ellis R. S., Silk J., 2011. MNRAS, **411**, 2148.

Kaviraj S. *et al.*, 2012. MNRAS, **423**, 49.

Kaviraj S., 2010. MNRAS, **406**, 382.

Kawara K. *et al.*, 2010. MNRAS, **402**, 335.

Kelvin L. S. *et al.*, 2012. MNRAS, **421**, 1007.

Kennicutt R. C., Evans N. J., 2012. ARA&A, **50**, 531.

Kennicutt, Jr. R. C., 1998a. ARA&A, **36**, 189.

Kennicutt, Jr. R. C., 1998b. ApJ, **498**, 541.

Kereš D., Katz N., Weinberg D. H., Davé R., 2005. MNRAS, **363**, 2.

Kessler M. F. *et al.*, 1996. A&A, **315**, L27.

Kewley L. J., Heisler C. A., Dopita M. A., Lumsden S., 2001. ApJS, **132**, 37.

Kewley L. J., Groves B., Kauffmann G., Heckman T., 2006. MNRAS, **372**, 961.

Kong X., Charlot S., Brinchmann J., Fall S. M., 2004. MNRAS, **349**, 769.

Kormendy J., Bender R., 2012. ApJS, **198**, 2.

Kozasa T., Nozawa T., Tominaga N., Umeda H., Maeda K., Nomoto K., 2009. In: *Cosmic Dust - Near and Far*, 43, eds Henning T., Grün E., Steinacker J.

Krause O., Birkmann S. M., Rieke G. H., Lemke D., Klaas U., Hines D. C., Gordon K. D., 2004. Nature, **432**, 596.

Kreysa E. *et al.*, 1998. In: *Society of Photo-Optical Instrumentation Engineers (SPIE) Conference Series*, p. 319, ed. Phillips T. G.

Kroupa P., 2012. *ArXiv:1210.1211*.

Krumholz M. R., Dekel A., 2010. MNRAS, **406**, 112.

Kuo T.-M., Hirashita H., 2012. MNRAS, **424**, L34.

Lanz L. *et al.*, 2013. *ArXiv:1302.5011*.

Lapi A. *et al.*, 2011. ApJ, **742**, 24.

Larson R. B., Tinsley B. M., Caldwell C. N., 1980. ApJ, **237**, 692.

Lawrence A. *et al.*, 2007. MNRAS, **379**, 1599.

Le Floc'h E. *et al.*, 2005. ApJ, **632**, 169.

Lee S.-K., Ferguson H. C., Somerville R. S., Wiklind T., Giavalisco M., 2010. ApJ, **725**, 1644.

Leeuw L. L., Sansom A. E., Robson E. I., Haas M., Kuno N., 2004. ApJ, **612**, 837.

Leeuw L. L., Davidson J., Dowell C. D., Matthews H. E., 2008. ApJ, **677**, 249.

Leitherer C. *et al.*, 1999. ApJS, **123**, 3.

Lilly S. J., Le Fevre O., Hammer F., Crampton D., 1996. ApJ, **460**, L1.

Lintott C. J. *et al.*, 2008. MNRAS, **389**, 1179.

Lintott C. *et al.*, 2011. MNRAS, **410**, 166.

Lo Faro B. *et al.*, 2013. ApJ, **762**, 108.

Lotz J. M. *et al.*, 2008. ApJ, **672**, 177.

Lutz D., Spoon H. W. W., Rigopoulou D., Moorwood A. F. M., Genzel R., 1998. ApJ, **505**, L103.

Lutz D. *et al.*, 2011. A&A, **532**, A90.

Madau P., Ferguson H. C., Dickinson M. E., Giavalisco M., Steidel C. C., Fruchter A., 1996. MNRAS, **283**, 1388.

Maeder A., 1992. A&A, **264**, 105.

Magdis G. E. *et al.*, 2012. ApJ, **760**, 6.

Magnelli B., Elbaz D., Chary R. R., Dickinson M., Le Borgne D., Frayer D. T., Willmer C. N. A., 2009. A&A, **496**, 57.

Magnelli B., Elbaz D., Chary R. R., Dickinson M., Le Borgne D., Frayer D. T., Willmer C. N. A., 2011. A&A, **528**, A35.

Magnelli B. *et al.*, 2012. A&A, **539**, A155.

Magorrian J. *et al.*, 1998. AJ, **115**, 2285.

Maiolino R. *et al.*, 2006. Mem. Soc. Astron. Italiana, **77**, 643.

Malmquist K. G., 1922. *Lund Medd. Ser. I*, **100**, 1.

Maraston C., Pforr J., Renzini A., Daddi E., Dickinson M., Cimatti A., Tonini C., 2010. MNRAS, **407**, 830.

Maraston C., 1998. MNRAS, **300**, 872.

Maraston C., 2005. MNRAS, **362**, 799.

Marigo P., Girardi L., 2007. A&A, **469**, 239.

Marigo P., 2000. A&A, **360**, 617.

Martin D. C. *et al.*, 2005. ApJ, **619**, L1.

Masters K. L. *et al.*, 2010a. MNRAS, **404**, 792.

Masters K. L. *et al.*, 2010b. MNRAS, **405**, 783.

Mathis J. S., Rumpl W., Nordsieck K. H., 1977. ApJ, **217**, 425.

Matsuura M. *et al.*, 2009. MNRAS, **396**, 918.

Matsuura M. *et al.*, 2011. *Science*, **333**, 1258.

Mattsson L., Andersen A. C., Munkhammar J. D., 2012. MNRAS, **423**, 26.

McKee C., 1989. In: *Interstellar Dust*, 431, eds Allamandola L. J., Tielens A. G. G. M.

Ménard B., Scranton R., Fukugita M., Richards G., 2010. MNRAS, **405**, 1025.

Menéndez-Delmestre K. *et al.*, 2009. ApJ, **699**, 667.

Meurer G. R., Heckman T. M., Calzetti D., 1999. ApJ, **521**, 64.

Michałowski M. J., Murphy E. J., Hjorth J., Watson D., Gall C., Dunlop J. S., 2010. A&A, **522**, A15.

Michałowski M. J., Dunlop J. S., Cirasuolo M., Hjorth J., Hayward C. C., Watson D., 2012. A&A, **541**, A85.

Michałowski M., Hjorth J., Watson D., 2010. A&A, **514**, A67+.

Michałowski M. J., Watson D., Hjorth J., 2010. ApJ, **712**, 942.

Moore B., Lake G., Katz N., 1998. ApJ, **495**, 139.

Moorwood A. F. M., 1996. Space Sci. Rev., **77**, 303.

Morgan H. L., Edmunds M. G., 2003. MNRAS, **343**, 427.

Morrissey P. *et al.*, 2007. ApJS, **173**, 682.

Mortier A. M. J. *et al.*, 2005. MNRAS, **363**, 563.

Moshir M., Kopman G., Conrow T. A. O., 1992. *IRAS Faint Source Survey, Explanatory supplement version 2*.

Murphy, Jr. T. W., Armus L., Matthews K., Soifer B. T., Mazzarella J. M., Shupe D. L., Strauss M. A., Neugebauer G., 1996. AJ, **111**, 1025.

Murphy E. J., Chary R.-R., Dickinson M., Pope A., Frayer D. T., Lin L., 2011. ApJ, **732**, 126.

Nagao T., Maiolino R., De Breuck C., Caselli P., Hatsukade B., Saigo K., 2012. A&A, **542**, L34.

Narayanan D., Davé R., 2012. *ArXiv:1210.6037*.

Negrello M. *et al.*, 2010. *Science*, **330**, 800.

Netzer H. *et al.*, 2007. ApJ, **666**, 806.

Neugebauer G. *et al.*, 1984. ApJ, **278**, L1.

Noeske K. G. *et al.*, 2007. ApJ, **660**, L43.

Noll S., Burgarella D., Giovannoli E., Buat V., Marcillac D., Muñoz-Mateos J. C., 2009. A&A, **507**, 1793.

Nonino M. *et al.*, 2009. ApJS, **183**, 244.

Nozawa T., Kozasa T., Umeda H., Maeda K., Nomoto K., 2003. ApJ, **598**, 785.

Nyman L.-Å., Andreani P., Hibbard J., Okumura S. K., 2010. In: *Society of Photo-Optical Instrumentation Engineers (SPIE) Conference Series*.

O'Connell R. W., 1999. ARA&A, **37**, 603.

Oliver S. J. *et al.*, 2012. MNRAS, **424**, 1614.

Oort J. H., van de Hulst H. C., 1946. Bull. Astron. Inst. Netherlands, **10**, 187.

Pagel B. E. J., Patchett B. E., 1975. MNRAS, **172**, 13.

Pagel B. E. J., 1997. *Nucleosynthesis and Chemical Evolution of Galaxies*.

Panter B., Jimenez R., Heavens A. F., Charlot S., 2007. MNRAS, **378**, 1550.

Papadopoulos P. P., Thi W.-F., Miniati F., Viti S., 2011. MNRAS, **414**, 1705.

Papovich C., Finkelstein S. L., Ferguson H. C., Lotz J. M., Giavalisco M., 2011. MNRAS, **412**, 1123.

Paradis D. *et al.*, 2010. A&A, **520**, L8.

Pascale E. o., 2011. MNRAS, **415**, 911.

Pei Y. C., 1992. ApJ, **395**, 130.

Peng Y.-j. *et al.*, 2010. ApJ, **721**, 193.

Pérez-González P. G. *et al.*, 2008. ApJ, **675**, 234.

Petrosian V., 1976. ApJ, **209**, L1.

Pilbratt G. L. *et al.*, 2010. A&A, **518**, L1+.

Pipino A., D'Ercole A., Chiappini C., Matteucci F., 2010. MNRAS, **407**, 1347.

Pipino A., Fan X. L., Matteucci F., Calura F., Silva L., Granato G., Maiolino R., 2011. A&A, **525**, A61.

Planck Collaboration *et al.*, 2011. A&A, **536**, A25.

Poggianti B. M., Smail I., Dressler A., Couch W. J., Barger A. J., Butcher H., Ellis R. S., Oemler, Jr. A., 1999. ApJ, **518**, 576.

Poggianti B. M., Bridges T. J., Komiyama Y., Yagi M., Carter D., Mobasher B., Okamura S., Kashikawa N., 2004. ApJ, **601**, 197.

Poglitsch A. *et al.*, 2010. A&A, **518**, L2+.

Pope A. *et al.*, 2008. ApJ, **675**, 1171.

Popescu C. C., Tuffs R. J., 2002. MNRAS, **335**, L41.

Popescu C. C., Misiriotis A., Kylafis N. D., Tuffs R. J., Fischera J., 2000. A&A, **362**, 138.

Pozzi F. *et al.*, 2012. MNRAS, **423**, 1909.

Puget J.-L., Abergel A., Bernard J.-P., Boulanger F., Burton W. B., Desert F.-X., Hartmann D., 1996. A&A, **308**, L5.

Reach W. T. *et al.*, 1995. ApJ, **451**, 188.

Reddy N. A., Pettini M., Steidel C. C., Shapley A. E., Erb D. K., Law D. R., 2012. ApJ, **754**, 25.

Rho J. *et al.*, 2008. ApJ, **673**, 271.

Rho J., Reach W. T., Tappe A., Hwang U., Slavin J. D., Kozasa T., Dunne L., 2009. ApJ, **700**, 579.

Riechers D. A. *et al.*, 2011. ApJ, **733**, L11.

Rieke G. H. *et al.*, 2004. ApJS, **154**, 25.

Rieke G. H., Alonso-Herrero A., Weiner B. J., Pérez-González P. G., Blaylock M., Donley J. L., Marcillac D., 2009. ApJ, **692**, 556.

Rigby E. E. *et al.*, 2011. MNRAS, **415**, 2336.

Roberts M. S., Haynes M. P., 1994. ARA&A, **32**, 115.

Robotham A. *et al.*, 2010. PASA, **27**, 76.

Rodighiero G. *et al.*, 2010. A&A, **518**, L25.

Rodighiero G. *et al.*, 2011. ApJ, **739**, L40.

Roseboom I. G. *et al.*, 2010. MNRAS, **409**, 48.

Roseboom I. G. *et al.*, 2012. MNRAS, **426**, 1782.

Rowlands K. *et al.*, 2012. MNRAS, **419**, 2545.

Rubin K. H. R., Weiner B. J., Koo D. C., Martin C. L., Prochaska J. X., Coil A. L., Newman J. A., 2010. ApJ, **719**, 1503.

Sadler E. M., Gerhard O. E., 1985. MNRAS, **214**, 177.

Sakamoto K., Aalto S., Costagliola F., Martín S., Ohyama Y., Wiedner M. C., Wilner D. J., 2013. ApJ, **764**, 42.

Salim S. *et al.*, 2007. ApJS, **173**, 267.

Salvato M. *et al.*, 2009. ApJ, **690**, 1250.

Sanders D. B., Mirabel I. F., 1996. ARA&A, **34**, 749.

Sanders D. B., Soifer B. T., Elias J. H., Madore B. F., Matthews K., Neugebauer G., Scoville N. Z., 1988. ApJ, **325**, 74.

Santini P. *et al.*, 2010. A&A, **518**, L154.

Savage B. D., Sembach K. R., 1996. ARA&A, **34**, 279.

Savoy J., Welch G. A., Fich M., 2009. ApJ, **706**, 21.

Schaller G., Schaerer D., Meynet G., Maeder A., 1992. A&AS, **96**, 269.

Schawinski K. *et al.*, 2007a. ApJS, **173**, 512.

Schawinski K., Thomas D., Sarzi M., Maraston C., Kaviraj S., Joo S., Yi S. K., Silk J., 2007b. MNRAS, **382**, 1415.

Schawinski K. *et al.*, 2009. MNRAS, **396**, 818.

Schlegel D. J., Finkbeiner D. P., Davis M., 1998. ApJ, **500**, 525.

Scott S. E. *et al.*, 2002. MNRAS, **331**, 817.

Searle L., Sargent W. L. W., 1972. ApJ, **173**, 25.

Shapiro K. L. *et al.*, 2010. MNRAS, **402**, 2140.

Siebenmorgen R., Krügel E., 2007. A&A, **461**, 445.

Silva L., Granato G. L., Bressan A., Danese L., 1998. ApJ, **509**, 103.

Skibba R. A. *et al.*, 2009. MNRAS, **399**, 966.

Skibba R. A. *et al.*, 2011. ApJ, **738**, 89.

Smail I., Ivison R. J., Blain A. W., 1997. ApJ, **490**, L5+.

Smith D. J. B. *et al.*, 2011. MNRAS, **416**, 857.

Smith A. J. *et al.*, 2012a. MNRAS, **419**, 377.

Smith D. J. B. *et al.*, 2012b. MNRAS, **427**, 703.

Smith M. W. L. *et al.*, 2012c. ApJ, **748**, 123.

Sobral D., Best P. N., Matsuda Y., Smail I., Geach J. E., Cirasuolo M., 2012. MNRAS, **420**, 1926.

Soifer B. T. *et al.*, 1984. ApJ, **278**, L71.

Soifer B. T., Neugebauer G., Houck J. R., 1987. ARA&A, **25**, 187.

Springel V. *et al.*, 2005. Nature, **435**, 629.

Stickel M., Klaas U., Lemke D., 2007. A&A, **466**, 831.

Stoughton C. s., 2002. AJ, **123**, 485.

Strateva I. *et al.*, 2001. AJ, **122**, 1861.

Sturm E. *et al.*, 2011. ApJ, **733**, L16.

Sugerman B. E. K. *et al.*, 2006. *Science*, **313**, 196.

Sutherland W., Saunders W., 1992. MNRAS, **259**, 413.

Swinbank A. M., Smail I., Chapman S. C., Blain A. W., Ivison R. J., Keel W. C., 2004. ApJ, **617**, 64.

Swinbank A. M., Chapman S. C., Smail I., Lindner C., Borys C., Blain A. W., Ivison R. J., Lewis G. F., 2006. MNRAS, **371**, 465.

Symeonidis M. *et al.*, 2013. MNRAS.

Tacconi L. J. *et al.*, 2006. ApJ, **640**, 228.

Tacconi L. J. *et al.*, 2008. ApJ, **680**, 246.

Tacconi L. J. *et al.*, 2012. *ArXiv:1211.5743*.

Targett T. A. *et al.*, 2012. *ArXiv:1208.3464*.

Taylor E. N. *et al.*, 2009. ApJS, **183**, 295.

Tecza M. *et al.*, 2004. ApJ, **605**, L109.

Temi P., Brighenti F., Mathews W. G., 2007. ApJ, **660**, 1215.

Temi P., Brighenti F., Mathews W. G., 2009a. ApJ, **695**, 1.

Temi P., Brighenti F., Mathews W. G., 2009b. ApJ, **707**, 890.

Temi P., Brighenti F., Mathews W. G., Bregman J. D., 2004. ApJS, **151**, 237.

Temim T., Sonneborn G., Dwek E., Arendt R. G., Gehrz R. D., Slane P., Roellig T. L., 2012. ApJ, **753**, 72.

Thomas D., Maraston C., Bender R., Mendes de Oliveira C., 2005. ApJ, **621**, 673.

Tielens A. G. G. M., Allamandola L. J., 1987. In: *Interstellar Processes*, p. 397, eds Hollenbach D. J., Thronson, Jr. H. A.

Tielens A. G. G. M., Whittet D. C. B., 1997. In: *IAU Symposium*, 45, ed. van Dishoeck E. F.

Tielens A. G. G. M., 1998. ApJ, **499**, 267.

Tinsley B. M., Gunn J. E., 1976. ApJ, **203**, 52.

Tinsley B. M., 1978. ApJ, **222**, 14.

Tinsley B. M., 1980. Fund. Cosmic Phys., **5**, 287.

Todini P., Ferrara A., 2001. MNRAS, **325**, 726.

Tremonti C. A. *et al.*, 2004. ApJ, **613**, 898.

Tresse L., Maddox S., Loveday J., Singleton C., 1999. MNRAS, **310**, 262.

Trumpler R. J., 1930. PASP, **42**, 214.

van de Hulst H. C., 1946. *Recherches Astronomiques de l'Observatoire d'Utrecht*, **11**, 2.

van de Voort F., Schaye J., Booth C. M., Haas M. R., Dalla Vecchia C., 2011. MNRAS, **414**, 2458.

van den Bergh S., 1962. AJ, **67**, 486.

van den Bergh S., 1976. ApJ, **206**, 883.

van Dokkum P. G., Franx M., 1995. AJ, **110**, 2027.

Vazdekis A., Sánchez-Blázquez P., Falcón-Barroso J., Cenarro A. J., Beasley M. A., Cardiel N., Gorgas J., Peletier R. F., 2010. MNRAS, **404**, 1639.

Vazdekis A., 1999. ApJ, **513**, 224.

Vlahakis C., Dunne L., Eales S., 2005. MNRAS, **364**, 1253.

Walcher C. J. *et al.*, 2008. A&A, **491**, 713.

Walcher J., Groves B., Budavári T., Dale D., 2011. Ap&SS, **331**, 1.

Wang W.-H., Cowie L. L., Barger A. J., Keenan R. C., Ting H.-C., 2010. ApJS, **187**, 251.

Wang W.-H., Cowie L. L., Barger A. J., Williams J. P., 2011. ApJ, **726**, L18.

Wardlow J. L. *et al.*, 2011. MNRAS, **415**, 1479.

Wei L. H., Kannappan S. J., Vogel S. N., Baker A. J., 2010. ApJ, **708**, 841.

Weiner B. J. *et al.*, 2009. ApJ, **692**, 187.

Weiß A. *et al.*, 2009. ApJ, **707**, 1201.

Whitaker K. E., van Dokkum P. G., Brammer G., Franx M., 2012. ApJ, **754**, L29.

White S. D. M., Rees M. J., 1978. MNRAS, **183**, 341.

ed. Whittet D. C. B. *Dust in the galactic environment*, 2003.

Wijesinghe D. B. *et al.*, 2011. MNRAS, **410**, 2291.

Wild V., Walcher C. J., Johansson P. H., Tresse L., Charlot S., Pollo A., Le Fèvre O., de Ravel L., 2009. MNRAS, **395**, 144.

Witt A. N., Thronson, Jr. H. A., Capuano, Jr. J. M., 1992. ApJ, **393**, 611.

Wolf C. *et al.*, 2009. MNRAS, **393**, 1302.

Wolf C., Gray M. E., Meisenheimer K., 2005. A&A, **443**, 435.

Worthey G., 1994. ApJS, **95**, 107.

Xilouris E. M., Alton P. B., Davies J. I., Kylafis N. D., Papamastorakis J., Trewhella M., 1998. A&A, **331**, 894.

Xilouris E. M., Georgakakis A. E., Misiriotis A., Charmandaris V., 2004. MNRAS, **355**, 57.

Yasuda N. *et al.*, 2001. AJ, **122**, 1104.

Yi S., Demarque P., Oemler, Jr. A., 1997. ApJ, **486**, 201.

Yi S. K. *et al.*, 2005. ApJ, **619**, L111.

York D. G. *et al.*, 2000. AJ, **120**, 1579.

Young L. M. *et al.*, 2011. MNRAS, **414**, 940.

Zhukovska S., Gail H.-P., Trieloff M., 2008. A&A, **479**, 453.